Self-Regulation of Star Formation and Outflows in the Low-Metallicity Interstellar Medium

INAUGURAL DISSERTATION

zur

Erlangung des Doktorgrades
der Mathematisch-Naturwissenschaftlichen Fakultät
der Universität zu Köln

vorgelegt von

Vittoria Brugaletta
aus Ragusa, Italien

angenommen im Jahr 2025

Berichterstatter (Gutachter):
Prof. Dr. Stefanie Walch-Gassner
Prof. Dr. Peter Schilke

La filosofia [della natura] è scritta in questo grandissimo libro che continuamente ci sta aperto dinanzi a gli occhi (io dico l'universo), ma non si può intendere se prima non s'impara a intender la lingua, e conoscere i caratteri ne' quali è scritto. Egli è scritto in lingua matematica, e i caratteri son triangoli, cerchi, ed altre figure geometriche, senza i quali mezi [sic] è impossibile a intenderne umanamente parola; senza questi è un aggirarsi vanamente per un oscuro laberinto.

Il Saggiatore, Galileo Galilei

Philosophy is written in this grand book, the universe, which stands continually open to our gaze. But the book cannot be understood unless one first learns to comprehend the language and read the letters in which it is composed. It is written in the language of mathematics, and its characters are triangles, circles and others geometric figures without which it is humanly impossible to understand a single word of it; without these, one wanders about in a dark labyrinth.

Translation by S. Drake [1]

---

[1] *Discoveries and Opinions of Galileo*, pp. 237–238.

Abstract

The evolution of the interstellar medium (ISM) and the self-regulation of star formation in low-metallicity environments remain open questions. These processes are crucial for understanding galaxy evolution in nearby dwarf galaxies, in the outer regions of the Milky Way, and in high-redshift galaxies. This thesis investigates the structure and evolution of the metal-poor ISM using magneto-hydrodynamic simulations of stratified ISM patches within the SILCC framework. The simulations include non-equilibrium chemistry, ISM heating and cooling, anisotropic cosmic ray (CR) transport, and comprehensive stellar feedback (stellar winds, far-UV and ionising radiation, supernovae, and CR injection). Following a bottom-up approach, we first examine the role of CR heating in the metal-poor gas by introducing a novel model that self-consistently derives the CR ionisation rate from the simulated CR energy density, allowing for spatial and temporal variability. We find that, due to the low dust content, CR heating can dominate over photoelectric heating in such environments. We then explore the effect of varying metallicity (from 0.02 to 1 $Z_{\odot}$) on the ISM structure and star formation. We find that lower metallicities reduce the mass fraction of cold and molecular (H_2) gas, but the star formation and mass outflow rates remain similar for $Z > 0.1\ \mathrm{Z}\odot$, with a decline only at lower metallicities. Building on these results, we apply our CR heating model in a broader investigation of star formation self-regulation and the possibility of the ISM reaching a steady state. We test with our simulations the "Pressure-Regulated, Feedback-Modulated" (PRFM) star formation theory, which assumes the ISM to be in a steady state, reproducing its numerical predictions. However, we argue that the ISM in our simulations is not in true steady state, as we observe strong feedback-driven outflows. We also analyse the properties of these outflows and find that the mass outflow rate at 1 kpc lags the star formation rate by approximately 15 Myr. Overall, this work highlights the importance of metallicity in shaping the ISM, and contributes to our understanding of the self-regulation of star formation and feedback-driven outflows, across galactic environments.

Contents

CHAPTER 1

INTRODUCTION

Since the dawn of humanity, we have gazed at the night sky with wonder. The bright, mysterious points of light, which we now know to be stars, have always seemed distant and removed from our everyday lives. Yet, in recent centuries, we have developed powerful tools to peer deeper into the universe, offering us unprecedented insights into the cosmos. This technological progress has granted us the extraordinary ability to look at celestial objects like stars, galaxies, and quasars in ways once thought impossible. With the construction of modern telescopes, we can now observe objects farther and farther away, effectively allowing us to look back in time at the universe's past. What did ancient galaxies and stars look like? How similar is the early universe to the one we observe today? And, if there are differences, what drives these changes?

Historically, observations have focused on galaxies within our cosmic neighborhood. However, with the advent of the James Webb Space Telescope (JWST), we are now able to study incredibly distant galaxies with unparalleled resolution. These far-off galaxies are known to be predominantly low-metallicity environments (Schneider, 2015), meaning regions where the abundance of elements heavier than hydrogen and helium is far lower than in galaxies like our own Milky Way. On the theoretical front, most studies have been confined to the properties of the solar neighborhood, which do not adequately capture the unique characteristics of metal-poor galaxies. While some work has attempted to address aspects of low-metallicity environments, the full complexity of these systems remains largely unexplored. To make sense of the extraordinary data provided by JWST, it is now imperative that we advance our theoretical models to better describe and understand these fascinating environments.

The structure and evolution of the low-metallicity interstellar medium (ISM) can be investigated through simulations, since they provide a time evolution and allow us to isolate and study the impact of varying physical parameters. In this thesis, we employ SILCC simulations (see Chapter 3) to model these environments in greater detail. The research is divided into three main papers, following a bottom-up approach. In Chapter 4 (Paper I), we focus on the dominant heating mechanisms in low-metallicity environments, to investigate how they affect the overall cooling of the gas. Specifically, we show that heating from low-energy cosmic rays surpasses the role of photoelectric heating, unlike in solar-neighborhood conditions. We propose a more accurate model for cosmic-ray heating and test its effects in an extremely metal-poor environment, where these influences are most pronounced. In Chapter 5 (Paper II), we use this updated model to understand how metallicity affects the properties of the ISM, meaning its structure, evolution, star formation history, and outflows, simulating environments with a range of metallicities. Finally, in Chapter 6 (Paper III), we build on the findings of Papers I and II to explore the relationship between star formation and the presence of cold gas. We challenge the traditional dynamical equilibrium theory of star formation on the spatial scales covered by our simulations. Moreover, we investigate the relation between the star formation and mass outflow rates, and how their variability drives the evolution of the ISM. Through these works, we offer both theorists and observers new insights into the behavior of low-metallicity ISM, providing a foundation for future research to decode the mysteries of these intriguing environments.

This thesis is structured as follows: In Chapter 2, we introduce the key concepts and summarize previous works necessary to understand the research. In Chapter 3, we describe our simulation code, setup, and the newly developed cosmic-ray heating model from Paper I. This chapter also includes a brief overview of the dendrogram algorithm used to analyze the fragmentation of the ISM in Paper II. In Chapters 4-6, we present the results of the three papers, detailing our findings. Finally, in Chapter 7, we offer our conclusions.

CHAPTER 2

THEORETICAL BACKGROUND

In this chapter we briefly introduce the key concepts underlying this thesis. Sec. 2.1 describes the interstellar medium and its components, while Sec. 2.2 outlines the main feedback processes considered in our simulations. A summary of our current understanding of low-metallicity environments is provided in Sec. 2.3, and the theoretical framework of the pressure-regulated, feedback-modulated theory, tested in Paper III, is presented in Sec. 2.4.

2.1 The interstellar medium

Figure 2.1

Image of the Tarantula Nebula, as captured by the Near-Infrared Camera (NIRCam) of the James Webb Space Telescope. Credit: NASA, ESA, CSA, and STScI.

DEFINITION 1 *The interstellar medium (ISM) is the ensemble of gas, dust, cosmic rays, magnetic fields and radiation fields that fills the space among stars in a galaxy. It plays a key role in regulating star formation, governing chemical evolution and shaping the energy balance of a galaxy.*

2.1.1 The interstellar gas

In this section, we describe the composition and density distribution of the interstellar medium, as well as some of its most important constituents.

Composition

The interstellar gas can be described in terms of its density, temperature, chemical composition, ionization degree, etc. As such, the characteristics of the gas can change dramatically depending on the environment considered. For example, according to Draine (2011), the total mass of our Milky Way is around 10^{11} $M_\odot$ within 15 kpc from the Galactic centre, of which 5×10^{10} $M_\odot$ is in stars, 5×10^{10} $M_\odot$ in dark matter, and 7×10^{9} $M_\odot$ in gas. The latter is mainly composed of hydrogen (70% by mass) and helium (28% by mass), with around 2% by mass of heavier elements, the so-called "metals". The precise composition of the interstellar medium in the solar neighbourhood is uncertain, and therefore it is assumed to be similar to that of the Sun, according to the measurements reported in Asplund et al. (2009). However, the interstellar medium in other galaxies might have different features, such as a different chemical composition. In fact, the chemical enrichment of galaxies is driven by supernovae (Nanni et al., 2020) and stellar winds (Marigo, 2001), which release heavy elements into the surrounding gas, affecting the formation of new stars. Therefore, different star formation histories lead to variations in enrichment of the medium. Over time, as stars evolve, the metallicity of the gas increases, affecting its cooling efficiency. However, metals can be locked in dust, or they can be removed via galactic winds, which carry away part of the midplane gas, causing the metal abundances to decrease. We will treat low-metallicity environments in more detail in Sec. 2.3.

Molecular clouds

Within a galaxy, the density distribution of the interstellar medium covers several orders of magnitude, spanning from 10^{-3}–10^{-2} particles/cm^3, to very dense regions, with densities of 10^3–10^6 particles/cm^3 (Draine, 2011). The former are usually characterized by the presence of diffuse, warm and hot gas, while the latter are associated with cold, molecular gas.

Molecular clouds, in particular, play a vital role in the evolution of a galaxy, as they are the place where stars can form. These clouds exhibit filamentary structures (André et al., 2010; Hacar et al., 2023), internally shaped by turbulence (Smith et al., 2016), shocks and gravity (Ganguly et al., 2023), and possibly maintained by magnetic fields (Hennebelle, 2013). Moreover, filaments in turbulent clouds are composed of networks of smaller subfilaments, which can fragment into star-forming cores (Smith et al., 2016). For a complete overview of the latest studies on molecular gas, the reader is referred to Chevance et al. (2020, 2023).

H II regions

H II regions are the regions in the interstellar medium surrounding massive stars, predominantly O and B type stars, which emit UV photons, capable of ionising the hydrogen gas at energies of 13.6 eV and above. H II regions have temperatures ranging from 7000 to 15000 K, depending on the metallicity of the gas and the temperature of the exciting star (Draine, 2011). The process opposite to photoionization, radiative recombination, occurs when thermal electrons recombine with protons, leading to neutralization. The balance between photoionization and radiative recombination determines the temperature and ionization state of the H II region.

H II regions are often associated with places of massive star-formation, where the newly-formed stars are embedded in cold, dense gas. As such, they are good tracers of star forming regions.

Interstellar radiation fields

The physical, thermal, and chemical state of the interstellar medium is determined by the interaction of the gas and dust with the interstellar radiation field (ISRF). The total ISFR in the solar neighbourhood consists of six main components, summarised from Draine (2011):

- *X-rays from hot plasma.* The hot (10^5– 10^8 K) plasma, produced by supernovae, radiates at X-rays and extreme ultraviolet (EUV) frequencies.

- *Starlight.* It is mainly composed of photons in the optical, near- and far-ultraviolet frequencies, which come from stellar atmospheres as a result of the nuclear fusion processes in stellar cores. A more detailed treatment can be found in Sec. 2.2.1.

- *Emission from plasma at 10^4 K.* The thermal plasma is a partially ionized gas, which emits radiation due to the thermal motions of its atoms and ions, by means of their free-free, free-bound and bound-bound transitions.

- *Far-infrared (FIR) and infrared (IR) emission from dust.* Dust grains absorb ultraviolet and visible light from stars, then re-emit this radiation at longer wavelengths, in the FIR and IR.

- *Galactic synchrotron emission.* This is the radiation produced by relativistic electrons spiraling through magnetic fields, typically emitting in the radio frequencies.

- *Cosmic microwave background (CMB)*. The CMB is the relic radiation from the Big Bang, and it is detected as a uniform background radiation, which is similar to that of a black body with a temperature of 2.7 K (Fixsen, 2009).

Dust

Interstellar dust consists of small solid grains, mainly made of silicates and graphite (Tielens, 2005), with sizes in the range 0.01 μm – 0.2 μm (Draine, 2011). Dust accounts for approximately 1% of the total mass of the interstellar medium (Klessen & Glover, 2016). It is in an important component of the ISM for several reasons. For example, many chemical species, including hydrogen, accrete onto dust grains and react, forming more complex molecules. In particular, the main formation channel for H_2 is via catalysis on dust grain surfaces. Dust also affects the gas temperature through photoelectrons ejected from grains. It depletes metals from the gas phase, thereby influencing the efficiency of gas cooling. Moreover, dust is the dominant opacity source for non-ionizing photons: it absorbs and scatters the incident radiation, and emits at wavelenghts in the range from 10 μm to a few mm.

Magnetic fields

Magnetic fields play a key role in star formation, because they provide support against gravitational collapse in star-forming clouds. However, even though they are able to slow down the collapse, magnetic fields are not strong enough to fully prevent it; thus, they regulate the dynamics of star-forming regions (Girart et al., 2009; Girichidis et al., 2018b; Hull & Zhang, 2019; Seifried et al., 2020). Moreover, magnetic fields reduce the star formation rate, as they limit the number of cores in filaments and, at small scales, dominate over turbulence in influencing star formation (Hennebelle & Inutsuka, 2019; Pattle et al., 2023). Furthermore, cosmic rays interact with magnetic fields, which in turn affect their transport through the interstellar medium. We will treat cosmic rays in more detail in Sec. 2.2.4.

2.1.2 Gas heating

Heating and cooling mechanisms depend on the local conditions of the interstellar medium, such as density, temperature, chemical abundances, dust-to-gas ratio, etc. Regarding heating, the total effect of the processes that cause the gas to be heated can be expressed with the heating rate Γ, with units of erg s^{-1}, which quantifies the amount of energy transferred to the interstellar medium per unit time. The main heating mechanisms are listed below.

Photoelectric heating

Photoelectric heating is one of the most important heating processes in diffuse interstellar gas. The interaction of UV photons with dust grains can lead to the ejection of photoelectrons. These photoelectrons have an energy equal to the difference between the energy of the incident photon and the binding energy of the dust grain. According to Klessen & Glover (2016), this energy can reach 1 eV or higher, and it is distributed into the surrounding medium via collisions (Bakes & Tielens, 1994; Wolfire et al., 2003). Incident photons are more likely to remove electrons from dust grain surfaces when the grains are negatively charged, as this lowers the energy barrier.

Cosmic ray heating

Cosmic rays are charged particles that travel through the interstellar medium, and will be discussed in greater detail in Sec. 2.2.4. The interaction of low-energy (a few GeV or lower) cosmic rays with the gas can ionize H and H_2, leading to the production of secondary electrons. These secondary electrons can subsequently interact with the surrounding medium, thereby generating heat (Glassgold & Langer, 1973). The heat transferred to the medium per ionization is around 10–20 eV, and depends on the gas composition (Dalgarno et al., 1999; Glassgold et al., 2012). This heating mechanism becomes dominant in the gas that is well shielded from the interstellar radiation field, where photoelectric heating becomes less important.

X-ray heating

X-ray heating affects the gas in a way similar to cosmic ray heating. In fact, the absorption of X-ray photons by atoms and molecules produces primary electrons, which are energetic enough to produce secondary ionizations. Part of the energy of these particles is then passed to the interstellar medium by means of collisions, resulting in gas heating. However, X-rays are more readily absorbed than cosmic rays. Therefore, X-ray heating is more important in the diffuse interstellar medium (Wolfire et al., 1995), and near X-ray sources such as active galactic nuclei (Hocuk & Spaans, 2010).

H_2 formation

Chemical reactions can also release energy in the interstellar medium. One example is the formation of H_2 molecules on dust grains, which releases 4.48 eV of energy for each H_2 molecule formed. This energy is initially in an excited rotational and/or vibrational state. This energy is radiated away in the diffuse gas, however, it can be dissipated via collisions in the dense gas, thereby heating the surrounding medium. In the dense gas, the heating due to H_2 formation may exceed the heating due to low-energy cosmic rays, provided that the efficiency of converting the energy into heat is not too small. However, the value of this efficiency is still debated, as some studies predict it to be low (Roser et al., 2003; Congiu et al., 2009), whereas others suggest it is non-negligible (Le Bourlot et al., 2012).

Photodissociation of H_2

The absorption of UV photons by H_2 molecules leads, in 85% of the cases (Draine, 2011), simply to the excitation of electrons in higher-energy states. However, in 15% of cases, this absorption leads to the dissociation of H_2 into two H atoms, whose energy is enough to heat the surrounding gas. On average, each dissociation produces a heating rate of 0.4 eV (Milgrom et al., 1973; Stephens & Dalgarno, 1973; Black & Dalgarno, 1977).

UV pumping

As seen in the previous section, the absorption of UV photons by H_2 does not always lead to photodissociation of H_2. In this case, H_2 becomes excited to higher energy levels, and it can release the absorbed energy by emitting a photon of the same energy. At high densities ($n > 10^4$ cm^{-3}, Tielens 2005), excited H_2 molecules can also be collisionally de-excited, when colliding with other particles and transferring their energy to them. This process leads to the heating of the surrounding gas.

Dust-gas heating

Dust grains and gas particles are not in thermal equilibrium, therefore their temperatures differ. If the dust is warmer than the gas, the atoms and molecules colliding with dust grains are heated up.

Dynamical processes

Dynamical processes can also heat the interstellar medium. For example, adiabatic compression of the gas in gravitationally-collapsing cores increases the temperature. Moreover, turbulence dissipation is another source of heating. Since turbulence heating is intermittent, its influence on cloud scales is negligible; however, very high heating rates can be obtained locally (Falgarone et al., 1995; Godard et al., 2009). Moreover, magnetic fields can also cause the heating of the gas via ambipolar diffusion. In fact, if the gas is partially ionized, the action of magnetic fields on the ions can generate a velocity difference between the ions and the neutral gas. As a result, some friction between them is developed, which heats the gas substantially (Padoan et al., 2000; Li et al., 2012).

2.1.3 Gas cooling

Radiative cooling of the interstellar medium takes place when atoms and molecules emit part of their energy as photons. The most important chemical species that contribute to the cooling of the gas are the metals, both in atomic and molecular form. We list the most important cooling processes below.

Electronic transition lines

Atomic and ionized gas at high temperatures can cool mainly via permitted electronic transitions from several atoms. For example, at temperatures of around 10^4 K, the dominant process is due to the excitation of the Lyman series of atomic hydrogen, mainly the Lyman-α line. In this case, an electron in the excited state n = 2 returns to the ground state n = 1, by emitting a UV photon. Lyman-α cooling depends on the availability of atomic hydrogen, which decreases as the temperature rises, since hydrogen becomes ionized. At a temperature of around 3×10^4 K, other permitted transitions start to dominate the cooling, e.g. C, O, Ne, and Fe (Gnat & Ferland, 2012a).

Fine structure lines

Fine structure transitions become important at temperatures below 10^4 K, since there are fewer energetic electrons in this regime able to excite the atoms to produce permitted transitions. Fine structure splitting is caused by the spin-orbit coupling, meaning the interaction between the spin and orbital angular momenta of the electrons inside the atom. The separation of the fine-structure energy levels is usually small and corresponds to a temperature of around 100 K (Klessen & Glover, 2016). Therefore, these transitions can occur even when the temperature of the gas is low. Even though the amount of metals in the interstellar medium is only around 2% in mass, the dominant species involved in fine structure transitions are C^+ at 158 μm, and O at 63 μm, at temperatures of 10^2–10^4 K, because hydrogen and helium have no fine structures in their ground states. In the denser gas, in the presence of enough dust shielding, C^+ recombines into C, and atomic carbon fine structure cooling becomes the dominant process (see e.g. Fig 4 in Klessen & Glover 2016).

Molecular hydrogen

The most important transitions involving H_2 are those associated with the rotation around its centre of mass. To each rotation corresponds a specific energy level, and the energy difference between adjacent levels corresponds to the amount of energy that can be emitted as a photon. The first possible rotational transition for H_2 is $J = 2 \rightarrow 0$, which has an energy separation of 510 K and therefore is difficult to excite at the lower temperatures at which H_2 is more abundant. In fact, H_2 cooling is inefficient at temperatures below 200 K and number densities higher than 10^4 cm^{-3}. Since a high H_2 fraction, as well as a temperature higher than 100 K, is needed, the H_2 cooling becomes efficient in regions of shocked molecular gas (Hollenbach & McKee, 1979, 1989; Pon et al., 2012).

Hydrogen Deuteride

Similarly to molecular hydrogen, the most important transitions for the hydrogen deuteride are rotational. However, the difference in energy levels is around 128 K and therefore smaller than for H_2. This means that in principle HD cooling should be more effective than H_2 cooling at low temperature. However, the abundance of HD is linked to the availability of deuterium, which in the local interstellar medium has a very low abundance of around D/H $\sim 10^{-5}$ (Linsky et al., 2006; Prodanović et al., 2010), four orders of magnitude smaller than the abundance of H_2. At temperatures below 50 K, HD cooling is more effective than H_2 cooling, but it is less efficient than the cooling provided by C^+, CO and C (Klessen & Glover, 2016).

Carbon Monoxide

CO is the second most abundant molecule in the interstellar medium and has very small energy separations between its excited rotational levels. Therefore, CO cooling is important at low temperatures, in the regime $T < 20$ K. At higher temperatures, fine structure lines from C and C^+ become more important. CO cooling becomes dominant when the fraction of carbon present in the gas is mostly in CO, which is the case for gas number densities of around 1000 cm^{-3}.

Dust-gas cooling

As already seen in the previous section, collisions between gas particles and dust grains allow energy to be transferred from one to the other. If the gas is warmer than the dust, this process becomes a cooling mechanism. However, the cooling due to gas-dust collisions becomes dominant for number densities of hydrogen higher than 1.5×10^4 cm^{-3} (Goldsmith & Langer, 1978).

2.1.4 Gas phases

As already seen above, heating and cooling mechanisms depend on the local conditions of the interstellar medium. Therefore, depending on the region of interest, different processes can become dominant. To treat this aspect more quantitatively, we can define the net cooling $\mathcal{L}$ as

$$\mathcal{L} \equiv n^2\Lambda - n\Gamma \tag{2.1}$$

with n the number density of the gas, Λ the total cooling rate, and Γ the total heating rate. The values of density, temperature and pressure for which $\mathcal{L} = 0$ are called the equilibrium curve, which is represented in Fig. 2.2. Above the equilibrium curve heating exceeds cooling, and vice versa for a point below the curve. At constant Γ/P per H atom, the equilibrium points are given by the horizontal line shown in Fig. 2.2 with the equilibrium curve. These equilibrium points are four, two thermally stable and two thermally unstable. The stable equilibrium points describe a cold and dense phase, the cold neutral medium (CNM), and a warm and diffuse phase, the warm neutral medium (WNM). Therefore, it is possible to have more than one solution, meaning that for a range of parameters (density, temperature, etc.) the interstellar medium is multiphase in nature.

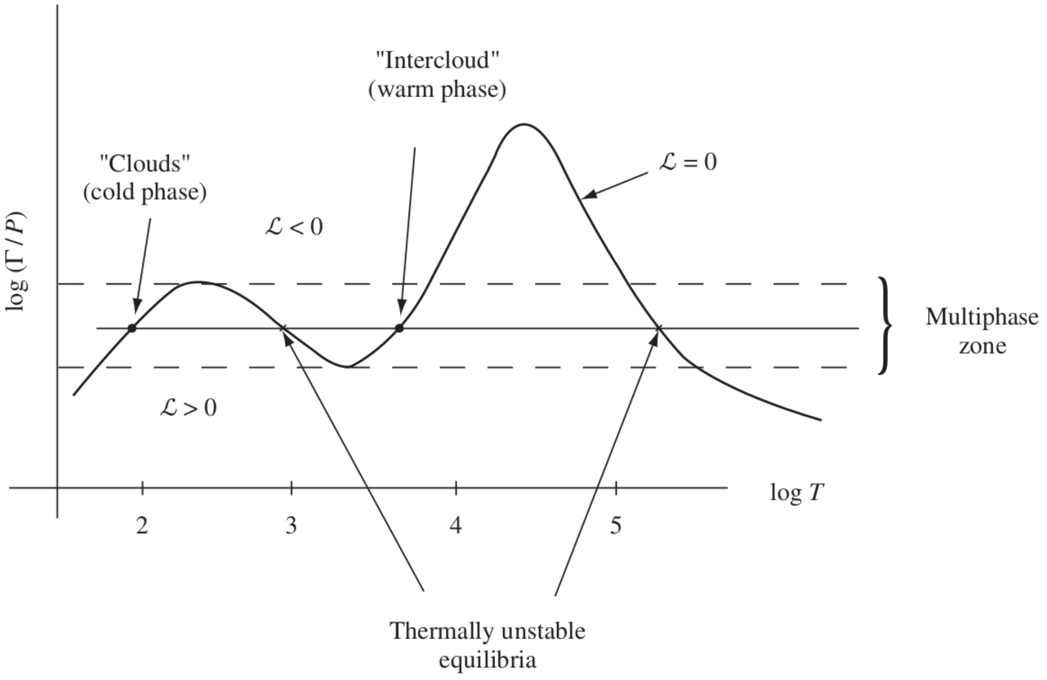

Figure 2.2

Schematic representation of the equilibrium curve computed as Γ/P, highlighting the domain where the cold and warm phases of the interstellar medium can coexist. Taken from Tielens (2005), their Fig.8.1, and references therein.

This two-phase model of the interstellar medium was developed in the 1960s (Field et al., 1969). However, more recent studies have identified two additional gas phases in the interstellar medium. The first is the warm ionized medium (WIM), the ionized gas around (massive) stars. The second is the hot ionized medium (HIM), heated up by shocks due to the presence of supernovae going off in the interstellar medium (McKee & Ostriker, 1977). The typical densities and temperatures, as well as dominant heating and cooling mechanisms for these phases, have been described in detail in Tielens (2005) and Draine (2011). We report a summary adapted from these works in Tab. 2.1.

Table 2.1

Schematic description of the gas phases in the interstellar medium, as presented in Tielens (2005) and Draine (2011). n_H is the number density, f_V is the volume filling factor.

Phase	Temperature [K]	n_H [cm^{-3}]	f_V [%]	Heating and Cooling
HIM	$> 10^{5.5}$–10^6	0.003 – 0.004	50	*Heating*: Shock-heating from supernovae *Cooling*: Adiabatic expansion X-ray emission
H II gas	10^4	0.3 – 10^4	10	*Heating*: Photoionization from H, He *Cooling*: [OII], [OIII], [NII] Free-free emission
WNM	5000 – 8000	0.5 – 0.6	30 – 40	*Heating*: Photoelectric heating *Cooling*: Optical line emission Fine structure line emission
CNM	80 – 100	30 – 50	1	*Heating*: Photoelectric heating *Cooling*: Fine structure line emission
Diffuse H_2	50	100	0.1	*Heating*: Photoelectric heating *Cooling*: Fine structure line emission
Dense H_2	10 – 50	10^3 – 10^6	10^{-2}	*Heating*: Photoelectric heating *Cooling*: CO line emission [C I]

2.2 Stellar feedback

Definition 2 *Stellar feedback is defined as the process by which stars influence the surrounding medium, thereby injecting mass, energy, and momentum. Examples of feedback mechanisms include supernovae, stellar winds, cosmic rays and radiation.*

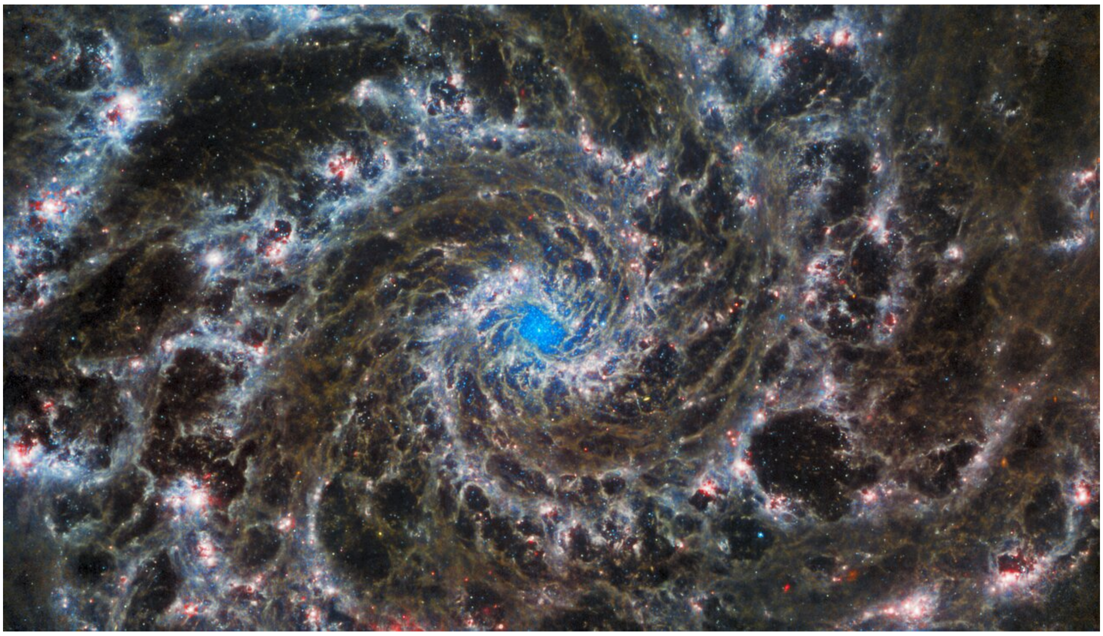

Figure 2.3

Centre of the M74 galaxy, also known as Phantom galaxy, as observed by JWST in the mid-infrared. The visible bubbles are created by stellar feedback. Image credit: ESA/Webb, NASA & CSA, J. Lee and the PHANGS-JWST Team. Acknowledgement: J. Schmidt

Stellar feedback is one of the key ingredients in shaping the structure and evolution of the interstellar medium. In particular, it impacts both star formation (Rosen, 2022), as well as the galactic dynamics, driving galactic winds and fountains (Veilleux et al., 2020; Reichardt Chu et al., 2022; Xu et al., 2024; Thompson & Heckman, 2024). In Fig. 2.3, we show a picture of the M74 galaxy taken in the mid-infrared with the James Webb Space Telescope (JWST). The gas forming the spiral arms presents a number of bubbles that are a consequence of the feedback from massive stars. In the following, we will describe more in detail the most important stellar feedback mechanisms, however we will not consider here protostellar outflows and jets.

2.2.1 Radiation

We have already explored the main components of the ISRF in Sec. 2.1.1. In this section, we will expand on how the radiation coming from stars interacts with the interstellar medium. In fact, stellar radiation, in the form of FUV and EUV photons, shapes the surrounding ISM and its chemical composition via key processes such as photoionization, molecular dissociations, and photoelectric heating. Radiation reduces ambient densities nearby stars, therefore playing a role in regulating star formation (McKee & Ostriker, 2007; Geen et al., 2015; Peters et al., 2017).

The main effects of radiation on the interstellar medium can be summarized as:

- *Photoionization*. The photoionization of the gas by massive stars leads to the formation of H II regions, described in Sec. 2.1.1. Both theoretical and simulation studies indicate that photoionization heating from massive stars is the main physical process responsible for the dispersal of molecular clouds and setting low star formation efficiencies in normal galactic discs (Sales et al., 2014; Kim et al., 2018; Zamora-Avilés et al., 2019; Kannan et al., 2020; Geen et al., 2020). Observations of H II regions find that ionization pressure dominates over direct and dust-processed radiation pressure, except in compact starburst zones (McLeod et al., 2019; Barnes et al., 2020, 2021; Olivier et al., 2021).

- *Radiation pressure*. Radiation can exert pressure on the surrounding gas, especially if this is dense close to the star. Radiation pressure is important for the dynamics of H II regions in the presence of massive star clusters, as it is the case near the Galactic centre or in starburst galaxies (Krumholz & Matzner, 2009). Radiation pressure also pushes away the dense gas from star-forming regions, allowing the supernovae to explode in a warmer and more diffuse environment (Wise et al., 2012). As seen above, radiation pressure is sub-dominant to ionization pressure, except in compact star clusters.

- *Photoelectric heating*. We have discussed the role of photoelectric heating in Sec. 2.1.2.

- *Molecular dissociation*. Photons from stellar atmospheres, especially in the UV range, can photodissociate molecules, the most abundant being H_2, followed by CO. This impacts the chemical composition of the gas, and the cooling rates, as seen in Sec. 2.1.3.

2.2.2 Stellar winds

Stellar winds have first been analytically described by Castor et al. (1975); Weaver et al. (1977). They inject mass, energy, and momentum into the interstellar medium, shaping the structure of the gas in the vicinity of stars. In fact, the wind is supersonic compared to the surrounding ambient medium, therefore it produces an outer shock, after which the shocked ambient medium accumulates. Moreover, a second shock is produced, internal to the outer shock, that expands slower than the wind particles travelling behind it, which decelerates the wind. The wind material passing through this internal shock will be shock-heated.

The most important contributions come from the young and hot OB stars, which inject strong winds with velocities in range of 1500 $\sim$ 3000 km/s. The structure and variability of stellar winds has been observed in the optical (Fullerton et al., 1992; Prinja & Fullerton, 1994; Rauw et al., 2001; Markova, 2002) and UV domains (Prinja

& Smith, 1992; Prinja et al., 1996; Massa et al., 1995; Kaper et al., 1998), following the line-profile variability of different lines coming from several regions, and studying the time-scale of their variations and patterns. A more modern approach is based on inferring wind features by means of Hα emission. With this method, a mass loss rate has been measured in the range of 10^{-6} – 10^{-7} $M_{\odot}$ yr^{-1} for O stars (Markova et al., 2005) and in the range of 10^{-7} – $10^{-5.8}$ $M_{\odot}$ yr^{-1} for B stars (Markova & Puls, 2008).

Several theoretical and observational works have attempted to understand the impact of stellar winds on the physics of the interstellar medium. Regarding simulations, Dale et al. (2014) states that the early feedback from massive stars, meaning the contribution of winds and radiation alone, is dominated by photoionization. Stellar winds contribute as a perturbation of the gas; however, they are able to change the morphology of the ionized gas by clearing out the gas. Mackey et al. (2015) show that stellar wind bubbles around O stars are asymmetric from the star's birth, due to stellar motion, and that they fill only around 10–20% of the H II region volume. When considering stellar winds and supernova feedback only, supernovae dominate the total energy injection in the interstellar medium by around a factor of 3 compared to the winds contribution (Gatto et al., 2017). Guszejnov et al. (2022) investigate how the stellar feedback affects star formation and the IMF, and they note that stellar winds play a minor role compared to radiative feedback (see also Haid et al., 2018).

Regarding observations, Lopez et al. (2011) assessed the role of different feedback mechanisms in 30 Doradus in the Large Magellanic Cloud. According to this study, up to a distance of 75 pc from the central star cluster, the dominant feedback is radiation pressure from stars. Further away, warm ionised gas pressure becomes dominant. Therefore, stellar winds do not play a major role. Similarly, McLeod et al. (2019) analysed N44 and N180, two HII region complexes in the Large Magellanic Cloud. They find that both ionised gas and stellar winds are responsible for the expansion of HII regions, the former being the dominant contributor.

2.2.3 Supernovae

One of the most powerful feedback mechanisms that can shape the interstellar medium on pc and kpc scales is supernova explosions (Mac Low & McCray, 1988; Mac Low & Klessen, 2004). The ambient medium where supernovae explode influences their impact on the interstellar medium (Kim & Ostriker, 2015; Li et al., 2015; Martizzi et al., 2015; Haid et al., 2016). The maximum effect is obtained when supernovae explode in a more diffuse environment, rather than inside a dense cloud (Creasey et al., 2013; Girichidis et al., 2016a; Fielding et al., 2017). Clustered supernovae generate hot superbubbles, which can drive galactic winds and fountains, depleting the gas in the galactic mid-plane (Korpi et al., 1999; Joung & Mac Low, 2006; Walch et al., 2015; Su et al., 2018; Rathjen et al., 2021, 2023; Orr et al., 2022; Oku et al., 2022). Moreover, they sustain turbulence across the disc (Joung et al., 2009; Iffrig & Hennebelle, 2017; Bieri et al., 2023). Supernovae exploding inside clouds can destroy a significant part of their mass, therefore disrupting star-forming regions and affecting star formation (Iffrig & Hennebelle, 2015). Furthermore, supernovae eject heavy elements that enrich the surrounding interstellar medium (Kobayashi et al., 2020; Farmer et al., 2023). This chemical enrichment plays a role in locally changing metal-cooling and dust abundances.

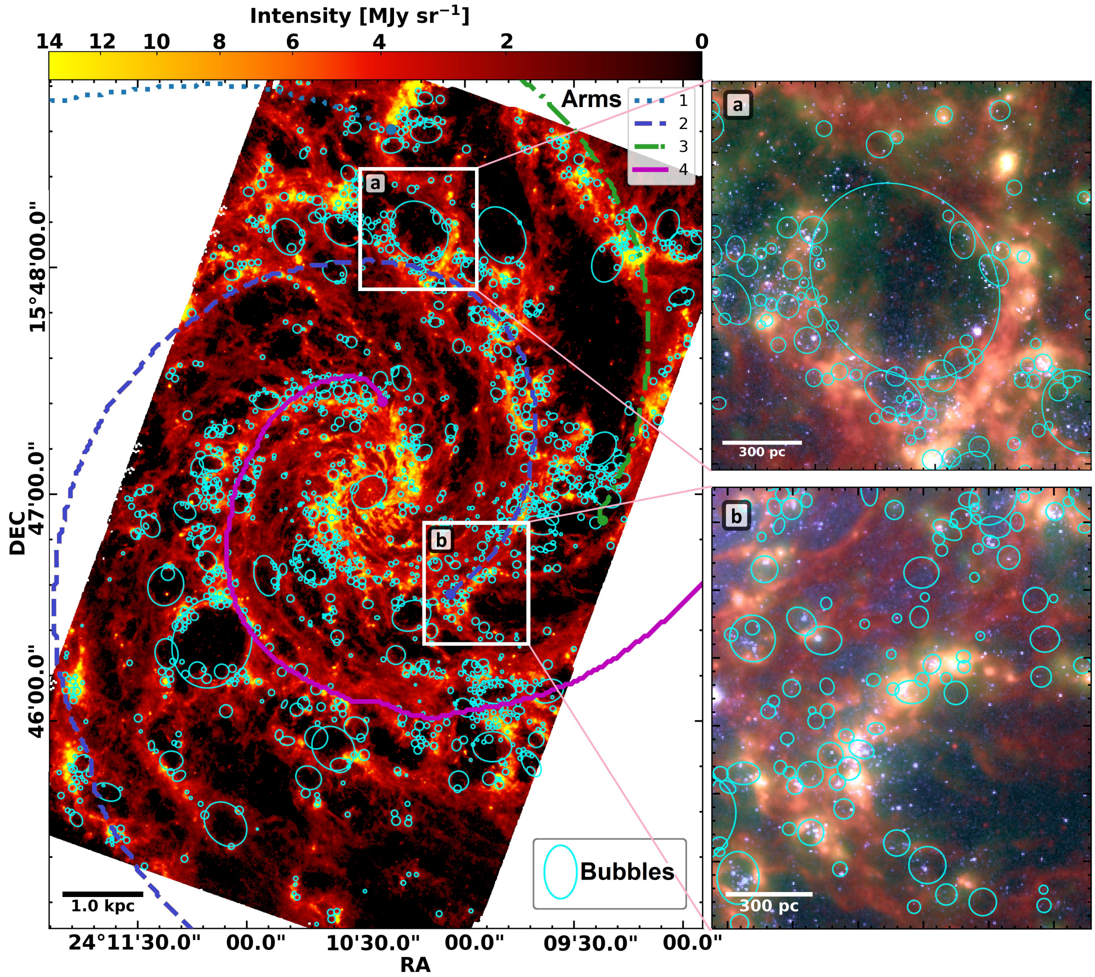

Figure 2.4

Catalogue of bubbles in NGC 628, from the PHANGS-JWST data sample. Left:MIRI F770W band map of NGC 628. The cyan ellipses show the location of the identified bubbles. The white boxes indicate the positions of the right panels, which are a zoom in of the left panel. Taken from Watkins et al. (2023), Fig. 3.

Very recent observations (Watkins et al., 2023) from the PHANGS-JWST data release, showed with unprecedented resolution the effects of stellar feedback on the interstellar medium, see Fig. 2.4. In this study, the bubble structures in NGC 628 were analysed. They note that the majority of these bubbles lie in the vicinity of a spiral arm, and they are oriented along the arm. Therefore, star formation, and so stellar feedback, are connected to the presence of these structures. The bubbles with sizes ≈ 6 pc are driven by pre-supernova feedback, whereas the larger ones are dominated by winds and supernovae.

2.2.4 Cosmic rays

Cosmic rays are very energetic charged particles, mainly protons and alpha particles, with a smaller amount of heavier nuclei, electrons and positrons, which travel with relativistic speeds. Their interaction with the interstellar medium plays a key role in this work, and therefore we will describe their most important characteristics. However, the interested reader can refer to the following reviews, Padovani et al. (2020); Gabici (2022); Ruszkowski & Pfrommer (2023), for further details.

Origin

Very early studies (Baade & Zwicky, 1934; Ginzburg & Syrovatskii, 1964) suggested that galactic cosmic rays with an energy in the GeV – TeV range are accelerated in supernova remnants. These are still considered to be the main accelerators of cosmic rays; however, we know that other processes can accelerate galactic cosmic rays. For example, recent observations have detected high levels of ionization near protostars (Ceccarelli et al., 2014; Fontani et al., 2017; Favre et al., 2018; Cabedo et al., 2023) and protostellar jets (Beltrán et al., 2016; Rodríguez-Kamenetzky et al., 2017; Osorio et al., 2017; Sanna et al., 2019). Moreover, stellar winds can contribute significantly at a pre-supernova stage (Seo et al., 2018). Therefore, cosmic rays can also be accelerated in less powerful local shocks, such as those caused by jets, stellar wind bubbles, massive runaway stars, and so on. Moreover, cosmic rays can also be accelerated by extragalactic sources, such as active galactic nuclei (AGNs) feedback (Koutsoumpou et al., 2025), structure formation shocks in galaxy clusters, and galactic winds (Brunetti & Jones, 2014).

Observations

Observations of cosmic rays can be divided into direct and indirect measurements. Direct observations include experiments performed by balloons and spacecrafts in the heliosphere (see Table 1 in Grenier et al. (2015) for a comprehensive list). However, only energetic (at least a few GeV) cosmic rays can reach these experiments in the vicinity of Earth without being hindered by the interaction with the magnetized solar wind, a phenomenon called solar modulation. Therefore, the energy spectrum of low-energy (< GeV) cosmic rays can be measured without this effect by probes that are found in the heliopause. At the time of writing, these are the *Voyager 1* (Cummings et al., 2016) and *Voyager 2* (Stone et al., 2019). On the other hand, some indirect measurements make use of the fact that cosmic rays usually ionize H and H_2. Even though H^+ and H_2^+ are not directly observable, they react with other species and produce H_3^+, OH^+ and H_2O^+, which are observable (see e.g. Indriolo et al., 2007, 2015; Muller et al., 2016; Bacalla et al., 2019; Kálosi et al., 2023). Other indirect measurements are based on the fact that cosmic-ray protons with energy higher than 1 GeV produce pions (π^0) when colliding with ambient atoms. Pions decay very rapidly into a pair of γ-ray photons, which can be observed (Ackermann et al., 2012, 2013; Yang et al., 2014; Neronov et al., 2017).

Energy spectrum

One of the most remarkable features of cosmic rays is their energy spectrum, which we show in Fig. 2.5, taken from Ruszkowski & Pfrommer (2023). We notice that both the spectrum, which in Fig. 2.5 is multiplied by the square of the particle energy, and the kinetic energy of cosmic rays span several orders of magnitude. At energies well below a few GeV, the spectrum is severely attenuated by solar modulation. Between a few GeV and up to around 10^{14} eV (near the "knee"), the energy spectrum decreases as $E^{-2.7}$, where E is the energy of the particles. This part of the spectrum is associated with cosmic rays that are accelerated in the shock waves of supernova remnants. Between the knee and 10^{18} eV (the "ankle") the spectrum decreases as $E^{-3.1}$, and it includes the contribution of heavier nuclei. At higher energies, cosmic rays are accelerated from extragalactic sources.

Energy losses

The basic energy loss processes for CRs include the formation of secondary particles. We summarise here the most important energy losses from Padovani et al. (2020), distinguishing between protons, electrons and positrons.

- *Protons*. At low energies, the dominant energy loss channels are ionization and Coulomb interactions, where CR protons can transfer their energy to the bound electrons of atoms and molecules, or to the free electrons. Above an energy threshold of 280 MeV, hadronic losses become important, where a CR proton collides with a proton from the gas and produces a neutral pion π^0, which then decays into two gamma-ray photons with equal energy. Hadronic losses become dominant at energies higher than 1 GeV.

- *Electrons and positrons*. At low energies, the dominant energy loss is due to ionization. At energies higher than 100 MeV, the losses due to Bremsstrahlung become dominant. In this case, the Coulomb scattering by the electrons and ions

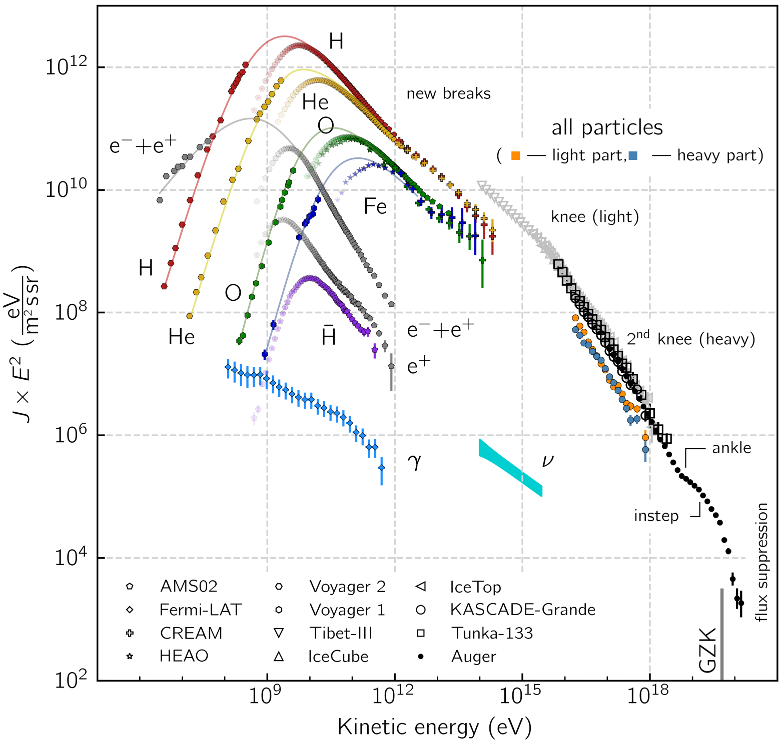

Figure 2.5

Cosmic-ray energy spectrum taken from Ruszkowski & Pfrommer (2023). The y-axis represents the spectrum multiplied by the square of the particle energy, which corresponds to the energy density per decade in particle energy. The spectrum peaks at an energy of a few GeV, and it decreases as a broken power law for energies higher than the peak. At energies lower than a few GeV, the cosmic-ray energy spectrum decreases as a power law.

brakes the CR electrons, and the corresponding energy is emitted as Bremsstrahlung gamma-ray photons. Above 1 TeV, synchrotron losses dominate, which are due to CR electrons and positrons travelling through magnetic fields and being subjected to an acceleration due to the magnetic fields. At high energies and in the diffuse gas, inverse Compton energy losses can be as important as synchrotron losses. The former is the inelastic scattering of high-energy CR electrons by low-energy photons, which results in the emission of gamma-ray photons.

Propagation

CRs are typically treated in the fluid approximation, however, their movement is not isotropic, in contrast to a thermal fluid. In fact, their motion is coupled to the magnetic field orientation, giving rise to an anisotropic distribution. CRs travel in the interstellar medium by means of advection, diffusion and streaming along the magnetic field lines. In the first case, CRs gyrate along the magnetic field lines, which in the ideal MHD case are frozen in the gas. Consequently, the gas motion drags the magnetic field, which in turn affects the motion of CRs. In a turbulent environment, CRs get scattered along the magnetic field lines by the irregularities of the perturbed magnetic field, giving rise to the diffusion of the CRs relative to the gas. Moreover, CRs streaming along the magnetic field lines excite Alfvén waves by means of the "streaming instability" (Kulsrud & Pearce, 1969), and then scatter off of these waves, transferring momentum from the CRs to the gas.

Impact on the ISM

The impact of CRs on the interstellar medium depends on their energy range. Low-energy CRs ($\sim$ MeV) are important for heating (see Sec. 2.1.2) and ionizing molecular clouds, since their cross section with the gas increases significantly at lower energies (Padovani et al., 2009). CRs with the energy of a few GeV are those dynamically relevant, because their energy density is comparable to the thermal, magnetic and kinetic energy densities in the ISM (Ferrière, 2001). In addition, these CRs add an additional pressure component in the ISM, whose gradient contributes in lifting the gas from the midplane, generating CR-driven outflows (Dorfi & Breitschwerdt, 2012; Girichidis et al., 2016b, 2018a; Simpson et al., 2016; Zweibel, 2017; Crocker et al., 2021; Rathjen et al., 2021; Habegger & Zweibel, 2024). CRs with higher energies ($> 10^2$ GeV) are rare, have small cross sections, and do not dynamically impact the interstellar medium.

2.3 The low-metallicity ISM

In this section, we analyse the role of metallicity in the evolution of the interstellar medium, and how low-metallicity environments differ from the interstellar medium in solar-neighbourhood conditions. As we will see in the rest of this thesis, metallicity plays a key role in the cooling, chemistry, and dynamics of the interstellar medium, as metals are the main coolants of the ISM for temperatures below a few 10^6 K.

Definition 3 *Metallicity is the abundance, in the interstellar medium or celestial object, of all chemical elements that are heavier than hydrogen and helium.*

Depending on the field of research, the value of metallicity can be expressed in different ways. For example, in observational studies, the relative abundance of two elements X and Y, expressed in terms of their respective number densities N_X and N_Y, with respect to the solar value, is used:

$$[X/Y] \equiv \log(N_X/N_Y) - \log(N_X/N_Y)_\odot \tag{2.2}$$

In observations of the interstellar gas, it is often used for simplicity X = O, whereas for stellar atmospheres, X = Fe is used. However, especially in simulations, the value of the metallicity is expressed in units of the solar abundances, where $Z = 1\ \mathrm{Z}_\odot$ indicates solar-neighbourhood conditions. The precise value of $\mathrm{Z}_\odot$ assumes different values in different studies, as the measurements of the solar abundances improve over time. In this work, we assume the abundances from Asplund et al. (2009), where $Z_\odot = 0.014$ is measured from the solar photosphere. In this thesis, environments that have a metallicity lower than $\mathrm{Z}_\odot$ are defined as "low-metallicity", "sub-solar" or "metal-poor".

Nearby low-metallicity environments, such as the Magellanic Clouds, the dwarf galaxies I Zwicky 18 and Sextans A, etc., are the ideal laboratory to understand the conditions under which primordial galaxies evolved, since they are very metal poor, providing insights into the formation and evolution of the first generation of stars. Moreover, they allow us to understand how the transition from metal-poor gas to a chemically-enriched medium occurred, and the relevant chemical processes and stellar feedback mechanisms that played a role in shaping galaxies in the early universe. Nearby low-metallicity environments include not only dwarf galaxies, but also the outskirts of the Milky Way. In fact, it has been observed in many studies (Shaver et al., 1983; Afflerbach et al., 1997; Maciel & Quireza, 1999; Rolleston et al., 2000) that a radial metallicity gradient is present in our Galaxy, with metallicity decreasing as a function of the galactocentric radius. However, an ancient metal-poor stellar population is found in the vicinity of the Galactic centre (Rix et al., 2022).

In the following, we will highlight the main differences between the metal-rich (around solar-neighbourhood metallicity) and metal-poor interstellar medium.

Dust

Some important features of dust change with metallicity: the dust-to-gas ratio, meaning the ratio of the dust mass to the gas mass; the dust-to-metal mass ratio, meaning the fraction of metals locked up in dust grains, rathen than remaining in the gas phase; the size distribution, and the composition of dust. The dust-to-gas ratio is measured using two different techniques. The first is employing multiwavelength observations, where the dust is observed in the mid- to far infrared (see e.g. Chastenet et al. 2021) and the HI gas distribution is traced by the 21 cm line and CO rotational lines. Using this method, Rémy-Ruyer et al. (2014) report that at higher metallicities the dust-to-gas ratio scales almost linearly with the metallicity, however at the lower metallicities this trend becomes steeper. They speculate that this behaviour could be due to the harder interstellar radiation field strength in low-metallicity dwarf galaxies, which alters the balance between dust formation and destruction by either limiting the accretion of dust grains, or enhancing their destruction. Moreover, using the same technique, Galliano et al. (2021) show that the dust-to-metal mass ratio is non-linear with metallicity, with lower dust-to-metal mass ratios at lower metallicity. However, the exact relation strongly depends on the observation method. The second technique is measuring the depletion by dust, meaning measuring the fraction of metals that are in dust (see e.g. Jenkins 2009). Using this method, Martínez-González et al. (2022) measure the depletions in the Milky Way (MW) and in the Large and Small Magellanic Clouds (LMC and SMC, respectively). They observe that the depletion increases as function of column density $N(H)$, meaning that more metals are found in dust rather than in the gas at high $N(H)$. Therefore, the dust-to-gas ratio increases by a factor of 3 - 4 in the range $N(H) = 10^{20}$–10^{22} cm^{-2} in all three galaxies. Moreover, they report that the fraction of metals in the gas phase increases for lower metallicity by a factor of six between the MW and the SMC. Therefore, both the dust-to-gas and the dust-to-metal ratios are observed to decrease with decreasing metallicity.

Regarding the distribution of dust size, Gordon et al. (2003) observe steeper UV extinction curves in the LMC and SMC, which are an indication of smaller average grain size (Greenberg & Chlewicki, 1983). Moreover, at low metallicity carbon stars contribute significantly to the dust production, which favours carbonaceous dust production over silicate dust (Zijlstra et al., 2006). Furthermore, it has been observed that low-metallicity environments are deficient in Polycyclic Aromatic Hydrocarbons (PAH), see e.g., Madden 2000; Draine et al. 2007.

Porosity

As seen in Sec. 2.3, the dust-to-gas ratio in metal-poor environments is lower, leading to an overall lower shielding by dust, and promoting more extended photodissociation regions. Therefore, the porosity of the interstellar medium, meaning how easily radiation can penetrate in the gas, increases as the metallicity decreases (Cormier et al., 2015, 2019). In the vicinity of star-forming regions, the enhanced porosity of the interstellar medium can allow the UV photons from H II regions to escape to larger regions (Ramambason et al., 2022). Moreover, low-metallicity stellar populations have a harder radiation field (Stanway et al., 2016), and metal-poor dwarf galaxies show a more intense interstellar radiation field (Hunt et al., 2010), which together with the increased porosity of the medium, modifies the thermal and chemical balance of the dense gas. Moreover, the reduced dust attenuation of the FUV field at low metallicity makes the photoelectric heating more efficient (Kim et al., 2024). All these effects together lead to the warming of the molecular clouds, endangering their survival.

Chemistry

Metallicity has a direct impact on the chemical species present in the interstellar medium. For instance, at lower metallicity the transition from atomic to molecular hydrogen is shifted towards higher shielding column densities (Krumholz et al., 2009; Schruba et al., 2018), and the maximum fraction of formed H_2 decreases, as the formation time of H_2 becomes longer than the lifetime of the molecular cloud (Polzin et al., 2024). Moreover, CO is photodissociated more easily because of the lack of dust (Wolfire et al., 2010; Glover & Mac Low, 2011; Schruba et al., 2012; Cormier et al., 2014), whereas H_2 is able to survive because it can self-shield more effectively. Therefore, in low-metallicity environments CO is not a good tracer of the H_2 gas distribution, because H_2 can also reside in [CI] and [CII]-emitting regions, which are outside of the CO core (Röllig et al., 2006; Wolfire et al., 2010; Glover & Clark, 2012a). In a recent CO survey in the northern region of the Small Magellanic Cloud, Tokuda et al. (2021) report that more than 90% of H_2 is CO-dark. Hence, some studies (see e.g. Poglitsch et al. 1995; Madden et al. 1997; Chevance et al. 2016; Jameson et al. 2018; Madden 2022) suggest CO-independent diagnostics, such as [CII], for tracing the molecular gas. Furthermore, it has been observed that the CO-to-H_2 conversion factor (X_{CO}) anticorrelates with metallicity (Leroy et al., 2011; Hunt et al., 2023; Sanders et al., 2023). This can be explained by the increasing fraction of CO-dark H_2 in metal-poor environments. In particular, Hunt et al. (2023) report that at a metallicity $Z \sim 1/3\ \mathrm{Z}_\odot$ the X_{CO} factor is up to three orders of magnitude higher than in solar-neighbourhood conditions. Moreover, they suggest that the X_{CO} factor does not depend exclusively on metallicity, but it can also be a function of the CO brightness temperature and the resolution (beam size). Hunt et al. (2015) suggest a dependence of the X_{CO} factor with metallicity as $X_{CO} \propto Z/Z_\odot^{-2}$, whereas Hu et al. (2022) suggest X_{CO} to be a multivariate function of the metallicity, line intensity, and beam size.

Heating and Cooling processes

Low metallicity affects some of the heating and cooling processes that we presented in Sec. 2.1.2 and Sec. 2.1.3. In the following, we will discuss the main heating and cooling mechanisms in every gas phase, and analyze the impact of metallicity on them. The main heating source of the ionized gas is photoionization of atomic hydrogen and helium, which does not depend on metallicity. However, the main coolants are collisionally excited emission lines from several ions, for example [OIII] and [SIII] (Draine, 2011), whose abundance decreases for lower metallicity. Since the balance between photoionization heating and collisional excitation cooling sets the temperature of the gas, a lack of metals causes an increase in the temperature of the H II region. As already discussed before, the metal-poor ionized gas is more porous and is characterized by the presence of harder radiation fields. Moreover, it has higher ionization parameter (Cormier et al., 2019). All these effects could be a precondition for the escape of ionizing photons from H II regions (Polles et al., 2019). [OIII] maps around the 30 Doradus region in the Large Magellanic Cloud reported by Kawada et al. (2011), have shown that the [OIII] emission extends on a larger region than that where massive stars in 30 Doradus are located. From this follows that ionizing photons can travel for significant distances from H II regions because of the enhanced porosity.

Regarding atomic gas, the main heating mechanism is the photoelectric heating from PAHs and small dust grains. As before, the amount of dust and PAHs decreases for low metallicity, therefore the photoelectric heating is more inefficient in metal-poor environments. Concerning cooling mechanisms, the main coolants are [CII] and [OI] fine structure lines (Tielens, 2005; Draine, 2011), where the abundance of C^+ and O depends on the metallicity of the gas. At metallicities lower than 0.1-0.2 $Z_\odot$ the dust-to-gas ratio scales superlinearly with the metallicity, therefore the photoelectric heating decreases faster than the metal cooling for decreasing metallicity. Therefore, the cold neutral medium in metal-poor environments is colder and more diffuse than in solar-neighbourhood conditions (Bialy & Sternberg, 2019). Dickey et al. (2000) find a fraction of cold gas in the SMC of around 15%, which is around half of the cold gas fraction found in solar-neighbourhood conditions. Moreover, they measure a temperature of the cold gas of around 40 K, whereas the temperature distribution in the metal-rich gas is around 50-100 K. More recently, Jameson et al. (2019) observed a mass fraction of the cold gas of 20% in the Small Magellanic Cloud, at a temperature of around 30 K. Similarly, Dempsey et al. (2022) observed a mass fraction of 11% of cold gas in the Small Magellanic Cloud, confirming that the low-metallicity cold gas has a lower temperature than at solar metallicity. Moreover, Welty et al. (2016) find a higher thermal pressure in the Magellanic Clouds, in line with the idea that metal-poor cold gas needs higher pressures to be stable.

Regarding molecular gas, the main heating sources are the photoelectric heating at low visual extinction, and heating due to low-energy cosmic rays for higher visual extinction. The former, as we have seen above, depends on the metallicity. The latter, however, is independent of metallicity. The main coolants are molecular rotational line emissions from H_2 and CO. As seen above, the abundances of both species are strongly dependent on the presence of dust.

Star formation

As seen above, low-metallicity environments exhibit key physical differences from their metal-rich counterparts: a lower dust-to-gas ratio, weaker dust shielding, harder interstellar radiation fields, and less efficient cooling. These properties lead to higher gas temperatures, which can inhibit the fragmentation of molecular clouds and thereby influence star formation and the effectiveness of stellar feedback. Understanding the impact of metallicity on these processes is crucial, particularly in the context of early galaxies and local dwarf systems, yet the topic remains under debate.

Simulations have yielded mixed results. For instance, Walch et al. (2011) find that when turbulence is continuously driven, the density and temperature distributions of the ISM are largely insensitive to metallicity. However, in decaying turbulence, metal-poor gas struggles to maintain cold phases, which suppresses star formation in the absence of strong turbulent driving. Similarly, Glover & Clark (2012c) report only a weak dependence of the star formation rate on metallicity in gravitationally bound clouds, while Peters et al. (2014) find that fragmentation is weakly dependent on metallicity, especially in the presence of magnetic fields, which stabilise the gas. In contrast, Kim et al. (2024), using stratified box simulations, find a positive correlation between star formation rate surface density and metallicity, with $\Sigma_{\rm SFR} \propto Z^{0.3}$. At extremely low metallicities, Chon & Omukai (2024) show that fragmentation is strongly suppressed at metallicities lower than 10^{-3} $Z_\odot$, promoting the formation of supermassive stars. The structure of star-forming clouds also appears to vary with metallicity. While star formation at solar metallicity typically occurs within filamentary molecular clouds (Mizuno et al., 1995; Nagahama et al., 1998; Onishi et al., 1999; Hacar et al., 2023), it remains unclear whether such structures form similarly in metal-poor environments (Chon et al., 2021; Tokuda et al., 2025). The conditions for fragmentation at low metallicity have been proposed by several studies. Bromm et al. (2001) argue that metal-line cooling becomes effective to trigger fragmentation at $Z > 5 \times 10^{-4}$ $Z_\odot$, while Schneider et al. (2006) highlight that dust cooling can drive fragmentation down to solar or sub-solar masses at metallicities as low as 10^{-6} $Z_\odot$. Dust likely plays a central role in the fragmentation process, as it is a more efficient coolant than metal-line cooling at high densities ($n_{\rm H} > 10^{12}$ cm^{-3}), as confirmed by several studies (e.g. Schneider et al., 2006, 2012; Clark et al., 2008; Dopcke et al., 2011).

The influence of metallicity on the initial mass function (IMF) is similarly contentious. While Krumholz (2011); Myers et al. (2011) and Bate (2014) report a near-invariant IMF, the latter over two orders of magnitude in metallicity, more recent studies suggest otherwise. For example, Bate (2019) find that low metallicities raise gas temperatures and delay star formation, but the resulting stellar populations remain similar. However, they observe an increase in the close binary fraction of low-mass stars at low metallicity. Other works suggest stronger trends: Chon et al. (2021); Tanvir & Krumholz (2024) and Sharda & Krumholz (2022) propose that the IMF evolves from top-heavy to bottom-heavy with increasing metallicity, as cooling mechanisms transition from H_2 cooling and metal-line cooling at a metallicity of $Z \sim 10^{-4}$ $Z_\odot$ to dust cooling, at a metallicity of $Z \sim 10^{-2}$ $Z_\odot$. In their model, the characteristic stellar mass declines from ~50 $M_\odot$ at $Z \sim 10^{-6}$ Z⊙ to ~0.3 M⊙ at solar metallicity. Furthermore, Sharda et al. (2023) argue that individual measured chemical abundances, especially C and O, must be considered explicitly rather than inferred from a global metallicity, as the IMF is very sensitive to the assumptions of the chemical abundances.

Observational evidence tends to support a metallicity-dependent IMF. Star clusters in the outer Galaxy show indications of a top-heavy IMF in metal-poor regions (Yasui et al., 2024). Similarly, the slope of the IMF correlates with metallicity gradients in nearby dwarf galaxies, with more top-heavy IMFs in metal-poor environments (Martín-Navarro et al., 2015; Parikh et al., 2018; Martín-Navarro et al., 2019, 2021; Chruślińska et al., 2020). In summary, whether metallicity influences star formation remains an open question. In this thesis, and in particular in Chapter 4 (Paper I) and Chapter 5 (Paper II), we will explore this issue employing our simulations, focusing how the lack of coolants in low-metallicity environments affects star formation.

Stellar feedback

The structural differences in the interstellar medium induced by low metallicity also modify the timing and impact of stellar feedback. In particular, radiation-driven stellar winds are significantly weaker in metal-poor environments due to the reduced line opacities (Hainich et al., 2015; Marcolino et al., 2022; Ou et al., 2023; Telford et al., 2024), diminishing their ability to inject energy and momentum into the surrounding gas. Additionally, a larger fraction of massive stars are expected to undergo direct collapse into black holes without a supernova explosion at low metallicity (Heger et al., 2003), reducing the overall energy and momentum returned to the ISM. Jecmen & Oey (2023) estimate that this leads to a decrease of approximately 40% in mechanical energy and 75% in momentum input at $0.4\,Z_\odot$, relative to solar metallicity. As a result, mechanical feedback is delayed, typically becoming effective only after 10Myr from the onset of star formation. This delay allows radiative feedback to dominate the early evolution, which may enhance star formation efficiencies and favour the formation of multiple stellar populations within clusters. Moreover, in dwarf galaxies, the ionising radiation emitted by young, metal-poor stellar populations plays a dominant role in regulating the ISM. Emerick et al. (2018, 2020a) show that ionising and Lyman-Werner radiation dominate over photoelectric heating and radiation pressure from atomic hydrogen in shaping the thermodynamic state and evolution of such galaxies. These findings underline that, in metal-poor conditions, feedback mechanisms shift from momentum-driven to radiation-dominated processes, with implications for both star formation and galactic outflows.

2.4 The connection between star formation and gas density

Understanding the process of star formation remains one of the central challenges in astrophysics due to the complexity and interplay of the many physical mechanisms involved. Star formation is governed not only by the availability of cold gas, the fundamental reservoir from which stars form, but also by the dynamical state of the interstellar medium (ISM), the gravitational potential, stellar feedback, and chemical processes within the ISM (McKee & Ostriker, 2007; Krumholz, 2014).

One of the most well-established empirical relations in this context is the Kennicutt–Schmidt (KS) relation, which links the surface density of gas in a galaxy to its star formation rate (SFR) surface density via a power law with an index of approximately 1.4 (Kennicutt, 1998; Genzel et al., 2010; Kennicutt & Evans, 2012). The non-linearity of this relation implies that star formation is not solely determined by the amount of gas present, but also by the local physical conditions. Specifically, a power-law index greater than unity suggests that star formation is more efficient in denser regions. Various modifications and alternatives to the KS relation have been proposed to better capture the underlying physics (see, e.g., Ballesteros-Paredes et al. 2024 for a recent review).

A key open question concerns how star formation is regulated by the availability of gas and by stellar feedback, and whether these processes maintain equilibrium in the ISM. We address this problem in Chapter 6, where we test the pressure-regulated, feedback-modulated star formation theory (Ostriker & Kim, 2022) using our SILCC simulations. This theoretical framework assumes that the ISM reaches a quasi-steady state in which vertical dynamical equilibrium is established. From this balance, an equilibrium star formation rate naturally emerges, in order to sustain the vertical structure of the galactic disc.

In Chapter 6 (Paper III), we first evaluate the validity of this theory in our simulations. We then examine whether a true steady state is achieved and how time variability in star formation and outflows influences the evolution of the ISM. The remainder of this section outlines the core principles of the pressure-regulated, feedback-modulated framework, with a more in-depth analysis presented in Chapter 6 (Paper III).

2.4.1 The Pressure-regulated, Feedback-modulated Star Formation Theory

The Pressure-regulated, Feedback-modulated (PRFM) star formation theory has been described in detail in Ostriker et al. (2010). In this section, we aim to describe this theory in a simplified manner, since we will analyse it more in depth in Chapter 6. The main idea of this model is that the diffuse interstellar medium in galactic discs is on average in a quasi-steady state, when considering either long-term time averages or large-scale ensemble averages. This equilibrium encompasses two different aspects: a force balance in the vertical direction, where outward-pointing pressure forces counterbalance the inward-pointing gravitational forces, and the equilibrium between heating and cooling processes. In the model presented in Ostriker et al. (2010) the main heating source is the far-ultraviolet (FUV) radiation coming from OB associations. Gravitationally bound clouds (GBCs) are treated separately from the diffuse gas, since they are self-gravitating and at a much higher pressure than the surrounding gas. It is assumed that all star formation takes place in GBCs, therefore, their presence is crucial, as stellar feedback constitutes the main energy source for the ISM. The diffuse gas is considered to be atomic gas in the interstellar medium. This atomic gas is assumed to be divided into a warm and a cold phase in pressure equilibrium, with a turbulent vertical velocity dispersion v_z^2 assumed to be the same for both phases.

The main reason to consider separately the star-forming clouds from the diffuse gas can be explained as follows. The main heating processes in the diffuse gas are due to stellar feedback; therefore, the specific heating rate Γ in the diffuse gas is proportional to the star formation rate, which in turn depends on the amount of available cold and dense gas. On the other hand, the specific cooling rate $n\Lambda$ in the diffuse gas is proportional to the gas density, which is linked to the thermal pressure. If vertical equilibrium holds, thermal pressure is proportional to the gravitational forces in the vertical direction, which in turn depend on the total surface density of the diffuse gas. Therefore, in this analysis the gas mass is split into gravitationally-bound clouds and diffuse gas, such that their ratio is proportional to the gravitational field in the vertical direction. In fact, if too much gas is present in the star-forming part, the enhanced star formation rate would make the heating exceed the cooling, and the cold and dense star-forming gas would be converted into diffuse gas. In this case, less cold gas would be available to form new stars, and this would lower the star formation rate, and so the consequent heating rate. Therefore, cooling processes would dominate over heating and would be able to form more cold gas. This would eventually lead to a quasi-steady state. In the following, we will present the derivation of the vertical equilibrium, the thermal equilibrium and the equilibrium star formation rate as computed in Ostriker et al. (2010).

We define here some quantities that will be used in the following analysis. A key quantity is the volume-weighted mean thermal pressure at the mid-plane, defined as

$$\langle P_{\rm th}\rangle_{\rm vol} = \frac{\int P_{\rm th} d^3x}{\int d^3x} = \frac{\int (P_{\rm th}/\rho)\rho d^3x}{\int d^3x} = \frac{\int \rho d^3x}{\int d^3x}\frac{\int v_{\rm th}^2 dm}{\int dm} = \rho_0 \langle v_{\rm th}^2\rangle_{\rm mass}, \quad (2.3)$$

where ρ_0 is the volume-weighted mean mid-plane density, and $\langle v_{\rm th}^2\rangle_{\rm mass}$ is the mass-weighted mean thermal velocity dispersion.

Supposing that the diffuse medium is composed of a warm and cold component, with temperatures T_w and T_c, and mass fractions f_w and $f_c = 1 - f_w$, respectively, we have that

$$\frac{\langle v_{\rm th}^2\rangle_{\rm mass}}{c_w^2} = f_w + \frac{T_c}{T_w}(1 - f_w) \equiv \tilde{f}_w, \quad (2.4)$$

where

$$c_w \equiv (P_w/\rho_w)^{1/2} \;=\; (kT_w/\mu)^{1/2}, \tag{2.5}$$

is the thermal speed of the warm gas, with P_w and ρ_w the pressure and the density of the warm gas, respectively. Since $T_w/T_c \sim 100$, it yields $\tilde{f}_w \approx f_w$, unless $f_w \ll 1$.

If the pressures of the cold and warm gas are the same, we obtain $\langle P_{\rm th}\rangle_{\rm vol} = P_w = \rho_w c_w^2$, and from Eq. 2.3 and Eq. 2.4,

$$\frac{\rho_w}{\rho_0} \;=\; \frac{\langle v_{\rm th}^2\rangle_{\rm mass}}{c_w^2} \;=\; \tilde{f}_w. \tag{2.6}$$

Assuming the warm and cold phases to have the same pressure in the mid-plane, we get that $\langle P_{\rm th}\rangle_{\rm vol} \rightarrow P_{\rm th}$.

Vertical dynamical equilibrium

Averaging the momentum equation of the diffuse gas horizontally and in time, and integrating it in the outward direction perpendicular to the mid-plane, the difference in the total vertical momentum flux across the disc thickness is equal to the total weight of the diffuse gas (Boulares & Cox, 1990; Piontek & Ostriker, 2007; Koyama & Ostriker, 2009). The total weight is composed of three different contributions, the first being the weight of the diffuse gas in its own gravitational field,

$$\int_0^{z_{\rm diff,max}} \rho\frac{d\Phi_{\rm diff}}{dz}dz \;=\; \frac{1}{8\pi G}\int_0^{z_{\rm diff,max}} \frac{d(\frac{d\Phi_{\rm diff}}{dz})^2}{dz}dz \;=\; \frac{\pi G\Sigma_{\rm diff}^2}{2}. \tag{2.7}$$

Here $\Sigma_{\rm diff}$ is the gas surface density of the diffuse gas, and it has been used $|d\Phi_{\rm diff}/dz|_{\rm zdiff,max} = 2\pi G\Sigma_{\rm diff}$. The second contribution comes from the gravity due to the presence of GBCs,

$$\int_0^{z_{\rm diff,max}} \rho\frac{d\Phi_{\rm GBC}}{dz}dz \approx \pi G\Sigma_{\rm GBC}\Sigma_{\rm diff}, \tag{2.8}$$

where $|d\Phi_{\rm GBC}/dz| \sim 2\pi G\Sigma_{\rm GBC}$ over the majority of the integral, since it has been assumed that the scaleheight of the GBCs is smaller than that of the diffuse gas. The third term comes from the contribution of the gravitational potential of stars and dark matter,

$$\int_0^{z_{\rm diff,max}} \rho\left(\frac{d\Phi_s}{dz} + \frac{d\Phi_{\rm dm}}{dz}\right)dz \equiv 2\pi\zeta_d G\frac{\rho_{\rm sd}\Sigma_{\rm diff}^2}{\rho_0}, \tag{2.9}$$

where $\rho_{\rm sd} = \rho_{\rm s} + \rho_{\rm dm}$ is the density of the stellar disc plus that of the dark matter halo in the mid-plane. ζ_d is a numerical parameter that depends on the vertical gas distribution.

Finally, equating the momentum flux difference with the total weight, we get

$$P_{\rm th}\left(1+\frac{v_t^2}{c_w^2\tilde{f}_w}\right) = \frac{\pi G}{2}\Sigma_{\rm diff}^2 + \pi G\Sigma_{\rm GBC}\Sigma_{\rm diff} + 2\pi\zeta_d G c_w^2\tilde{f}_w\frac{\rho_{\rm sd}\Sigma_{\rm diff}^2}{P_{\rm th}}. \tag{2.10}$$

Here Eq. 2.3 and Eq. 2.4 have been used to substitute ρ_0^{-1} with $\tilde{f}_w c_w^2/P_{\rm th}$ in the right-hand side. If $\Sigma_{\rm GBC}$ and $P_{\rm th}$ are known, Eq. 2.10 can be solved to obtain the surface density of the diffuse gas

$$\Sigma_{\rm diff} = \frac{2\alpha P_{\rm th}}{\pi G\Sigma_{\rm GBC} + [(\pi G\Sigma_{\rm GBC})^2 + 2\pi G\alpha(P_{\rm th} + 4\zeta_d c_w^2\tilde{f}_w\rho_{\rm sd})]^{1/2}}, \tag{2.11}$$

where α is defined as

$$\alpha \equiv 1+\frac{v_t^2}{c_w^2\tilde{f}_w} = \frac{\langle v_{\rm th}^2\rangle + v_t^2}{\langle v_{\rm th}^2\rangle} = \frac{P_{\rm th}+\rho_0 v_z^2 + \Delta(B^2/2 - B_z^2)/(4\pi)}{P_{\rm th}}. \tag{2.12}$$

We can also solve Eq. 2.10 for the thermal pressure as a function of $\Sigma_{\rm diff}$, $\Sigma_{\rm GBC}$, $\rho_{\rm sd}$, α and $\tilde{f}_{\rm w}$,

$$P_{\rm th} = \frac{\pi G\Sigma_{\rm diff}^2}{4\alpha}\left\{1+2\frac{\Sigma_{\rm GBC}}{\Sigma_{\rm diff}} + \left[\left(1+2\frac{\Sigma_{\rm GBC}}{\Sigma_{\rm diff}}\right)^2 + \frac{32\zeta_d c_w^2\tilde{f}_w\alpha}{\pi G}\frac{\rho_{\rm sd}}{\Sigma_{\rm diff}^2}\right]^{1/2}\right\}. \tag{2.13}$$

Here the term proportional to $\rho_{\rm sd}$ dominates, such that Eq. 2.13 can be rewritten as

$$P_{\rm th} \sim \Sigma_{\rm diff}(2G\rho_{\rm sd})^{1/2}\left(\frac{\pi\zeta_{\rm d}\tilde{f}_w}{\alpha}\right)^{1/2} c_w, \tag{2.14}$$

therefore the thermal pressure increases proportionally to $\Sigma_{\rm diff}$, for fixed $\rho_{\rm sd}$ and Σ. Multiplying Eq. 2.14 by α, and assuming $\alpha\tilde{f}_{\rm w} = (\langle v_{\rm th}^2\rangle + v_t^2)/c_{\rm w}^2$, yields

$$P_{\rm tot} \sim \Sigma_{\rm diff}(2G\rho_{\rm sd})^{1/2}(\langle v_{\rm th}^2\rangle + v_t^2)^{1/2} \tag{2.15}$$

which is formally similar to the formula for mid-plane pressure adopted in Blitz & Rosolowsky (2004, 2006). Using $\rho_{\rm s} = \pi G\Sigma_{\rm s}^2/(2v_{z,s}^2)$ and taking $\Sigma_{\rm GBC}$, $\rho_{\rm dm} \to 0$, we obtain

$$P_{\rm tot} \sim \frac{\pi G\Sigma^2}{2}\left(1+\frac{[(\langle v_{\rm th}^2\rangle + v_t^2)^{1/2}]^{1/2}\Sigma_s}{v_{z,s}\Sigma}\right), \tag{2.16}$$

recovering the result from Elmegreen (1989).

Thermal equilibrium of diffuse gas

In the previous paragraph, we have described the vertical equilibrium condition in the PRFM theory. In this paragraph, we outline the second condition deriving from a steady state, meaning the thermal equilibrium of the diffuse gas. As seen in Eq. 2.13, the thermal pressure of the diffuse gas must counterbalance the weight of the disc. Since the two-phase model states that the atomic gas is found in a cold and in a warm phase, we expect that $P_{\rm min,cold} < P_{\rm th} < P_{\rm max,warm}$, where $P_{\rm min,cold}$ and $P_{\rm max,warm}$ are the minimum pressure value for which the existence of a cold medium is possible, and the maximum pressure that allows the existence of a warm phase, respectively. According to Wolfire et al. (2003), the local thermal pressure is comparable to the geometrical mean of these two pressure extrema, such that

$$P_{\rm two-phase} \equiv (P_{\rm min,cold} P_{\rm max,warm})^{1/2}. \tag{2.17}$$

where $P_{\rm two-phase}$ is defined by the thermal equilibrium curve. Piontek & Ostriker (2005, 2007) found that the mean mid-plane pressure towards $P_{\rm two-phase}$ for a broad range of vertical gravitational fields and ratios of the warm to the cold mass. Therefore, we expect that the mid-plane thermal pressure in the diffuse gas is comparable to $P_{\rm two-phase}$. Assuming that the main heating mechanism is the photoelectric heating, $P_{\rm two-phase}$ scales approximately with the FUV intensity. Using the equation given in Wolfire et al. (2003), assuming that $P_{\rm two-phase}$ scales with $P_{\rm min,cold}$, and normalizing by the solar-neighbourhood value, it follows

$$\frac{P_{\rm two-phase}}{k} = 12000\ {\rm K cm^{-3}} \frac{G'_0 Z'_{\rm d}/Z'_{\rm g}}{1 + 3.1(G'_0 Z'_{\rm d}/\zeta'_{\rm t})^{0.365}}. \tag{2.18}$$

Here G'_0 is the mean FUV intensity relative to the solar neighbourhood value $J_{\rm FUV,0} = 2.1 \times 10^{-4}$ erg cm^{-2} s^{-1} sr^{-1}. $Z'_{\rm d}$ and $Z'_{\rm g}$ are, respectively, the dust and gas abundances relative to solar-neighbourhood values, and $\zeta'_{\rm t}$ is the total ionization rate due to cosmic rays, EUV radiation, and X-rays, relative to the value 10^{-16} s^{-1}.

Since the FUV radiation is produced by OB associations, we can assume that the FUV intensity scales with the star formation rate surface density. In particular, we can write

$$G'_0 \equiv \frac{J_{\rm FUV}}{J_{\rm FUV,0}} \approx \frac{\Sigma_{\rm SFR}}{\Sigma_{\rm SFR,0}} = \frac{\Sigma_{\rm SFR}}{2.5 \times 10^{-9} {\rm M_\odot\ pc^{-2}\ yr^{-1}}}, \tag{2.19}$$

where $\Sigma_{\rm SFR,0} = 2.5 \times 10^{-9}$ M$_\odot$ pc^{-2} yr^{-1} is the solar-neighbourhood value of the star formation rate surface density. If we assume that the high-energy ionization rate $\zeta_{\rm t}$ is proportional to the local value of $\Sigma_{\rm SFR}$, and inversely proportional to the gas surface density Σ (Wolfire et al., 2003), we have that

$$\frac{G'_0}{\zeta'_{\rm t}} = \frac{\Sigma}{\Sigma_0}, \tag{2.20}$$

with Σ_0 being the surface density of neutral gas at the solar circle.

Setting $\Sigma_0 = 10\ \mathrm{M_\odot\ pc^{-2}}$, $Z'_\mathrm{d}/Z'_g = 1$, $P_\mathrm{th} = P_\mathrm{two-phase}$ and substituting in Eq. 2.18, it follows

$$\Sigma_\mathrm{SFR} \approx 6 \times 10^{-10}\ \mathrm{M_\odot\ pc^{-2}\ yr^{-1}} \left(\frac{P_\mathrm{th}/k}{3000\ \mathrm{K\ cm^{-3}}}\right) \times \left[1 + 3\left(\frac{Z'_\mathrm{d}\Sigma}{10\ \mathrm{M_\odot\ pc^{-2}}}\right)^{0.4}\right]. \tag{2.21}$$

The equilibrium star formation rate

After describing the vertical dynamical equilibrium and thermal equilibrium conditions of the PRFM theory, we present here the derivation of the equilibrium star formation rate. This is the star formation rate needed to maintain both vertical and thermal equilibrium on long time scales. We compute here the star formation rate surface density as a function of the total gas surface density $\Sigma = \Sigma_\mathrm{diff} + \Sigma_\mathrm{GBC}$ and of the mid-plane stellar+dark matter density ρ_sd. Given that star formation is assumed to happen only in GBCs, we can write Σ_SFR as a function of Σ as in the following:

$$\Sigma_\mathrm{SFR} = \frac{\Sigma_\mathrm{GBC}}{t_\mathrm{SF,GBC}} = \frac{\Sigma - \Sigma_\mathrm{diff}}{t_\mathrm{SF,GBC}}, \tag{2.22}$$

where the depletion time t_GBC can be written, based on empirical results, as

$$t_\mathrm{SF,GBC} = t_\mathrm{SF,mol}\Sigma_\mathrm{GBC}/\Sigma_\mathrm{mol}, \tag{2.23}$$

if $t_\mathrm{SF,mol}$, the depletion time of the molecular gas, is a constant value.

Assuming $\Sigma_\mathrm{diff} = \Sigma - \Sigma_\mathrm{GBC}$, with $\Sigma_\mathrm{GBC} = t_\mathrm{SF}\Sigma_\mathrm{SFR}$, and substituting the value of P_th with Σ_SFR using Eq. 2.21, we can rewrite Eq. 2.11 as

$$\frac{P_\mathrm{th,low}}{k} = \frac{1700\ \mathrm{K\ cm^{-3}}}{\alpha}\left(\frac{\Sigma}{10\ \mathrm{M_\odot\ pc^{-2}}}\right)^2 \times \left\{1 + \left[1 + 50\tilde{f}_\mathrm{w}\alpha\frac{\left(\frac{\rho_\mathrm{sd}}{0.1\ \mathrm{M_\odot pc^{-3}}}\right)}{\left(\frac{\Sigma}{10\mathrm{M_\odot pc^{-2}}}\right)^2}\right]\Bigg]\right\}, \tag{2.24}$$

which is valid in the diffuse-dominated ISM, where the star formation rate is low. Substituting this result in Eq. 2.21, we get

$$\begin{aligned}\Sigma_\mathrm{SFR,low} = 3 \times 10^{-10}\ \mathrm{M_\odot\ pc^{-2}\ yr^{-1}} &\left(\frac{\Sigma}{10\ \mathrm{M_\odot\ pc^{-2}}}\right) \\ \times &\left[1 + 3\left(\frac{Z'_\mathrm{d}\Sigma}{10\ \mathrm{M_\odot\ pc^{-2}}}\right)^{0.4}\right] \\ \times &\left[\frac{2}{\alpha}\left(\frac{\Sigma}{10\ \mathrm{M_\odot\ pc^{-2}}}\right) + \left(\frac{50\tilde{f}_\mathrm{w}}{\alpha}\right)^{1/2}\left(\frac{\rho_\mathrm{sd}}{0.1\ \mathrm{M_\odot\ pc^{-3}}}\right)^{1/2}\right].\end{aligned} \tag{2.25}$$

This equation applies in the solar neighbourhood, where the gravity due to the stellar potential and dark matter is dominant. An approximation for the entire range $\Sigma \leq 100\ \mathrm{M}_\odot\ \mathrm{pc}^{-2}$ is given by

$$\Sigma_{\mathrm{SFR}} \approx \left[\frac{t_{\mathrm{SF}}}{\Sigma} + \frac{1}{\Sigma_{\mathrm{SFR,low}}}\right]^{-1}. \tag{2.26}$$

In Chapter 6 (Paper III), we will investigate the validity of this theory, although in a simplified manner, using a set of our SILCC simulations. The reader is referred to Chapter 6 for more details.

Chapter 3

Methods

In this chapter, we give an overview of the most important numerical methods we employ in our simulations, as well as of the setup. In particular, we introduce our modified version of the Flash code in Sec. 3.1, and we present our new implementation of cosmic-ray heating in Sec. 3.2. Sec. 3.3 describes our simulation setup, and Sec. 3.4 explains the dendrogram algorithm that we have used to characterize the fragmentation of the gas in Chapter 5 (Paper II).

3.1 The Flash code

For our simulations we use the 3D adaptive mesh refinement (AMR) code Flash version 4.6 (Fryxell et al., 2000; Dubey et al., 2008, 2009), developed by the Flash Center for Computational Science at the University of Chicago and the University of Rochester. The code is written in Fortran and C, and it uses the Message-Passing Interface (MPI) for the communication among processors, the HDF5[1] library to handle parallel I/O, and the PARAMESH library (MacNeice et al., 2000) to handle the AMR structure. The AMR structure is tree-like, where each node of the tree describes a part of the computational domain. Each parent node is split recursively into eight child nodes, until reaching the last level, that of the leaf-nodes, that covers the entire computational domain.

3.1.1 Magneto-hydrodynamic equations

We model the evolution of the interstellar medium (ISM) solving the magneto-hydrodynamic (MHD) equations, which in our case include source terms such as supernovae, stellar winds, cosmic rays, heating and cooling (see below). We use the Bouchut HLL3R solver (Bouchut et al., 2007, 2010; Waagan, 2009; Waagan et al., 2011), which has been extended to handle CRs (see Sec. 3.1.5). The MHD equations read

$$\frac{\partial \rho}{\partial t} + \nabla \cdot (\rho \boldsymbol{v}) = 0, \tag{3.1}$$

$$\frac{\partial \rho \boldsymbol{v}}{\partial t} + \nabla \cdot \left(\rho \boldsymbol{v} \boldsymbol{v}^T - \frac{\boldsymbol{B}\boldsymbol{B}^T}{4\pi} \right) + \nabla P_{\mathrm{tot}} = \rho \boldsymbol{g} + \dot{\boldsymbol{q}}_{\mathrm{sn}}, \tag{3.2}$$

---

[1] `https://github.com/HDFGroup/hdf5`

$$\frac{\partial e}{\partial t} + \nabla \cdot \left[(e + P_{\rm tot})\boldsymbol{v} - \frac{\boldsymbol{B}(\boldsymbol{B}\cdot\boldsymbol{v})}{4\pi} \right] = \rho \boldsymbol{v} \cdot \boldsymbol{g} + \nabla \cdot (\mathbf{K}\nabla e_{\rm cr}) + \dot{u}_{\rm chem} + \dot{u}_{\rm sn} + Q_{\rm cr}, \quad (3.3)$$

$$\frac{\partial \boldsymbol{B}}{\partial t} - \nabla \times (\boldsymbol{v} \times \boldsymbol{B}) = 0, \quad (3.4)$$

$$\frac{\partial e_{\rm cr}}{\partial t} + \nabla \cdot (e_{\rm cr}\boldsymbol{v}) = -P_{\rm cr}\nabla \cdot \boldsymbol{v} + \nabla \cdot (\mathbf{K}\nabla e_{\rm cr}) + Q_{\rm cr}, \quad (3.5)$$

$$\nabla \cdot \mathbf{B} = 0. \quad (3.6)$$

Here, ρ is the gas density, $\mathbf{v}$ is the velocity of the gas, $\mathbf{B}$ is the magnetic field. $P_{\rm tot} = P_{\rm th} + P_{\rm magnetic} + P_{\rm cr}$ is the total pressure of the gas, with $P_{\rm th}$, $P_{\rm magnetic}$, $P_{\rm cr}$ thermal, magnetic and CR pressures, respectively. Moreover, $\mathbf{g}$ is the gravitational acceleration of the gas (see Sec. 3.1.2), $\mathbf{q}_{\rm sn}$ is the momentum input rate of unresolved supernovae. The total energy density is $e = \frac{\rho v^2}{2} + e_{\rm thermal} + e_{\rm cr} + \frac{B^2}{8\pi}$, where $e_{\rm thermal}$ is the thermal energy density and $e_{\rm cr}$ is the energy density of cosmic rays. $\mathbf{K}$ is the cosmic ray diffusion tensor, $\dot{u}_{\rm chem}$ is the change in energy due to heating and cooling processes (see Sec. 3.1.3), $\dot{u}_{\rm sn}$ is the thermal energy input from resolved supernovae. For the diffusion tensor $\mathbf{K}$ we assume the two constant components to be $K_{\parallel} = 10^{28}$ cm^2 s^{-1} and $K_{\perp} = 10^{26}$ cm^2 s^{-1}, which are parallel and perpendicular to the magnetic field lines, respectively (Strong et al., 2007; Nava & Gabici, 2013). The source term $Q_{\rm cr} = Q_{\rm cr,injection} + \Lambda_{\rm hadronic}$ accounts for the injection of cosmic ray energy, in the amount of 10^{50} erg, equal to 10% of the explosion energy of a supernova (Ackermann et al., 2013). The loss term $\Lambda_{\rm hadronic}$ accounts for hadronic and adiabatic losses, according to (Pfrommer et al., 2017)

$$\Lambda_{\rm hadronic} = -7.44 \times 10^{-16} \times \left(\frac{n_{\rm e}}{\rm cm^{-3}}\right) \times \left(\frac{e_{\rm cr}}{\rm ergcm^{-3}}\right) {\rm erg\ s^{-1}cm^{-3}}. \quad (3.7)$$

3.1.2 Gravity

The gravitational field in our simulations is composed of four different contributions: the self-gravity of the gas, the gravity due to the presence of sink particles (see Sec. 3.1.4), a gravitational potential due to the presence of an old stellar disc, and the gravitational field of a dark matter potential. We describe the modelling of these four terms in the following.

Self-gravity

To compute the self-gravity of the gas, we need to solve the Poisson equation

$$\Delta\Phi_{\mathrm{gas}} = 4\pi G\rho, \tag{3.8}$$

such that the resulting gravitational acceleration can be written as

$$\mathbf{g}_{\mathrm{gas}} = -\nabla\Phi_{\mathrm{gas}}. \tag{3.9}$$

We solve Eq. 3.8 using the TreeRay implementation of Wünsch et al. (2018), which is based on the OctTree algorithm by (Barnes & Hut, 1986). This method takes advantage of the tree structure of the Flash data to quickly traverse the domain. When evaluating the gravitational potential at each point, the algorithm walks the tree to decide whether to use the mass stored in the node, or to open the node and consider its children. A node is accepted (so it is not opened) if

$$\frac{h}{|\mathbf{r} - \mathbf{r}_a|} < \theta_{\mathrm{lim}}, \tag{3.10}$$

where h is the linear size of the node, $\mathbf{r}$ is the position of the target point, $\mathbf{r}_a$ is the position of the centre of mass of the node, and θ_{lim} is a user-defined opening angle. The masses of all the accepted nodes are then summed up, to compute the gravitational potential. We refer to Wünsch et al. (2018) for the details of its implementation and execution.

Sink particles

The gravity due to sink particles (see Sec. 3.1.4) can be divided into three different terms, which are listed in Federrath et al. (2010). First of all, sink particles feel a gravitational acceleration due to the gas component. This acceleration of the sink particles because of the gas can be computed from Eq. 3.9, where $\mathbf{g}_{\mathrm{gas}}$ is interpolated from the grid onto the sink particles, using a first-order method (see Federrath et al., 2010, for more details).

Sink particles also exert a gravitational attraction onto the gas. This acceleration is computed as direct sum involving all the n sink particles and all computational cells,

$$\mathbf{g}_{\mathrm{s-g}}(i,j,k) = -\sum_n \frac{GM_n}{|\mathbf{r}_n(i,j,k)|^3}\mathbf{r}_n(i,j,k), \tag{3.11}$$

where (i,j,k) indicates the centre of each cell, $\mathbf{r}_n$ the distance of a cell from each particle, and M_n is the mass of the n^{th} particle.

Lastly, a sink particle n attracts gravitationally all the other m sink particles. The resulting acceleration is computed as direct sum,

$$\mathbf{g}_{\mathrm{s-s},n} = -\sum_{m \neq n} \frac{G M_m}{|\mathbf{r}_{nm}|^3} \mathbf{r}_{nm}, \tag{3.12}$$

where $|\mathbf{r}_{nm}|$ is the distance between the n^{th} and m^{th} particle.

Eqs. 3.11 and 3.12 diverge if the distances at the denominator are zero, or sufficiently small. To avoid this issue, gravitational softening is applied for distances smaller than a softening radius r_{soft}, such that the gravitational acceleration goes to zero as the distance approaches zero. The gravity due to sink particles is computed using an Hermite integrator of fourth order, developed by Dinnbier & Walch (2020).

Old stellar disc

We include an old stellar disc, whose distribution in space is modelled according to an isothermal sheet (Spitzer, 1942). In this model, the low-mass stars are assumed to be distributed in a thin sheet in the galactic plane. Following Walch et al. (2015), the vertical distribution can be written as

$$\rho_*(R, z) = \rho_*(R, 0)\mathrm{sech}^2(z/2z_d), \tag{3.13}$$

with R galactocentric radius, z height above the disc ($z = 0$ is the midplane), and z_{d} is the scaleheight of the stellar disc.

We can write the midplane density $\rho_*(R, 0)$ as a function of the stellar surface density $\Sigma_*(R)$:

$$\rho_*(R, 0) = \frac{\Sigma_*(R)}{4z_{\mathrm{d}}} \tag{3.14}$$

where we assume $\Sigma_* = 30\ \mathrm{M}_\odot\ \mathrm{pc}^{-2}$ and $z_{\mathrm{d}} = 300$ pc. The gravitational potential of the stellar disc is computed by solving the Poisson's equation

$$\Delta\Phi_* = 4\pi G \rho_*, \tag{3.15}$$

and the gravitational acceleration is found using

$$g_{\mathrm{ext}}(z) = -\frac{\partial \Phi_*}{\partial z}. \tag{3.16}$$

Dark matter

To model the gravitational potential of dark matter, we employ a NFW profile (Navarro et al., 1996), which reads

$$\rho_{\mathrm{dm}}(R) = \frac{\rho_s}{(R/r_s)(1 + R/r_s)^2}, \tag{3.17}$$

where R is the radial spherical coordinate, ρ_s and r_s are the characteristic density and scale radius of the dark matter halo. It is useful to define the virial radius $R_{\rm vir}$ as the edge of the halo, which is related to the scale radius r_s via the concentration parameter c,

$$R_{\rm vir} = c r_s. \tag{3.18}$$

In our setup we assume $R_{\rm vir} = 200$ kpc, $c = 12$ and a distance $R = 8$ kpc from the galactic centre.

3.1.3 Chemistry, Heating and Cooling

In our simulations we model heating, cooling and chemical abundances using the network for hydrogen chemistry presented in Glover & Mac Low (2007a,b), supplemented with the carbon chemistry model introduced in Nelson & Langer (1997). We follow the evolution of seven chemical species, H, H^+, H_2, CO, C^+, O, and free electrons, by solving a continuity equation in the form

$$\frac{\partial \rho_i}{\partial t} + \nabla \cdot (\rho_i \mathbf{v}) = C_i\,(\rho, T, \ldots) - D_i\,(\rho, T, \ldots), \tag{3.19}$$

where i denotes the chemical species, C_i and D_i are the creation and destruction rates of the species i, which depend on density, temperature, abundances, etc. Therefore, a set of coupled partial differential equations has to be solved. To handle this computation more efficiently, an operator splitting of the advection and source terms is employed. With this method, the advection terms and source terms are handled separately. For the advection step, which handles the chemical abundances as if they were constant, Eq. 3.19 simplifies to

$$\frac{\partial \rho_i}{\partial t} + \nabla \cdot (\rho_i \mathbf{v}) = 0. \tag{3.20}$$

The evolution of chemical abundances is then computed in a separate chemistry step, where we solve a set of coupled ordinary differential equations in the form

$$\frac{d\rho_i}{dt} = C_i\,(\rho, T, \ldots) - D_i\,(\rho, T, \ldots), \tag{3.21}$$

which are solved simultaneously with the heating and cooling.

The fractional abundances of the chemical species we model are constrained using different conservation laws, for example the conservation of total charge, which leads to

$$x_{\rm e} = x_{\rm H^+} + x_{\rm C^+} + x_{\rm Si^+}, \tag{3.22}$$

where x_i is the fractional abundance of the species i relative to the total abundance of hydrogen nuclei. Moreover, the total abundances of hydrogen, carbon and oxygen are conserved, from which we can derive the abundances of atomic hydrogen, ionized carbon and atomic oxygen from the respective conservation laws,

$$x_{\rm H} = 1 - 2x_{\rm H_2} - x_{\rm H^+}, \tag{3.23}$$

$$x_{\rm C^+} = x_{\rm C,tot} - x_{\rm CO}, \tag{3.24}$$

$$x_{\rm O} = x_{\rm O,tot} - x_{\rm CO}. \tag{3.25}$$

Here $x_{\rm C,tot}$ and $x_{\rm O,tot}$ are the total fractional abundances of carbon and oxygen, respectively, relative to hydrogen abundance. Moreover, we model the formation of H_2 and CO taking into account the attenuation of the interstellar radiation field due to H_2, CO self-shielding and dust shielding by means of the TreeCol algorithm (see Clark et al., 2012, for more details). The local visual extinction $A_{\rm V}$ is computed as (Bohlin et al., 1978)

$$A_{\rm V} = \frac{N_{\rm H,tot}}{1.87 \times 10^{21} {\rm cm}^{-2}} \times Z, \tag{3.26}$$

where $N_{\rm H,tot}$ is the 3D-averaged column density computed by TreeRay/OpticalDepth (more details in Wünsch et al. 2018), and Z is the metallicity of the gas in units of solar metallicity.

In our simulations we adopt a wide range of different abundances and dust-to-gas ratios. In our runs with solar metallicity, we assume a dust-to-gas ratio of 1% and the abundances of total carbon, oxygen and silicon as $x_{\rm C,tot} = 1.41 \times 10^{-4}$, $x_{\rm O,tot} = 3.16 \times 10^{-4}$ and $x_{\rm Si,tot} = 1.5 \times 10^{-5}$, respectively (Sembach et al., 2000). For the runs with sub-solar metallicity, we linearly scale the abundances and the dust-to-gas ratio by the chosen metallicity.

We model the the cooling of the gas including contributions from the fine structure lines of C^+, O, Si^+, Lyman-α cooling, the rotational and vibrational lines of H_2 and CO, and energy transfer from gas to dust, following the cooling function from Glover et al. (2010); Glover & Clark (2012b). At temperatures higher than 10^4 K we assume the helium and metals to be in collisional ionization equilibrium, and we adopt the cooling rates from Gnat & Ferland (2012b). We also include cooling from collisional ionization of H, H^+ recombination and collisional dissociation of H_2 (see Glover & Mac Low, 2007a,b; Glover & Clark, 2012b).

Concerning heating mechanisms, we include photoelectric heating from dust grains and polycyclic aromatic hydrocarbons, heating due to low-energy cosmic rays, heating due to H_2 formation, H_2 photodissociation and UV pumping of H_2. Regarding the photoelectric heating, we model the heating rate as

$$\Gamma_{\rm pe} = 1.3 \times 10^{-24}\, \epsilon\, G_{\rm eff}\, n\ [{\rm erg\ s^{-1}\ cm^{-3}}], \tag{3.27}$$

with $G_{\rm eff} = G_0 \exp(-2.5 A_V)$, n the gas number density, ϵ being the photoelectric heating efficiency given by Bakes & Tielens (1994); Wolfire et al. (2003) as

$$\epsilon = \frac{0.049}{1 + (\psi/963)^{0.73}} + \frac{0.037(T/10000)^{0.7}}{1 + (\psi/2500)}, \tag{3.28}$$

with

$$\psi = \frac{G_{\rm eff} T^{1/2}}{n_{\rm e}}. \tag{3.29}$$

The cosmic ray heating rate can be expressed as (Goldsmith & Langer, 1978)

$$\Gamma_{\rm cr} = 20\ \zeta_{\rm H}\ n\ [\rm eV\ s^{-1} cm^{-3}] = 3.2\ \times 10^{-11}\ \zeta_{\rm H}\ n\ [\rm erg\ s^{-1}\ cm^{-3}] \tag{3.30}$$

For the calculation of $G_{\rm eff}$ and $\zeta_{\rm H}$ we refer to Sec. 3.1.5 and Sec. 3.2, respectively.

3.1.4 Star formation

Star formation is a multiscale problem, concerning the structure and evolution of the gas in molecular clouds (which are in the order of tens, hundreds of pc) down to the size of stars (with diameters in the order of solar radii). This is a difference of around 10 orders of magnitude in lenght scale. Moreover, since the free-fall time scale decreases for increasing density, following the free-fall collapse from from molecular clouds densities to stellar densities requires around 10 orders of magnitude in timescales.

Therefore, modelling appropriately the interplay between turbulence and gravity that allows for the fragmentation of molecular clouds and the subsequent star formation is non-trivial, and needs to employ ad hoc solutions. To overcome this problem, a common remedy is employing sink particles (see e.g. Bate et al., 1995; Krumholz et al., 2004), which are useful to model the gravitational collapse of the gas into stars and the accretion of gas onto stars. They represent regions of the gas flow where the inflowing material exceeds a density threshold, however, they are not internally resolved, therefore they cause no resolution problems.

Federrath et al. (2010) implemented in Flash the sink particles method, such that sinks are able to freely move within the domain without being bound to the underlying grid, meaning moving in the Lagrangian frame of reference, on contrary of the grid points that are fixed in space, i.e. in the Eulerian frame of reference. The creation of a sink particle is dependent on a series of tests, that are performed to avoid the formation of spurious particles in regions that are not undergoing gravitational collapse. The first test consists in verifying whether cells with a density higher than a user-defined threshold $\rho_{\rm sink}$ are present. If so, a spherical region centred on the cell and with a radius $r_{\rm acc}$ is created. Inside this region, it is then checked whether the gas is

- gravitationally bound;
- Jeans-unstable;
- in a converging flow;
- in a gravitational potential minimum;
- on the highest refinement level in all cells within $r_{\rm acc}$;
- not within a distance $r_{\rm acc}$ from another sink particle.

If the gas within $r_{\rm acc}$ is at a density higher than $\rho_{\rm sink}$, it gets accreted onto the sink particle. It is important to note that sink particles in our code can describe both single stars and star clusters, however, only the latter solution is used in this work. In fact, we do not include runaway stars in the simulations performed in this works, for which single-star sink particles would be needed.

In our setup we follow the evolution of massive stars (≥ 9 M$_\odot$) individually, since they are the main feedback drivers, and we account for the presence of low-mass stars only for their gravity and far-UV (FUV) emission. Every time that 120 M$_\odot$ of gas is converted into, or accreted on to, a sink particle, one massive star is formed with an initial mass sampled using a Salpeter-like initial mass function (Salpeter, 1955) in the mass range 9 – 120 M$_\odot$. The difference between 120 M$_\odot$ and the sampled initial mass gives the gas mass that is converted in low-mass stars. Therefore, we assume in our prescription a cluster formation efficiency of 100%, since all the available gas is converted into stars. The number of stars in a sink particle (star cluster) can vary according to the specific sink and simulation time. In fact, cluster-sink particles have the possibility to accrete gas in time, and when the accreted gas hits the 120 M$_\odot$ threshold, they form a new massive star.

3.1.5 Stellar feedback

The stellar feedback mechanisms included in our code are non-ionizing FUV and ionizing (EUV) radiation from stars, stellar winds, supernovae, and cosmic rays. We model the evolution of massive stars, meaning the time evolution of their surface temperature, mass loss rate, bolometric luminosity, terminal velocity of the wind using either the Geneva tracks (Ekström et al., 2012) for the solar metallicity runs, or the BoOST models (Brott et al., 2011; Szécsi et al., 2022) for the sub-solar metallicity runs. In the following, we will describe the numerical methods that implement these mechanisms.

FUV radiation

Rathjen et al. (2024) implement a novel method to compute self-consistently the FUV radiation emitted from star clusters. Following Rathjen et al. (2024), the FUV interstellar radiation field strength is usually measured in Habing units (Habing, 1968):

$$G_0 = \frac{u_{\rm FUV}}{5.29 \times 10^{-14}\ {\rm erg\ cm^{-3}}}, \tag{3.31}$$

with $u_{\rm FUV}$ the energy density in the FUV photon energy range 5.6–13.6 eV. They assume a background value $G_{\rm bg} = 0.0948$, which has been computed as the sum of a background value from Haardt & Madau (2012) and a static value coming from the assumption of the presence of a static old stellar disc with stellar surface density of $\Sigma_* = 30\ {\rm M_\odot\ pc^{-2}}$.

The FUV intensity in Habing units $G_{\rm clus}$ of each star cluster is computed as the sum of the contribution from low-mass stars and massive stars. In the first case, the FUV emitted from low-mass stars is computed using tabulated Starburst99 models, with a total star cluster mass of $10^6\ {\rm M_\odot}$ sampled with a Kroupa initial mass function (Kroupa, 2001), and in the individual mass range 0.1–9 $\rm M_\odot$. The resulting spectrum calculated by Starburst99 is then integrated in the energy interval 5.6–13.6 eV to obtain the total FUV luminosity of this $10^6\ {\rm M_\odot}$ star cluster. After that, this value of total FUV luminosity is scaled by the mass in low-mass stars present in the considered star cluster. Regarding massive stars, whose evolution is tracked individually, their black body spectrum is computed, given their effective temperature from the stellar models, and then this is integrated in the 5.6–13.6 eV range and divided by the integral of the spectrum over the entire energy range. This ratio is then multiplied by the bolometric luminosity of the star, which gives the star's FUV luminosity. The two contributions from low-mass and massive stars are then added together, giving $G_{\rm clus}$.

The value of $G_{\rm clus}$ is then diluited in the region surrounding the star cluster using the inverse square law,

$$G_{\rm clus}(R) \propto R^2, \tag{3.32}$$

with R radial distance from the cluster. Therefore, the local unattenuated ISRF strenght reads

$$G_0 = \left(\sum_{\rm N_{cluster}} G_{\rm clus} \right) + G_{\rm bg}. \tag{3.33}$$

Dust attenuation must also be taken into account, therefore the value of G_0 is scaled as (van Dishoeck & Black, 1988)

$$G_{\rm eff} = G_0 \times \exp(-2.5 A_{\rm V}). \tag{3.34}$$

EUV radiation

As already seen above, Wünsch et al. (2018) have implemented a tree solver to compute the gravity and the optical depth. To compute the radiation transport equation, necessary to take into account the propagation of radiation in the interstellar medium, Wünsch et al. (2021) have implemented a module for the tree solver called TreeRay/OnTheSpot. This module takes into account only ionizing radiation, and adopts the On-The-Spot approximation to model the interaction of the UV field radiation emitted by massive stars with the interstellar medium (Osterbrock, 1988). This means that TreeRay/OnTheSpot handles only photons from sources (stars), and that recombination photons produced in the gas are immediately reabsorbed locally, therefore they are not transported through the computational domain.

TreeRay is a backward radiative transfer method, hence it is independent of the number of sources. To compute the radiation transport equation, TreeRay builds for each cell in the computational domain a HealPIX sphere (Górski et al., 2005) with 48 pixels, casts rays from its centre, and solves the radiation transport along these directions. The fraction of ionizing radiation coming from each star cluster is computed assuming a black body spectrum for each massive star, described by their effective temperature, which is taken from the stellar models. For each massive star in the cluster and at each time step, the black body is integrated for energies higher than 13.6 eV, and divided by the integral of the spectrum in the total energy range. The total energy density of the ionizing radiation of the star cluster is then injected in the cell where the cluster is found.

Stellar winds

For the calculation of the impact of stellar winds we use the mass loss rate and the wind velocity from the stellar models. In the case of the Geneva tracks (Ekström et al., 2012), the terminal velocity of the wind is computed as explained in Gatto et al. (2017). The stellar models compute the evolution of massive stars from their Zero Age Main Sequence until the pre-supernova phase, without including the protostellar stage. After a star has formed, we do not include any time delay to account for the protostellar phase, and we start directly with the main sequence evolution.

Following Gatto et al. (2017), the modelling of the stellar wind is done in a few steps. First, the total mechanical luminosity of each star cluster is computed at each time step, adding up all the wind coming from the N_* massive stars,

$$L_{\text{tot}} = \frac{1}{2} \sum_{i=1}^{N_*} \dot{M}_{\text{wind,i}} \times v^2_{\text{wind,i}} \ [\text{erg s}^{-1}], \tag{3.35}$$

where $\dot{M}_{\text{wind,i}}$ is the mass loss rate of the i^{th} massive star, and $v_{\text{wind,i}}$ its terminal wind velocity.

Then the total mass lost by the stars in a cluster is computed,

$$\dot{M}_{\rm tot} = \sum_{i=1}^{N_*} \dot{M}_{\rm wind,i}. \tag{3.36}$$

In a time step Δt, the total mass lost by the cluster $\dot{M}_{\rm tot} \times \Delta t$ is added to the wind injection region, which is set equal to $r_{\rm acc}$. The injected mass is then evenly distributed within the cells belonging to the injection region. The mass of the cluster is decreased accordingly. The internal energy carried by the injected mass is taken into account. Moreover, the wind feedback is injected as kinetic energy $e_{\rm inj}$, which is evenly distributed within $r_{\rm acc}$. This can be written as

$$e_{\rm inj} = \dot{e}_{\rm inj} \times \Delta t = L_{\rm tot} \times \Delta t = \frac{1}{2} M_{\rm inj} v_{\rm r}^2, \tag{3.37}$$

where $M_{\rm inj} = M_{\rm inj,old} + \dot{M}_{\rm tot} \times \Delta t$ is the sum of the mass of the material present already in the injection region and that of the newly injected material; $v_{\rm r}$ is the radial velocity. The radial velocity to be applied within the injection region can be therefore written as

$$v_{\rm r}^2 = 2 \frac{L_{\rm tot} \times \Delta t}{M_{\rm inj}}. \tag{3.38}$$

Supernovae

All massive stars formed in our simulations are assumed to explode as supernovae Type II at the end of their life. If the Sedov-Taylor phase can be resolved with at least three cells, we inject 10^{51} erg in the form of thermal energy in a spherical region with radius $r_{\rm acc}$. Therefore, the material present in the injection region is heated up to 10^6–10^7 K, which corresponds to a sound speed $c_{\rm s}$ of the order of a few hundred km s^{-1}. Following Gatto et al. (2015), this causes a Sedov-Taylor blast wave to expand in the surrounding medium. To capture the evolution of the blast wave, the time step is decreased according to a modified Courant-Friedrichs-Lewy condition, in the form

$$\Delta t = C_{\rm CFL} \frac{\Delta x}{\max(|v| + c_{\rm s})}. \tag{3.39}$$

If the Sedov-Taylor phase is not resolved, we switch to momentum injection to prevent overcooling. Following Gatto et al. (2015), the momentum is computed as (Blondin et al., 1998),

$$p_{\rm ST} = 2.6 \times 10^5 \left(\frac{E_{\rm SN}}{10^{51} {\rm erg}} \right)^{16/17} \left(\frac{\overline{n}}{\rm cm^{-3}} \right)^{-2/17} {\rm M_\odot~km~s^{-1}}. \tag{3.40}$$

This momentum is deposited in the density distribution of the injection region, by adding the corresponding outward-pointing velocity

$$v_{\text{inj}} = \frac{p_{\text{ST}}}{M_{\text{inj}}}. \tag{3.41}$$

At the same time, the temperature of the gas in the injection region is brought to 10^4 K, guaranteeing that the momentum injection is accounted for, despite the energy losses.

Cosmic rays

In our code cosmic rays (CRs) are treated as a separate relativistic fluid, which is coupled to the MHD equations, in the advection-diffusion approximation (Schlickeiser & Lerche, 1985). Following Girichidis et al. (2014), the addition of CRs to the modelling of the gaseous system must fulfil the hydrodynamic limit, where the gyroradius of CRs,

$$r_{\text{gyro,cr}} = \frac{p_\perp}{|q|B}, \tag{3.42}$$

is smaller than the size of one grid cell. Here, $p_\perp$ is the momentum of the particles perpendicular to the magnetic field lines, q is the electric charge and B is the modulus of the magnetic field.

The CR transport in the advection-diffusion approximation is given by Eq. 3.5. Its first term on the left-hand side of the equation is the time evolution of the CR energy, whereas the second term is the advection term. On the right side of the equation, we find the adiabatic term, followed by the diffusion term and the source term. CRs coupled to the gas exert a pressure that lifts the gas from the midplane (Hanasz et al., 2013; Girichidis et al., 2016b, 2018a), which reads

$$P_{\text{CR}} = (\gamma_{\text{CR}} - 1) e_{\text{CR}}, \tag{3.43}$$

where γ_{CR} is the adiabatic index of the CR fluid, and e_{CR} is the energy density of CRs. The contribution of the CR pressure and of the CR energy density are added to Eq. 3.2 and Eq. 3.3, respectively. The diffusion is treated in an anisotropic approach (Ryu et al., 2003),

$$\mathbf{K} = K_{ij} = K_\perp \delta_{ij} + \left(K_\parallel - K_\perp\right) n_i n_j \tag{3.44}$$

with $K_\perp$ and $K_\parallel$ being the diffusion coefficients perpendicular and parallel to the magnetic field, respectively, and $n_i = B_i/|\mathbf{B}|$. In our code, we assume a gray CR spectrum, meaning that we do not bin CR energies as done in Girichidis et al. (2014).

3.2 A new implementation of cosmic-ray heating

As already seen above, the heating rate due to low-energy cosmic rays is described by Eq. 3.30. In the previous works of the SILCC collaboration, the parameter ζ has been set constant and equal to 3×10^{-17} s^{-1}. In Paper I, we implement a new method to compute ζ, where instead of having it as a fixed parameter, we consider it as a variable and compute its distribution. In order to achieve that, we linearly scale the energy density of CRs to obtain ζ, as

$$\zeta = 3 \times 10^{-17} \left(\frac{e_{\mathrm{cr}}}{1 \text{ eV cm}^{-3}} \right) \mathrm{s}^{-1}. \tag{3.45}$$

We take into account CR attenuation in the dense gas, where the 3D-averaged column density computed by TreeRay/OpticalDepth, $N_{\mathrm{H,tot}}$, exceeds a threshold value $N_{\mathrm{thr}} > 10^{20}$ cm^{-2}. This threshold value is chosen to match the threshold value for CR attenuation shown in Fig. C1 in Padovani et al. (2022). We compute an attenuation factor

$$c_{\mathrm{att}} = (N_{\mathrm{H,tot}}/N_{\mathrm{thr}})^{-0.423}, \tag{3.46}$$

where the exponent is the prescription from Padovani et al. (2009) for protons. In the case of $N_{\mathrm{H,tot}} > N_{\mathrm{thr}}$, we multiply the right-hand side of Eq. 3.45 by c_{att}.

It should be noted that here we use the total column density $N_{\mathrm{H,tot}}$, instead of the H_2 column density N_{H_2} used in the prescription by Padovani et al. (2009, 2022) for proton impacts on H_2 gas. This is due to the fact that in low-metallicity environments, the amount of H_2 is small (see Chapter 5), therefore we would underestimate CR attenuation if we were using N_{H_2}. We speculate that using $N_{\mathrm{H,tot}}$ instead of N_{H_2} affects the attenuation of ζ with an uncertainty of a factor of 2 (Glassgold & Langer, 1974). More details can be found in Chapter 4 (Paper I).

3.3 Simulation setup

Our setup is a tall box with size 500 pc × 500 pc × ± 4 kpc, which aims to study the evolution of the interstellar medium and of galactic outflows in a galaxy patch far away from the galactic centre, neglecting the possible presence of spiral arms and shearing effects due to galaxy dynamics. Near the midplane we adopt a resolution of around 3.9 pc, whereas for $|z| > 1$ kpc the resolution is a factor of two lower. In the beginning of each simulation, the gas is distributed in the vertical direction according to a Gaussian profile,

$$\rho(z) = \rho_0 \exp\left[- \left(\frac{z}{h_z} \right)^2 \right] \tag{3.47}$$

where ρ_0 is the midplane density, h_z is the scaleheight of the disc, and both change depending on $\Sigma_{\rm gas}$. The Gaussian distribution is cut at a height z for which the disc density is equal to the background density $\rho_{\rm amb} = 10^{-27}$ g cm^{-3}. The temperature at the beginning of the run is set to 5000 K. The magnetic field is initialized in the x-direction, varying in the z-direction as

$$B_x(z) = B_{x,0}\sqrt{\rho(z)/\rho_0}, \tag{3.48}$$

where $B_{x,0}$ depends on the choice of $\Sigma_{\rm gas}$ (see Paper I – III for more details). An example snapshot can be seen in Fig. 3.1, taken from the Σ`050` run.

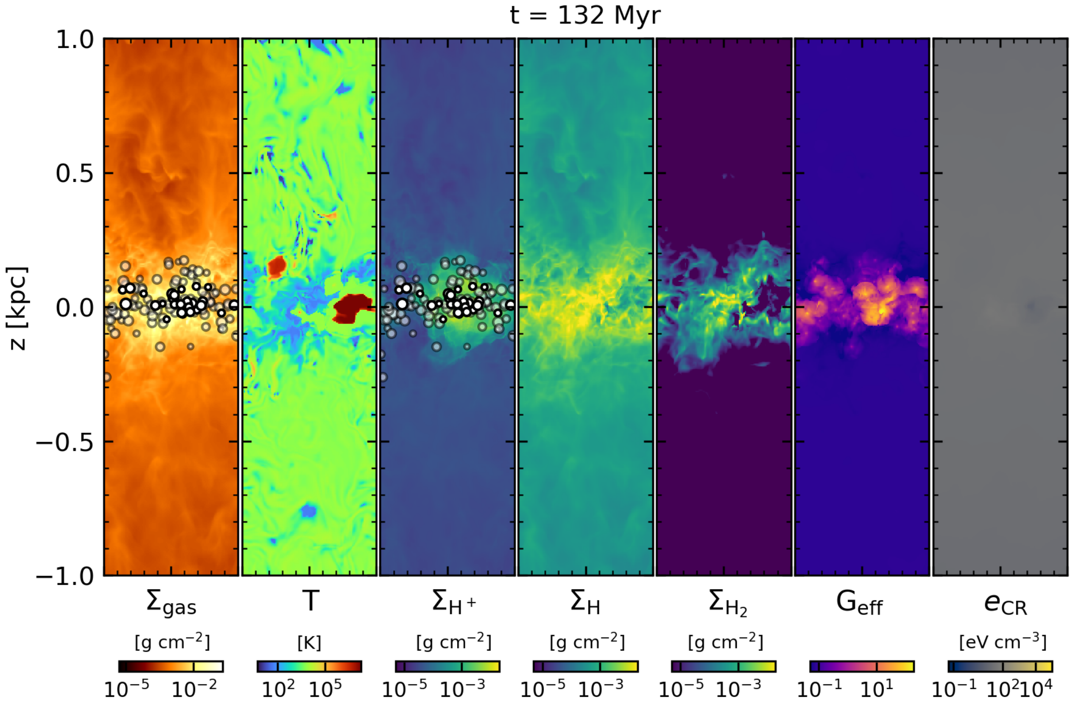

Figure 3.1

Snapshot of the Σ`050` run at t = 132 Myr. The seven panels show the edge-on view of the following quantities: the column density $\Sigma_{\rm gas}$ of the gas, a slice of the temperature, the column density of H$^+$, H, H$_2$, a density-weighted projection of $G_{\rm eff}$, and a slice of the energy density of CRs, $e_{\rm CR}$. The white circles are active (opaque) and inactive (transparent) star clusters.

3.3.1 List of all simulations

For a better overview of the SILCC simulations performed in this work, we list all our runs in Table 3.1.

Table 3.1

List of all simulations performed in this thesis. $\Sigma_{\rm gas}$ is the gas surface density, Z the metallicity, G_0 the interstellar radiation field strength in Habing units, ζ the cosmic ray ionization rate. The runtime is counted from the onset of star formation.

Name	$\Sigma_{\rm gas}$ [$M_\odot$ pc^{-2}]	Z [$Z_\odot$]	G_0	ζ [s^{-1}]	Runtime [Myr]	Publication
`(Σ010-)Z0.02`	10	0.02	1.7	$3{\times}10^{-17}$	200	Paper I/II
`Z0.02-vG0`	10	0.02	Variable	$3{\times}10^{-17}$	200	Paper I
`Z0.02-vG0-vζ`	10	0.02	Variable	Variable	200	Paper I
`Z0.02-vG0-vζ-BS`	10	0.02	Variable	Variable	200	Paper I
`Σ010(-Z1)`	10	1	Variable	Variable	300	Paper II/III
`Σ010-Z0.6`	10	0.6	Variable	Variable	200	Paper II
`Σ010-Z0.3`	10	0.3	Variable	Variable	200	Paper II
`Σ010-Z0.2`	10	0.2	Variable	Variable	200	Paper II
`Σ010-Z0.1`	10	0.1	Variable	Variable	200	Paper II
`Σ010-Z0.04`	10	0.04	Variable	Variable	200	Paper II
`Σ050`	50	1	Variable	Variable	300	Paper III
`Σ050-Z0.1`	50	0.1	Variable	Variable	300	Paper III
`Σ050-Z0.02`	50	0.02	Variable	Variable	300	Paper III
`Σ100`	100	1	Variable	Variable	300	Paper III
`Σ100-Z0.1`	100	0.1	Variable	Variable	300	Paper III
`Σ100-Z0.02`	100	0.02	Variable	Variable	300	Paper III
`Σ300-Z0.02`	300	0.02	Variable	Variable	300	Paper III

3.4 Dendrogram analysis

In Paper II we employ the dendrogram algorithm to determine the features of the dense gas in our simulations. In this section, we therefore explain in more detail what a dendrogram is and how it works. To calculate dendrograms we employ the ASTRODENDRO[2] Python package.

3.4.1 What is a dendrogram?

A dendrogram is a tree-like diagram that helps visualizing hierarchical relationships among the points of a data set. In our case, we use this tool to identify dense structures in our simulation data.

Dendrograms are composed of three parts: *leaves*, which are the smallest structures, without no sub-structures inside them; *branches*, which are structures that can split in smaller sub-structures, being either other branches or leaves; the *trunk*, which is the main structure and presents no parent structures. An example of a two-dimensional hierarchical structure and its dendrogram are shown in Fig. 3.2.

---

[2] `https://dendrograms.readthedocs.io/`

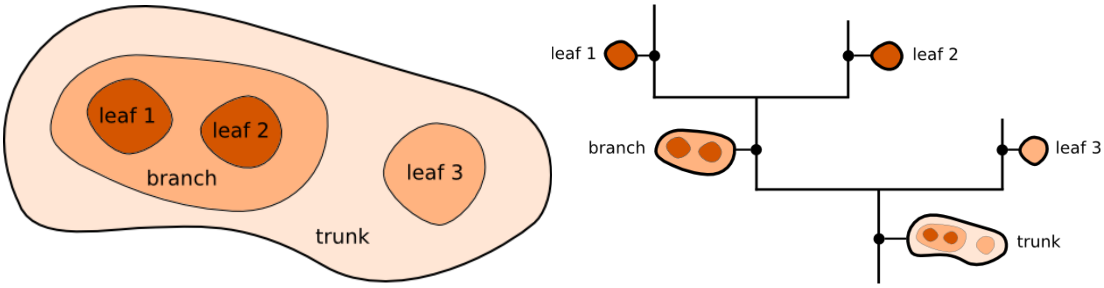

(a) Example of hierarchical structure. (b) Corresponding dendrogram.

Figure 3.2

An example of dendrogram, computed from a generic hierarchical structure. Taken from the ASTRODENDRO documentation.

3.4.2 How does the dendrogram algorithm work?

The dendrogram algorithm can be applied to data sets of any number of dimensions, however, in the following we will consider a one-dimentional data set for the sake of clarity. Given a quantity q that the data set represents, the first step of the algorithm is to find the element of the array (which in the ASTRODENDRO's jergon is named *pixel*), for which q is maximum. This is the beginning of the first structure, which is a leaf. After that, the second highest value is found, and it is decided whether this pixel has to be added to the first structure, or if it constitutes a structure on its own. If this second pixel is a local maximum, meaning that it is higher than its immediate neighbours, then it will form a new structure, otherwise it will be added to the first. This process goes on looking for the remaining highest values of q. When it is reached a pixel that is not a local maximum, but that it is adiacent to two existing structures, the latter are merged into a branch. This process is continued until all detected structures are merged into a single tree-structure, whose highest-level part is the trunk.

3.4.3 Dendrogram parameters

To fine-tune the dendrogram computation, some tuning parameters come at hand, which are especially useful to remove from the computation the noise present in the data. These parameters are described in the following.

Minimum significance

Unless specified, all pixels in the data set are taken for the computation of the dendrogram. However, the smallest values might represent noise, for which the tree would measure nothing physical. Therefore, a minimum value of the quantity q can be specified, via the parameter `min_value`, above which the pixels are considered for computation. This practice removes all structures that peak below the specified `min_value`.

Minimum number of cells

The parameter `min_npix` defines the minimum number of cells for which a leaf can be considered independent. If a leaf contains a number of cells lower than `min_npix`, it is not added to the tree as independent structure, rather it is merged to the nearest branch or leaf.

Minimum peak difference

The `min_delta` parameter describes the minimum height that a structure must have to be independent, to filter out noise-generated features. A higher value of `min_delta` results in fewer, larger structures, whereas a lower value results in a more detailed dendrogram tree.

3.4.4 Example

In this section, we explain how the computation of the dendrogram on the data of Paper II has been performed. In this case, we are interested in capturing the fragmentation of the gas, therefore we apply the dendrogram to understand the shape of structures of the density field. In Paper II, we perform this analysis in 3D. Here, for simplicity, we show the calculation in 2D, applying the computation to the density projected along the z-direction into the x-y plane of our simulations.

Since both 3D density and column density span several orders of magnitude, we compute the dendrogram after taking the log10 of the data. In this way we reduce the number of structures which would otherwise be identified if we were using the linear data. In Paper II, we have adopted the following parameters: `min_value` = 10^{-23} g cm^{-3}, `min_delta` = 0.1 (in log space), `min_npix` = 100 cells. For more convenience, in this 2D example we choose `min_value` = 10^{-22} g cm^{-3}, which is then converted into a column density threshold by multiplying by the resolution in the midplane ($\approx$ 3.9 pc). We also choose `min_npix` to be the number of cells that fit an area of a square with a 20 pc side.

The result of this computation can be seen in Fig. 3.3. In each panel we represent the column density in the x- and y-plane of the seven simulations of Paper II at 100 Myr after the onset of star formation. The black contour indicates the regions that encompass the density values higher than `min_value`, whereas the red contour highlights the structure of the leaves. The full analysis, as well as the results, can be found in Paper II.

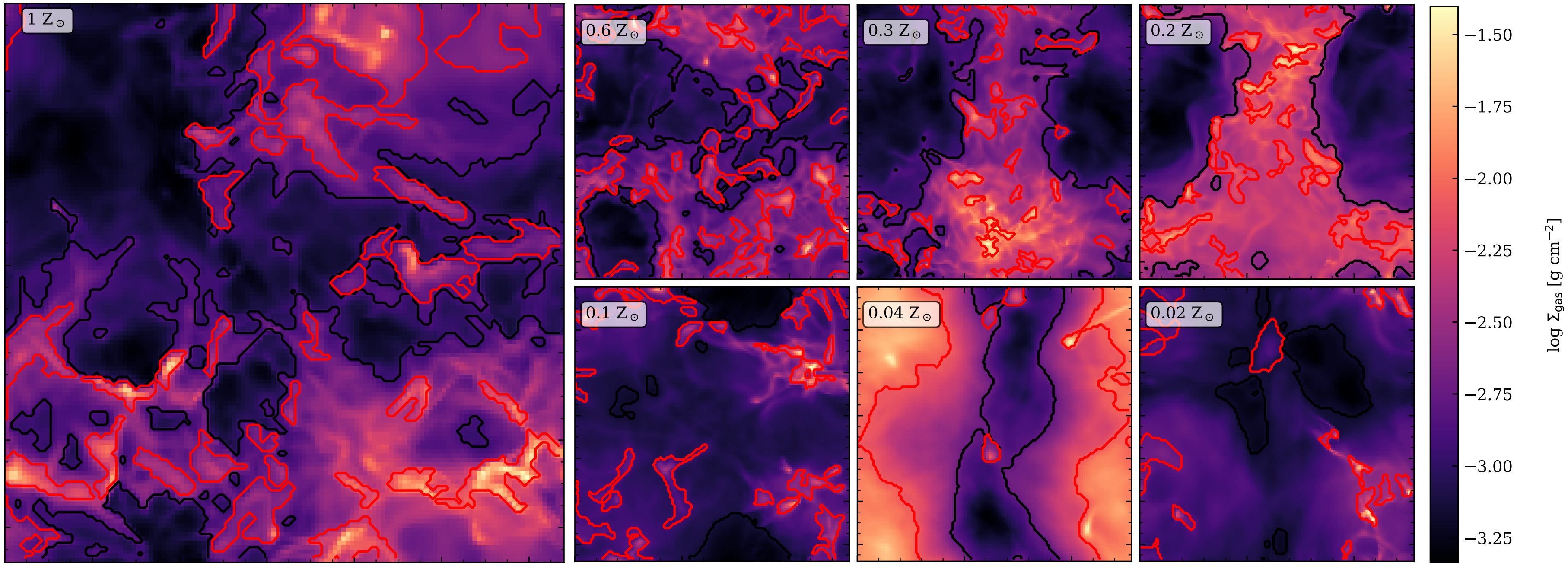

Figure 3.3

Example of dendrogram calculation on the column density of each simulation of Paper II at 100 Myr after the onset of star formation. The numbers in the box indicate the metallicity of the ISM in each run. The black contour indicates the minimum embeds the cells with a column density higher than the minimum value, and the red contours denote the boundaries of the leaves.

3.5 Other tools

Following the rules of the University of Cologne at the time of this writing, the AI tool ChatGPT (OpenAI, 2023) has been used as grammar and spell check for the text of this thesis, which has been written entirely by the author. No text has been generated exclusively by ChatGPT.

CHAPTER 4

PAPER I

In this chapter, we present our new method to compute the cosmic ray ionization rate self-consistently from the energy density of cosmic rays. We test the importance of cosmic ray heating, in comparison with photoelectric heating, in very low metallicity environments (0.02 $Z_\odot$).

4.1 Publication

This work has been published in the Monthly Notices of the Royal Astronomical Society as V. Brugaletta, S. Walch et al., MNRAS, 537, 482, with title "The impact of cosmic-ray heating on the cooling of the low-metallicity interstellar medium".

In this work, the implementation of the new method, the simulations, the data analysis, and the writing of the publication have been performed by Vittoria Brugaletta. The coauthors S. Walch, T. Naab, P. Girichidis, T.-E. Rathjen, D. Seifried, P. C. Nürnberger, R. Wünsch, and S. C. O. Glover engaged in helpful discussions for the development of this work, and have proof-read the manuscript before submission to the journal.

Monthly Notices
of the
ROYAL ASTRONOMICAL SOCIETY

MNRAS **537,** 482–499 (2025)
Advance Access publication 2025 January 10

https://doi.org/10.1093/mnras/staf039

The impact of cosmic-ray heating on the cooling of the low-metallicity interstellar medium

Vittoria Brugaletta ,[1,2]★ Stefanie Walch ,[1] Thorsten Naab ,[2] Philipp Girichidis ,[3]
Tim-Eric Rathjen ,[1] Daniel Seifried ,[1] Pierre Colin Nürnberger,[1] Richard Wünsch [4]
and Simon C. O. Glover [3]

[1] *I. Physikalisches Institut, Universität zu Köln, Zülpicher Straße 77, D-50937 Köln, Germany*
[2] *Max Planck Institute for Astrophysics, Karl-Schwarzschild-Straße 1, D-85748 Garching, Germany*
[3] *Universität Heidelberg, Zentrum für Astronomie, Institut für Theoretische Astrophysik, Albert-Ueberle-Straße 2, D-69120 Heidelberg, Germany*
[4] *Astronomical Institute of the Czech Academy of Sciences, Boční II 1401, CZ-141 00 Prague, Czech Republic*

Accepted 2024 December 20. Received 2024 December 20; in original form 2024 October 24

ABSTRACT

Low-metallicity environments are subject to inefficient cooling. They also have low dust-to-gas ratios and therefore less efficient photoelectric (PE) heating than in solar-neighbourhood conditions, where PE heating is one of the most important heating processes in the warm neutral interstellar medium (ISM). We perform magnetohydrodynamic simulations of stratified ISM patches with a gas metallicity of 0.02 $Z_\odot$ as part of the SILCC project. The simulations include non-equilibrium chemistry, heating, and cooling of the low-temperature ISM as well as anisotropic cosmic-ray (CR) transport, and stellar tracks. We include stellar feedback in the form of far-ultraviolet and ionizing (FUV and extreme ultraviolet, EUV) radiation, massive star winds, supernovae, and CR injection. From the local CR energy density, we compute a CR heating rate that is variable in space and time. In this way, we can compare the relative impact of PE and CR heating on the metal-poor ISM and find that CR heating can dominate over PE heating. Models with a uniform CR ionization rate of $\zeta = 3 \times 10^{-17}\ \mathrm{s}^{-1}$ suppress or severely delay star formation, since they provide a larger amount of energy to the ISM due to CR heating. Models with a variable CR ionization rate form stars predominantly in pristine regions with low PE heating and CR ionization rates where the metal-poor gas is able to cool efficiently. Because of the low metallicity, the amount of formed stars in all runs is not enough to trigger outflows of gas from the mid-plane.

Key words: ISM: abundances – cosmic rays – ISM: jets and outflows – ISM: kinematics and dynamics – ISM: structure – galaxies: ISM.

1 INTRODUCTION

Cosmic rays (CR) are highly energetic charged particles, mainly protons and electrons, but also heavier nuclei, that can travel within the interstellar medium (ISM) and influence both its dynamics and chemistry. At lower energies, below 200 MeV, electrons dominate the composition, whereas at higher energies protons dominate (Cummings et al. 2016). Early studies (Baade & Zwicky 1934; Ginzburg & Syrovatskii 1964) suggest that supernova (SN) remnants in the Milky Way are the main contributors in accelerating GeV–TeV Galactic CRs via diffusive shock acceleration (Krymskii 1977; Axford et al. 1978; Blandford & Ostriker 1978; Bell 1978a, b). At lower energies other acceleration mechanisms are important, in particular, shocks in the ISM (see e.g. a review from Padovani et al. 2020; Hanasz et al. 2021; Ruszkowski & Pfrommer 2023; Meyer 2024). The CR energy spectrum spans more than ten orders of magnitude, and around 32 orders of magnitude in flux (Swordy 2001). The main contribution to the energy density of CRs is provided by protons with energies of a few GeV, whereas for higher energies the energy spectrum declines as a broken power law (e.g. Ruszkowski & Pfrommer 2023). The energy density of CRs measured at Earth was estimated by Webber (1998) to be around 1.8 eV cm^{-3}, which is comparable to the thermal, kinetic, and magnetic energy densities measured in the Milky Way (Boulares & Cox 1990; Cox 2005). This approximate equipartition suggests that CRs are important for the dynamics and evolution of the ISM, and, possibly, also for the regulation of star formation.

CRs travel through the ISM via advection with the gas, anisotropic diffusion, and streaming along the magnetic field. Due to their reduced cooling efficiency, they are capable of retaining a substantial energy density over extended periods. However, due to their rapid diffusion, local variations in CR energy density are rapidly smoothed out. The CR pressure gradient is typically much smaller than the thermal pressure gradient. Consequently, SNe are able to locally shape the structure of the ISM, whereas the effect of CRs is visible only on larger temporal and spatial scales (Girichidis et al. 2018a; Rathjen et al. 2023). However, the CR pressure gradient is able to slowly lift the gas from the disc (Girichidis et al. 2016b, 2018a;

★ E-mail: brugaletta@ph1.uni-koeln.de

Rathjen et al. 2023), supporting galactic outflows even during periods of low star formation activity (Hanasz et al. 2013; Rathjen et al. 2023).

However, low-energy CRs up to 1 GeV play a key role in the chemistry of the ISM because they are responsible for the ionization and heating of the gas (Field, Goldsmith & Habing 1969), substantially impacting its evolution. In particular, low-energy CRs are able to penetrate deeply into dense clouds, to a depth where the ultraviolet (UV) radiation emitted by stars is hindered by dust absorption. Consequently, they are an important source of heating and ionization for the cold and dense gas (see e.g. Caselli et al. 1998; Bergin & Tafalla 2007; Padovani et al. 2020). The CR ionization rate of atomic hydrogen was estimated by Spitzer & Tomasko (1968) to be 6.8×10^{-18} s^{-1} in the proximity of Earth, where solar modulation affects the measurement of the low-energy (< 1 GeV) CR spectrum. In fact, the interaction of low-energy CRs with the magnetized solar wind causes their deflection, preventing them from reaching the vicinity of Earth. On the other hand, more energetic CRs (few GeV at least) can reach Earth without being affected. The low-energy CR energy spectrum has been measured without the effects of solar modulation by the probes Voyager 1 (Cummings et al. 2016) and Voyager 2 (Stone et al. 2019) once they have passed the heliopause, after which the low-energy CRs are out of range to interact with the turbulent, magnetized solar wind. In more recent times, values of the CR ionization rate in the range 10^{-18}–10^{-16} s^{-1} (Sabatini et al. 2020; Sabatini, Bovino & Redaelli 2023; Socci et al. 2024) and up to $10^{-14.5}$ s^{-1} (Pineda et al. 2024) have been measured for the molecular hydrogen in star-forming regions, and in the range 10^{-16}–10^{-14} s^{-1} for nearby protostars (Ceccarelli et al. 2014; Fontani et al. 2017; Favre et al. 2018; Cabedoet al. 2023). This variation, both in space and time is expected to lead to a locally changing CR heating rate.

The role of CR heating, due to the interaction of low-energy CRs with the ISM, is of primary importance in low-metallicity environments, and will be analysed in detail in this work. At a temperature below few 10^6 K, the cooling of the ISM is dominated by metals. In metal-poor environments, the ISM therefore cools much less efficiently. These environments therefore tend to be warmer than environments in solar-metallicity conditions (Brugaletta et al., in preparation). It is therefore even more important to carefully consider the heating mechanisms that play a role in such environments. Previous works of the SILCC collaboration (Walch et al. 2015; Girichidis et al. 2016a, 2018b Gatto et al. 2017; Peters et al. 2017; Rathjen et al. 2021, 2023) have analysed the solar-metallicity ISM employing a constant value for the interstellar radiation field (ISRF) strength, parameterised using G_0 in Habing units (Habing 1968). Only lately (Rathjen et al. 2024), they have adopted an on-the-fly calculation of the far-ultraviolet (FUV) ISRF, which is dependent on the present stellar population. Since the PE heating rate scales linearly with the dust-to-gas ratio, it becomes comparable to the CR heating rate in low-metallicity gas (see Section 2.4). The latter depends linearly on the CR ionization rate ζ, which has been assumed to be constant in the previous SILCC studies except for a control run in Girichidis et al. (2018a). In this paper, we introduce a novel method that scales the CR ionization rate from the spatially and temporally variable CR energy density that is already computed within our code. To test this implementation, we adopt a metallicity of $0.02\,\mathrm{Z}_\odot$, for which we expect to observe a strong impact. Such low metallicities are measured in some local dwarf galaxies, for example, the blue compact dwarf galaxy I Zw 18 (Zwicky 1966; French 1980), but are also seen in the early phases of the Universe (Heintz et al. 2023; Vanzella et al. 2023; Curti et al. 2024).

This paper is organized as follows. In Section 2, the numerical methods and the simulation setup are explained, including a description of the new treatment to compute the CR ionization rate from the energy density of CRs that is already computed in our code. In Section 3.1, a qualitative description of the behaviour of our simulations is provided. Section 3 illustrates the results of our work, followed by a discussion (Section 4) and our summary and conclusions (Section 5).

2 NUMERICAL METHODS AND SIMULATION SETUP

In our simulations, we employ the same setup as the SILCC framework (Walch et al. 2015; Girichidis et al. 2016a, b Gatto et al. 2017; Peters et al. 2017; Rathjen et al. 2021, 2023, 2024). We model the evolution of the gas in as stratified disc by solving the ideal magnetohydrodynamic (MHD) equations with the three-dimensional, adaptive mesh refinement code FLASH version 4.6 (Fryxell et al. 2000; Dubey, Reid & Fisher 2008; Dubey et al. 2009).

Our computational domain is an elongated box of size 500 pc × 500 pc ×± 4 kpc. Near the mid-plane, we adopt a resolution $\Delta x \sim 3.9$ pc, whereas for $|z| > 1$ kpc the resolution can reach up to 7.8 pc. In the beginning of each run, the spatial distribution of the gas along the z-direction follows a Gaussian centred in the mid-plane with a scale height of 30 pc, whereas in the x–y plane the gas distribution is uniform. The gas surface density, Σ_{gas}, is set to be $10\,\mathrm{M}_\odot\,\mathrm{pc}^{-2}$ for consistency with previous SILCC works. However, this value could be an upper limit for low-mass dwarf galaxies (Jaiswal & Omar 2020), or too low to describe the central regions of compact blue dwarf galaxies like I Zw 18 (Lelli et al. 2012). We have periodic boundary conditions in the x- and y-directions, and outflow conditions in the z-direction. This means that the gas is able to exit the simulation box in the z-direction but it is not able to fall back in. To avoid a sudden gravitational collapse and, consequently, a starburst in the very beginning of the simulation, we mix the gas via turbulence driving. Kinetic energy is injected for the first 20 Myr at large scales corresponding to the size of the box (500 pc), such that the mass-weighted root mean square velocity of the gas is initially equal to 10 km s^{-1}.

Using a tree-based method (Wünsch et al. 2018), we consider four different contributions to gravity: (i) the gas self-gravity; (ii) the gravity due to the presence of sink particles which represent star clusters (Dinnbier & Walch 2020, see below); (iii) an external gravitational potential to mimic the presence of an old stellar population; (iv) a constant dark matter potential. A more in-depth treatment of gravitational effects can be found in Walch et al. (2015) and Gatto et al. (2017).

All runs have a magnetic field initially oriented along the x-axis which changes in the vertical direction as

$$B_x(z) = B_{x,0}\sqrt{\rho(z)/\rho(z=0)}, \tag{1}$$

where $B_{x,0} = 6$ µG and $\rho(z)$ is the density at a height z from the mid-plane.

To model the star formation due to gravitational collapse happening in high-density regions, we include collisionless and accreting star-cluster-sink particles (Bate, Bonnell & Price 1995; Federrath et al. 2010; Gatto et al. 2017; Dinnbier & Walch 2020). A sink particle is created in a cell when specific criteria are met. These include a threshold density $\rho_{\mathrm{thr}} = 2 \times 10^{-21}$ g cm^{-3}, and the gas must be in a converging flow, Jeans-unstable, and in a gravitational potential minimum. The sink particles are responsible for the injection of momentum and thermal energy in the ISM in the form of radiation, stellar winds, SN explosions, and the injection of CRs that are accelerated in SN shocks. One massive star is formed inside a cluster for every 120 $\mathrm{M}_\odot$ of gas accreted on to that cluster. The initial mass of the new massive star is sampled from an IMF with a Salpeter-like slope (Salpeter 1955) in the range 9–120 $M_{\odot}$. We assume that the remaining amount of gas forms lower mass stars inside the cluster, which are not considered individually. We follow the time-evolution of massive stars by means of the BOOST models (Brott et al. 2011; Szécsi et al. 2022), considering their wind velocity, bolometric luminosity, mass-loss rate and effective temperatures. At the end of their life, all massive stars are assumed to explode as Type II SNe, injecting thermal energy or momentum depending on whether the Sedov–Taylor phase is resolved (Gatto et al. 2015). In fact, if the radius at the end of the Sedov–Taylor phase is resolved with at least three cells, thermal energy of 10^{51} erg is injected at the explosion site. This region is defined as the volume of the sphere centred on the SN and with three-cells radius (~ 11.7 pc in physical space). However, if the ambient density is too high to resolve the radius at the end of the Sedov–Taylor phase ($n_{\mathrm{crit}} = 3.3\,\mathrm{cm}^{-3}$, see Rathjen et al. 2021), the expected momentum that the gas would have if the SN explosion were resolved is injected instead (see Walch et al. 2015). In both cases, the mass of the progenitor is added to the mass of the gas that was present in the injection region before the explosion.

Feedback from radiation originating in stellar sources plays an important role in our simulations, influencing the chemistry of the ISM and, in the case of ionizing photons, creating H II regions. To treat the interaction of extreme ultraviolet (EUV) photons with the ISM, we include the radiative transfer module TREERAY (Wünsch et al. 2021), which uses the On-The-Spot approximation (Osterbrock 1988). All photons with an energy higher than 13.6 eV are able to ionize atomic hydrogen and are treated with TREERAY/ONTHESPOT. We compute the fraction of ionizing photons assuming each star to be a blackbody whose spectrum can be computed by means of the star's effective temperature, taken from the stellar models. At every time-step, ionizing photons emitted by all stars in a sink particle are injected in the cell where the sink is located. The TREERAY module uses the octal-tree already employed in the gravity solver (Wünsch et al. 2018) to propagate the radiation in the computational domain using a backwards radiative transfer method. For every cell in the computational domain, TREERAY creates a HEALPIX sphere (Górski et al. 2005) with (in this case) 48 rays cast from the centre of each target cell and oriented normal to the surface of the HEALPIX sphere. The radiation transport equation is solved along each ray for each cell.

Important in our simulations is the implementation of heating and cooling processes, computed on-the-fly using a chemical network (Nelson & Langer 1997, Glover & Mac Low 2007a, b) based on the calculation of non-equilibrium abundances of seven chemical species, namely H, H^+, H_2, CO, C^+, O, and free electrons. We assume that all the H_2 is formed on the surface of dust grains, following the prescription from Hollenbach & McKee (1989), since this channel dominates over the H_2 formation via the H^- ion, even at the low metallicities considered in this study (Glover 2003). It also dominates over the three-body channel, which becomes important for high gas densities ($n > 10^8\ \mathrm{cm}^{-3}$, Palla, Salpeter & Stahler 1983) and much lower metallicities ($Z < 10^{-6}\ Z_{\odot}$, Omukai et al. 2005) than those treated here. H_2 is mainly destroyed because of photodissociation by the ISRF, however, also cosmic-ray ionization and collisional dissociation in the hot gas are taken into account. In our treatment, we compute the photodissociation rate of H_2 following

$$R_{\mathrm{pd}} = R_{\mathrm{pd,H_2,thin}} f_{\mathrm{dust,H_2}} f_{\mathrm{shield,H_2}}, \tag{2}$$

where

$$R_{\mathrm{pd,H_2,thin}} = 3.3 \times 10^{-11} \sum_i (G_{\mathrm{cluster},i} R_i^{-2})\,\mathrm{s}^{-1}, \tag{3}$$

is the photodissociation rate of H_2 in the optically thin gas (Draine & Bertoldi 1996), and $G_{\mathrm{cluster},i} R_i^{-2}$ is the geometrically attenuated ISRF of clusters. The factor $f_{\mathrm{dust,H_2}} = \exp(-4.18 \times A_{\mathrm{V,3D}})$, whose exponent is taken from Heays, Bosman & van Dishoeck (2017), with the local visual extinction $A_{\mathrm{V,3D}}$ determined by TREERAY/OPTICALDEPTH (Wünsch et al. 2018), accounts for the effects of dust extinction encountered by the radiation that photodissociates H_2 molecules. The visual extinction is computed as (Bohlin, Savage & Drake 1978)

$$A_{\mathrm{V,3D}} = N_{\mathrm{H,tot}}/(1.87 \times 10^{21}\ \mathrm{cm}^{-2}) \times Z, \tag{4}$$

with the local 3D-averaged column density $N_{\mathrm{H,tot}}$ obtained from TREERAY/OPTICALDEPTH (Wünsch et al. 2018), and Z the metallicity. The factor $f_{\mathrm{shield,H_2}}$ accounts for the effects of H_2 self-shielding. Regarding heating processes, we include, among others, PE heating by dust grains and heating due to CRs. We describe them in more detail in Section 2.3. Concerning the cooling of the gas with temperatures higher than 10^4 K, we assume collisional ionization equilibrium for helium and metals, and employ the tabulated cooling rates from Gnat & Ferland (2012). In this regime, the Lyman-α cooling is computed using the non-equilibrium abundance of atomic hydrogen that is already computed in our chemistry network. We do not include chemical enrichment due to stellar feedback.

2.1 The ADAPTIVEG0 module

We utilize an updated and self-consistent approach to modelling the FUV radiation field ($E_{\gamma} = 6$–13.6 eV), as introduced in Rathjen et al. (2024). Departing from a static ISRF solely subject to local dust attenuation (using TREERAY/OPTICALDEPTH, see below), we now incorporate the intensity of the FUV radiation field from all formed star clusters individually. We first compute the FUV luminosity for each star cluster i, $G_{\mathrm{cluster,i}}$, given its mass and age, using STARBURST99 single-stellar population synthesis models (Leitherer et al. 1999). Then, we apply a geometrical attenuation and sum over all clusters to obtain G_0 for each cell:

$$G_0 = \sum_i G_{\mathrm{cluster,i}} \times R_i^{-2}. \tag{5}$$

Here, R_i is the distance from the considered cell to the ith cluster. Next, we apply a minimum floor $G_{\mathrm{bg}} = 0.0948$ to the calculated G_0 as done in Rathjen et al. (2024). This background value is computed for a cosmic UV background from Haardt & Madau (2012) plus the contribution of a static low-mass stellar population with a stellar surface density of $\Sigma_{\star} = 30\ M_{\odot}\ \mathrm{pc}^{-2}$.

Finally, as for the runs with constant G_0, we apply the local extinction by dust attenuation to obtain an effective ISRF at each cell, G_{eff}:

$$G_{\mathrm{eff}} = G_0 \times \exp(-2.5\ A_{\mathrm{V,3D}}). \tag{6}$$

2.2 Cosmic rays

We include CRs in the form of a separate relativistic fluid within an advection–diffusion approximation. Therefore, we solve modified MHD equations, for example, including an additional CR energy source term Q_{cr} (Girichidis et al. 2016b, 2018a). The equations read

$$\frac{\partial \rho}{\partial t} + \nabla \cdot (\rho \boldsymbol{v}) = 0, \tag{7}$$

$$\frac{\partial \rho \boldsymbol{v}}{\partial t} + \nabla \cdot \left(\rho \boldsymbol{v}\boldsymbol{v}^T - \frac{\boldsymbol{B}\boldsymbol{B}^T}{4\pi} \right) + \nabla P_{\mathrm{tot}} = \rho \boldsymbol{g} + \dot{\boldsymbol{q}}_{\mathrm{sn}}, \tag{8}$$

$$\frac{\partial e}{\partial t} + \nabla \cdot \left[(e + P_{\rm tot})\boldsymbol{v} - \frac{\boldsymbol{B}(\boldsymbol{B}\cdot\boldsymbol{v})}{4\pi} \right]$$
$$= \rho \boldsymbol{v} \cdot \boldsymbol{g} + \nabla \cdot (\mathbf{K}\nabla e_{\rm cr}) + \dot{u}_{\rm chem} + \dot{u}_{\rm sn} + Q_{\rm cr}, \quad (9)$$

$$\frac{\partial \boldsymbol{B}}{\partial t} - \nabla \times (\boldsymbol{v} \times \boldsymbol{B}) = 0, \quad (10)$$

$$\frac{\partial e_{\rm cr}}{\partial t} + \nabla \times (e_{\rm cr}\boldsymbol{v}) = -P_{\rm cr}\nabla \cdot \boldsymbol{v} + \nabla \cdot (\mathbf{K}\nabla e_{\rm cr}) + Q_{\rm cr}, \quad (11)$$

where ρ is the density, $\boldsymbol{v}$ is the velocity of the gas, $\boldsymbol{B}$ is the magnetic field, $P_{\rm tot} = P_{\rm thermal} + P_{\rm kinetic} + P_{\rm cr}$ is the total pressure, $\boldsymbol{g}$ is the gravitational acceleration, $\dot{\boldsymbol{q}}_{\rm sn}$ is the momentum input of unresolved SNe, $e = \frac{\rho v^2}{2} + e_{\rm thermal} + e_{\rm cr} + \frac{B^2}{8\pi}$ is the total energy density, $\boldsymbol{K}$ is the CR diffusion tensor, $\dot{u}_{\rm chem}$ is the change in thermal energy due to heating and cooling processes, $\dot{u}_{\rm sn}$ is the thermal energy input from resolved SNe, $Q_{\rm cr} = Q_{\rm cr,\,injection} + \Lambda_{\rm hadronic}$. The term $Q_{\rm cr}$ accounts for the injection of 10^{50} erg of energy per SN explosion in form of CRs (see e.g. Hillas 2005; Ackermann et al. 2013), and the cooling of CRs via hadronic and adiabatic losses (see e.g. Pfrommer et al. 2017; Girichidis et al. 2020). For the latter, we follow Pfrommer et al. (2017) assuming

$$\Lambda_{\rm hadronic} = -7.44 \times 10^{-16} \times \left(\frac{n_{\rm e}}{\rm cm^{-3}}\right)$$
$$\times \left(\frac{e_{\rm cr}}{\rm erg\ cm^{-3}}\right) \ {\rm erg\ s^{-1}cm^{-3}}. \quad (12)$$

For the diffusion tensor, we adopt two constant components for the diffusion coefficient, $K_{\parallel} = 10^{28}$ cm^2 s^{-1} and $K_{\perp} = 10^{26}$ cm^2 s^{-1} parallel and perpendicular to the magnetic field lines, respectively (Strong, Moskalenko & Ptuskin 2007; Nava & Gabici 2013). CR diffusion is solved in an operator-split manner. We evolve the modified MHD equations on a hydrodynamical time-step, computed via a modified effective sound speed using ($P_{\rm th+cr} = P_{\rm th} + P_{\rm cr}$). The diffusion is solved with an explicit solver in sub-cycling with a local diffusion time-step for each sub-cycle

$$\Delta t_{\rm diff} = \min\left(\Delta t_{\rm hydro}, 0.5\, C_{\rm CFL}\frac{(\Delta x)^2}{K_{\parallel} + K_{\perp}}\right). \quad (13)$$

2.3 PE and CR heating rates

Low-metallicity environments cool less efficiently due to the lack of metals, the main coolants of the ISM for temperatures below few 10^6 K (see e.g Wolfire et al. 1995; Bialy & Sternberg 2019). Therefore, the ISM is more sensitive to the different heating processes. The two most important heating mechanisms in this case are the PE heating, which is the main heating mechanism in the warm ISM, also at higher metallicities, and the CR heating.

In the local ISM, the heating rate for photoelectric (PE) heating $\Gamma_{\rm pe}$ is given by (Bakes & Tielens 1994; Bergin et al. 2004)

$$\Gamma_{\rm pe} = 1.3 \times 10^{-24} \epsilon G_{\rm eff} n d \quad [{\rm erg\ s^{-1}cm^{-3}}], \quad (14)$$

where n is the number density of hydrogen nuclei, d is the dust-to-gas mass ratio in per cent, with $d = 1$ (1 per cent) in solar-neighbourhood conditions. The PE heating efficiency ϵ reads (Bakes & Tielens 1994; Wolfire et al. 2003)

$$\epsilon = \frac{0.049}{1 + (\psi/963)^{0.73}} + \frac{0.037(T/10^4)^{0.7}}{1 + (\psi/2500)}, \quad (15)$$

with

$$\psi = \frac{G_{\rm eff}T^{0.5}}{n_e}, \quad (16)$$

where T is the temperature of the gas, and n_e is the electron number density. This expression for the PE heating efficiency was derived for conditions comparable to those in the local ISM. For simplicity, we assume that it also holds in the low-metallicity environment studied in this paper. In practice, this is unlikely to be the case: low-metallicity galaxies are strongly deficient in polycyclic aromatic hydrocarbons (see e.g. Draine et al. 2007; Sandstrom et al. 2012), which make a substantial contribution to the total PE heating rate. It is therefore likely that the true PE heating efficiency in the very metal-poor ISM will be significantly smaller than the value given by equation (15), which would render PE heating even less effective than we find in this study.

The CR heating rate we adopt follows Goldsmith & Langer (1978) assuming that each ionization deposits 20 eV as heat, and reads

$$\Gamma_{\rm cr} = 20\zeta(n_{\rm H_2} + n_{\rm H}) \quad [{\rm eV\ s^{-1}cm^{-3}}]$$
$$= 3.2 \times 10^{-11}\zeta(n_{\rm H_2} + n_{\rm H}) \quad [{\rm erg\ s^{-1}cm^{-3}}], \quad (17)$$

where ζ is the CR ionization rate expressed in units of s^{-1}, $n_{\rm H_2}$ is the number density of H$_2$, and $n_{\rm H}$ is the number density of H.

In previous works (e.g. Rathjen et al. 2021, 2023), both the parameters G_0 for the PE heating and ζ for the CR heating rates have been assumed to be constant and in the range $G_0 = 1.7$–42.7 (with $G_0 = 1.7$ valid for solar-neighbourhood conditions; Draine 1978) and in the range $\zeta = 3\times 10^{-17}$–3×10^{-16} s^{-1} depending on the adopted gas surface density, respectively. In this case, the PE and CR heating rates were already variable, but assuming constant values of G_0 and ζ. Therefore, a PE heating similar to that of solar-neighbourhood environments has been assumed even in the absence of massive stars, as well as CR heating in the absence of SNe accelerating galactic CRs. We show that these conditions deeply affect the possibility of stars forming in the metal-poor ISM (see Section 3).

In Fig. 1, we show both $\Gamma_{\rm pe}$ and $\Gamma_{\rm cr}$ divided by the number density of hydrogen nuclei and the sum $n_{\rm H_2} + n_{\rm H}$, respectively. They are computed for different metallicities ranging from 1 Z$_\odot$ down to 0.02 Z$_\odot$. We compute these values with our chemistry module in standalone mode for 1 Gyr, after which the gas has reached chemical and thermal equilibrium. The rates were computed assuming a constant $G_0 = 1.7$, optically thin gas with $A_{\rm V,3D} = 0$, and four different constant values of ζ. Regarding the PE heating, we note that the rate computed for solar metallicity is around two orders of magnitude higher than the same rate at a metallicity of 0.02 Z$_\odot$. This is due to the fact that, for this specific calculation, we are scaling the dust-to-gas ratio linearly with metallicity, meaning that $d = 0.02$ per cent at 0.02 Z$_\odot$. Therefore, at low metallicity, PE heating plays a less important role in the heating of the gas compared to solar-neighbourhood conditions. Concerning the CR heating, we see that the rate depends on the value of ζ, and hence is metallicity-invariant. Therefore, even without any shielding by dust, PE and CR heating rates are comparable in the range of densities relevant in our low-metallicity simulations, meaning that the way we model CR heating can strongly affect our results.

2.4 Implementation of a variable cosmic-ray ionization rate

In this work, we aim at modelling the CR ionization rate, ζ, consistently with the CR energy density, $e_{\rm cr}$, that is already computed by our code. As seen in the previous section, for every SN explosion we inject 10^{50} erg of energy in the form of CRs, which are treated in the fluid approximation.

To compute ζ from $e_{\rm cr}$, we consider the local total hydrogen column density, $N_{\rm H,tot}$, which is an average over all 48 directions computed by TreeRay/OpticalDepth. We use $N_{\rm H,tot}$ instead of the

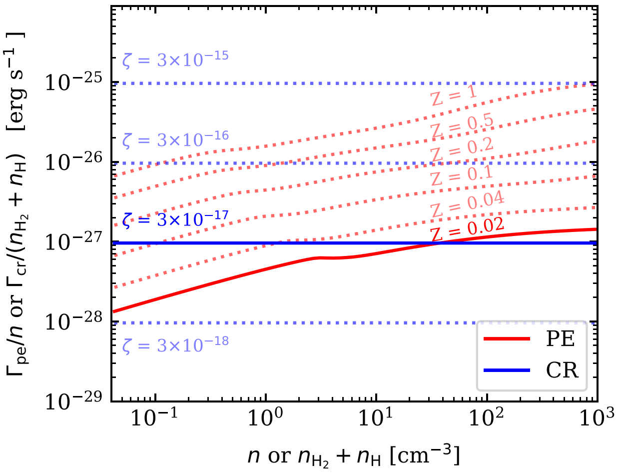

Figure 1. Ratio of the PE heating rate (PE) with the number density of hydrogen nuclei, and ratio of the CR heating rate (CR) with the sum ($n_{H_2} + n_H$), following equation (17). Both heating rates are computed for a number of different metallicities, ranging from 0.02 to 1 $Z_\odot$, using our chemistry module in standalone mode. The PE heating rate has been computed for optically thin conditions assuming $G_0 = 1.7$, and it varies with metallicity as it scales linearly with the dust-to-gas ratio, which is a function of metallicity. The CR heating rate has been computed also for a number of different CR ionization rates (ζ), as it does not depend on metallicity. The blue solid line highlights the heating rate with $\zeta = 3 \times 10^{-17}$ s^{-1}, which is the value assumed in previous works of the SILCC collaboration for a gas surface density of 10 $M_\odot$ pc^{-2}. The red solid line marks the PE heating rate computed at the metallicity relevant for this work, assuming a linear scaling of the dust-to-gas ratio with metallicity. We note that in this case the CR heating rate is similar, if not more important, than the PE heating rate at high densities.

H_2 column density, N_{H_2}, as reported by Padovani, Galli & Glassgold (2009) and Padovani et al. (2022). This is due to the small amount of H_2 at the low metallicity we consider, therefore we would greatly underestimate the CR attenuation if we were using only the H_2 column density. In the following, we will nevertheless apply the prescription from Padovani et al. (2009, 2022) obtained for proton impact on the H_2 gas, since no analogous relation for the atomic gas is provided. With this choice we speculate our attenuation of ζ to be affected by an uncertainty of around a factor of 2 (Glassgold & Langer 1974), compared to the attenuation shown in fig. C1 in Padovani et al. (2022).

We define a threshold column density $N_{H,thres} = 10^{20}$ cm^{-2}, above which we attenuate the value of ζ. The choice of this value is based on Fig. C.1 from Padovani et al. 2022, where the attenuation of ζ starts for $N_{H_2} = 10^{20}$ cm^{-2}. Since no data are available below this threshold, we assume no attenuation in this range. We therefore compute ζ from e_{cr} as in the following.

(i) In the more diffuse gas where $N_{H,tot} < N_{H,thres}$, we scale ζ linearly with e_{cr} according to

$$\zeta = 3 \times 10^{-17} \left(\frac{e_{cr}}{1 \text{ eV cm}^{-3}} \right) \text{ s}^{-1}. \quad (18)$$

This is to connect the value 3×10^{-17} s^{-1} of the CR ionization rate used in previous SILCC works with the e_{cr} that is on average observed in runs with $\Sigma_{gas} = 10$ $M_\odot$ pc^{-2}, of around 1 eV cm^{-3} (Rathjen et al. 2021).

(ii) In the denser gas where $N_{H,tot} > N_{H,thres}$, we multiply the linear scaling given in equation (18) with an additional attenuation factor, c_{att}, defined as

$$c_{att} = (N_{H,tot}/N_{H,thres})^{-0.423}, \quad (19)$$

where the exponent -0.423 is given by the prescription for the spectrum of protons and heavy nuclei in Padovani et al. (2009), which is reasonable for diffuse clouds. This is physically motivated by the idea that a low-energy CR travelling in a very dense medium will interact several times with the atoms and molecules of that medium, losing part of its energy and therefore its capability of ionizing new atoms. We verified that this exponent is well in accordance with the average slope, computed in logarithmic scale, that we obtain from fig. C.1 in Padovani et al. (2022) considering the two most extreme models shown there, their $\mathcal{L}$ model and their model with power-law index $\alpha = -1.2$.

As initial conditions for our simulations we set e_{cr}, and therefore ζ, to zero. The CRs relevant for the energy computation are those injected from SN explosions and the only source of CRs would be those coming from nearby galaxies. However, the CRs able to travel for such long distances (more than 500 pc, the length of our box) are few in number and have a cross-section for collisions with the gas which is very small (Padovani et al. 2022). Hence, we assume their contribution to the CR energy density to be negligible.

2.5 Simulation parameters

In this work, we run four simulations, as listed in Table 1, where we vary our prescription for the PE and CR heating. In one of our simulations (Z0.02), we assume the presence of a constant ISRF, whose strength is expressed in units of the Habing field (Habing 1968), $G_0 = 1.7$. This value is valid for solar-neighbourhood conditions (Draine 1978), therefore we could expect this value to be not optimal for very metal-poor environments. In run Z0.02, as in all our simulations, we attenuate the ISRF according to the local dust attentuation, which is determined from the local total column density $N_{H,tot}$ (see Walch et al. 2015). Overall, the setup of Z0.02 is the same as in Rathjen et al. 2023, except for the different metallicity and different stellar tracks.

All the other simulations employ the novel ADAPTIVEG0 module from Rathjen et al. (2024), described in Section 2.1, which computes the value of G_{eff} consistently from the distribution of young star clusters. Regarding the CR heating, a constant value of the CR ionization rate $\zeta = 3 \times 10^{-17}$ s^{-1} is assumed for runs Z0.02 and Z0.02-vG$_0$, whereas for the two simulations Z0.02-vG$_0$-vζ and Z0.02-vG$_0$-vζ-BS, ζ is computed using the scaling explained in Section 2.4. In this way, we aim to explore the impact of the variability of the ISRF and/or of ζ on the PE and CR heating rates and the resulting properties of the low-metallicity ISM. The only difference between the Z0.02-vG$_0$-vζ and Z0.02-vG$_0$-vζ-BS runs is the scaling of the dust-to-gas ratio with metallicity. In all simulations but Z0.02-vG$_0$-vζ-BS, the dust-to-gas ratio is scaled linearly with the metallicity of the run, assuming $d = 1$ (1 per cent) at solar metallicity. Recent observations of low-metallicity galaxies suggest that the scaling of the dust-to-gas ratio with metallicity becomes steeper than linear in low-metallicity regimes (Rémy-Ruyer et al. 2014). Therefore, we analyse the impact of a different scaling in the Z0.02-vG$_0$-vζ-BS run, where we adopt the power-law scaling from Bialy & Sternberg 2019, which holds for metallicities lower than 0.2 $Z_\odot$, and reads

$$d = Z_0'(Z'/Z_0')^{\alpha}, \quad (20)$$

where $Z_0' = 0.2$ and $Z' = 0.02$ is the metallicity of the gas and $\alpha = 3$. This results in a value $d \approx 10^{-4}$ in percentage.

Table 1. List of simulations performed in this work (first column). G_0 (second column) describes the strength of the ISRF in Habing units (Habing 1968) and ζ (third column) is the CR ionization rate in s^{-1}. In the fourth column, the scaling of the dust-to-gas ratio (d) with metallicity is specified. In the last column, we give t_{SF}, which is the simulation time at which the first star cluster has been formed, if star formation takes place.

Simulation	G_0	ζ (s^{-1})	d scaling	t_{SF} (Myr)
Z0.02	1.7	3×10^{-17}	Linear	No star formation
Z0.02-vG$_0$	Variable	3×10^{-17}	Linear	128.2
Z0.02-vG$_0$-vζ	Variable	Variable	Linear	44.2
Z0.02-vG$_0$-vζ-BS	Variable	Variable	Bialy & Sternberg (2019)	44.5

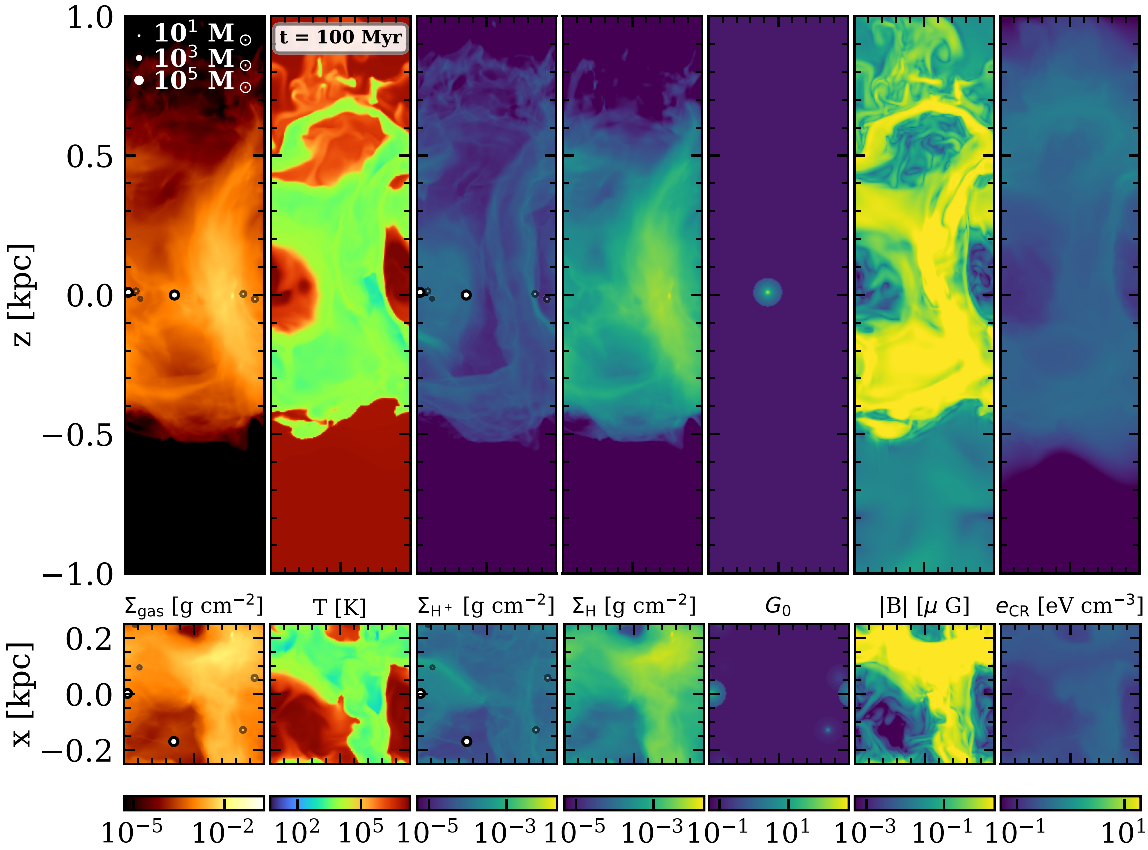

Figure 2. Snapshot of the Z0.02-vG$_0$-vζ-BS run at $t = 100$ Myr (simulation time). The top row shows the edge-on view and the bottom row the face-on view of the following quantities: the column density of the gas Σ_{gas}, a temperature slice, the column density of H$^+$, H, a slice of the variable G$_0$, a slice of the amplitude of the magnetic field B, a slice of the energy density of CRs e_{cr}, respectively. In the vertical direction, the box is not shown in its entirety as it is cut for clarity reasons at ± 1 kpc. Slices are taken at $y = 0$ (top row) or $z = 0$ (bottom row). The opaque circles represent the active star clusters (not in scale with the figure), whereas the transparent circles represent the inactive star clusters.

3 RESULTS

3.1 Global evolution

We show a representative snapshot of run Z0.02-vG$_0$-vζ-BS in Fig. 2. The initial conditions for our simulations are described in detail in Walch et al. (2015). In the beginning of every run, the gas is mixed by the initial turbulence driving, while it is slowly collapsing towards the mid-plane because of cooling and gravity. During this phase, the gas can form dense and cold regions where stars are born. The time when the sink formation criteria are fulfilled greatly depends on the individual run.

In our simulations, all stars are spawned in clusters and start their evolution directly on the main sequence, injecting energy and momentum into the ISM because of their radiation, stellar winds and SNe. This results in an increase in the ionized hydrogen abundance in the regions close to the newly born clusters, becoming more and more extended as the clusters accrete, forming more new stars. During their life, star clusters can accrete gas as well as lose gas because of stellar winds.

At the end of their life, all the massive stars explode as Type II SNe, whose overall effect is to heat the gas and to push it in the vertical direction, making the scale height of the disc thicker. Since we follow star formation self-consistently, and do not use a fixed star formation rate (SFR), more intense periods of star formation are followed by those of lower star-forming activity. As a consequence, when the majority of stars have already exploded and no new stars are being formed, the outflow-driving force exerted on the gas weakens. Therefore, the gas starts to fall back down towards the mid-plane. When a certain amount of gas has already reached the original disc,

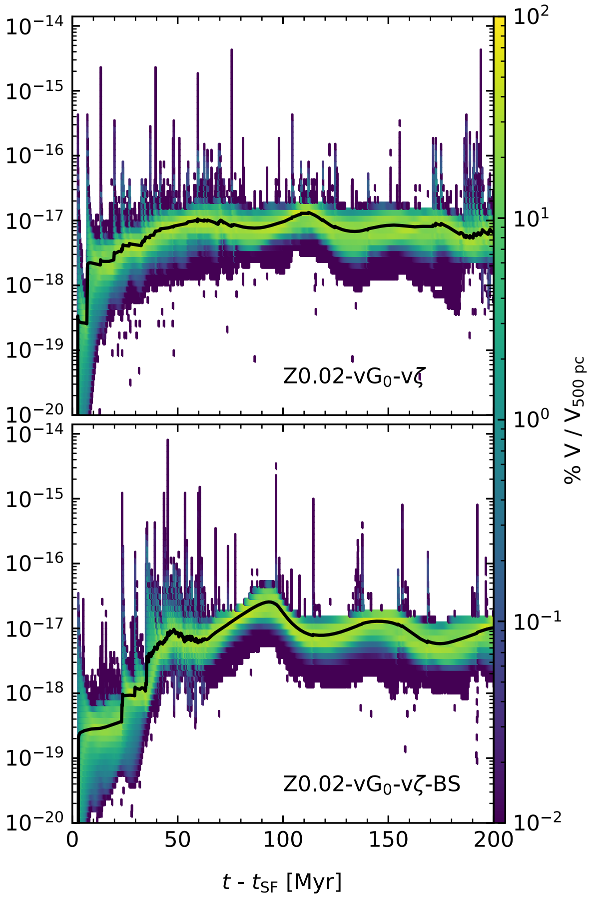

Figure 3. Local and temporal variations of ζ for runs Z0.02-vG$_0$-vζ (top panel) and Z0.02-vG$_0$-vζ-BS (bottom panel) in a region of$|z| \leq 250$ pc from the disc mid-plane and in a 200 Myr interval after the onset of star formation, happening at a time t_{SF} (see Table 1). The colour map indicates the percentage of cells in the computational domain that, at a given time, have a certain value of ζ. The solid line indicates the volume-weighted mean value of ζ. From this plot, we can see that ζ strongly varies in both space and time.

the density is high enough to create new molecular clouds, which, in turn, form new star clusters (see e.g. Rathjen et al. 2021). After stars are born, the gas is pushed outwards by feedback until the majority of the stars are not active anymore. Then, it will fall down toward the mid-plane creating new star clusters, restarting the cycle.

3.2 The spatial and temporal variability of ζ

Before analysing how the new prescription for the CR ionization rate affects the ISM in our simulations, we briefly describe the local and temporal variation of ζ, which can be seen in Fig. 3. Here, we present ζ for the runs Z0.02-vG$_0$-vζ (top panel) and Z0.02-vG$_0$-vζ-BS (bottom panel) in a region$|z| \leq 250$ pc. For every snapshot, we bin the values of ζ into 100 equally spaced bins in logarithmic scale and we compute the percentage of cells that belong to a certain bin. By repeating the procedure for the entire time evolution of the simulation, we obtain the time-dependent histogram presented in Fig. 3. The several peaks that can be observed correspond to the injections in CR energy subsequent to SN explosions. In these cases, the maximum ζ reaches values up to almost 10^{-14} s^{-1}, in accordance with the values obtained by Pineda et al. (2024) for molecular hydrogen. The CR ionization rate computed for molecular hydrogen is twice the value of the CR ionization rate computed for atomic hydrogen. At times later than 50 Myr after the onset of star formation, the lower limit for ζ settles to around 10^{-18} s^{-1}. Moreover, the value of ζ typically varies by at least three orders of magnitude, in a range that is around one or two orders of magnitude lower than the estimates provided by Padovani et al. (2022). This is expected, as we have much lower SFRs than in solar-neighbourhood conditions. Regarding the volume-weighted average of ζ, we notice that around 100 Myr after the onset of star formation, which happens at a time t_{SF} (see Table 1), the average value settles to a value of around 10^{-17} s^{-1}, similar to the value of the CR ionization rate estimated by Spitzer & Tomasko (1968) for atomic hydrogen. Hence, the CR ionization rate computed using this new implementation varies in space and time, affecting the local heating due to CRs and, consequently, the conditions for star formation.

3.3 The effects of varying ζ

In Fig. 4, we show the temperature–density and pressure–density phase plots for the four runs. For Z0.02, the ISM is unable to cool down to lower temperatures, therefore it remains as a single-phase warm gas and star formation is inhibited. In this case, both the values of G_0 and ζ are such that the corresponding heating rates are too large to let the gas cool down. As these parameters are the same as the ones employed in previous works of the SILCC collaboration (e.g. Rathjen et al. 2021, 2023) for solar-metallicity conditions where star formation does take place, this shows that comparable G_0 and ζ values can have a different impact when the ISM is metal poor. Considering the Z0.02-vG$_0$ simulation, which has a variable ISRF, we observe that the gas reaches lower temperatures and higher densities compared to the Z0.02 run, being able to form a few stars; however, star formation is severely weakened by CR heating. A higher mass fraction of cold gas and, therefore, a larger number of stars can form in runs Z0.02-vG$_0$-vζ and Z0.02-vG$_0$-vζ-BS, where both G_0 and ζ are variable. The temperature–density and pressure–density phase plots for these runs look similar as the stellar feedback changes the distribution of temperatures, pressures, and densities analogously. Therefore, it seems that a different scaling of the dust-to-gas ratio with metallicity does not significantly alter the overall thermal structure of the ISM.

In Fig. 5, we show the energy provided to the ISM by means of PE and CR heating. In the top panel, we compare the cumulative distributions of the energy due to PE heating with that of CR heating for all simulations. The energy due to CR heating is higher than that from PE heating for the runs with constant ζ (Z0.02 and Z0.02-vG$_0$) and for the Z0.02-vG$_0$-vζ-BS run. In the first case (in the Z0.02 and Z0.02-vG$_0$ runs), this is due to the fact that the CR heating for $\zeta = 3 \times 10^{-17}$ s^{-1} is higher than the PE heating rate with $G_0 = 1.7$ or less (see Fig. 1). Moreover, the energy provided to the gas by CRs in the Z0.02-vG$_0$ run is higher than in Z0.02, as the few formed stars provide additional CR heating when exploding as SNe. In the second case, in the Z0.02-vG$_0$-vζ-BS run, this is due to the power-law scaling of the dust-to-gas ratio with respect to the metallicity in run Z0.02-vG$_0$-vζ-BS, which leads to a PE heating rate that is approximately two orders of magnitude lower than in the case of a linear scaling of d with metallicity.

In the second panel of Fig. 5, we show the cumulative distributions of the sum of the two contributions and we add the cumulative distributions of the energy provided by SNe (dashed lines) for the same runs. We compute the SN contribution by multiplying the number of SNe by 10^{51} erg. The largest total energy due to PE and CR heating provided to the ISM are, again, found in the runs Z0.02 and Z0.02-vG$_0$. Between these, the total energy is slightly higher in

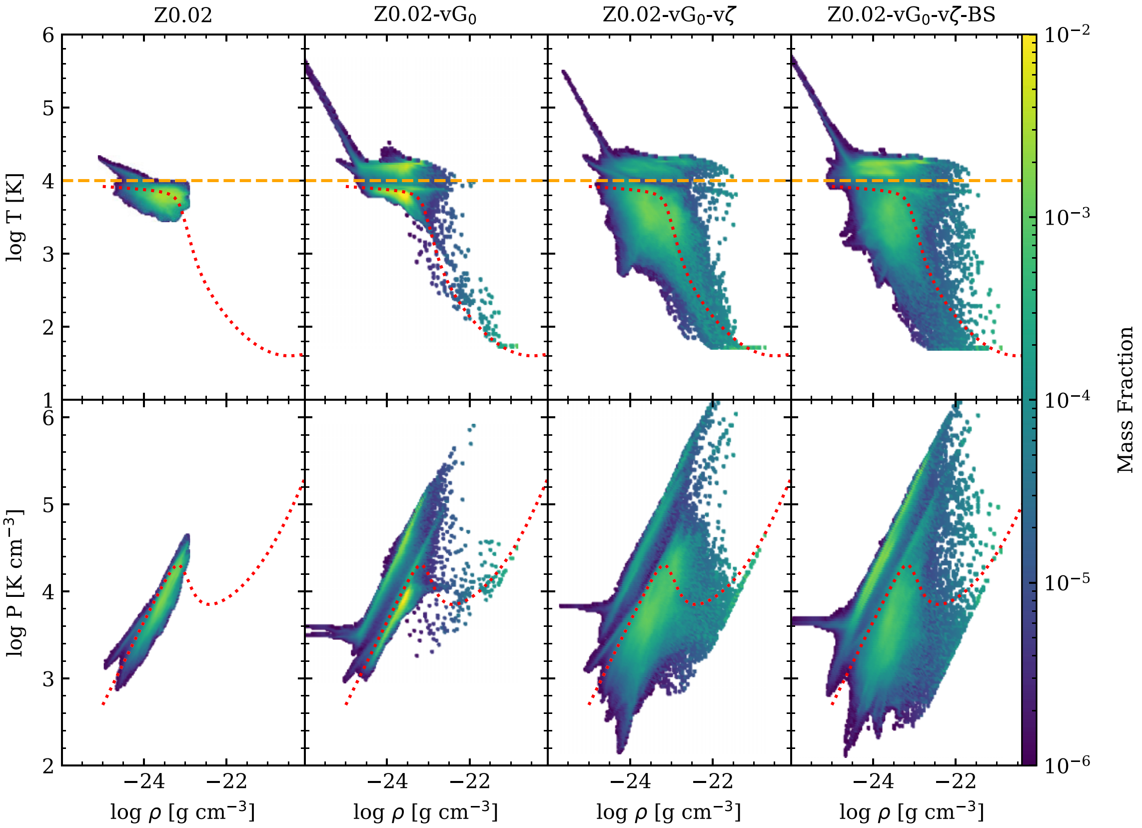

Figure 4. Temperature–density and pressure–density phase plots for the four runs, computed in a region $|z| < 250$ pc around the disc mid-plane. The dotted line is the equilibrium curve computed for $G_0 = 1.7$, $\zeta = 3 \times 10^{-17}$ s^{-1} and a shielding column of 10^{20} cm^{-2}. The dashed line indicates $T = 10^4$ K. We note that the structure of the ISM changes dramatically depending on the prescription of the two heating mechanisms. Only the simulations with a variable ζ are able to cool down and form a substantial number of stars.

the case of run Z0.02-vG$_0$ because the few generated star clusters lead to a higher PE and CR heating compared to the case where $G_0 = 1.7$. Moreover, allowing both G$_0$ and ζ to vary, decreases the total energy by around an order of magnitude compared to that of the Z0.02-vG$_0$ run. Comparing the contributions of the PE and CR heating with that due to SNe, we note that the energy provided by SNe is slightly higher (Z0.02-vG$_0$-vζ) or one order of magnitude higher (Z0.02-vG$_0$-vζ-BS) than the former. Only in the case of the Z0.02-vG$_0$ run the energy due to SNe is around two orders of magnitude lower than that provided by the PE and CR heating, since this run forms only a few massive stars, and as a consequence, it has only few SNe. In the Z0.02-vG$_0$-vζ-BS run, the energy provided by PE and CR heating together is the lowest, and the energy provided by SNe is the highest, compared to the other runs. The total heating, counting SNe, PE, and CR heating, is higher in the Z0.02-vG$_0$-vζ-BS than in the Z0.02-vG$_0$-vζ run. This explains why the temperature–density phase plot for this run (see Fig. 4) shows slightly less cold gas than the corresponding plot for run Z0.02-vG$_0$-vζ.

If both the PE and CR heating rates are allowed to vary in space and time, we can ask the question of whether there are regions where one or the other is dominant. We explore this aspect in Fig. 6, where we present gas density slices taken at the mid-plane (top row), the two heating rates (second and third rows), and the normalized difference of the two (bottom row). For each run, we select a snapshot where active star clusters are present near the mid-plane. In the second row, the spherical regions of high $\Gamma_{\rm pe}$ surrounding the star clusters are due to the R^{-2} law, which is a model parameter (see Section 2.1) of the G$_0$ field. For the Z0.02-vG$_0$-vζ-BS (second row, fourth column) the power-law scaling of the dust-to-gas ratio with metallicity reduces the PE heating rate by around two more orders of magnitude compared to Z0.02-vG$_0$-vζ, therefore these structures are not visible in the plot. In the last row we compare the PE and CR heating rates taking their difference, and normalizing by their sum, such that we can obtain values in range [–1, 1] where the range (0, 1] indicates a dominating PE heating rate, and the [–1, 0) a dominating CR heating rate. We note that PE heating strongly dominates in regions close to star clusters, whereas CR heating is prevalent in the more diffuse gas further away from star-forming regions. The reason for that is the R^{-2} law of the G$_0$ and the attenuation of the ζ parameter for high column densities (see equation 19).

3.4 Gas phases and structure

In this section, we analyse the gas phases and structure, which is important to understand star formation in low-metallicity environments. We divide the gas in a cold ($T < 300$ K), a warm ($300 < T < 3 \times 10^5$ K) and a hot ($T > 3 \times 10^5$ K) phase. The warm phase can either be neutral or ionized considering the neutral and ionized species present. We show the volume-filling and mass fractions of these gas phases averaged over 100 Myr and computed in a region $|z| < 250$ pc around the disc mid-plane in Fig. 7. The values are summarized in Table 2.

In the runs with constant ζ, no (Z0.02) or very little cold gas (mass fraction of 0.25 per cent, Z0.02-vG$_0$) forms. Therefore, the variations of the G$_0$ field do not play a key role in the gas cooling at this very low metallicity. On the other hand, in the Z0.02-vG$_0$-vζ

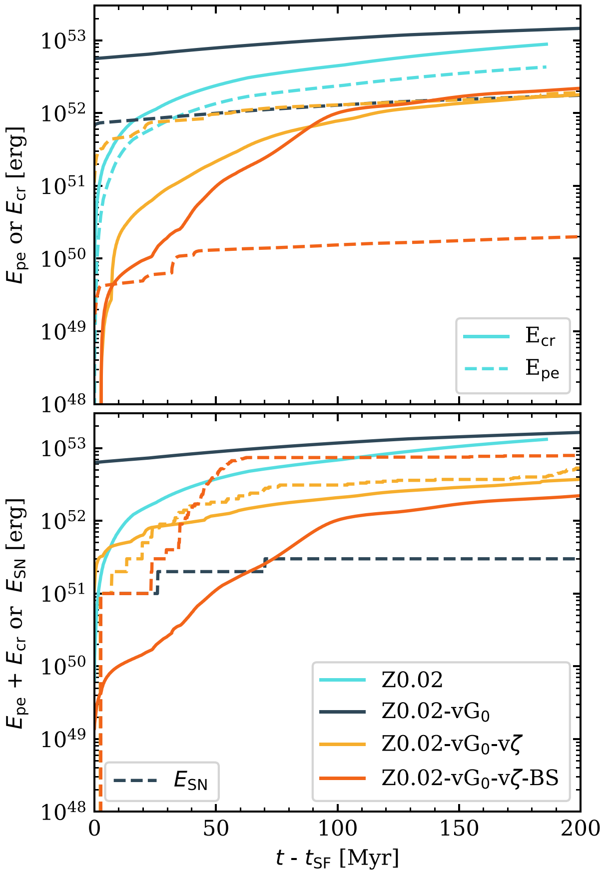

Figure 5. Top panel: cumulative distributions of the energy injected in the ISM due to either PE heating or CR heating, considering a region of ± 250 pc around the disc mid-plane. For the runs with constant ζ, the contributions of the CR heating are higher than that of PE heating. The same behaviour is observed for run Z0.02-vG$_0$-vζ-BS. In Z0.02-vG$_0$-vζ, the opposite behaviour is observed. Bottom panel: cumulative distributions of the sum of the PE heating and CR heating energy injected in the ISM (solid lines), and of the energy due to SN injections (dashed lines), in the same region as above. We note that the largest energy provided by PE and CR heating is in the case of Z0.02-vG$_0$, followed by Z0.02. For the runs with variable ζ, the energy provided to the system is almost an order of magnitude lower. The total energy contribution due to both PE and CR heating is slightly lower (Z0.02-vG$_0$-vζ) or one order of magnitude lower (Z0.02-vG$_0$-vζ-BS) than the energy provided by SNe. Note that, since the value of t_{SF} is undefined for run Z0.02, we simply show its entire evolution.

and Z0.02-vG$_0$-vζ-BS runs the spatial variability of ζ allows the gas to cool and form some more cold gas, whose mass fraction is around 3–4 per cent depending on the run. As no corresponding values obtained from observations are available at this low metallicity, we compare our results with those presented in Tielens (2005), which measure 50 per cent of cold gas mass fraction for solar neighbourhood conditions. This value is considerably higher than that found in our runs, which can be attributed to the inefficient cooling of the gas.

In Fig. 8, we show the time evolution of the atomic, ionized, and molecular hydrogen. We compute the mass in each phase within $|z| < 250$ pc divided by the total mass M_0 of the gas in the same region. Regarding atomic hydrogen (top panel), we notice that there is not much variation in time since, in all four simulations, most of the gas is atomic. A small change can be seen for the runs that form stars, for which a slight decrease in atomic hydrogen mass fraction corresponds to an increase in ionized hydrogen mass fraction, due to the presence of H II regions around star clusters. However, the mass fraction of H$^+$ is almost constant and around 1 per cent for the Z0.02 and Z0.02-vG$_0$ runs, where no (or almost no) H II regions are present. This value corresponds to the mass fraction of H$^+$ in the equilibrium state for a density of around 10^{-24} g cm^{-3}. Regarding the molecular gas (bottom panel), we note that its mass fraction is in the interval 10^{-9}–10^{-4} depending on the simulation, with the Z0.02-vG$_0$-vζ having the highest H$_2$ mass fraction. This mass fraction range is compatible with that obtained for the G1D001 dwarf galaxy simulation in Hu et al. 2016, computed at a metallicity of 0.1 Z$_\odot$ and a dust-to-gas ratio of 0.01 per cent. Even though the Z0.02-vG$_0$-vζ and Z0.02-vG$_0$-vζ-BS have almost the same amount of cold gas, there is a three to four orders of magnitude difference in the amount of molecular gas because the Z0.02-vG$_0$-vζ-BS run has a much smaller dust-to-gas ratio. For this reason, there is less formation of H$_2$ on dust grains as well as less dust shielding to protect H$_2$ from dissociation by the ISRF.

We show the density (top panels) and velocity (bottom panels) probability density functions (PDFs) in Fig. 9 at two different times, t = 44 and 125 Myr, computed in a region $|z| < 250$ pc. The velocity v is computed as

$$v = \sqrt{(v_x - v_{\rm CM,x})^2 + (v_y - v_{\rm CM,y})^2 + (v_z - v_{\rm CM,z})^2}, \qquad (21)$$

where v_i is the velocity of the gas in every cell and $v_{\rm CM,i}$ is the bulk velocity of the gas in the directions $i = x, y, z$. We choose the first time to understand the density structure of the gas right before the first star cluster is formed in the runs Z0.02-vG$_0$-vζ and Z0.02-vG$_0$-vζ-BS and the second time to investigate the structure of the gas when their ISM has already been shaped by the stellar feedback. In the case of Z0.02-vG$_0$, the time t = 125 Myr is right before the formation of the first star cluster.

At t = 44 Myr, the density PDFs of runs Z0.02-vG$_0$-vζ and Z0.02-vG$_0$-vζ-BS exhibit a power-law tail at high densities, which could be associated with gravitational collapse (Klessen 2000; Slyz et al. 2005; Schneider et al. 2012; Girichidis et al. 2014). On the other hand, no high-density regime is present at this time for runs Z0.02 and the Z0.02-vG$_0$, as the CR heating with constant ζ is preventing/delaying the gas cooling for run Z0.02/Z0.02-vG$_0$. We note the presence of gas with a density lower than 10^{-26} g cm^{-3}, due to the fact that at this time the scale height of the disc is smaller than 250 pc, therefore a part of the initial ambient gas is present in this region. At t = 125 Myr, however, only the two runs that have not formed stars (Z0.02 and Z0.02-vG$_0$) present this very diffuse gas. Moreover, the high-density regime is present in the case of Z0.02-vG$_0$, as the gas temperature had more time to decrease, whereas the gas in Z0.02 is simply unable to cool down and become denser. Regarding the velocity PDFs at 44 Myr, we note one peak at around 10 km s^{-1}, which is due to the $v_{\rm rms}$ velocity of the turbulence injected in the ISM in the first 20 Myr of evolution. We observe a second peak in the velocity range 40–60 km s^{-1} due to the motion of the diffuse gas in the outer parts of the disc which is initially falling towards the disc. Toward higher velocities, the PDF decreases almost as a power law for all runs. At a time of 125 Myr, the initial turbulence has decayed, and the maximum velocities are in the range 50–100 km s^{-1}. These velocity values can be explained as at this time there are no active star clusters in all the runs, and in the case of the Z0.02-vG$_0$-vζ and the Z0.02-vG$_0$-vζ-BS the gas velocity has been driven by SNe that have exploded 5–15 Myr before.

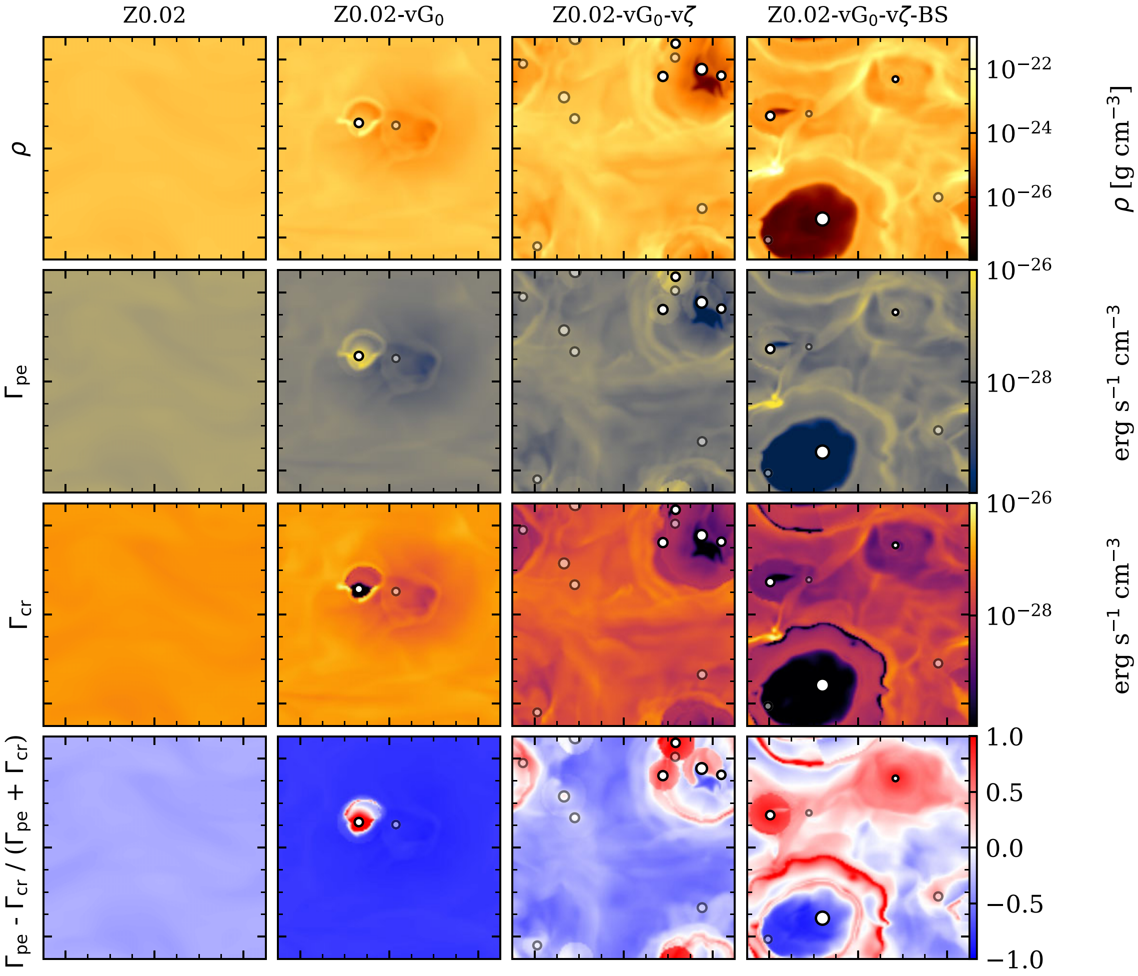

Figure 6. Slices at the disc mid-plane of the density (first row), PE heating rate (second row), CR heating rate (third row), and the difference between PE and CR heating rates normalized by the sum of the two (fourth row), for every run (columns). From left to right panels, the simulation time of the selected snapshots is 185.9, 144, 106, and 83.4 Myr, respectively. The last row shows that PE heating dominates near star-forming regions, whereas CR heating dominates in the more diffuse gas.

3.5 Star formation

In this section, we analyse the properties of the gas that forms stars. As already seen above, in the absence of a variable ζ the ISM is either not able to cool down (Z0.02) or, if a variable G$_0$ field is present, the gas can cool but is able to form only a few stars (Z0.02-vG$_0$) after a much longer cooling time than in case of variable ζ. Therefore, unless both G$_0$ and ζ are variable quantities, no substantial star formation takes place in our simulations. In Fig. 10, we analyse four important quantities, meaning the distribution of the shielded ISRF $G_{\rm eff}$, the PE heating rate $\Gamma_{\rm pe}$, the CR ionization rate ζ, and the CR heating rate $\Gamma_{\rm cr}$. Taking as example the Z0.02-vG$_0$-vζ run, we identify the coordinates where each star cluster forms, and analyse these four quantities in a snapshot exactly before the moment in which each sink particle is formed. Since the gas is moving, starting from the coordinates at which each sink particle is formed, we trace back the position that the star-forming gas would have one snapshot before the creation of the sink particle. We then consider all the cells of a region centred on these coordinates and with a radius $r_{\rm accr}\sim$ 11.7 pc, which is the accretion radius of the sink particles. We take into account only the cells of this region that have a density higher than 5 × 10^{-22} g cm^{-3}, which is slightly lower than the density threshold $\rho_{\rm thr}$ used for sink formation. We represent as opaque distributions the quantities measured in these selected cells, and we refer to this gas as ‘star-forming’.

Additionally, we show the total distributions of the four quantities in all selected snapshots as transparent histograms. These distributions include all cells in a region $|z| <$ 250 pc. In order to facilitate a comparison, all distributions have been normalized such that they fall between 0 and 1. All distributions are mass-weighted. We find clear selection effects. In fact, the majority of the cells where star formation is about to take place have values of $G_{\rm eff}$ < 1, $\Gamma_{\rm pe}$ around 10^{-26}–10^{-25} erg s^{-1} cm^{-3}, $\zeta \sim 10^{-18}$ s^{-1}, and $\Gamma_{\rm cr} < 10^{-26}$ erg s^{-1} cm^{-3}. From equation (14), we see that $\Gamma_{\rm pe}$ depends on $G_{\rm eff}$ and the density, therefore even if the values of $G_{\rm eff}$ in the star-forming gas are lower than the total distribution, we still find large values of the $\Gamma_{\rm pe}$ because of the high density. However, the total distributions present higher values of these four quantities, meaning that PE and CR heating are stronger in the cells where no star formation is taking place.

We further analyse the impact of both, variable G$_0$ and ζ, on the star formation efficiency (SFE). Therefore, in Fig. 10, we overplot the mean of $G_{\rm eff}$, $\Gamma_{\rm pe}$, ζ and $\Gamma_{\rm cr}$ for all gas. We show run Z0.02-vG$_0$-vζ (i.e. $\overline{G_{\rm eff}}$, $\overline{\Gamma_{\rm pe}}$, $\overline{\zeta}$ and $\overline{\Gamma_{\rm cr}}$) using dashed vertical lines and run Z0.02 (i.e. $\overline{G_{\rm eff,Z0.02}}$, $\overline{\Gamma_{\rm pe,Z0.02}}$, $\overline{\zeta_{\rm Z0.02}}$ and $\overline{\Gamma_{\rm cr,Z0.02}}$) with solid

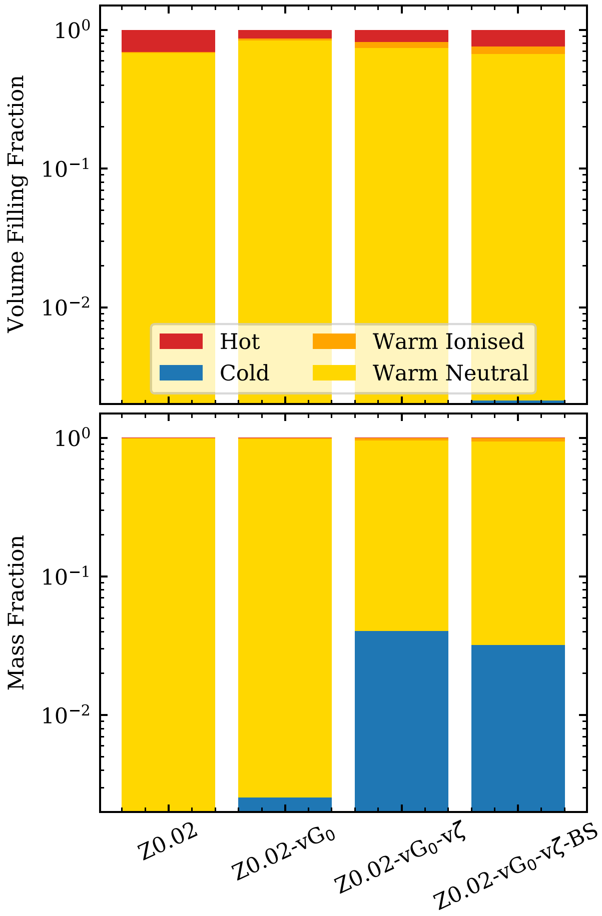

Figure 7. Average mass and volume-filling fractions of the four runs, computed in a region $|z| < 250$ pc around the disc mid-plane and in a time interval of 100 Myr after the onset of star formation. In run, Z0.02 no cold gas is found, whereas in run Z0.02-vG$_0$ less than 1 per cent of the total gas mass is cold. On the other hand, with variable ζ, around 3–4 per cent of the mass is available as cold gas.

lines, respectively. As expected, for run Z0.02 where G_0 and ζ are constant, we have $\overline{G_{\mathrm{eff,Z0.02}}} = 1.7 \times \exp(\text{-}2.5\ A_{\mathrm{V,3D}}) \sim 1.69$, and $\overline{\zeta_{\mathrm{Z0.02}}} = 3 \times 10^{-17}\ \mathrm{s}^{-1}$. The value of $\overline{G_{\mathrm{eff,Z0.02}}}$ does not differ much from the unattenuated value of 1.7, because assuming a minimum external column density $N_{\mathrm{ext}} = 10^{20}\ \mathrm{cm}^{-2}$ and a metallicity of 0.02 $\mathrm{Z}_\odot$, according to equation (4) we obtain a minimum $A_{\mathrm{V,3D}}$ of around 0.001. Since the gas in run Z0.02 does not reach higher column densities than N_{ext}, the minimum value of the $A_{\mathrm{V,3D}}$ is similar to the average $\mathrm{A}_{\mathrm{V,3D}}$ found in this run. In run Z0.02-vG$_0$-vζ, the mean values are $\overline{G_{\mathrm{eff}}} = 0.11$ and $\overline{\zeta} = 6.55 \times 10^{-18}\ \mathrm{s}^{-1}$. Regarding the heating rates, we find $\overline{\Gamma_{\mathrm{pe}}} = 10^{-28}\ \mathrm{erg\ s^{-1}\ cm^{-3}}$, $\overline{\Gamma_{\mathrm{pe,Z0.02}}} = 2.8 \times 10^{-28}$, $\overline{\Gamma_{\mathrm{cr}}} = 2.4 \times 10^{-28}$, and $\overline{\Gamma_{\mathrm{cr,Z0.02}}} = 6.5 \times 10^{-28}$.

We clearly see that choosing the constant values of $G_0 = 1.7$ and $\zeta_0 = 3 \times 10^{-17}\ \mathrm{s}^{-1}$ in run Z0.02 leads to higher CR and PE heating rates than the corresponding means computed for the Z0.02-vG$_0$-vζ run. Therefore, the explanation for the inefficiency of star formation in the Z0.02 run lies in the choice of these values. At the same time, we highlight the importance of implementing variable models for G_0 and ζ, since choosing a single value for these parameters does not reflect the diverse conditions that occur in the ISM. The wide distribution of ζ, shown in the third panel of Fig. 10, confirms that a constant (lower) value of ζ is not able to properly describe the CR heating in all gas.

When looking at the star-forming gas (opaque distributions in Fig. 10), we see that star formation takes place in environments where G_{eff} is comparable to, or even higher than, the mean $\overline{G_{\mathrm{eff}}}$. However, ζ of the star-forming gas is actually much lower than $\overline{\zeta}$. In Section 3.4, we show that a constant ζ but variable G$_0$ (run Z0.02-vG$_0$) still leads to very little cool gas and basically no star formation. Since heating by CRs apparently dominates over PE heating at the low metallicity we investigate (see Section 3.3), choosing a constant $\zeta = \overline{\zeta}$ would again result in a lower SFE than the one we find. Hence, our results support the need for spatially and time-variable G$_0$ and ζ implementations.

In Fig. 11, we represent the time-averaged SFR surface density Σ_{SFR} as a function of Σ_{gas}, which is the sum of the gas surface density of atomic and molecular hydrogen. The Σ_{SFR} is defined following Gatto et al. 2017 as

$$\Sigma_{\mathrm{SFR}} = \frac{\mathrm{SFR}}{A} = \frac{1}{A}\sum_{i=1}^{N(t)} \frac{120\ \mathrm{M}_\odot}{t_{\mathrm{OB}}}, \qquad (22)$$

where $A = (0.5\ \mathrm{kpc})^2$ is the area of the computational domain, $N(t)$ the number of active massive stars at time t, t_{OB} is the lifetime of massive stars as computed from the stellar models. Therefore, Σ_{SFR} corresponds to the SFR rescaled by a constant factor A. We average both Σ_{SFR} and Σ_{gas} in a time interval of 200 Myr after the onset of star formation in each run. As a reference, we add the Kennicutt–Schmidt relation (KS, Kennicutt 1998), and we fit our data with the theoretical star formation law for low-metallicity environments by Krumholz, McKee & Tumlinson (2009, hereafter K09). For $\Sigma_{\mathrm{gas}} < 85\ \mathrm{M}_\odot\ \mathrm{pc}^{-2}$ (the relevant surface density range for our simulations), this relation reads

$$\Sigma_{\mathrm{SFR}} = f_{\mathrm{H}_2}\frac{\Sigma_{\mathrm{gas}}}{2.6\ \mathrm{Gyr}} \times \left(\frac{\Sigma_{\mathrm{gas}}}{85\ M_\odot\ \mathrm{pc}^{-2}}\right)^{-0.33}, \qquad (23)$$

where the mass fraction of molecular gas f_{H_2} is given by

$$f_{\mathrm{H}_2} \sim 1 - \left[1 + \left(\frac{3}{4}\frac{s}{1+\delta}\right)^{-5}\right]^{-1/5}, \qquad (24)$$

with $s = \ln(1 + 0.6\ \chi)/(0.04\ \Sigma_{\mathrm{gas}} cZ)$, $\chi = 0.77\ (1 + 3.1\ Z^{0.365})$, $\delta = 0.0712(0.1\ \mathrm{s}^{-1} + 0.675)^{-2.8}$, with c clumping factor and Z the metallicity of the gas in solar units. Fitting this formula to our data

Table 2. Mass- and volume-filling fractions of the cold, warm neutral, warm ionized, and hot gas (see the text for definition) computed for the four runs in a region of $|z| < 250$ pc and averaged over 100 Myr after the onset of star formation.

Run	$\overline{\mathrm{VFF}}_{\mathrm{cold}}$ $\times 10^{-2}$ (per cent)	$\overline{\mathrm{VFF}}_{\mathrm{WNM}}$ (per cent)	$\overline{\mathrm{VFF}}_{\mathrm{WIM}}$ (per cent)	$\overline{\mathrm{VFF}}_{\mathrm{hot}}$ (per cent)	$\overline{\mathrm{MF}}_{\mathrm{cold}}$ (per cent)	$\overline{\mathrm{MF}}_{\mathrm{WNM}}$ (per cent)	$\overline{\mathrm{MF}}_{\mathrm{WIM}}$ (per cent)	$\overline{\mathrm{MF}}_{\mathrm{hot}}$ $\times 10^{-3}$ (per cent)
Z0.02	0 ± 0	68.0 ± 0.2	1.6 ± 0.1	30.3 ± 0.2	0 ± 0	98.8 ± 0.1	1.14 ± 0.01	9.9 ± 0.1
Z0.02-vG$_0$	0.28 ± 0.01	84.0 ± 0.3	2.9 ± 0.1	13.1 ± 0.2	0.25 ± 0.01	98.0 ± 0.1	1.7 ± 0.1	3.5 ± 0.1
Z0.02-vG$_0$-vζ	8.49 ± 0.17	74.1 ± 0.6	8.2 ± 0.2	17.6 ± 0.6	4.05 ± 0.09	92.1 ± 0.2	3.84 ± 0.14	11.5 ± 0.6
Z0.02-vG$_0$-vζ-BS	21.3 ± 1.1	67.3 ± 0.9	9.0 ± 0.5	23.5 ± 0.8	3.21 ± 0.15	91.2 ± 0.4	5.59 ± 0.37	20.6 ± 1.0

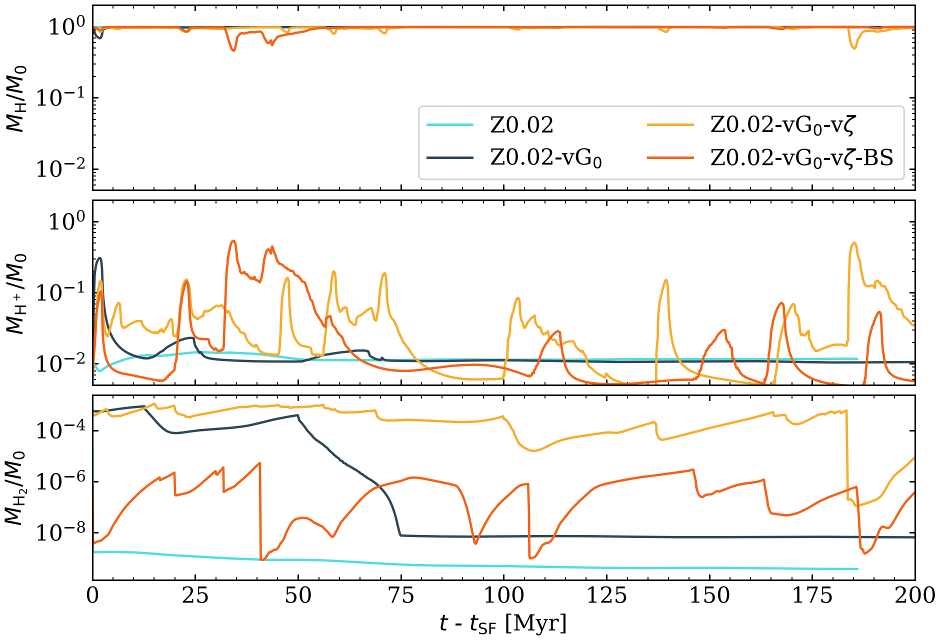

Figure 8. Volume-weighted, normalized mass fractions of H, H^+, H_2 as a function of time, computed in a region $|z| < 250$ pc. t_{SF} is the time of the first episode of star formation (see Table 1). Top panel: the H mass fraction is almost always close to one; however, it is slightly affected by stellar feedback for the runs that form stars. Central panel: the ionized hydrogen fraction is affected by star formation for the runs with stars, whereas it is stable and around 10^{-2} for Z0.02. Bottom panel: the H_2 mass fraction is highest for the Z0.02-vG$_0$-vζ and lowest for Z0.02 (highest heating rates). Since the value of t_{SF} is undefined for the Z0.02 run, we represent here its entire evolution.

gives a clumping factor of 27.3 ± 3.1, from which it follows a value of $f_{H_2} \sim 10^{-2}$. This value is around one order of magnitude higher than the mass fraction of H_2 found for our Z0.02-vG$_0$-vζ run. In the K09 model, $c \rightarrow 1$ if the resolution of observations is approaching 100 pc. We also add two lines computed for $c = 50$ (solid black line) and $c = 15$ (dashed). We note that the choice of the clumping factor strongly influences the value of the Σ_{SFR} computed for a given Σ_{gas}. Additionally, we note that the average value of Σ_{SFR} is very similar in our Z0.02-vG$_0$-vζ and Z0.02-vG$_0$-vζ-BS runs, despite the orders of magnitude of difference in the amount of molecular hydrogen mass present. This suggests that, in low-metallicity environments, the cold gas determines the SFR rather than the molecular gas (Glover & Clark 2012; Krumholz 2012; Hu et al. 2016). However, the Σ_{SFR} is around of one magnitude lower than the value predicted by the KS relation for the Z0.02-vG$_0$-vζ and Z0.02-vG$_0$-vζ-BS runs, and two orders of magnitude lower for the Z0.02-vG$_0$ run. This discrepancy is due to the very low value of the metallicity in our runs. Measures of Σ_{SFR} for the IZw18 galaxy have been reported by Aloisi, Tosi & Greggio (1999) to be around 10^{-2} M$_\odot$ yr^{-1} kpc^{-2} for the main body and (3–10) × 10^{-3} M$_\odot$ yr^{-1} pc^{-2} for the secondary body. The Σ_{SFR} computed for the Z0.02-vG$_0$-vζ and Z0.02-vG$_0$-vζ-BS runs is almost one order of magnitude lower than the value measured for the secondary body. This difference can be attributed to the fact that the environmental conditions of our simulations do not align perfectly with those of the IZw18 galaxy.

In Fig. 12, we represent the SFR surface density Σ_{SFR} as a function of time for the runs in which stars are able to form. The SFR surface density oscillates in time, with peaks that reach around 2 × 10^{-3} M$_\odot$ yr^{-1} kpc^{-2} in the case of Z0.02-vG$_0$-vζ-BS. This value is around one order of magnitude less than what has been found for solar metallicity and without the variability of G$_0$ and ζ by Rathjen et al. (2023). Since these setups are not directly comparable, we add a line indicating the value expected from the star formation law by K09 computed for a clumping factor of 1 and a metallicity of 0.02 Z$_\odot$, at a gas surface density of 10 M$_\odot$ pc^{-2}. This value is in agreement with the peak in Σ_{SFR} obtained for Z0.02-vG$_0$-vζ-BS, and around one to two orders of magnitude higher for the other two runs. The reason for having so few stars can be traced back to the very little cold gas formed at this metallicity.

The second panel of Fig. 12 represents the mass outflow rate $\dot{M}$, meaning the mass passing through a surface at ± 1 kpc from the mid-plane, in time. The peaks in $\dot{M}$ are delayed compared to the peaks in Σ_{SFR}, as the most massive stars need at least a few million years before going off as SNe and pushing the gas out of the disc mid-plane. However, even the largest values of $\dot{M}$ obtained in our simulations are very low. Therefore, we observe neither a thermally driven nor a CR-driven outflow from the mid-plane. According to Gatto et al. (2017), at solar metallicity a hot gas volume-filling fraction of at least 50 per cent is needed to launch an outflow from the disc. This is by far not reached in any of our runs (see Fig. 7), as the maximum average volume-filling fraction is reached by the Z0.02 run, around 30 per cent, followed by the Z0.02-vG$_0$-vζ-BS run, around 23 per cent. The amount of hot gas depends on the SN rate, which, in turn, depends on the SFR. We conclude that Σ_{SFR} in our low-metallicity runs is too low to sustain a hot volume-filling phase and to launch a thermally driven outflow. We also do not observe a CR-driven outflow. CR injection events are rare due to the low SN rate. The CRs then diffuse rapidly, thus smoothing out local fluctuations in their energy density and pressure distributions and a CR pressure gradient that would be able to lift the gas from the disc cannot be maintained.

For the Z0.02-vG$_0$-vζ-BS run, we show several quantities as times-series in Fig. 13, to represent the evolution of the gas and the related physical quantities. We show the density projection and slices for

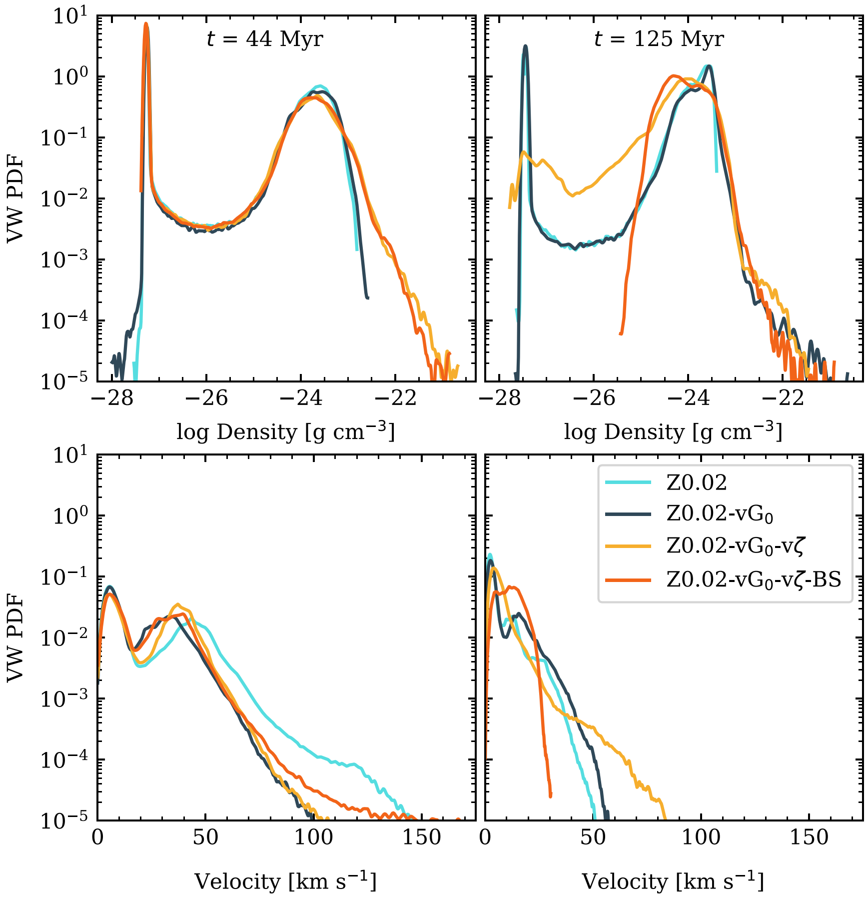

Figure 9. Top row: volume-weighted density PDF of the four runs right before Z0.02-vG$_0$-vζ and Z0.02-vG$_0$-vζ form the first star cluster (at around 44 Myr, left panel) and at a later time (125 Myr, right panel). Bottom row: volume-weighted velocity PDF of the four runs, computed at the same time as the corresponding above panels. Both the density and velocity PDFs are computed in a region $|z| < 250$ pc.

temperature, PE and CR heating. We note that no real outflow develops, as already seen in Fig. 12, however, at around 60 Myr the gas reaches slightly less than 1 kpc in the vertical direction. After that, the evolution continues without relevant changes in the thickness of the disc. Regarding the PE and CR heating, they depend on density, therefore their distribution follows strictly that of the gas distribution.

4 DISCUSSION

4.1 Computation of ζ

As already discussed above, the energy spectrum of CRs peaks at energies of a few GeV, and it declines steeply at lower and higher energies. Therefore, the energy density of CRs in the ISM is dominated by the contribution of CRs whose energy is of a few GeV. On the other hand, the CR ionization rate is determined by low-energy CRs, meaning in the eV–MeV range. Here, we simply assume that the CR ionization rate scales with the CR energy density, without treating the different physics that actually regulates low-energy CRs, such as energy-dependent cooling and CR transport. In this way, we assume a grey spectrum for CRs, where losses are considered to be the same regardless of the energy interval under consideration or the local thermal and magnetic conditions. However, there are six orders of magnitude of difference in energy between the GeV CRs at the peak of the spectrum, and those mainly responsible for CR heating. Therefore, a more detailed treatment in future works is needed in order to take into account the missing physics necessary to describe the energy losses, possible re-acceleration, and diffusion of the low-energy CRs. This could for example be done by simulating live CR spectra (Girichidis et al. 2020, 2022, 2024). Our choice of using the scaling for the attenuation proposed by Padovani et al. (2009) partly solves this issue, as the observationally motivated relationship between ζ and the column density of the gas naturally takes into account all the relevant physics.

4.2 Comparison to previous works

Girichidis et al. (2018a) have implemented a variable CR ionization rate computed by linearly scaling the energy density of CRs without any attenuation and employing a setup similar to ours. They compare their runs with a variable ζ with those where the CR ionization rate is constant, and they observe no systematic change in the dynamics of the gas, in net contrast to our results. We can identify two reasons to explain this difference. The first lies in the different characterization of the SN rate. In fact, Girichidis et al. (2018a) employ a fixed SN rate, where the positions and times of each SN are provided as a simulation input. Contrary, we follow the formation and evolution of massive stars and the resulting SN rate depends on the population of massive stars. The local change in CR ionization rate locally affects the CR heating, which in turn impacts the star formation, allowing us to form stars even at this very low metallicity. The second reason

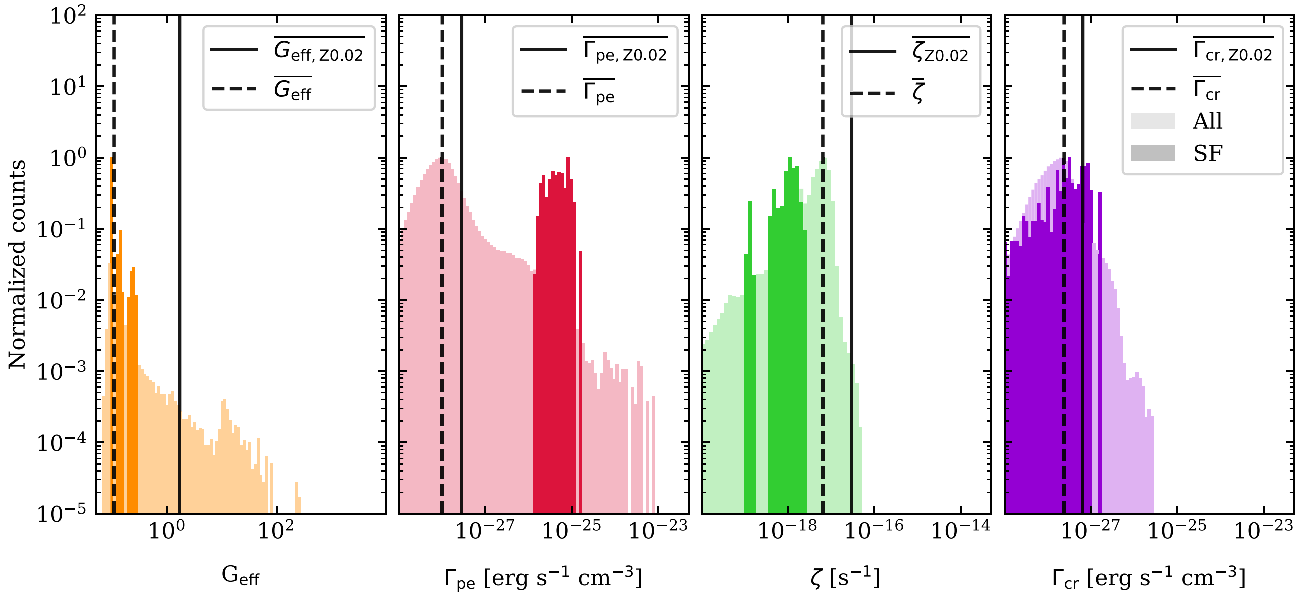

Figure 10. Initial conditions for star formation in our Z0.02-vG$_0$-vζ simulation. For every sink particle that is created, we analyse the gas conditions in the formation region one snapshot before sink formation (see the text for details). From left to right, we show the distribution of $G_{\rm eff}$, $\Gamma_{\rm pe}$, ζ, and $\Gamma_{\rm cr}$. Considering all star clusters, we represent the resulting distributions as dark-shaded histograms. We add as transparent histograms the distributions of these quantities computed for all these snapshots and all cells in a region $|z| < 250$ pc around the mid-plane, as a comparison. All distributions are normalized to be between 0 and 1. The star-forming gas has values of $G_{\rm eff} < 1$, $\zeta \sim 10^{-18}$ s^{-1}, $\Gamma_{\rm pe} \sim 10^{-26}$–$10^{-25}$ erg s^{-1} cm^{-3}, and $\Gamma_{\rm cr} < 10^{-26}$ erg s^{-1} cm^{-3}. We add in the first and third panels the mean of the distributions for all gas for run Z0.02-vG$_0$-vζ (dashed vertical lines), and, for comparison, for run Z0.02 (solid vertical lines).

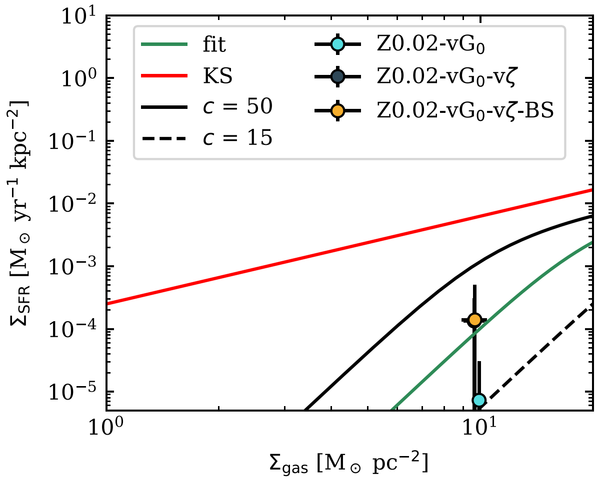

Figure 11. $\Sigma_{\rm SFR}$ against the gas surface density of the gas averaged over 200 Myr after the onset of star formation. We add the theoretical star formation law for low-metallicity environments from K09, computed for a value of c = 50 (solid black line) and c = 15 (dashed). We add the fit to our data assuming c to be a free parameter (green), and the KS relation (red). The markers of the Z0.02-vG$_0$-vζ and the Z0.02-vG$_0$-vζ-BS coincide.

concerns the metallicity of the gas. Girichidis et al. (2018a) study solar-neighbourhood conditions. As already seen in Section 2.3, at solar metallicity the PE heating plays a much more important role than CR heating in regulating the gas temperature. Consequently, changes in the CR ionization rate have a much smaller impact on the phase balance between cold and warm gas in their simulations, compared to our models. This could explain why they do not observe significant variations in the dynamics of the gas when changing the local CR ionization rate.

Kim et al. (2023) present the TIGRESS–NCR simulations, which adopt a simulation setup similar to that used in this work. They do not include CR transport via advection, diffusion, and streaming along magnetic field lines, therefore they neglect any possible effect of the presence of CRs on the dynamics of the gas. However, they take into account CR heating employing a temporally variable CR ionization rate which scales according to the SFR surface density and the gas surface density. In particular, they adopt an unattenuated value of the CR ionization rate (in our notation) $\zeta_0 = 2 \times 10^{-16}$ s^{-1} $\times\, \Sigma'_{\rm SFR,40}/\Sigma'_{\rm gas}$, where $\Sigma'_{\rm SFR,40}$ is the SFR surface density computed considering the last 40 Myr of evolution divided by the solar neighbourhood value $\Sigma_{\rm SFR} = 2.5 \times 10^{-3}$ M$_\odot$ kpc^{-2} yr^{-1}, and $\Sigma'_{\rm gas}$ is the instantaneous gas surface density normalized by the solar-neighbourhood value $\Sigma_{\rm gas} = 10$ M$_\odot$ pc^{-2}. For an effective shielding column density $N_{\rm eff}$ higher than a threshold value $N_0 = 9.35 \times 10^{20}$ cm^{-2} the CR ionization rate ζ_0 is attenuated by a factor of $(N_{\rm eff}/N_0)^{-1}$. The exponent of their attenuation factor (–1) is assumed from Neufeld & Wolfire (2017), which is more than double compared to the exponent employed in this work (–0.423), taken from Padovani et al. (2009). This implies that the CR ionization rate is more heavily attenuated in the dense gas in TIGRESS–NCR simulations compared to ours meaning that, for the same ζ_0, the CR heating is higher in our simulations. Since they simulate the ISM at solar metallicity, for which different conditions apply compared to the very metal-poor medium analysed in this work, we cannot directly compare with our results. This will be done in a follow-up paper (Brugaletta et al. in preparation), where we study different metallicities. However, regarding the method, we can speculate that their value of the unattenuated CR ionization rate ζ_0 would be too large to allow star formation in a metal-poor environment if $\Sigma'_{\rm SFR,40} \sim \Sigma'_{\rm gas}$. In fact, as seen in Fig. 3, a value of around 10^{-16} s^{-1} is reached only in few cells in the vicinity of SNe.

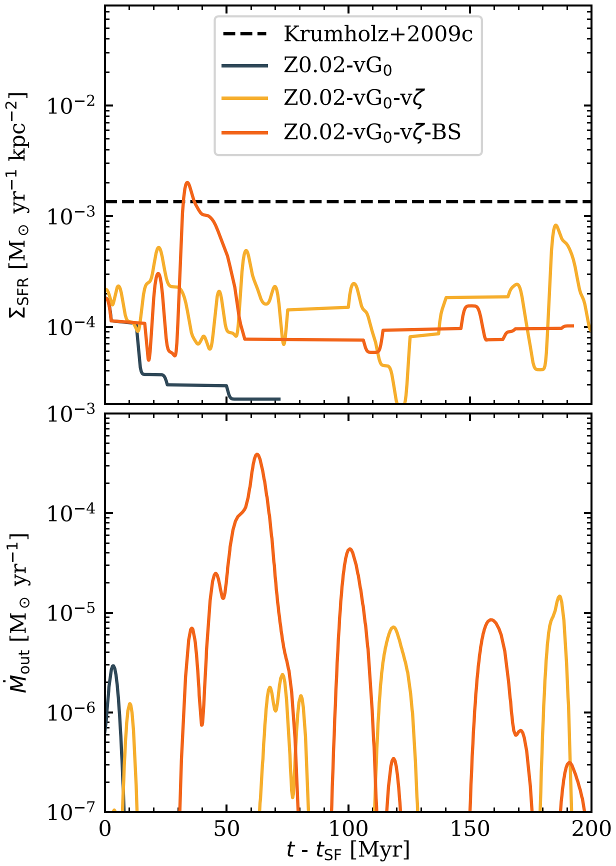

Figure 12. Top panel: SFR surface density as a function of time for the simulations that can form stars. The dashed line indicates the expected SFR surface density estimated from the K09 star formation relation for a gas surface density of 10 $M_\odot$ pc^{-2}, at a metallicity of 0.02 $Z_\odot$ and with a clumping factor $c = 1$. We note that this value is in accordance with the peak in $\Sigma_{\rm SFR}$ found for the Z0.02-vG$_0$-vζ-BS run, whereas it is higher for the other two runs. Bottom panel: mass outflow rate, meaning the mass of the gas crossing a surface a $z = \pm$ 1 kpc, as a function of time.

An extension of this work has been presented in Kim et al. (2024), where they expand their analysis at metallicities from three times solar down to 0.1 $Z_\odot$, which is five times higher than the value adopted in this work. A direct comparison is, again, non-trivial, and will be done in a follow-up paper (Brugaletta et al in preparation).

4.3 Considerations for high-redshift environments

The setup used in our simulations is suitable to describe the ISM at redshift zero, typical for nearby dwarf galaxies. However, low-metallicity environments are also common in high-redshift galaxies. To adapt our current setup in order to describe the high-redshift ISM, a few adjustments are needed.

First of all, the temperature of the cosmic microwave background (CMB), which sets the temperature floor of the gas, depends on the redshift as

$$T_{\rm CMB}(z) = T_0(1 + z), \tag{25}$$

where $T_{\rm CMB}$ is the temperature of the CMB, z is the redshift, and $T_0 = 2.725 \pm 0.002$ K (Mather et al. 1999) is the value at the present epoch. Since the temperature of the CMB depends on the redshift only linearly, it will change only slightly if we do not choose high redshifts, for example, $z = 20$. Therefore, the change in temperature of the CMB can probably be neglected if the redshift of interest is sufficiently low.

Moreover, H_2 formation would be affected by the lack of dust in pristine gas. In this work, we adopt a simplified treatment for the production of H_2, assuming that it can form only on the surface of dust grains, following the results from Hollenbach & McKee 1989. However, molecular hydrogen can also form in the gas, and its formation channels there can dominate over formation on dust grains at sufficiently low metallicities. For example, H_2 formation via the H^- ion becomes more important than grain surface formation for dust-to-gas ratios $\sim$ 1 per cent of the solar value or smaller (Glover 2003), while formation via the three-body channel becomes important at high gas densities ($n > 10^8$ cm^{-3}, Palla et al. 1983) and very low metallicities ($Z < 10^{-6}$ $Z_\odot$, Omukai et al. 2005). We have discussed above that molecular gas is not needed at this metallicity to form stars, therefore these production mechanisms do not play an important role in describing star formation at high redshift.

In addition, in galaxies with masses higher than 10^{10} $M_\odot$ the gas fraction, i.e. the ratio of gas mass to stellar mass, increases as a function of redshift (Carilli & Walter 2013). Moreover, according to Markov et al. (2022), high-redshift galaxies present a starburst phase, therefore their KS relation is shifted towards higher SFR surface densities.

5 SUMMARY AND CONCLUSIONS

In this work, we present our new treatment of the heating due to low-energy CRs implemented in the framework of the SILCC simulations. Our MHD simulations include feedback from massive stars in form of non-ionizing (FUV) and ionizing (EUV) radiation, stellar winds, SNe and CRs. In our new prescription for CR heating, we treat the CR ionization rate ζ as a variable, instead of a constant parameter, such that it varies as a function of the energy density of CRs. We assume a linear scaling of ζ with the energy density of CRs if the column density of the gas is lower than 10^{20} cm^{-2}, otherwise we attenuate this linear scaling with a power law. The other main important heating mechanism in the ISM is PE heating, which we compute from the FUV radiation field using the novel method presented in Rathjen et al. (2024).

We test this implementation at a metallicity of 0.02 $Z_\odot$, for which the CR heating computed for a reference value of $\zeta = 3 \times 10^{-17}$ s^{-1} is comparable with the PE heating rate computed for a reference value of $G_0 = 1.7$ and the chosen metallicity. We run four different simulations with (i) constant G_0 and ζ, (ii) variable G_0 and constant ζ, (iii) both parameters variable and a linear scaling of the dust-to-gas ratio with the metallicity, (iv) both parameters variable and a power-law scaling of the dust-to-gas ratio with metallicity. Our main results are listed as follows:

(i) The variability in space and time of the CR ionization rate plays a major role in allowing the gas to cool. In fact, having both constant G_0 and ζ hinders the cooling and therefore star formation. Moreover, having a variable G_0 but a constant ζ allows only a very small fraction of the gas to cool and form stars. Only the variability of the two parameters allows a substantial number of stars to form, however, the different scaling of the dust-to-gas ratio with metallicity does not produce important differences.

(ii) The ability of the gas to cool to temperatures suitable for star formation is dictated by the amount of energy provided by PE and CR heating. The runs with constant ζ are those whose total energy given by these heating mechanisms is larger, whereas the runs with a variable ζ provide almost an order of magnitude less energy.

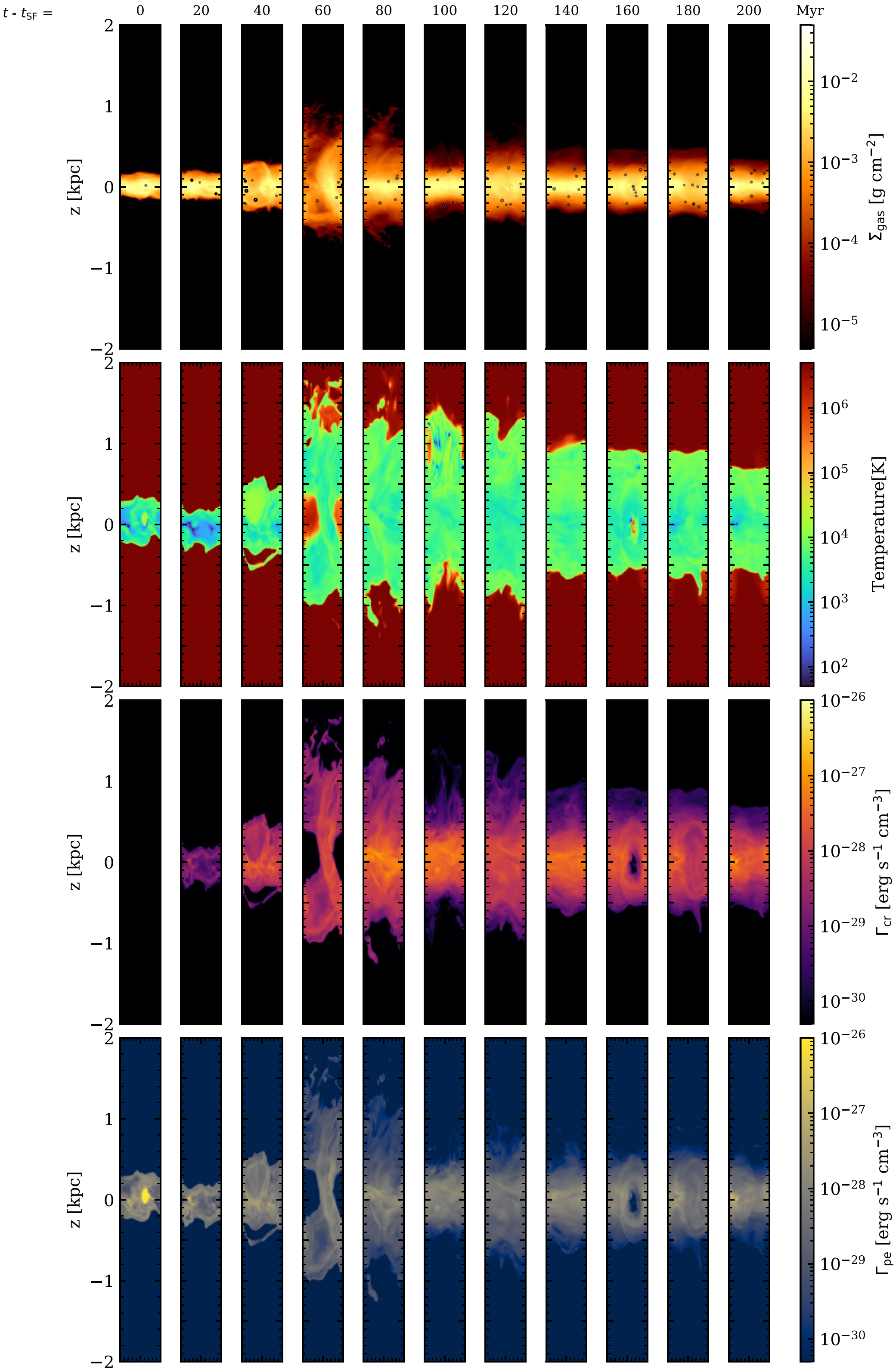

Figure 13. Time-series for Z0.02-vG$_0$-vζ-BS. In the first row, the projection of the density is represented, in the second the slice of temperature, in the third the slice of the CR heating rate, in the last the slice of the PE heating rate. The circles in the first row represent the star clusters.

(iii) The direct effect is the amount of cold gas formed in our runs. In fact, the runs with variable ζ result in 3–4 per cent of the total gas mass to be cold. On the other hand, in the Z0.02-vG$_0$ run, only 0.25 per cent of the gas is cold.

(iv) We analyse the spatial distribution of the PE and CR heating rates, and we compare them. We note that the PE heating rate dominates in the immediate vicinity of star-forming regions, whereas the CR heating rate seems to dominate in the more diffuse gas, far away from massive star formation sites.

(v) We observe different behaviours in the density PDFs, as the runs able to form stars develop a power-law tail at high density, whereas the runs with no stars do not have a high-density phase.

(vi) We note selection effects in the local distributions of $G_{\rm eff}$, ζ, $\Gamma_{\rm pe}$, $\Gamma_{\rm cr}$ in the volume where a star cluster will be forming. For a star cluster to form, it is necessary to have a $G_{\rm eff} < 1$, a value of ζ around $10^{-18}\,{\rm s}^{-1}$, $\Gamma_{\rm pe}$ and $\Gamma_{\rm cr}$ below $10^{-25}\,{\rm erg\,s}^{-1}\,{\rm cm}^{-3}$. The values of ζ for which star formation takes place are lower than the mean of the distribution computed for all gas.

(vii) Because of the above points, substantial star formation takes place only in the runs with variable ζ, where small values of ζ can be locally possible. However, the SFR surface density is around one order of magnitude lower than what is expected from the star formation relation for low-metallicity environments (K09).

(viii) Since only a few stars are formed in all runs, there are only a few SN explosions in our simulation domain. Therefore, neither thermally driven nor CR-driven outflows develop in our simulations.

ACKNOWLEDGEMENTS

The authors thank the anonymous referee for improving this work with useful comments. VB, SW, T-ER, DS, and PCN thank the Deutsche Forschungsgemeinschaft (DFG) for funding through the SFB 1601 ‘Habitats of massive stars across cosmic time’ (subprojects B1, B4 and B6). SW, T-ER, and DS further acknowledge support by the project ‘NRW-Cluster for data-intensive radio astronomy: Big Bang to Big Data (B3D)’ funded through the programme ’Profilbildung 2020’, an initiative of the Ministry of Culture and Science of the State of North Rhine-Westphalia. VB and SW thank the Bonn-Cologne Graduate School. TN acknowledges support from the DFG under Germany’s Excellence Strategy – EXC-2094 – 390783311 from the DFG Cluster of Excellence ‘ORIGINS’. PG and SCOG acknowledge funding by the European Research Council via the ERC Synergy Grant ‘ECOGAL’ (project ID 855130). RW acknowledges support by the institutional project RVO:67985815. SCOG also acknowledges support from the Heidelberg Cluster of Excellence EXC 2181 (Project-ID 390900948) ‘STRUCTURES: A unifying approach to emergent phenomena in the physical world, mathematics, and complex data’ supported by the German Excellence Strategy. The software used in this work was in part developed by the DOE NNSA-ASC OASCR Flash Centre at the University of Rochester (Fryxell et al. 2000; Dubey et al. 2009). Part of the data visualization has been done with the PYTHON package YT (Turk et al. 2011) and the FLASH_AMR_TOOLSPYTHON package (https://pypi.org/project/flash-amr-tools/) developed by PCN. The data analysis has been performed using the following Python packages: NUMPY (van der Walt, Colbert & Varoquaux 2011), MATPLOTLIB (Hunter 2007), H5PY (Collette et al. 2020), IPYTHON (Perez & Granger 2007), and SCIPY (Virtanen et al. 2020).

DATA AVAILABILITY

The derived data underlying this article will be shared on reasonable request to the corresponding author. The simulation data will be made available on the SILCC data web page: http://silcc.mpa-garching.mpg.de.

REFERENCES

Ackermann M. et al., 2013, Science, 339, 807
Aloisi A., Tosi M., Greggio L., 1999, AJ, 118, 302
Axford W. I. et al., 1978, in Dergachev V. A., Kocharov G. E.,eds, Cosmophysics, Xth Leningrad seminar on cosmophysics, p. 125,
Baade W., Zwicky F., 1934, Phys. Rev., 46, 76
Bakes E. L. O., Tielens A. G. G. M., 1994, ApJ, 427, 822
Bate M. R., Bonnell I. A., Price N. M., 1995, MNRAS, 277, 362
Bell A. R., 1978a, MNRAS, 182, 147
Bell A. R., 1978b, MNRAS, 182, 443
Bergin E. A., Tafalla M., 2007, ARA&A, 45, 339
Bergin E. A., Hartmann L. W., Raymond J., Ballesteros-Paredes J., 2004, ApJ, 612, 921
Bialy S., Sternberg A., 2019, ApJ, 881, 160
Blandford R. D., Ostriker J. P., 1978, ApJ, 221, L29
Bohlin R. C., Savage B. D., Drake J. F., 1978, ApJ, 224, 132
Boulares A., Cox D. P., 1990, ApJ, 365, 544
Brott I. et al., 2011, A&A, 530, A115
Cabedo V., Maury A., Girart J.M., Marco P., Patrick H., Qizhou Z., 2023, A&A, 669, A90
Carilli C. L., Walter F., 2013, ARA&A, 51, 105
Caselli P., Walmsley C. M., Terzieva R., Herbst E., 1998, ApJ, 499, 234
Ceccarelli C., et al., 2014, ApJ, 790, L1
Collette A. et al., 2020, h5py/h5py: 3.1.0, https://zenodo.org/records/4250762
Cox D. P., 2005, ARA&A, 43, 337
Cummings A. C. et al., 2016, ApJ, 831, 18
Curti M. et al., 2024, A&A, 684, A75
Dinnbier F., Walch S., 2020, MNRAS, 499, 748
Draine B. T., 1978, ApJS, 36, 595
Draine B. T., Bertoldi F., 1996, ApJ, 468, 269
Draine B. T. et al., 2007, ApJ, 663, 866
Dubey A., Reid L. B., Fisher R., 2008, Phys. Scr., T132, 014046
Dubey A., Reid L. B. et al., 2009, preprint (arXiv:0903.4875)
Favre C. et al., 2018, ApJ, 859, 136
Federrath C., Banerjee R., Clark P. C., Klessen R. S., 2010, ApJ, 713, 269
Field G. B., Goldsmith D. W., Habing H. J., 1969, ApJ, 155, L149
Fontani F. et al., 2017, A&A, 605, A57
French H. B., 1980, ApJ, 240, 41
Fryxell B. et al., 2000, ApJS, 131, 273
Gatto A. et al., 2015, MNRAS, 449, 1057
Gatto A. et al., 2017, MNRAS, 466, 1903
Ginzburg V. L., Syrovatskii S. I., 1964, The Origin of Cosmic Rays, Elsevier
Girichidis P., Konstandin L., Whitworth A. P., Klessen R. S., 2014, ApJ, 781, 91
Girichidis P. et al., 2016a, MNRAS, 456, 3432
Girichidis P. et al., 2016b, ApJ, 816, L19
Girichidis P., Naab T., Hanasz M., Walch S., 2018a, MNRAS, 479, 3042
Girichidis P. et al. 2018b, MNRAS, 480, 3511
Girichidis P., Pfrommer C., Hanasz M., Naab T., 2020, MNRAS, 491, 993
Girichidis P., Pfrommer C., Pakmor R., Volker S., 2022, MNRAS, 510, 3917
Girichidis P., Werhahn M., Pfrommer C., Pakmor R., Volker S., 2024, MNRAS, 527, 10897
Glassgold A. E., Langer W. D., 1974, ApJ, 193, 73
Glover S. C. O., 2003, ApJ, 584, 331
Glover S. C. O., Clark P. C., 2012, MNRAS, 421, 9
Glover S. C. O., Mac Low M.-M., 2007a, ApJS, 169, 239
Glover S. C. O., Mac Low M.-M., 2007b, ApJ, 659, 1317
Gnat O., Ferland G. J., 2012, ApJS, 199, 20
Goldsmith P. F., Langer W. D., 1978, ApJ, 222, 881
Górski K. M. et al., 2005, ApJ, 622, 759
Haardt F., Madau P., 2012, ApJ, 746, 125
Habing H. J., 1968, Bull. Astron. Inst. Neth., 19, 421
Hanasz M., Lesch H., Naab T., Gawryszczak A., Kowalik K., Wóltański D., 2013, ApJ, 777, L38
Hanasz M. et al., 2021, Liv. Rev. Comp. Astrophys., 7, 2
Heays A. N., Bosman A. D., van Dishoeck E. F., 2017, A&A, 602, A105
Heintz K. E. et al., 2023, ApJ, 944, L30
Hillas A. M., 2005, J. Phys. G Nucl. Phys., 31, R95
Hollenbach D., McKee C. F., 1989, ApJ, 342, 306
Hu C.-Y., Naab T., Stefanie W., Simon C. O. G. , Paul C. C., 2016, MNRAS, 458, 3528

Hunter J. D., 2007, Comput. Sci. Eng., 9, 90
Jaiswal S., Omar A., 2020, MNRAS, 498, 4745
Kennicutt R. C. J., 1998, ApJ, 498, 541
Kim C.-G., Kim J.-G., Gong M., Ostriker E. C., 2023, ApJ, 946, 3
Kim C.-G. et al., 2024, ApJ, 972, 25
Klessen R. S., 2000, ApJ, 535, 869
Krumholz M. R., 2012, ApJ, 759, 9
Krumholz M. R., McKee C. F., Tumlinson J., 2009, ApJ, 699, 850 (K09)
Krymskii G. F., 1977, Akad. Nauk SSSR Dokl., 234, 1306
Leitherer C. et al., 1999, ApJS, 123, 3
Lelli F., Verheijen M., Fraternali F., Sancisi R., 2012, A&A, 537, A72
Markov V. et al., 2022, A&A, 663, A172
Mather J. C., Fixsen. D. J., Shafer. R. A., Mosier. C., Wilkinson. D. T., 1999, ApJ, 512, 511
Meyer D. M. A., 2024, MNRAS, 530, 539
Nava L., Gabici S., 2013, MNRAS, 429, 1643
Nelson R. P., Langer W. D., 1997, ApJ, 482, 796
Neufeld D. A., Wolfire M. G., 2017, ApJ, 845, 163
Omukai K., Tsuribe T., Schneider R., Ferrara A., 2005, ApJ, 626, 627
Osterbrock D. E., 1988, PASP, 100, 412
Padovani M., Galli D., Glassgold A. E., 2009, A&A, 501, 619
Padovani M. et al., 2020, Space Sci. Rev., 216, 29
Padovani M. et al., 2022, A&A, 658, A189
Palla F., Salpeter E. E., Stahler S. W., 1983, ApJ, 271, 632
Perez F., Granger B. E., 2007, Comput. Sci. Eng., 9, 21
Peters T. et al., 2017, MNRAS, 466, 3293
Pfrommer C. et al., 2017, MNRAS, 465, 4500
Pineda J. E. et al., 2024, A&A, 972, 25
Rathjen T.-E. et al., 2021, MNRAS, 504, 1039
Rathjen T.-E., Thorsten N., Stefanie W., Daniel S., Philipp G., Richard W., 2023, MNRAS, 522, 1843
Rathjen T.-E., et al., 2024 preprint (arXiv:2410.00124)
Rémy-Ruyer A. et al., 2014, A&A, 563, A31
Ruszkowski M., Pfrommer C., 2023, A&A Rev., 31, 4
Sabatini G. et al., 2020, A&A, 644, A34
Sabatini G., Bovino S., Redaelli E., 2023, ApJ, 947, L18
Salpeter E. E., 1955, ApJ, 121, 161
Sandstrom K. M. et al., 2012, ApJ, 744, 20
Schneider N. et al., 2012, A&A, 540, L11
Slyz A. D., Devriendt J. E. G., Bryan G., Silk J., 2005, MNRAS, 356, 737
Socci A., et al., 2024, A&A, 687, 14
Spitzer Lyman J., Tomasko M. G., 1968, ApJ, 152, 971
Stone E. C. et al., 2019, Nat. Astron., 3, 1013
Strong A. W., Moskalenko I. V., Ptuskin V. S., 2007, Ann. Rev. Nucl. Part. Sci., 57, 285
Swordy S. P., 2001, Space Sci. Rev., 99, 85
Szécsi D., Agrawal P., Wünsch R., Langer N., 2022, A&A, 658, A125
Tielens A. G. G. M., 2005, The Physics and Chemistry of the Interstellar Medium, Cambridge University Press
Turk M. J. et al., 2011, ApJS, 192, 9
van der Walt S., Colbert S. C., Varoquaux G., 2011, Comput. Sci. Eng., 13, 22
Vanzella E. et al., 2023, A&A, 678, A173
Virtanen P. et al., 2020, Nat. Methods, 17, 261
Walch S. et al., 2015, MNRAS, 454, 238
Webber W. R., 1998, ApJ, 506, 329
Wolfire M. G. et al., 1995, ApJ, 443, 152
Wolfire M. G., McKee C. F. , David H., Tielens A. G. .G. M., 2003, ApJ, 587, 278
Wünsch R., Walch S., Dinnbier F., Whitworth A., 2018, MNRAS, 475, 3393
Wünsch R. et al., 2021, MNRAS, 505, 3730
Zwicky F., 1966, ApJ, 143, 192

This paper has been typeset from a TEX/LATEX file prepared by the author.

CHAPTER 5

PAPER II

In this chapter we apply our new method to compute self-consistently the cosmic ray ionization rate, described in Chapter 4 (Paper I), to study the impact of metallicity on the structure and evolution of the interstellar medium. In this study, we employ SILCC simulations with different initial metallicities, ranging from 1 down to 0.02 $Z_{\odot}$.

5.1 Publication

This manuscript has been submitted to the Monthly Notices of the Royal Astronomical Society Main Journal. In this work, the simulations, the data analysis and the writing of the publication have been performed by Vittoria Brugaletta. The coauthors S. Walch, T. Naab, P. Girichidis, T.-E. Rathjen, D. Seifried, P. C. Nürnberger, R. Wünsch and S. C. O. Glover have provided useful guidance and ideas to the improvement of this work, and have proof-read the manuscript.

Figure 5 of this work has been inspired by the work of Sanjit Pal for his M.Sc. thesis. Section 3.5 of this paper has been inspired from Lukas Wasmuth's B.Sc. thesis, although the dendrogram analysis employed in this work differs substantially from that performed in his thesis.

MNRAS **000**, 1–25 (2025) Preprint 3 July 2025 Compiled using MNRAS LaTeX style file v3.0

SILCC – IX. The multi-phase interstellar medium at low metallicity

Vittoria Brugaletta[1,2]*, Stefanie Walch[1], Thorsten Naab[2], Tim-Eric Rathjen[1], Philipp Girichidis[3], Daniel Seifried[1], Pierre Colin Nürnberger[1], Richard Wünsch[4], Simon C. O. Glover[3], Sanjit Pal[1] and Lukas Wasmuth[1]
[1] *I. Physikalisches Institut, Universität zu Köln, Zülpicher Str. 77, 50937 Köln, Germany*
[2] *Max Planck Institute for Astrophysics, Karl-Schwarzschild-Str. 1, 85748 Garching, Germany*
[3] *Universität Heidelberg, Zentrum für Astronomie, Institut für Theoretische Astrophysik, Albert-Ueberle-Str. 2, D-69120 Heidelberg, Germany*
[4] *Astronomical Institute of the Czech Academy of Sciences, Boční II 1401, 141 00 Prague, Czech Republic*

Accepted XXX. Received YYY; in original form ZZZ

ABSTRACT

The gas-phase metallicity affects heating and cooling processes in the star-forming galactic interstellar medium (ISM) as well as ionising luminosities, wind strengths, and lifetimes of massive stars. To investigate its impact, we conduct magnetohydrodynamic simulations of the ISM using the FLASH code as part of the SILCC project. The simulations assume a gas surface density of 10 $M_\odot$ pc^{-2} and span metallicities from 1/50 $Z_\odot$ to 1 $Z_\odot$. We include non-equilibrium thermo-chemistry, a space- and time-variable far-UV background and cosmic ray ionisation rate, metal-dependent stellar tracks, the formation of HII regions, stellar winds, type II supernovae, and cosmic ray injection and transport. With the metallicity decreasing over the investigated range, the star formation rate decreases by more than a factor of ten, the mass fraction of cold gas decreases from 60% to 2.3%, while the volume filling fraction of the warm gas increases from 20% to 80%. Furthermore, the fraction of H_2 in the densest regions drops by a factor of four, and the dense ISM fragments into approximately five times fewer structures at the lowest metallicity. Outflow mass loading factors remain largely unchanged, with values close to unity, except for a significant decline at the lowest metallicity. Including the major processes that regulate ISM properties, this study highlights the strong impact of gas phase metallicity on the star-forming ISM.

Key words: methods:numerical – ISM: structure – ISM: jets and outflows – ISM: kinematics and dynamics – ISM: abundances – galaxies: ISM

1 INTRODUCTION

The ISM consists mainly of hydrogen and helium, with a small fraction of heavier elements (i.e., metals). This metal abundance, called metallicity, can play a very important role in shaping the ISM. Cooling in low-metallicity environments is inefficient, primarily due to the lack of major coolants like C^+, O, and dust (see e.g. Tielens 2005; Draine 2011). Moreover, the chemical abundances found at low metallicity cannot simply be explained by scaling solar-metallicity abundances, as the involved chemical reactions for the creation and destruction of species change with metallicity (Guadarrama et al. 2022), and because of a different enrichment by stellar nucleosynthesis (Bisbas et al. 2024). Metal-poor environments exhibit lower dust-to-gas ratios (Issa et al. 1990; Walter et al. 2007), which allow dissociating UV radiation to enter deeper into molecular clouds, as dust shielding is reduced. This affects the star formation activity in dense clumps, possibly reducing the star formation efficiency at low metallicity (Tanaka et al. 2018; Fukushima et al. 2020), and impacting the structure of giant molecular clouds (Maloney & Black 1988; Elmegreen 1989; McKee 1989; Rubio et al. 1993; Papadopoulos et al. 2002; Pelupessy et al. 2006; Bolatto et al. 2008; Leroy et al. 2009; Hughes et al. 2010; Chevance et al. 2016; Jameson et al. 2018). Low-metallicity environments also seem to experience a lower degree of fragmentation (Omukai et al. 2005, 2010; Walch et al. 2011; Glover & Clark 2012c; Corbett Moran et al. 2018; Bate 2019; Whitworth et al. 2022). Therefore, metallicity could have an effect on the galaxy-wide stellar initial mass function (Jeřábková et al. 2018; Sharda et al. 2023; Bate 2025).

Stellar feedback is an important source of energy and momentum to modulate star formation in the ISM, and this is affected in part by metallicity. For example, metal-poor stars are brighter and hotter than metal-rich ones with the same initial mass. Metal-poor massive stars have less wind mass loss (Maeder & Meynet 2000), resulting in a slower chemical enrichment of the ISM and weaker stellar winds. In addition, for massive stars, metallicity can influence the ratio of blue to red supergiants (Langer & Maeder 1995), and determine their final fate (Heger et al. 2003). All of these effects together will modify the impact of stellar feedback on the ISM.

We can find metal-poor environments on several scales and cosmic distances from us. For instance, massive star-forming disc galaxies, including the Milky Way, show different metallicity gradients along the galactocentric radius (Aller 1942; Searle 1971; Shaver

---

* E-mail: brugaletta@ph1.uni-koeln.de

et al. 1983; Balser et al. 2011; Belfiore et al. 2017; Méndez-Delgado et al. 2022; Piatti 2023; Sextl et al. 2024). At large radii, a negative metallicity gradient with increasing galactocentric radius is observed to be almost exponential (Wyse & Silk 1989; Zaritsky 1992). Therefore, disc galaxies host more low-metallicity gas in their outskirts. In the case of our Galaxy, Lian et al. (2023) report that the integrated stellar metallicity profile in the Milky Way shows a positive gradient between the centre and 6.9 kpc, with a slope of 0.031 ± 0.010 dex kpc^{-1}, and a negative gradient from 6.9 kpc to the edge, with a slope of -0.052 ± 0.008 dex kpc^{-1}. Less massive galaxies, however, can have flatter gradients (see e.g. Mingozzi et al. 2020; Ju et al. 2025). Additionally, low mass galaxies are known to be metal-poor environments according to the mass-metallicity relationship (Tremonti et al. 2004). Metal-poor environments are also characteristic of high-redshift galaxies, where the chemical enrichment owing to the presence of a stellar population had less time to pollute the ISM with metals (Savaglio et al. 2005). With the launch of JWST, low mass galaxies have raised general interest, as we are now able to observe them with unprecedented resolution, allowing us to better investigate metal-poor environments (e.g. Cameron et al. 2023; Curti et al. 2023; Heintz et al. 2023; Tacchella et al. 2023; Doan et al. 2024).

A complete theoretical study by means of simulations of the multiphase ISM in metal-poor environments, involving a detailed description of the stellar feedback (in the form of stellar winds, supernovae, radiation and cosmic rays), has not yet been performed. Kim et al. (2024) have run simulations similar to ours, for a range of metallicities, however they focus more on the validity of their dynamical equilibrium theory for star formation. We aim to fill this gap by providing state-of-the-art simulations of representative parts of the ISM of a galaxy with the same initial conditions except for the gas metallicity and the gas-to-dust mass ratio.

We discuss seven different initial metallicities representative of the solar neighbourhood, a randomly selected patch of the Milky Way (MW), the Large and Small Magellanic Clouds (LMC, SMC, respectively), the irregular dwarf galaxy Sextans A, the globular cluster NGC1904, and the blue compact dwarf galaxy I Zwicky 18 (I Zw 18). In particular, metallicities comparable to those of the LMC and SMC environments are useful because of the richness of observational studies to which we can compare our results. The Magellanic Clouds have been the subject of numerous studies regarding their structure and the kinematics of the gas (e.g. van der Marel 2006; Fujii et al. 2014; Weiß et al. 2023; Grishunin et al. 2024 for the LMC, Goldman 2007; Jameson et al. 2018; Smart et al. 2019; Murray et al. 2019 for the SMC), their star formation history (e.g. Baumgardt et al. 2013; Meschin et al. 2013 for LMC, Sabbi et al. 2009; Rubele et al. 2009; Ramachandran et al. 2019 for SMC), and the episodes of star formation triggered by the interaction between the two (Bekki et al. 2004).

On the other hand, the dwarf galaxy I Zwicky 18 (Zwicky 1966) is one of the most metal-poor galaxies in our surroundings, with a distance of around 18 Mpc (Aloisi et al. 2007; Contreras Ramos et al. 2011; Musella et al. 2012). The structure of this galaxy has been analysed by Dufour et al. (1996), who found a secondary partner associated with the main body of I Zwicky 18. Contreras Ramos et al. (2011) suggest that the very low metallicity of I Zwicky 18 could be explained by the accretion of primordial or very metal-poor gas, which diluted its ISM, or the removal of metals due to galactic winds. Moreover, the nature of its star formation history has been debated. Garnett et al. 1997; Legrand 2000; Legrand et al. 2001 assume a continuous and low star formation rate for a time equal to the Hubble time, to explain the observed abundances. On the other hand, Aloisi et al. 1999 claim that there has also been starburst activity in addition to a continuous star formation phase. Bortolini et al. (2024) observe the presence of stars of all ages; however, they agree on the low star formation rate scenario for epochs older than 1 Gyr, which could be the origin of its low metal abundance.

The structure of our paper is as follows. In Section 2, the numerical methods and the setup of the simulations are described. Our results are analysed in Sec. 3, and we discuss the main caveats of our work in Sec. 4. Finally, our summary and conclusions can be found in Sec. 5.

2 NUMERICAL METHODS AND SIMULATION SETUP

To describe the structure and evolution of the low-metallicity ISM, we perform magnetohydrodynamic (MHD) simulations with the adaptive mesh refinement code Flash version 4.6 (Fryxell et al. 2000; Dubey et al. 2008; Dubey et al. 2009). The setup generally follows the stratified box simulations carried out in the SILCC Project (Walch et al. 2015; Girichidis et al. 2016a; Gatto et al. 2017; Peters et al. 2017; Girichidis et al. 2018b; Rathjen et al. 2021, 2023, 2025; Brugaletta et al. 2025), which we briefly describe below.

2.1 Structure

Our simulation domain is an elongated box with size 500 pc × 500 pc × ± 4 kpc, which represents a small portion of a galaxy centered around the galactic midplane. The region is assumed to be far away from a central black hole. Due to the vertical elongation, we may study the development of outflows from the galactic disc. To better resolve the evolution of the gas near the midplane, where massive stars are forming, we fix our resolution Δx to be uniform and equal to around 3.9 pc for $|z| < 1$ kpc, and up to 7.8 pc for $|z| > 1$ kpc. We adopt periodic boundary conditions in the x- and y-directions, while we allow for outflow along the z-direction. However, the gas exiting the box in the z-direction is not allowed to fall back in.

The total gravity in our setup consists of four different contributions: an external static dark matter potential following the NFW dark-matter profile from Navarro et al. 1996, with $R_{\rm vir}$ = 200 kpc, distance from galactic centre R = 8 kpc and concentration parameter c = 12; an external static potential due to the presence of an old stellar population with stellar surface density $\Sigma_* = 30\ \mathrm{M_\odot\ pc^{-2}}$ and vertical scale height H_* = 300 pc; the self-gravity of the gas computed on-the-fly using the tree-based algorithm from Wünsch et al. 2018; and the gravity due to the presence of star cluster particles followed in the simulation (Dinnbier & Walch 2020).

At the beginning of each simulation the gas is distributed according to a Gaussian distribution centered on the midplane and with a scale height of 30 pc, assuming a gas surface density of 10 $\mathrm{M_\odot\ pc^{-2}}$. The Gaussian distribution is cut off at a height for which the disc density is equal to the uniform background density $\rho_{\rm b} = 10^{-27}\ \mathrm{g\ cm^{-3}}$.

We also employ a magnetic field oriented initially in the x-direction with a strength varying in the z-direction as

$$B_x(z) = B_{x,0}\sqrt{\rho(z)/\rho(z=0)}, \tag{1}$$

with $B_{x,0} = 6\ \mu$G and $\rho(z)$ the density at a height z from the midplane. To avoid sudden gravitational collapse at the beginning of the runs, we stir the gas for the first 20 Myr of evolution. This is achieved by injecting kinetic energy in the computational domain on the largest scale in the x- and y- directions, such that the mass-weighted root mean square of the velocity of the gas is 10 km s^{-1}.

2.2 MHD and cosmic rays

The evolution of the gas is modelled by solving the ideal MHD equations. We also add cosmic rays protons, which can propagate in the ISM via anisotropic diffusion and advection (Girichidis et al. 2016b, 2018a). For each supernova event (see Sec. 2.3), we inject 10% of its energy (10^{50} erg, Ackermann et al. 2013) in cosmic rays, which are treated as a separate relativistic fluid and are coupled to the MHD equations adding a pressure gradient and an additional energy source term $Q_{\rm cr}$. The latter takes into account the injection energy due to supernovae and the cooling of cosmic rays via hadronic and adiabatic losses (Pfrommer et al. 2017; Girichidis et al. 2020). The modified MHD equations read:

$$\frac{\partial \rho}{\partial t} + \nabla \cdot (\rho \boldsymbol{v}) = 0, \tag{2}$$

$$\frac{\partial \rho \boldsymbol{v}}{\partial t} + \nabla \cdot \left(\rho \boldsymbol{v}\boldsymbol{v}^T - \frac{\boldsymbol{B}\boldsymbol{B}^T}{4\pi} \right) + \nabla P_{\rm tot} = \rho \boldsymbol{g} + \dot{\boldsymbol{q}}_{\rm sn}, \tag{3}$$

$$\begin{aligned}\frac{\partial e}{\partial t} + \nabla \cdot \left[(e + P_{\rm tot})\boldsymbol{v} - \frac{\boldsymbol{B}(\boldsymbol{B}\cdot\boldsymbol{v})}{4\pi} \right] \\ = \rho \boldsymbol{v}\cdot\boldsymbol{g} + \nabla\cdot(\mathbf{K}\nabla e_{\rm cr}) + \dot{u}_{\rm chem} + \dot{u}_{\rm sn} + Q_{\rm cr},\end{aligned} \tag{4}$$

$$\frac{\partial \boldsymbol{B}}{\partial t} - \nabla \times (\boldsymbol{v} \times \boldsymbol{B}) = 0, \tag{5}$$

$$\frac{\partial e_{\rm cr}}{\partial t} + \nabla \times (e_{\rm cr}\boldsymbol{v}) = -P_{\rm cr}\nabla\cdot\boldsymbol{v} + \nabla\cdot(\mathbf{K}\nabla e_{\rm cr}) + Q_{\rm cr}, \tag{6}$$

with ρ the density, $\boldsymbol{B}$ the magnetic field, $\boldsymbol{v}$ the velocity of the gas, $P_{\rm tot} = P_{\rm thermal} + P_{\rm magnetic} + P_{\rm cr}$ the total pressure, with $P_{\rm cr}$ the pressure due to cosmic rays, $\boldsymbol{g}$ the gravitational acceleration, $e = \frac{\rho v^2}{2} + e_{\rm thermal} + e_{\rm cr} + \frac{B^2}{8\pi}$ the total energy density, $\dot{\boldsymbol{q}}_{\rm sn}$ the momentum input of unresolved SNe, $\boldsymbol{K}$ the cosmic ray diffusion tensor, $\dot{u}_{\rm chem}$ the change in thermal energy due to heating and cooling processes, $\dot{u}_{\rm sn}$ the thermal energy input from resolved supernovae, $Q_{\rm cr} = Q_{\rm cr,\,injection} + \Lambda_{\rm hadronic}$. The latter term is assumed to be (Pfrommer et al. 2017)

$$\Lambda_{\rm hadronic} = -7.44\,\times\,10^{-16} \times \left(\frac{n_e}{\rm cm^{-3}}\right) \times \left(\frac{e_{\rm cr}}{\rm erg\ cm^{-3}}\right)\ {\rm erg\ s^{-1}cm^{-3}}. \tag{7}$$

In the diffusion tensor we adopt constant diffusion coefficients of $K_\parallel = 10^{28}$ cm^2 s^{-1} parallel to the magnetic field lines and $K_\perp = 10^{26}$ cm^2 s^{-1} perpendicular to them (Strong et al. 2007; Nava & Gabici 2013).

2.3 Star formation and stellar feedback

We model star formation in our simulations assuming that stars can form in star clusters, which are treated as collisionless sink particles (Bate et al. 1995; Federrath et al. 2010; Gatto et al. 2017; Dinnbier & Walch 2020). To form a sink particle in a cell, the gas must be denser than a threshold density $\rho_{\rm sink} = 2 \times 10^{-21}$ g cm^{-3}, Jeans unstable, in a gravitational potential minimum, and found in a converging flow. Once a sink particle is created, for every 120 M$_\odot$ of gas accreted onto the sink, we form one massive star whose initial mass is randomly sampled in the interval 9–120 M$_\odot$ from a Salpeter-like IMF (Salpeter 1955). The remaining mass is assumed to form low-mass stars inside the cluster, which we consider only for their gravitational effects and for their far-ultraviolet (FUV) radiation. We do not form isolated massive stars unless sink accretion is really inefficient. We follow the evolution of individual massive stars employing the BoOST massive star model tracks (Brott et al. 2011; Szécsi et al. 2022) or the Geneva models (Ekström et al. 2012), as described in the following section.

During their lifetime massive stars shape the surrounding ISM via stellar feedback in the form of stellar winds, their radiation, supernova explosions, and cosmic rays. At the end of their lifetime all massive stars explode as Type II supernovae, injecting either energy or momentum into the ISM depending on the ambient density of the supernova. If the radius at the end of the Sedov-Taylor phase can be resolved with at least three grid cells (corresponding to around 11.7 pc), thermal energy of 0.9×10^{51} erg is injected in a volume centred on the supernova and with a radius of three cells. Otherwise, the momentum at the end of the Sedov-Taylor phase is injected (see Kim & Ostriker 2015; Gatto et al. 2015; Naab & Ostriker 2017). The remaining mass of the progenitor is added to the mass already present in the injection region.

2.4 Stellar models

We use Geneva stellar tracks (Ekström et al. 2012) for our solar-metallicity model as done in previous works of the SILCC collaboration (e.g Gatto et al. 2017; Rathjen et al. 2021, 2023, 2025). For all our subsolar-metallicity runs we employ the stellar models for single, slowly rotating massive stars from the BoOST project version 1.3 (Brott et al. 2011, Szécsi et al. 2022).

For FLASH, we provide input data consisting of the time evolution of the effective temperature, bolometric luminosity, mass loss rate, and wind terminal velocity for 112 models for each metallicity. These models cover an initial mass range from 9 to 120 M$_\odot$ with increments of 1 M$_\odot$. The BoOST models describe the evolution of massive stars from the Zero-Age Main Sequence (ZAMS) until the core-helium depletion, whereas the Geneva models also include the core-carbon-burning phase, which does not affect considerably the duration of the lifetimes of the models. In Appendix A we analyse the parameters that mainly influence the stellar feedback in our simulations, such as the lifetime of stellar models, their wind and bolometric luminosities, and the fraction of ionising radiation for both Geneva and BoOST stellar models.

2.5 Shielding and ionising radiation with TreeRay

To treat the (self-)shielding of the gas by dust and molecules, as well as the radiation transport of extreme ultraviolet (EUV) radiation from massive stars, we employ the TreeRay module (Wünsch et al. 2018, 2021), which makes use of the octal tree already used by the gravity solver. TreeRay creates a HEALPix sphere (Górski et al. 2005) with (in this work) 48 pixels around the center of each cell and for all cells in the computational domain. Rays are cast through the centre of each HEALPix pixel, and the radiation transport, as well as the shielding column densities, are computed along these directions.

Using the TreeRay/OpticalDepth module, we compute the shielding column densities. TreeRay/OpticalDepth is based on the original TreeCol algorithm from Clark et al. (2012). The local visual extinction $A_{\rm V,3D}$ is computed as (Bohlin et al. 1978)

$$A_{\rm V,3D} = \frac{N_{\rm H,tot}}{1.87 \times 10^{21}\ {\rm cm^{-2}}} \times Z, \tag{8}$$

with $N_{\rm H,tot}$ the local 3D-averaged column density of the gas computed by TreeRay/OpticalDepth, and Z is the metallicity in units of solar metallicity $Z_\odot$.

To solve the radiation transport equation, all Lyman continuum photons ($E_\gamma > 13.6$ eV) are treated with the module TreeRay/OnTheSpot, a backward-propagating radiation transport scheme that makes use of the On-The-Spot approximation (Osterbrock 1988). In this method, the propagation of radiation is almost independent of the number of sources and each cell can be a source of radiation. We compute the fraction of ionising photons assuming the spectrum of each massive star to be a black body with a given effective temperature and integrating the black body spectrum for energies higher than 13.6 eV. For each timestep, the energy density of ionising radiation emitted by all stars within a given sink particle is injected into the cell where the sink is located. Hence, star cluster sink particles are sources of radiation. The FUV radiation emitted from massive and low-mass stars is approximated with a simpler method than TreeRay (see below, Sec. 2.6).

2.6 Chemistry, heating and cooling mechanisms

Comprehending how metallicity influences the evolution of the ISM is heavily dependent on our treatment of the heating and cooling processes. Many of them depend on the chemical abundances of metals, which in turn are given by the metallicity. We compute these processes on-the-fly using a chemical network based on Nelson & Langer (1997) and Glover & Mac Low (2007a,b), which calculates the non-equilibrium abundances of seven species: H, H^+, H_2, CO, C^+, O, and free electrons. We assume fixed, metallicity-dependent elemental abundances for C, O, and Si, for which we adopt the values of $x_{\rm C} = 1.4 \times 10^{-4}$, $x_{\rm O} = 3.2 \times 10^{-4}$, $x_{\rm Si} = 1.5 \times 10^{-5}$ (Sembach et al. 2000) at solar metallicity. For sub-solar metallicities, we linearly scale these values with Z. This implies that the ratio of the gas-phase metals to the total amount of metals is metallicity-invariant, as we do not consider depletion onto dust.

We assume that H_2 can only form on the surface of dust grains (Hollenbach & McKee 1989), neglecting gas phase formation through the H^- and H_2^+ ions and the three-body channel (Glover 2003), which becomes important at high gas densities (Palla et al. 1983) and lower metallicities than those treated in this work (Omukai et al. 2005). The dominant process that destroys H_2 is photodissociation by the interstellar radiation field (ISRF), although the model also accounts for collisional dissociation of H_2 in hot gas.

Regarding cooling processes, if the temperature of the gas is higher than 10^4 K we assume collisional ionisation equilibrium for helium and metals, and use the tabulated cooling rates from Gnat & Ferland 2012. Cooling from atomic hydrogen is always calculated using the non-equilibrium H and e^- abundances provided by the chemical model. At lower temperatures, we also account for cooling from a number of other processes, including the fine structure lines of C^+ and O, and the rotational and vibrational lines of H_2, as described in more detail in Glover & Clark (2012b). Concerning heating processes, we include, among others, photoelectric heating (PE) by dust grains and heating due to low-energy cosmic rays.

PE heating is variable in space and time and is modelled using the new AdaptiveG0 module from Rathjen et al. (2025). We computed the intensity of FUV radiation from each star cluster by integrating the black body spectrum of each massive star and at each timestep in the range of 6 – 13.6 eV, plus employing Starburst99 single-stellar population synthesis models for all low-mass stars in the cluster sink. The total FUV radiation emitted by each cluster sink i is called $G_{\rm cluster,i}$ and given in units of the Habing field (Habing 1968). The local, unattenuated FUV field in each grid cell, G_0, is then obtained by summing up the contributions from all sources within a maximum distance of 50 pc from the cell

$$G_0 = \sum_i G_{\rm cluster} \times R_i^{-2}, \tag{9}$$

with R_i the distance of the star cluster i from the cell of interest and the inverse square law is applied. We then apply a background ISFR $G_{\rm bg} = 0.0948$ to the computed G_0 as done in Rathjen et al. (2025). The G_0 field is also attenuated by dust to obtain the effective ISRF $G_{\rm eff}$ for each cell:

$$G_{\rm eff} = G_0 \times \exp(-2.5 A_{\rm V,3D}). \tag{10}$$

The PE heating rate is computed as (Bakes & Tielens 1994; Bergin et al. 2004),

$$\Gamma_{\rm pe} = 1.3 \times 10^{-24} \epsilon G_{\rm eff} n d \; [\rm erg\ s^{-1} cm^{-3}], \tag{11}$$

where

$$\epsilon = \frac{0.049}{1 + (\psi/963)^{0.73}} + \frac{0.037 (T/10^4)^{0.7}}{1 + (\psi/2500)}, \tag{12}$$

with

$$\psi = \frac{G_{\rm eff} T^{0.5}}{n_e}, \tag{13}$$

with n the number density of hydrogen nuclei, d the dust-to-gas mass ratio in per cent, with $d = 1$ (1 per cent) in solar-neighbourhood conditions, T the temperature of the gas, and n_e the electron number density. This prescription of the PE heating is valid in solar-neighbourhood conditions, however, we extend it to metal-poor environments for simplicity. This approximation may break at the lowest metallicities that we treat in our work, as the abundance of polycyclic aromatic hydrocarbons (PAHs) seems to experience a superlinear drop with decreasing metallicity (Draine et al. 2007; Sandstrom et al. 2012; Whitcomb et al. 2024). Since PAHs contribute substantially to the total PE heating rate, the real PE heating rate could be smaller than the value obtained in Eq. 11.

Regarding cosmic ray heating, we employ the new method developed by Brugaletta et al. (2025), where the CR ionisation rate, ζ, is computed scaling the local energy density of CRs, which is already computed by our CR-MHD solver. If the column density of the gas, $N_{\rm H,tot}$, is lower than a threshold value $N_{\rm H,thresh} = 10^{20}$ cm^{-2}, we scale ζ linearly with the energy density of CRs, $e_{\rm cr}$, following

$$\zeta = 3 \ \times 10^{-17} \left(\frac{e_{\rm cr}}{1 \ {\rm eV\ cm^{-3}}} \right) {\rm s^{-1}}. \tag{14}$$

If $N_{\rm H,tot} > N_{\rm H,thresh}$, we multiply the linear scaling of Eq. 14 by the attenuation factor

$$c_{\rm att} = (N_{\rm H,tot}/N_{\rm H,thresh})^{-0.423}, \tag{15}$$

where the exponent is given by Padovani et al. (2009), who obtained it for the spectrum of protons and heavy nuclei, and considered the H_2 column density rather than the total column density. Since no equivalent is provided for the atomic gas column density, we apply the prescription from Padovani et al. (2009, 2022) obtained for the H_2 column density using the H column density instead. Given the small amount of H_2 formed at the low metallicities of this work, we would underestimate the CR attenuation when only using the H_2 column density. With this choice, we suppose that our estimate of the CR attenuation is around a factor of 2 (Glassgold & Langer 1974) different compared to the attenuation shown in Fig. C1 in Padovani et al. (2022).

The rate for CR heating is computed assuming that each ionisation

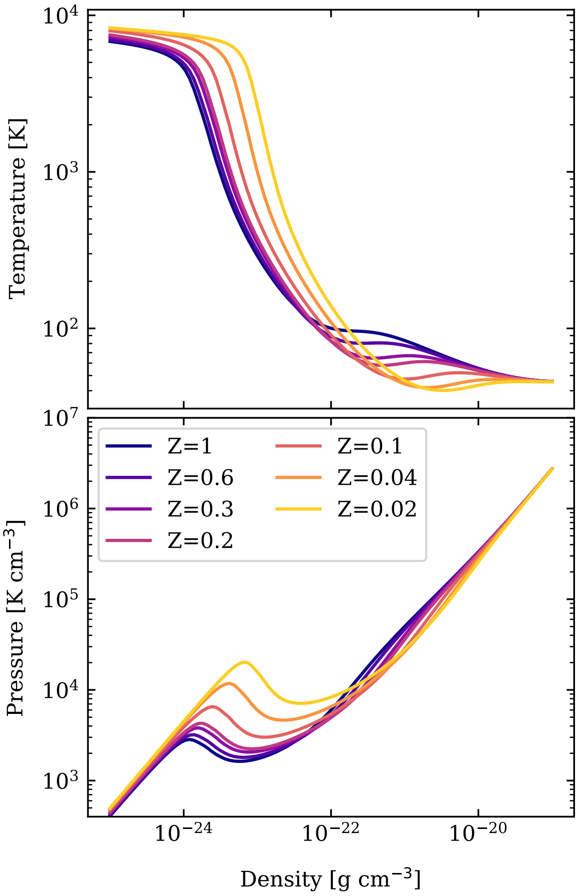

Figure 1. Equilibrium temperature (upper panel) and pressure (bottom panel) as a function of the gas density, for every metallicity analysed in this work. These equilibrium curves are computed using our chemical network without considering the self-shielding of H_2 and CO, assuming a constant external hydrogen column density $N_{\mathrm{H,\,tot}} = 10^{20}$ cm^{-2}, a constant $G_0 = 1.7$ and a constant $\zeta = 3 \times 10^{-17}$ s^{-1}.

deposits 20 eV as heat, following the prescription from Goldsmith & Langer (1978),

$$\Gamma_{\mathrm{cr}} = 20\,\zeta\,(n_{\mathrm{H_2}} + n_{\mathrm{H}}) \quad [\mathrm{eV\ s^{-1}cm^{-3}}]$$
$$= 3.2 \times 10^{-11} \zeta (n_{\mathrm{H_2}} + n_{\mathrm{H}}) \quad [\mathrm{erg\ s^{-1}cm^{-3}}], \qquad (16)$$

where $n_{\mathrm{H_2}}$ is the number density of H_2 and n_{H} is the number density of H.

2.7 The low-metallicity ISM

In this section, we briefly describe the thermal structure of the ISM at solar metallicity and discuss how it changes in metal-poor environments. For a more detailed treatment of all relevant heating and cooling processes, the reader can refer to Wolfire et al. (1995); Glover & Mac Low (2007a,b); Glover & Clark (2014); Bialy & Sternberg (2019), and Sec. 2.6. Here we compute the equilibrium curves (see Fig. 1) corresponding to the conditions of the gas simulated in our runs using our chemical network for a single cell evolving for 1 Gyr, after which the gas has surely reached thermal and chemical equilibrium. For this test, we assume an optically thin gas with $A_{\mathrm{V,3D}} = 0$, $G_0 = 1.7$ and $\zeta = 3 \times 10^{-17}$ s^{-1} and neglect any self-shielding due to surrounding H_2 and CO. Note that all these parameters are locally variable in the 3D simulations.

If we consider for now only the equilibrium curve at solar metallicity (dark violet line in Fig. 1), we notice that for a density lower than 10^{-24} g cm^{-3} the temperature remains almost constant. In fact, for densities below 10^{-24} g cm^{-3}, the PE heating is balanced by the Lyα cooling, which is a strong function of the temperature. In this regime, the Lyα cooling rate slowly increases with increasing density and, correspondingly, the gas temperature slowly decreases to balance the almost constant heating rate. This is why the equilibrium temperature for densities below 10^{-24} g cm^{-3} does not vary significantly. Note that this is different in the 3D simulations, where shock heating dominates this density regime (see e.g. Hu et al. 2016).

For a threshold density of around 10^{-24} g cm^{-3} the Lyα cooling becomes comparable to the metal (C^+, O) fine-structure line cooling, which dominates for higher densities (Dalgarno & McCray 1972). In this regime, we observe a steep drop in temperature, which is due to the weak dependency of the C^+ and O fine structure cooling rates on temperature. In fact, when the density increases, the metal cooling rates increase as well; as a result, heating and cooling balance at a significantly lower temperature (Field et al. 1969). The temperature drop occurs just after the local pressure peak shown in the bottom panel of Fig. 1.

At a density of around 10^{-22} g cm^{-3}, corresponding to an equilibrium temperature of $\sim 10^2$ K, the curve slightly flattens again because metal line cooling becomes exponentially dependent on temperature. For higher densities, H_2 formation heating becomes important, increasing the equilibrium temperature. This effect is strongly seen here because we compute the equilibrium curves without H_2 self-shielding. In a real cloud, the gas would be almost fully molecular at these densities; therefore the H_2 formation heating could be less important than what we find here. For even higher densities, the conversion of atomic to molecular hydrogen suppresses the H_2 heating, as this is efficient in atomic gas (Bialy & Sternberg 2019), causing the drop for densities higher than 10^{-21} g cm^{-3}.

With decreasing Z, the equilibrium curves are shifted to higher temperatures at the same density, or analogously they shift towards higher pressures. In our approach, the dust-to-gas ratio scales linearly with the metallicity, meaning that the PE heating rate and the metal cooling rate scale in the same way. However, as the importance of PE heating decreases for metal-poor gas, CR heating becomes increasingly important because it does not depend on metallicity (Kim et al. 2023, Brugaletta et al. 2025). Therefore, the cooling and heating rates are balanced at a higher temperature, for constant ζ, than in solar-neighbourhood conditions.

2.8 Simulation parameters

We run seven different simulations with Z between 0.02 – 1 $Z_\odot$ (see Table 1). The chosen values for the gas metallicity in our runs follow the availability of stellar models with the same initial metallicity (see Sec. 2.4). Since no stellar models with solar metallicity are provided within BoOST, we run the solar-metallicity run, i.e. run Σ010-Z1, employing the Geneva tracks from Ekström et al. (2012). We use almost identical initial conditions, such as a constant gas surface density of 10 $M_\odot$ pc^{-2}, except for those parameters affected by metallicity. We change the initial metallicity of the gas by linearly scaling the carbon, oxygen and silicon abundances as well as the dust-to-gas mass ratio (see Sec. 2.6). Overall, the names of the runs listed in the first column of Table 1, indicate the simulated metallicity in units of solar metallicity. We note that run Σ010-Z0.02 has been presented in Brugaletta et al. 2025, where it was called run Z0.02-

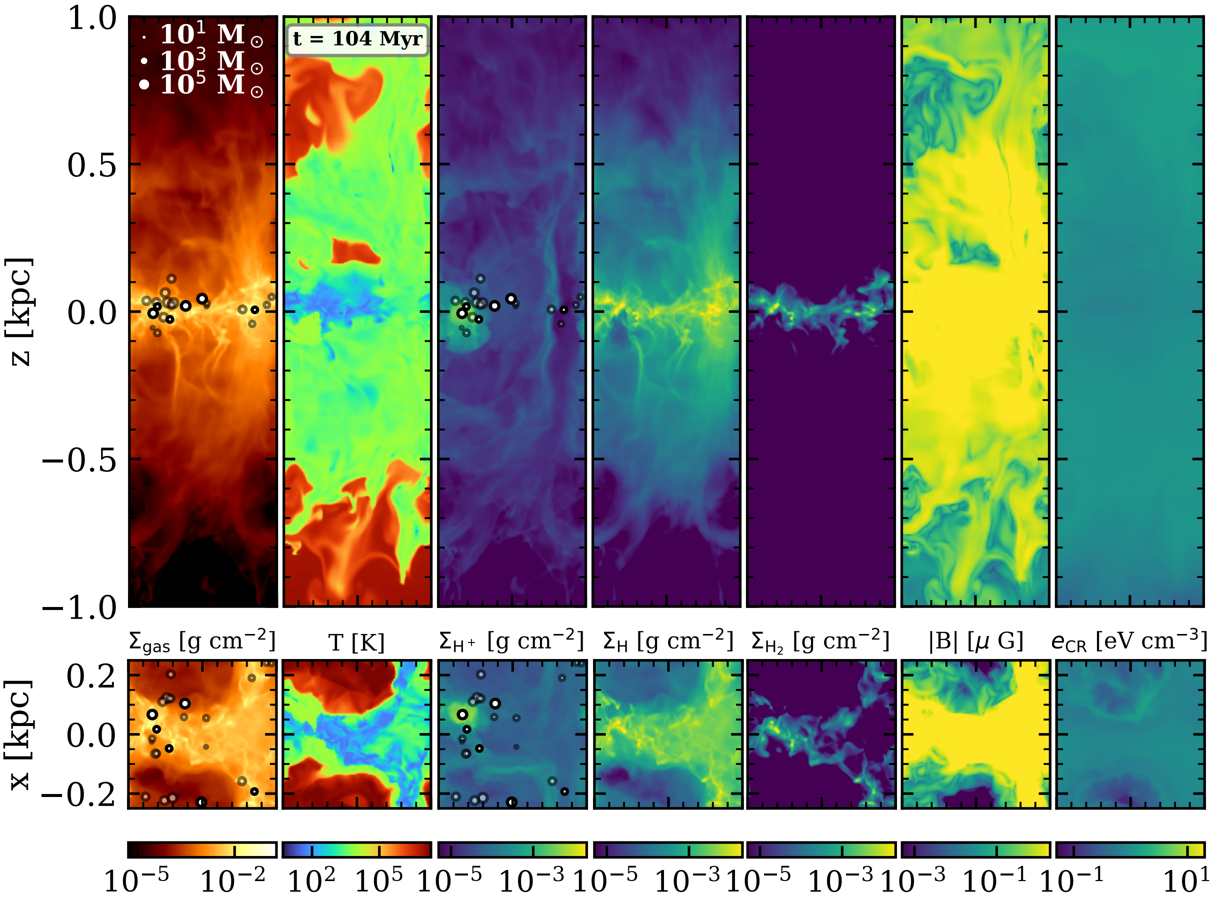

Figure 2. Snapshot of the Σ010-Z0.2 run at $t = 104$ Myr. The top row represents an edge–on view of the simulation box, the bottom squares show the corresponding face–on views. From left to right we depict the total gas column density Σ_{gas} (projection), the temperature T (slice), the column densities of H^+, H, and H_2 (projections), the magnetic field strength B (slice), and the energy density of CRs e_{CR} (slice). The top elongated panels show only a part of the box (1 kpc around the midplane instead of 4 kpc). All slices are taken at $y = 0$ (upper panels), and $z = 0$ (bottom panels). The projections are computed along the y-axis (upper panels) or along the z-axis (bottom panels), respectively. The white circles in the first and third panel represent the active star clusters, whereas the transparent circles represent star clusters that are no longer active. The stellar feedback due to the presence of star clusters shapes the structure and governs the evolution of the multiphase ISM.

Table 1. List of the performed simulations. The main parameter is the initial gas metallicity, Z_{gas}, according to which we rescale the abundances of C, O, and Si relative to hydrogen and the dust-to-gas ratio as seen in Sec. 2.6. The metallicity of the stars in the stellar tracks is Z_{stars}, and it has been obtained from Table 1 in Szécsi et al. (2022) and dividing by 0.014 (Asplund et al. 2009). Note that we presented the Σ010-Z0.02 run in Brugaletta et al. 2025 in greater detail.

Run name	Z_{gas} [$Z_\odot$]	Z_{stars} [$Z_\odot$]	Object with comparable Z	Stellar models
Σ010-Z1	1	1	Solar neighbourhood	Geneva
Σ010-Z0.6	0.63	0.63	Milky Way	BoOST
Σ010-Z0.3	0.34	0.34	Large Magellanic Cloud	BoOST
Σ010-Z0.2	0.24	0.15	Small Magellanic Cloud	BoOST
Σ010-Z0.1	0.10	0.075	Sextans A or NGC 362	BoOST
Σ010-Z0.04	0.04	0.03	NGC 1904	BoOST
Σ010-Z0.02	0.02	0.015	I Zwicky 18	BoOST

vG_0-vζ. For simplicity and because we use a variable FUV and cosmic ray ionisation rate in all runs presented here, we shorten the name of this simulation.

3 RESULTS

3.1 Qualitative evolution

In the beginning of our simulations, we stir turbulence in the gas to avoid a fast collapse towards the midplane that would generate an unphysical starburst. As described in Sec. 2, the initial stirring is applied for the first 20 Myr and influences the local conditions for the formation of the first stars. As overdense regions are formed, stars form in accreting star cluster sink particles.

As soon as massive stars are born, they start shaping the ISM via their stellar winds and ionising radiation that leads to the formation of expanding H II regions. At the end of their life, all massive stars are assumed to explode as Type II supernovae, injecting energy or momentum and CRs into the ISM. The combined explosion of several supernovae distributed in different star clusters residing near the midplane dramatically shapes the ISM creating superbubbles and launching outflows from the disc. Galactic fountains and outflows remove gas mass available for new star formation near the disc midplane, slowing down the star formation rate. When the majority of the formed stars have exploded and new star formation proceeds at a lower rate, the outward force exerted on the gas by stellar feedback weakens, until it stops pushing the gas in the vertical direction. Subse-

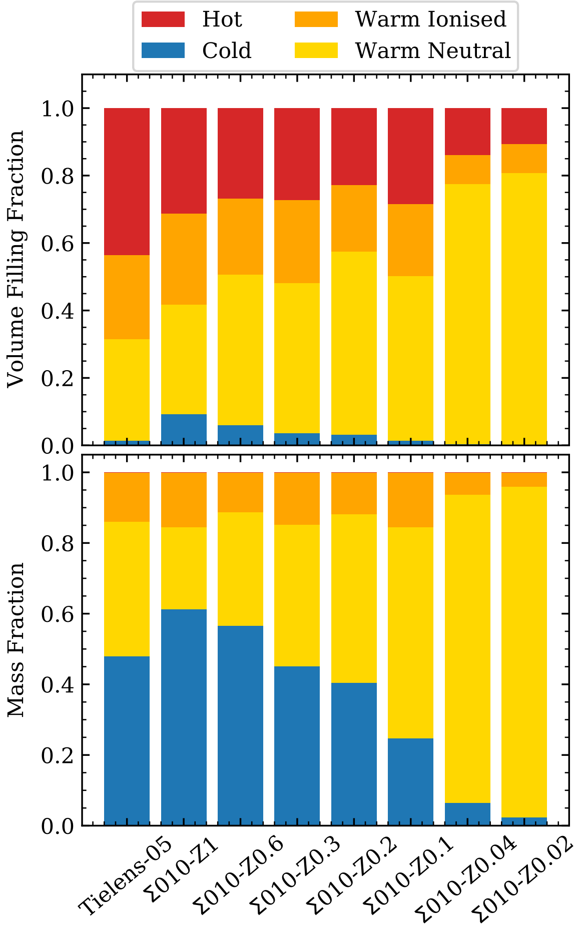

Figure 3. Volume-weighted average filling fraction (top) and average mass fraction (bottom) for the different gas phases defined in the text. The averages are computed in the 200 Myr period after the beginning of star formation, in the region where $|z| < 250$ pc. We note that the warm gas occupies around 50% or more of the volume, and constitutes a large fraction of the gas mass, especially at low metallicity. The hot gas volume filling fraction shows a correlation with metallicity, whereas the cold gas volume and mass fractions decrease for lower metallicity. We add the values measured by Tielens (2005) in the Solar neighbourhood as a comparison.

quently, the gas that is not unbound can fall back onto the midplane because of the overall gravity of the disc and reforms a reservoir for future star formation. This cycle continues until one eventually runs out of gas (far beyond the simulated time). A snapshot of run Σ010-Z0.2 at a time of 104 Myr can be seen in Fig. 2.

3.2 Gas phases

We distinguish four different gas phases, following the definitions already adopted in Walch et al. 2015; Gatto et al. 2017; Rathjen et al. 2021, 2023, 2025; Brugaletta et al. 2025 (here we omit the definition of molecular gas):

- $T \leq 300$ K : cold gas (CM);
- $300 < T < 3 \times 10^5$ K and H mass fraction above 50%: warm neutral medium (WNM);
- $300 < T < 3 \times 10^5$ K and H^+ mass fraction above 50%: warm ionised medium WIM;
- $T \geq 3 \times 10^5$ K: hot gas.

The presence of hot gas is mainly due to supernovae that (overlap to) heat the gas, whereas stellar winds, radiation, and CRs influence the amount of warm gas (Naab & Ostriker 2017; Rathjen et al. 2021).

We compute the volume-weighted average volume filling fractions (VFF) and mass fractions (MF) of the three phases for each run, as shown in Fig. 3 and reported in Table 2. To reduce the impact of our initial conditions, we compute these averages in a time interval [$t_{\rm SF}$, $t_{\rm SF}$ + 200 Myr], with $t_{\rm SF}$ being the time at which the first star is born (see Table 5), and inside the region $|z| < 250$ pc. For a comparison, we provide the VFFs and/or MFs of the gas phases as reported by Draine (2011) and Tielens (2005) for solar-neighbourhood conditions in Table 2, and we add the values from Tielens (2005) in Fig. 3.

The warm gas phase (neutral plus ionised) overall dominates the VFF, contributing more than 50% of the total volume (top panel of Fig. 3). The VFF of the WNM is similar for runs with $Z \geq 0.1$ Z$_\odot$, but it reaches up to 70 – 80% for runs Σ010-Z0.04 and Σ010-Z0.02. Its MF increases with decreasing metallicity, going from 23% at solar metallicity to 97% at 0.02 Z$_\odot$. On the other hand, the VFF of the WIM is around 20 – 27% for the runs with $Z \geq 0.1$ Z$_\odot$, but it is around 8% in the Σ010-Z0.04 and Σ010-Z0.02 runs. A similar trend is seen for its MF, which is around 11 – 15% for $Z \geq 0.1$ Z$_\odot$ and below 7% for the two most metal-poor runs. This trend can be explained in relation the results of Sec. 3.6. Metal-poor runs form fewer stars; therefore, the total amount of radiation emitted by star clusters is lower than in metal-rich runs, despite metal-poor stars having a higher surface temperature, leading to a lower VFF of the WIM. Therefore, even though the fraction of energy emitted in the EUV increases with decreasing metallicity, as shown in Fig. A3, the effect of having a reduced star formation rate dominates.

The hot phase occupies around 10 – 30% of the volume around the midplane, depending on the metallicity. Since the presence of the hot phase is connected to the presence of supernovae, the decrease of the hot phase VFF with decreasing metallicity is partly linked to the lower number of supernovae present in the low-metallicity runs (see Sec. 3.7). The hot gas MF is negligible (less than 1%), since the hot gas is very diffuse, with densities typically around 10^{-28} – 10^{-27} g cm^{-3}.

The CM occupies only a few per cent of the total volume, about 0.05 – 9%, scaling with the metallicity. Its MF dominates at metallicities higher than 0.3 Z$_\odot$, with an average mass fraction in the range 56 – 61.2%, showing a positive correlation with metallicity. This is due to more efficient cooling at higher Z. Here we notice that in the Σ010-Z1 run the MF of the CM is higher than the MF of the CM reported by Tielens (2005) by around 13%. Moreover, the VFF of the CM in the Σ010-Z1 run is around 9 times higher than the value measured by Tielens (2005). The reason for these discrepancies could be attributed to our new treatment of the CR heating, since having a variable ζ allows the gas to reach very low values of around $\zeta \sim 10^{-20}$– 10^{-19} s^{-1} (see Sec. 3.7.2), which triggers the formation of cold gas, instead of the typical value of 3×10^{-17} s^{-1} (see Sec. 2.7). Moreover, the presence of diffuse cold gas at solar metallicity (see Fig. 3.4, Rathjen et al. 2025) can explain the higher VFF of the cold gas. In the Σ010-Z0.02 run we get cold gas only due to our variable CR ionization rate (see Brugaletta et al. 2025).

3.3 Temperature-density and pressure-density phase diagrams

In this section, we analyse the temperature and pressure distributions as a function of density. In Fig. 4 we present the temperature-density (left column) and pressure-density (right column) phase diagrams, computed in a region $|z| < 250$ pc, for all our simulations at a time at which the presence of the H II regions (at around 10^4 K) is mostly

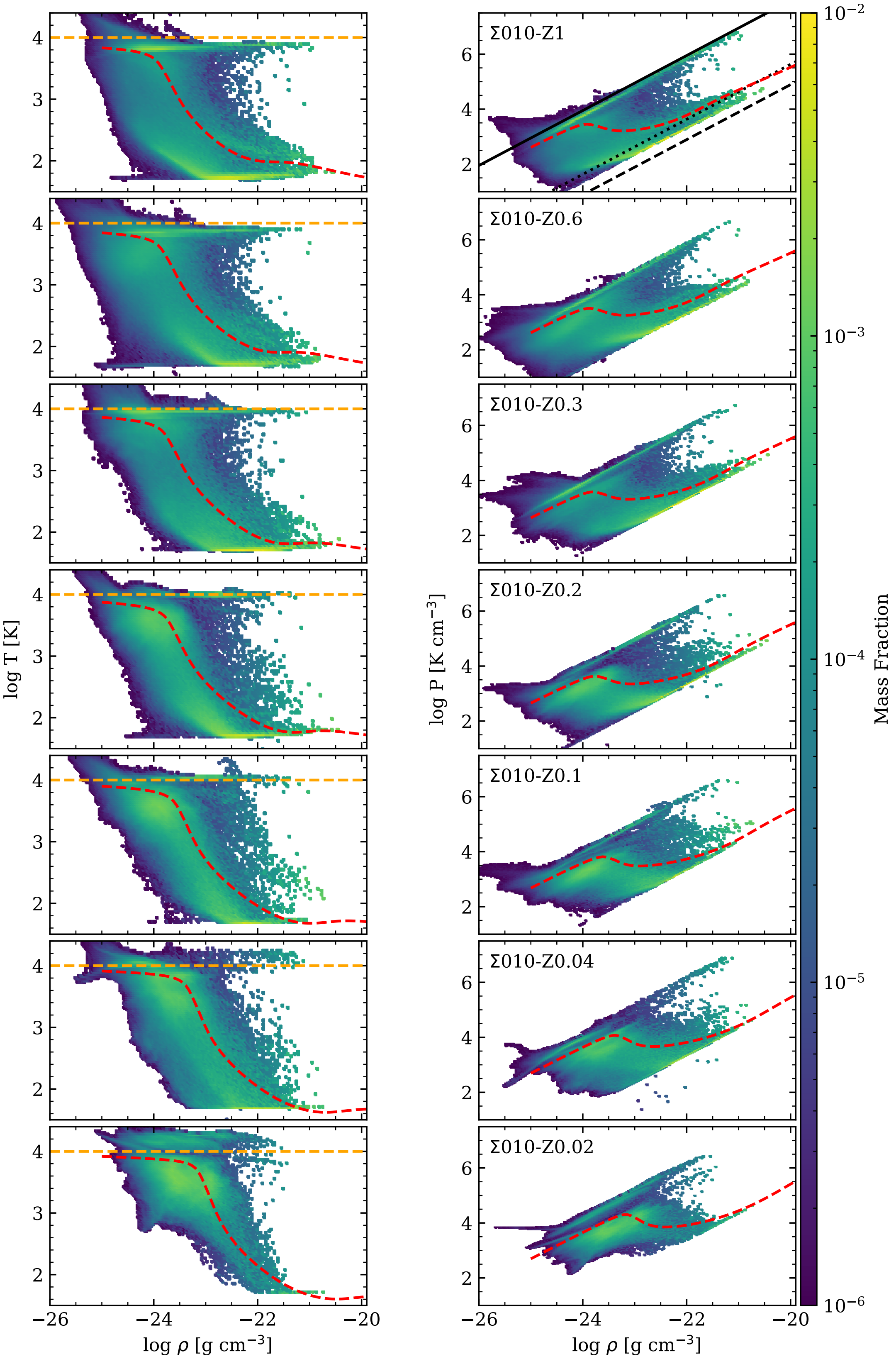

Figure 4. Temperature-density (left column) and pressure-density (right column) phase diagrams of all our simulations, at a time in which the H II region branch is most visible in every run. From top to bottom, the metallicity goes from 1 to 0.02 $Z_\odot$, and the selected snapshots are at simulation times t = 45.3, 68.4, 43.1, 104.5, 72.4, 52.2, 45.3 Myr, respectively. We take into consideration the region $|z| < 250$ pc. We overplot the unshielded equilibrium curves (red dashed lines) from Fig. 1, computed assuming $G_0 = 1.7$ and $\zeta = 3 \times 10^{-17}$ s^{-1}, and a (orange dashed) line corresponding to T = 10^4 K in the left column. In the pressure panel for Σ010 we add black isothermal lines corresponding to 10^4 K (solid), 100 K (dotted), 30 K (dashed). The presence of the two-phase medium is less evident at low Z due to the lack of cold gas.

Table 2. Average volume filling fractions ($\overline{\mathrm{VFF}}$) and average mass fractions ($\overline{\mathrm{MF}}$) for all gas phases. The values are computed in the time interval [t_{SF}, t_{SF} + 200 Myr]. We add the values reported from Draine 2011 and Tielens 2005 for solar-neighbourhood conditions.

Run	$\overline{\mathrm{VFF}}_{\mathrm{cold}}$ [%]	$\overline{\mathrm{VFF}}_{\mathrm{WNM}}$ [%]	$\overline{\mathrm{VFF}}_{\mathrm{WIM}}$ [%]	$\overline{\mathrm{VFF}}_{\mathrm{hot}}$ [%]	$\overline{\mathrm{MF}}_{\mathrm{cold}}$ [%]	$\overline{\mathrm{MF}}_{\mathrm{WNM}}$ [%]	$\overline{\mathrm{MF}}_{\mathrm{WIM}}$ [%]	$\overline{\mathrm{MF}}_{\mathrm{hot}}$ [10^{-2} %]
Draine	1	40	10	50	-	-	-	-
Tielens-05	1.05	30	25	~50	48	38	14	-
Σ010-Z1	9.3 ± 0.1	32.5 ± 0.4	27.1 ± 0.4	31.2 ± 0.4	61.2 ± 0.3	23.2 ± 0.2	15.6 ± 0.3	4.3 ± 0.1
Σ010-Z0.6	6.1 ± 0.1	44.6 ± 0.5	22.5 ± 0.3	26.8 ± 0.4	56.6 ± 0.3	32.1 ± 0.3	11.2 ± 0.2	5.4 ± 0.1
Σ010-Z0.3	3.6 ± 0.1	44.4 ± 0.5	24.7 ± 0.4	27.3 ± 0.4	45.1 ± 0.3	40.0 ± 0.3	14.8 ± 0.3	5.6 ± 0.1
Σ010-Z0.2	3.2 ± 0.1	54.4 ± 0.7	19.7 ± 0.3	22.8 ± 0.5	40.4 ± 0.3	47.7 ± 0.3	11.9 ± 0.3	6.1 ± 0.2
Σ010-Z0.1	1.4 ± 0.1	48.9 ± 0.7	21.2 ± 0.5	28.5 ± 0.6	24.8 ± 0.4	59.7 ± 0.5	15.5 ± 0.5	5.2 ± 0.1
Σ010-Z0.04	0.3 ± 0.1	77.2 ± 0.8	8.5 ± 0.4	13.9 ± 0.6	6.5 ± 0.3	87.1 ± 0.5	6.4 ± 0.4	2.2 ± 0.1
Σ010-Z0.02	0.05± 0.01	80.7 ± 0.4	8.7 ± 0.2	10.6 ± 0.3	2.3 ± 0.1	93.6 ± 0.2	4.0 ± 0.2	0.87 ± 0.04

visible by eye, and we overplot the unshielded equilibrium curves from Fig. 1. We also add a line indicating a temperature $T = 10^4$ K. Regarding the temperature-density plots, we choose a temperature range in the y-axis that highlights the warm and cold gas phases already defined in Sec. 3.2 for all our runs. It can be observed that, with decreasing metallicity, the presence of the two-phase medium (warm and cold gas) becomes less evident, since less cold gas is formed (compare with Fig. 3). This can be attributed to the reduced cooling in metal-poor environments. However, at solar metallicity, the mass fraction of the cold gas is of a few per cent in the density range 10^{-24}–10^{-22} g cm^{-3}. This gas is located in cells that are far away from star clusters and hence that are characterized by a small value of G_0.

We observe a broad distribution of temperature values associated with each density value. As already seen in Walch et al. 2015, the reason for that is the different conditions that characterise every cell. In fact, shielded cells can cool to temperatures lower than those expected from unshielded equilibrium curves. For example, it can be seen in Fig. 4 that the temperature distribution in the higher-metallicity runs is offset below the equilibrium curves, which is due to shielding. Furthermore, local turbulence and/or the presence of shocks can quickly heat cells to temperatures higher than those predicted by the equilibrium curves. Moreover, the broader density distribution can be attributed to a variable value of the G_0 parameter (as seen already in Walch et al. 2015; Rathjen et al. 2025) and of the ζ parameter (Brugaletta et al. 2025), which results in different equilibrium conditions in every cell. We note that the "branch" in the temperature-density plots at around 10^4 K corresponding to H II regions becomes slightly hotter with decreasing metallicity, starting from around ~ 7000 K at solar metallicity and reaching ~ 12000 K in the most metal-poor run (Haid et al. 2018). Depending on the snapshot considered, some of this cold gas is found in a more diffuse phase (as already discussed in Rathjen et al. 2025, and further analysed in a follow-up paper). Moreover, the relative differences in the mass distribution appear to be smaller in the pressure-density plots for varying metallicities.

3.4 Molecular hydrogen

Several studies have seen a correlation between star formation and the presence of molecular gas (see e.g. Wong & Blitz 2002; Kennicutt et al. 2007; Bigiel et al. 2008; Leroy et al. 2008; Krumholz et al. 2011). Therefore, in this section we aim to investigate how the amount of molecular hydrogen present in our simulations varies with metallicity. The formation of molecular hydrogen mainly occurs via

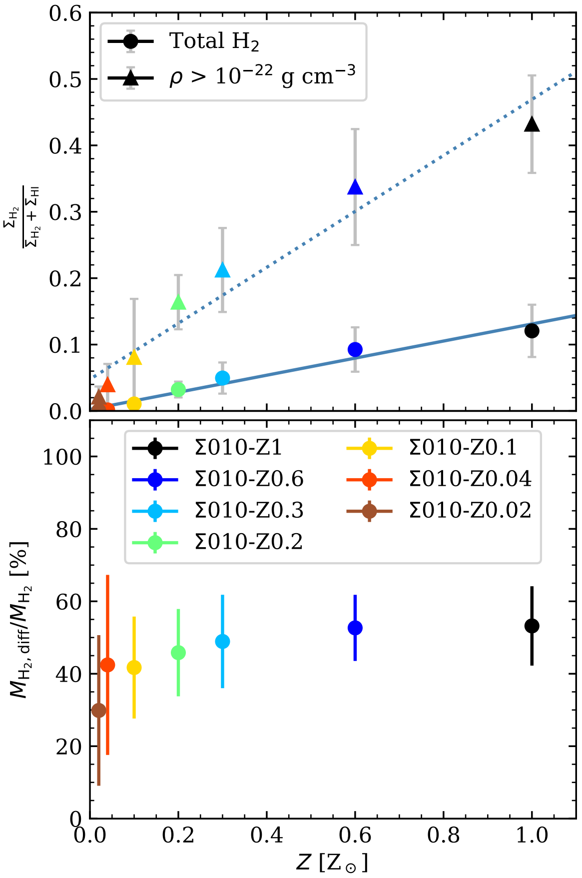

Figure 5. Top panel: average ratio of the molecular hydrogen surface density over the sum of molecular and atomic surface densities, as a function of the metallicity. The average has been computed considering a time interval of 200 Myr. In the region $|z| < 250$ pc we consider either the total amount of H_2 and H (round markers) or the amount of H_2 and H found for a gas denser than 10^{-22} g cm^{-3} (triangles). The solid and dotted lines represent the best fit for the total amount and that for dense gas, respectively. Bottom panel: average mass fraction of diffuse H_2, as a function of metallicity. We find this fraction to be around 50% for the highest Z, and around 30% for the lowest.

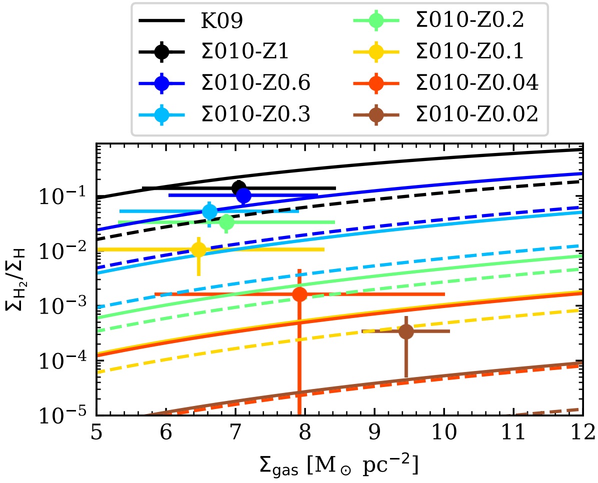

Figure 6. Time-averaged ratio of molecular and atomic hydrogen surface density as a function of the gas surface density. The coloured lines represent the predicted values from the Krumholz et al. (2009) model, where the colour matches that of the marker they refer to. The dashed lines have been computed using the fiducial values from Krumholz et al. (2009), whereas the solid lines have been computed using the average density of the CM, and the average G_0, taken from the simulations.

reaction of two hydrogen atoms on the surface of dust grains (Omukai et al. 2010). However, molecular hydrogen gets photodissociated by FUV photons. Dust grains can shield H_2 molecules from FUV radiation, preventing them from being photodissociated. The formation and destruction of molecular hydrogen is therefore dependent on the availability of dust grains and hence the value of the dust-to-gas mass ratio, which is a function of metallicity. However, we should point out that the amount of molecular gas that forms in our simulations also depends on our numerical resolution (Seifried et al. 2017; Joshi et al. 2019) and the sink particle density threshold $\rho_{\rm sink}$, especially for the low-metallicity runs. In fact, given the chosen value of $\rho_{\rm sink}$, for the low-metallicity runs the H_2 formation time is usually longer than the typical molecular cloud lifetime; therefore, we find smaller H_2 fractions. At higher resolution, we would allow for the formation of denser regions in the ISM that would help to form more molecular gas.

3.4.1 Molecular hydrogen mass fraction

The mass fraction of H_2 is expected to decrease for lower metallicity (Krumholz et al. 2009; Polzin et al. 2024), and at very low metallicities star formation can possibly occur in atomic gas (Krumholz 2012; Glover & Clark 2012a; Hu et al. 2016, 2017). Therefore, in the top panel of Fig. 5, we show how the time-averaged ratio of Σ_{H_2} over the sum of $\Sigma_{H_2} + \Sigma_{HI}$ varies as a function of Z for all gas (circles) and dense gas with $\rho > 10^{-22}$g cm^{-3} (triangles). We note that in both cases this ratio decreases for lower metallicity, as expected from the lower dust-to-gas mass ratio that characterises metal-poor environments. The different behaviour, considering the total gas or only the dense gas, can be attributed to the lower amount of atomic gas present in the denser gas, which increases the ratio. We fit a linear function to the dependence of the $\Sigma_{H_2}/(\Sigma_{HI} + \Sigma_{H_2})$ ratio with metallicity, and we find a slope of 0.13 ± 0.01 when considering all of the H_2, and a slope of 0.42 ± 0.04 when considering only the dense gas. We adopt a linear function for our best fit, as the dust-to-gas mass ratio, which

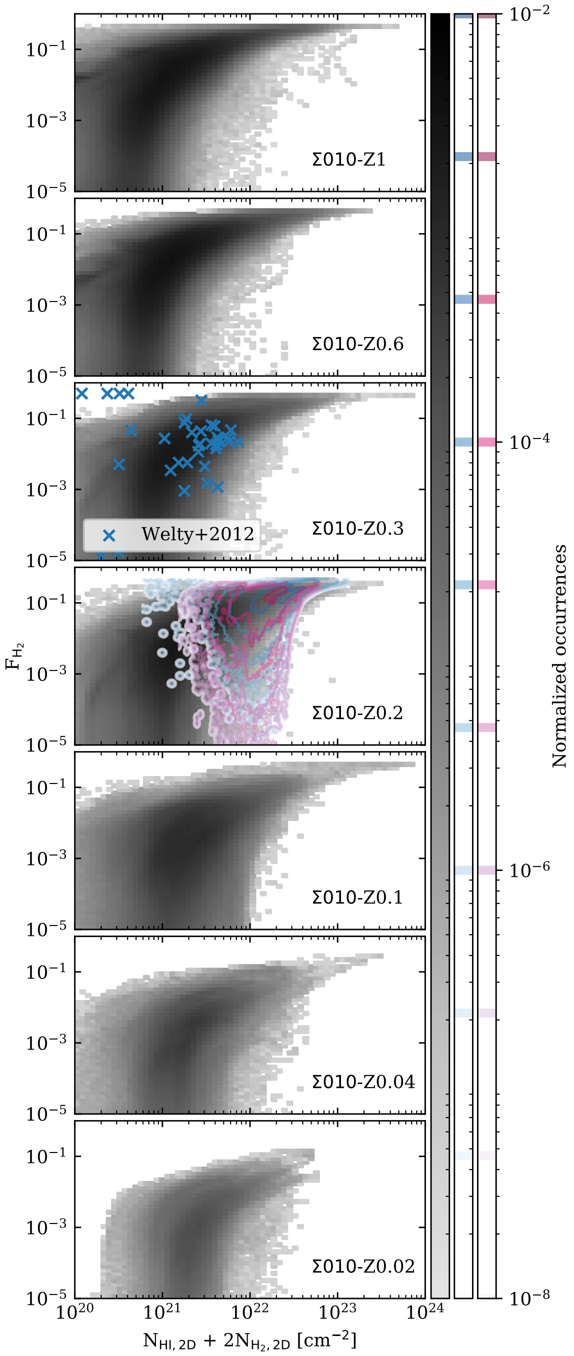

Figure 7. 2D histogram of the projected molecular hydrogen fraction F_{H_2} as a function of column density of atomic and molecular gas. The column densities of the atomic and molecular hydrogen have been computed by projecting the 3D HI and H_2 densities along the z-direction. The histogram has been computed using all snapshots after the onset of star formation for all runs, and the occurrences have been normalized by the total number of occurrences in each run. We over plot the observational data from Welty et al. (2012) for the Large Magellanic Cloud, and from Bolatto et al. (2011); Jameson et al. (2016), in blue and pink contours, respectively, for the Small Magellanic Cloud.

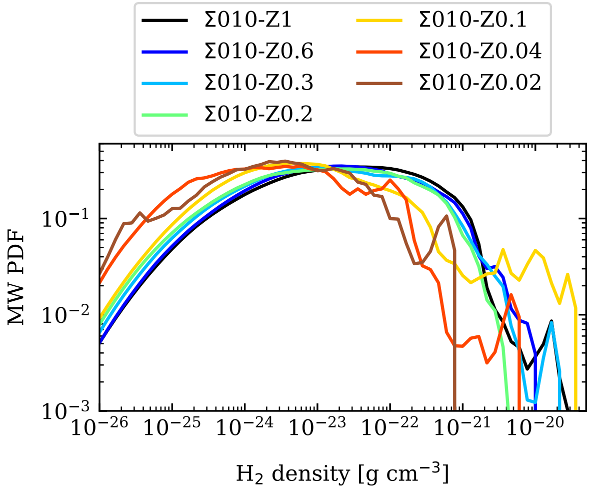

Figure 8. Mass-weighted PDF of the H_2 density, for all our runs, computed using their entire evolution after the onset of star formation. We note that H_2 spans a wide range of densities, from 10^{-26} to slightly above 10^{-20} g cm^{-3}.

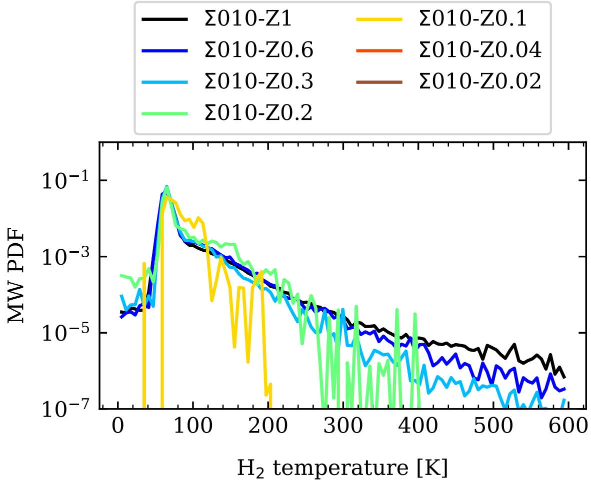

Figure 9. Mass-weighted PDF of the H_2 temperature. We consider the temperature of all the cells with an H_2 mass fraction above 50%. In the Σ010-Z0.04 and Σ010-Z0.02 runs, no cell fulfils this criterion, therefore no H_2 temperature PDF is shown. We note that the PDF peaks at around 60 K, however temperatures up to 600 K are present.

is a key ingredient for the formation of H_2, scales linearly with the metallicity in our simulations. The two different slopes that we find indicate that with increasing metallicity, there is a higher fraction of molecular gas in denser environments.

Moreover, we investigate how much H_2 can be found in the diffuse gas ($\rho < 10^{-22}$ g cm^{-3}) as a function of metallicity. In the bottom panel of Fig. 5 we show the mass fraction of diffuse H_2, defined as $M_{H_2,\mathrm{diff}}/M_{H_2}$, with $M_{H_2,\mathrm{diff}} = M_{H_2,\mathrm{tot}}$ - $M_{H_2,\mathrm{dense}}$. The latter term is the mass of H_2 found at densities higher than 10^{-22} g cm^{-3}. We note that for a metallicity higher than 0.2 $Z_\odot$ the mass fraction of the diffuse H_2 is almost constant and around 50%. At lower metallicity, this fraction drops down to around 30% for the most metal-poor run. This is due to the fact that in the metal-rich ISM the colder gas and higher shielding allow the H_2 to survive in diffuser environments.

In Fig. 6 we show the time-averaged Σ_{H_2}/Σ_H ratio, Σ_H being the surface density of atomic hydrogen, as a function of the gas surface density. We overplot the expected values from the Krumholz et al. (2009) model as coloured lines, where the colour of each line is the same as that of the point to which it refers. The Krumholz et al. (2009) model takes as input the metallicity of the gas, the gas surface density, the average density of the cold neutral medium, and the average value of the G_0 parameter. We compute the dashed lines using the fiducial values they adopt in Krumholz et al. (2009). The solid lines are computed using the values of the temporal and spatial average number density of the cold gas and of G_0 provided by our data. We note that, in certain cases, the solid lines are one order of magnitude higher than the dashed ones. However, except for the two most metal-rich runs, we tend to overestimate the molecular hydrogen fraction compared to that predicted by Krumholz et al. (2009) by about one or two orders of magnitude. This difference can be attributed to the uniform density adopted in the model from Krumholz et al. (2009), which hinders the formation of cold gas at very low metallicity, since the conversion from warm to cold gas occurs at higher densities and pressures (see Fig. 1). In our simulations, turbulence and shocks can compress the gas, and facilitate the formation of cold gas, and consequently, of H_2 gas. Nevertheless, the Σ_{H_2}/Σ_H ratio for the two most-metal rich runs is comparable to the values shown in Fig. 13 in Schruba et al. (2011), which consider massive spirals with metallicities close to solar.

In Fig. 7 we show a 2D-histogram of the projected molecular hydrogen fraction $F_{H_2} \equiv N_{H_2,2D}/(N_{HI,2D} + 2N_{H_2,2D})$ as a function of the total column density of atomic and molecular hydrogen $N_{HI,2D} + 2N_{H_2,2D}$. The column densities $N_{H_2,2D}$ and $N_{HI,2D}$ are the projection of the molecular and atomic gas 3D density along the z-axis, respectively. For every run, we calculate the corresponding histogram using the entire evolution after the onset of star formation and normalize by the total number of occurrences. The value of F_{H_2} increases for higher densities, until it flattens to a value of around 0.5 at column densities higher than 10^{23} cm^{-2}. This saturation at 0.5 means that the gas becomes fully molecular. However, in the Σ010-Z0.04 run the high-density distribution of F_{H_2} flattens to a value of around 0.3, and for run Σ010-Z0.02 there is no high column density distribution present, and the maximum value of F_{H_2} is around 0.1. This is consistent with the lower H_2 mass fractions shown in Fig. 5-6. Moreover, this is well in accordance with the idea that, at the column densities in which star formation takes place, the metal-poor gas is still dominated by the atomic rather than the molecular gas, in accordance with Glover & Clark (2012a) and Krumholz (2012). Comparing our results for the Σ010-Z0.6 and Σ010-Z0.2 simulations with the values of F_{H_2} in Fig. 2 in Polzin et al. (2024), we note that our simulations reach column densities that are between one and two orders of magnitude higher. This can be explained because our midplane resolution of 3.9 pc is higher than the 10 pc resolution in the simulations by Polzin et al. (2024). We also over-plot observational data from Welty et al. (2012) for the Large Magellanic Cloud, and from Bolatto et al. (2011), as blue contours, and Jameson et al. (2016), as pink contours, for the Small Magellanic Cloud. We note a very good agreement between the observational data and the values from our simulations.

3.4.2 *H_2 density and temperature*

In this section we want to give an overview of the conditions in which the H_2 present in our simulations is found. Fig. 8 shows the mass-weighted probability density function (PDF) of the H_2 density, computed accounting for the entire evolution of the runs after the onset of star formation. We see that the H_2 density PDF spans a large density

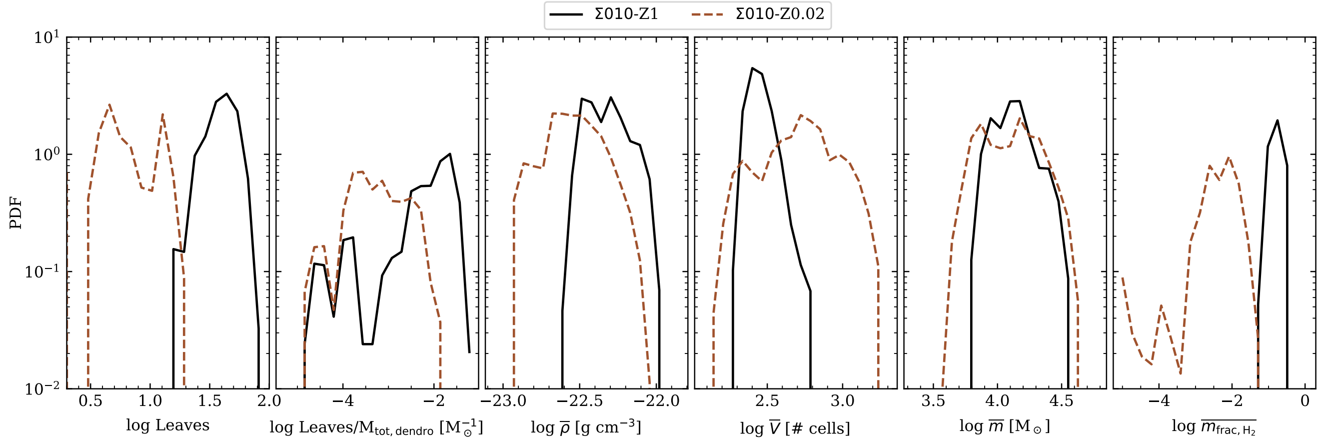

Figure 10. Probability density functions computed for the dendrogram sub-structures found. From left to right, we plot the distribution of the number of leaves, the ratio of the number of leaves and the total gas mass $M_{\mathrm{tot,dendro}}$ that enters the dendrogram calculation, the distribution of the snapshot-averaged density of the leaves, as well as their snapshot-averaged volume, mass, and H_2 mass fraction. The distributions for all simulation runs can be found in Fig. B1.

range, from 10^{-26} to slightly above 10^{-20} g cm^{-3}. There is no clear peak, rather a wide density range (10^{-24}–10^{-21} g cm^{-3}) where the PDF is almost constant and at its maximum. This demonstrates that the large amount of diffuse H_2 that we find in our simulations is not an artifact of our choice to adopt a density threshold of 10^{-22} g cm^{-3} to distinguish between diffuse and dense gas; we could decrease this value by an order of magnitude or more and would still find very similar results. For the two most metal-poor runs, the broad peak in the PDF is slightly shifted (10^{-25} g cm^{-3}–10^{-23} g cm^{-3}), which possibly just reflects the fact that these runs form less dense gas overall. In the high-density regime, we see a power-law tail for all runs. We also note that the amount of H_2 above the density threshold for star formation, $\rho_{\mathrm{sink}} = 2 \times 10^{-21}$ g cm^{-3}, is less than the amount of diffuse H_2.

In Fig. 9 we show the mass-weighted PDF of the H_2 temperature. In this computation, we take into account all cells in our computational domain whose H_2 mass fraction is higher than 50%. In the case of the two most metal-poor runs, Σ010-Z0.02 and Σ010-Z0.04, no cell fulfils this criterion, therefore no temperature PDF is computed. Lowering this threshold implies that the majority of the gas in the cell is atomic, which biases the cell's temperature toward that of the atomic phase. The H_2 temperature PDF peaks at around 60 K for all runs, but it extends to much higher temperatures. In particular, the maximum temperature depends on the metallicity. For a metallicity equal or higher than 0.3 $Z_\odot$, we find the H_2 temperature to reach up to 600 K. On the other hand, the Σ010-Z0.2 run reaches an H_2 temperature of around 400 K, whereas the Σ010-Z0.1 run reaches 200 K. This anticorrelation with metallicity can be explained by the reduced dust shielding in metal-poor gas, which prevents H_2 from surviving at higher temperatures. Our results are in agreement with the idea of an H_2 temperature power law presented by Togi & Smith (2016), necessary to recover the distribution of mid-infrared rotational H_2 emission observed by Spitzer at solar metallicity. They also find warm H_2 with a temperature of above 100 K.

3.5 Gas fragmentation

As seen in Sec. 3.2, the amount of cold gas found in the ISM decreases with metallicity. The degree of fragmentation of the gas and the subsequent formation of dense clumps can influence the formation of stars. In this section, we investigate the fragmentation of the cold and dense gas in our simulations using the open-source dendrogram algorithm ASTRODENDRO[1].

We provide ASTRODENDRO with the logarithm of the 3D total gas density. As a minimum density to be considered for the calculation, we assume the threshold of $\rho_{\mathrm{min,dendro}} = 10^{-23}$ g cm^{-3}. We choose this threshold value because the low-metallicity ISM tends to be more diffuse than a solar metallicity ISM, and choosing a higher value for the density threshold would underestimate the number of substructures detected with the dendrogram method. Further, we assume a step width (min_delta value) in log scale of 0.1 dex and a minimum number of 100 cells required per substructure in order to reduce the noise due to the presence of very small, fluctuating substructures that do not form stars anyway. The outcome of our dendrogram analysis is shown in Figs. 10 and B1, and reported in Table 3. Our analysis takes into account the fragmentation of the gas in the 200 Myr interval after the onset of star formation.

For clarity reasons, in Fig. 10 we show the distributions of some key dendrogram quantities only for the Σ010-Z1 and the Σ010-Z0.02 runs. An important quantity to describe the degree of fragmentation of the gas is the number of leaves of the dendrogram, since they are the smallest independent structures found in the gas. As we can see in the left panel of Fig. 10, the PDF of the distribution of the number of leaves in the Σ010-Z0.02 run is shifted to the left compared to that of the Σ010-Z1 run, meaning that at low metallicity the number of leaves formed is much smaller than at solar metallicity.

Moreover, in the second panel we show the PDF of the distribution of the ratio of the number of leaves and the respective mass that enters the dendrogram calculation, $M_{\mathrm{tot,dendro}}$, meaning the total mass above the density threshold of 10^{-23} g cm^{-3}. Note that $M_{\mathrm{tot,dendro}}$ changes for each run and every snapshot, since the structure of the ISM continuously changes. The value of this ratio can be understood as the amount of leaves that can form in the ISM per $M_\odot$ of gas denser than $\rho_{\mathrm{min,dendro}}$. We see a similar behaviour as for the PDF of the number of leaves, showing that the solar-metallicity ISM is able to form more sub-structures per unit mass. Since we use the entire

---

[1] https://dendrograms.readthedocs.io/en/stable/

Table 3. Mean values of the quantities shown in Fig. 10 and Fig. B1. We also provide the volume in units of pc^3, obtained multiplying the number of cells by the volume of one cell, (3.9 pc)^3.

Run	Leaves	Leaves/$M_{\rm tot,dendro}$ [10^{-3} M$_\odot^{-1}$]	Density [10^{-23} g cm^{-3}]	Volume [# cells]	Volume [10^3 pc^3]	Mass [10^3 M$_\odot$]	H_2 Mass Fraction [%]
Σ010-Z1	38.7 ± 10.2	10.0 ± 8.7	4.8 ± 1.5	292.4 ± 54.6	17.3 ± 3.2	14.0 ± 5.1	0.14 ± 0.05
Σ010-Z0.6	35.9 ± 8.5	7.4 ± 7.7	5.1 ± 1.8	305.7 ± 68.0	18.1 ± 4.0	15.0 ± 6.2	0.12 ± 0.04
Σ010-Z0.3	31.3 ± 8.9	7.2 ± 7.1	5.1 ± 2.1	317.9 ± 56.2	18.9 ± 3.3	15.5 ± 6.7	0.07 ± 0.03
Σ010-Z0.2	30.0 ± 6.5	7.1 ± 6.9	5.0 ± 1.5	312.1 ± 67.8	18.5 ± 4.0	14.8 ± 5.1	0.05 ± 0.02
Σ010-Z0.1	22.3 ± 5.0	4.0 ± 5.0	4.7 ± 2.1	354.1 ± 94.0	21.0 ± 5.6	15.1 ± 7.1	0.02 ± 0.01
Σ010-Z0.04	6.9 ± 6.5	1.4 ± 2.3	4.1 ± 2.6	328.2 ± 101.2	19.5 ± 6.0	11.4 ± 7.7	0.01 ± 0.01
Σ010-Z0.02	7.5 ± 4.1	1.2 ± 1.7	3.1 ± 1.2	583.9 ± 299.3	34.6 ± 17.8	13.9 ± 7.0	0.007 ± 0.006

evolution after the onset of star formation, we compute for each snapshot the average volume and mass of all leaves, and the average of the leaf-averaged density. We represent these quantities in the third to fifth panels. The leaves in the Σ010-Z1 run are on average denser and smaller in volume than those of the Σ010-Z0.02 run. However, both exhibit almost the same average mass distribution. Finally, we plot the average mass fraction of molecular hydrogen found in the leaves (right panel). As already seen in Fig. 5, the amount of H_2 found in our simulations depends on metallicity, which explains why metal-poor leaves exhibit a much smaller amount of H_2.

We represent the same quantities computed for all runs in Fig. B1 in the Appendix and report the mean values of the analysed quantities in Table 3. Regarding the number of leaves and its ratio with $M_{\rm tot,dendro}$, we see that the ability of the gas to fragment and form smaller, denser cores scales with metallicity. However, for a metallicity larger than 0.1 Z$_\odot$, there seems to be only a weak trend. Within the uncertainty, all results are more or less comparable. On the other hand, we see a much stronger trend for metallicities lower than 0.1 Z$_\odot$. Regarding the average density of the leaves, we note no substantial difference for metallicities larger than 0.1 Z$_\odot$, whereas at the lowest metallicities the leaves tend to be more diffuse. Furthermore, we see larger average volumes for lower metallicities, but similar average masses. The average H_2 mass fraction in the leaves clearly increases with metallicity.

3.6 Star formation

3.6.1 Local conditions for star formation

As seen in the previous paragraph, the degree of fragmentation of the dense gas is similar for metallicities higher than 0.1 Z$_\odot$, but it is clearly lower for the metal-poor gas. This suggests that the conditions under which stars form vary with metallicity. To explore this aspect, we investigate the distributions of $G_{\rm eff}$, the PE heating rate, $\Gamma_{\rm pe}$, ζ, and the CR heating rate, $\Gamma_{\rm cr}$ for all gas (transparent) and for star-forming gas (opaque) in Fig. 11. All distributions are mass-weighted and normalized such that they fall between 0 and 1. For all gas, we consider the gas near the midplane within $|z| < 250$ pc. To trace the star-forming gas, we find the coordinates of each star cluster at the time of its creation. We then calculate the coordinates that the star-forming gas would have had one snapshot before its formation given its velocity at birth. Then we compute above quantities in a region centred on these coordinates and with a radius $r_{\rm accr} \sim 11.7$ pc. We consider only cells whose density is larger than 5×10^{-22} g cm^{-3}, which is a bit lower than the density threshold for sink particle formation. We also show the median values of the distributions for the star-forming gas as black vertical lines, and we report them with their 25th and 75th percentiles in Table 4.

From Fig. 11 we see that the median value of $G_{\rm eff}$ is comparable to the $G_{\rm bg}$ value. Since $G_{\rm eff}$ is computed within a spherical radius of 50 pc from each star cluster, a large volume fraction has $G_{\rm eff} \lesssim G_{\rm bg}$. Smaller values are possible because $G_{\rm bg}$ is locally attenuated (see Sec. 2). In run Σ010-Z1 the median of $G_{\rm eff}$ is slightly higher than the background because more stars are formed. The median $\Gamma_{\rm pe}$ is in the range of $10^{-26} - 10^{-24}$ erg s^{-1} cm^{-3} and scales with metallicity. This is expected as $\Gamma_{\rm pe}$ depends on the dust-to-gas ratio, which scales linearly with the metallicity. The median ζ is around $2 - 8 \times 10^{-18}$ s^{-1} for the most metal-rich runs, and around $2 - 8 \times 10^{-19}$ s^{-1} for the most metal-poor runs. The median $\Gamma_{\rm cr}$ scales with metallicity and is in the range of $10^{-28} - 10^{-26}$ erg s^{-1} cm^{-3}. The only exception is the Σ010-Z0.04 run, for which the median of $\Gamma_{\rm cr}$ is around 5×10^{-29} erg s^{-1} cm^{-3}. This discrepancy from the scaling with metallicity is due to the lower number of formed stars, and will be addressed in Sec. 3.6.2.

Moreover, we notice that in every run the PE heating rate dominates over the CR heating rate, both in all gas and in the star-forming gas. Furthermore, the PE and CR heating rates above which star formation is suppressed drop with decreasing metallicity, owing to the less efficient cooling, and this behaviour is particularly accentuated in the two most metal-poor runs. Comparing the star-forming gas distributions with their respective total distributions, we notice a few features. For example, we see selection effects in the value of $G_{\rm eff}$ in the star-forming gas mostly at $Z < 0.1$ Z$_\odot$, whereas at higher metallicity larger values of $G_{\rm eff}$ are apparent. We also note that the distribution of $\Gamma_{\rm pe}$ for the star-forming gas matches the higher-end of the corresponding total gas distribution. The reason for this is the dependence of $\Gamma_{\rm pe}$ on the density, which in the star-forming gas is around the value of $\rho_{\rm sink}$. A similar behaviour is found for the $\Gamma_{\rm cr}$ distribution in the star-forming gas. Moreover, we observe selection effects in the ζ distribution for the star-forming gas with respect to all gas. In fact, we notice that the highest values of ζ, beyond which star formation is suppressed, are around two orders of magnitude lower than the highest values found in all gas.

To summarise, the star-forming gas at low metallicity experiences lower PE and CR heating than in solar-neighbourhood conditions. This is due to the interplay of two different, yet connected, effects. First, in the lower metallicity runs the star formation rate surface density is lower than for solar-neighbourhood conditions (see Sec. 3.6.2), therefore there is a lower production of UV radiation and cosmic rays. As a consequence, the total distributions of $G_{\rm eff}$ and ζ show reduced values. Second, the inefficient cooling at low metallicity implies that lower PE and CR heating rates are needed to prevent the gas from cooling and collapsing.

Using the same method as in Fig. 11, we show in Fig. 12 the distribution of the molecular to atomic hydrogen mass ratio for both the

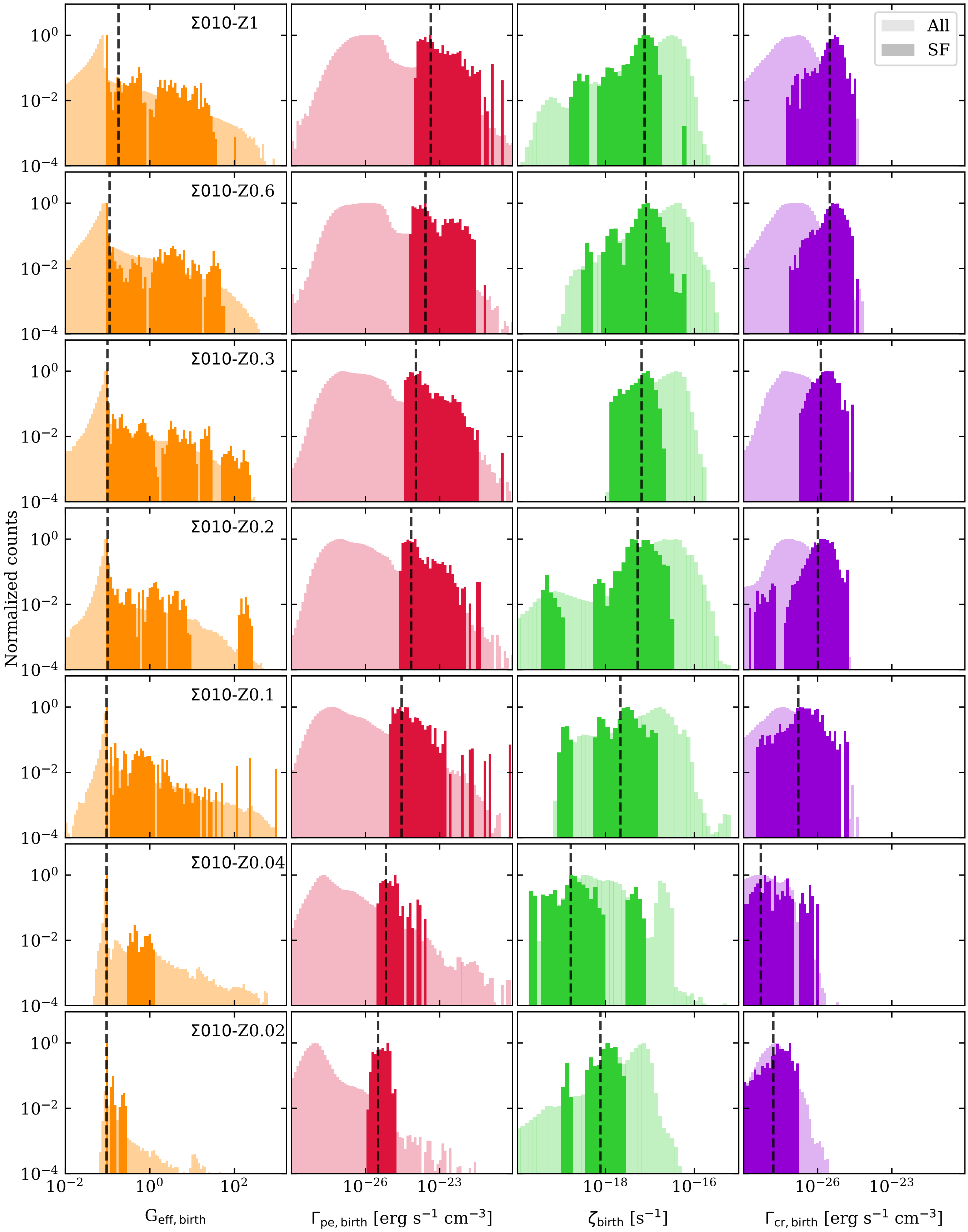

Figure 11. Distributions of $G_{\rm eff}$, $\Gamma_{\rm pe}$, ζ and $\Gamma_{\rm cr}$ for all gas and for star-forming (SF) gas for all runs. The black vertical lines are the medians of the SF gas distributions as listed in Table 4.

Table 4. Median values of $G_{\rm eff,birth}$, $\Gamma_{\rm pe,birth}$, $\zeta_{\rm birth}$, $\Gamma_{\rm cr,birth}$ and $M_{\rm H_2,birth}/M_{\rm H,birth}$ distributions computed for the star-forming gas in Fig. 11. The subscripts and superscripts are the 25th and 75th percentiles, respectively.

Run	$G_{\rm eff,birth}$	$\Gamma_{\rm pe,birth}$ [10^{-25} erg s^{-1} cm^{-3}]	$\zeta_{\rm birth}$ [10^{-18} s^{-1}]	$\Gamma_{\rm cr,birth}$ [10^{-27} erg s^{-1} cm^{-3}]	$M_{\rm H_2,birth}/M_{\rm H,birth}$
Σ010-Z1	$0.18\,^{1.76}_{0.09}$	$44\,^{220}_{20}$	$7.6\,^{10}_{4.7}$	$31\,^{48}_{17}$	$2.4^{3.8}_{1.6}$
Σ010-Z0.6	$0.11\,^{3.2}_{0.09}$	$27\,^{220}_{12}$	$8.2\,^{12}_{5.2}$	$31\,^{53}_{16}$	$1.4^{2.3}_{1.0}$
Σ010-Z0.3	$0.10\,^{0.8}_{0.09}$	$11\,^{52}_{6.2}$	$6.5\,^{9.5}_{2.6}$	$13\,^{25}_{5.7}$	$0.6^{0.9}_{0.5}$
Σ010-Z0.2	$0.10\,^{0.84}_{0.09}$	$7.1\,^{26}_{4.0}$	$5.3\,^{9.2}_{3.4}$	$10\,^{19}_{4.9}$	$0.4^{0.6}_{0.3}$
Σ010-Z0.1	$0.09\,^{0.54}_{0.09}$	$2.9\,^{8.1}_{1.6}$	$2.2\,^{3.7}_{0.8}$	$1.6\,^{3.3}_{0.6}$	$0.2^{0.2}_{0.1}$
Σ010-Z0.04	$0.09\,^{0.10}_{0.09}$	$0.7\,^{1.3}_{0.5}$	$0.2\,^{3.1}_{0.02}$	$0.1\,^{0.2}_{0.02}$	$0.06^{0.1}_{0.05}$
Σ010-Z0.02	$0.09\,^{0.09}_{0.09}$	$0.3\,^{0.5}_{0.2}$	$0.8\,^{1.5}_{0.5}$	$0.2\,^{0.3}_{0.05}$	$0.03^{0.04}_{0.02}$

total (transparent distribution) and star-forming gas (opaque). The median values of this ratio for the star-forming gas are shown as vertical dashed yellow lines, and their values are reported in Table 4 together with their 25th and 75th percentile. Moreover, we add a vertical solid black line that indicates $M_{\rm H_2,birth}/M_{\rm H,birth} = 1$, meaning when the mass of molecular and atomic hydrogen are the same. We note that the median for the star-forming gas decreases as a function of the metallicity, and becomes lower than 1 at a metallicity of 0.3 $Z_\odot$. However, when considering the entire distribution for the star-forming gas, we note that the gas is almost fully atomic at a metallicity of 0.04 $Z_\odot$ and lower. We also note, that the highest values of the molecular to atomic hydrogen mass ratios, computed for the total gas, do not correspond to the values for the star-forming gas, apart for the two most metal-rich runs. This means that, for metallicities of 0.3 $Z_\odot$ or lower, there are cells in our domain which present a high mass fraction of H_2, without forming stars. This can happen even if the total density of the gas in the cell is higher than $\rho_{\rm sink}$, but the other criteria for sink formation are not fulfilled (see e.g. Gatto et al. 2017, for more details). All in all, we show here that star formation occurs in atomic gas in the low-metallicity ISM.

3.6.2 *Star formation rates*

Star formation plays a central role in determining the dynamical and chemical evolution of the gas. We measure the star formation rate in our simulations by means of the "observable" star formation rate surface density, $\Sigma_{\rm SFR}$, described in Gatto et al. 2017 as

$$\Sigma_{\rm SFR}(t) = \frac{{\rm SFR}(t)}{A} = \frac{1}{A}\sum_{i=1}^{N_*(t)} \frac{120\ {\rm M}_\odot}{t_{{\rm OB},i}}, \tag{17}$$

where $A = (0.5\ {\rm kpc})^2$ is the area of the computational domain in the midplane, $N_*(t)$ is the number of active massive stars at time t, and $t_{{\rm OB},i}$ is the lifetime of the i$^{\rm th}$ formed massive star. Eq. 17 takes into account that for each formed massive star, a total gas mass of 120 $M_\odot$ is converted into stars. On the x-axis, we subtract the time at which the first star is born in every simulation, $t_{\rm SF}$ (see Table 5). We show the time evolution of $\Sigma_{\rm SFR}$ in Fig. 13, and we list the median values in Table 5, where we also report the 25th and 75th percentiles. In the following paragraphs, we will discuss physical quantities evolving in the time interval [$t_{\rm SF}$, $t_{\rm SF}$ + 200 Myr].

We find that $\Sigma_{\rm SFR}$ oscillates in time with a period of a few tens of Myr, depending on the particular simulation. As already seen in Sec. 3.1, the stellar feedback originating from all existing clusters pushes the gas away from the midplane in the vertical direction, depleting the gas reservoir of the midplane. At the same time, the gas that has been pushed in the vertical direction is too hot and diffuse to give birth to new star clusters; therefore, the total star formation activity in the simulation box decreases. This drop is also seen in the $\Sigma_{\rm SFR}$, which reaches a local minimum in this case. However, after all clusters have become inactive, meaning that all the massive stars have exploded as supernovae, the expelled gas is no longer exposed to the high pressure driven by stellar feedback. It therefore falls back towards the midplane due to gravity. As the gas accumulates further near the midplane, it again reaches the conditions for another starburst.

From Fig. 13 we note that the more metal-rich runs show only small differences in $\Sigma_{\rm SFR}$, whereas the Σ010-Z0.04 and Σ010-Z0.02 runs clearly show a much lower $\Sigma_{\rm SFR}$. These differences are quantified with the median $\Sigma_{\rm SFR}$ (see Table 5), which decreases roughly with metallicity. In particular, in run Σ010-Z0.02 the number of formed stars is only around 4% of those formed in run Σ010-Z1. Although $\Sigma_{\rm SFR}$ depends on the availability of cold gas, which we have seen decreasing as a function of metallicity in Fig. 3, it also depends on the degree of fragmentation of the gas. As seen in Table 3, there are significant differences in the fragmentation of the gas for the lowest metallicity runs.

3.7 Stellar feedback

3.7.1 *Stellar winds, supernovae, radiation*

During their entire lifetime, stars inject energy in the ISM in the form of stellar winds, radiation, and supernova explosions. However, these three different energy inputs depend on several factors, e.g. the metallicity, the number of formed stars, and for how long stars live. In turn, these energy injections profoundly affect the shape and evolution of the ISM. Therefore, it is worth analysing the total amount of energy injected due to these three different feedback channels.

In Fig. 14, we show the cumulative distribution of the energy injected because of winds, radiation, and supernovae, which sums up the contribution of all stars formed in our simulations. In the case of stellar winds, the injected energy has been computed by integrating the wind luminosity of every model in time, as defined in Eq. A1. We calculate the cumulative contribution of radiation by integrating the bolometric luminosity of the stellar models in time. The energy injection due to supernovae is derived by multiplying the number of supernovae, which corresponds to the number of formed massive stars, by 10^{51} erg (as seen in Sec. 2). Therefore, the cumulative energy input from supernovae is directly dependent on the number of massive stars formed (as reported in Table 5).

We note that the total contribution of stellar winds scales as a

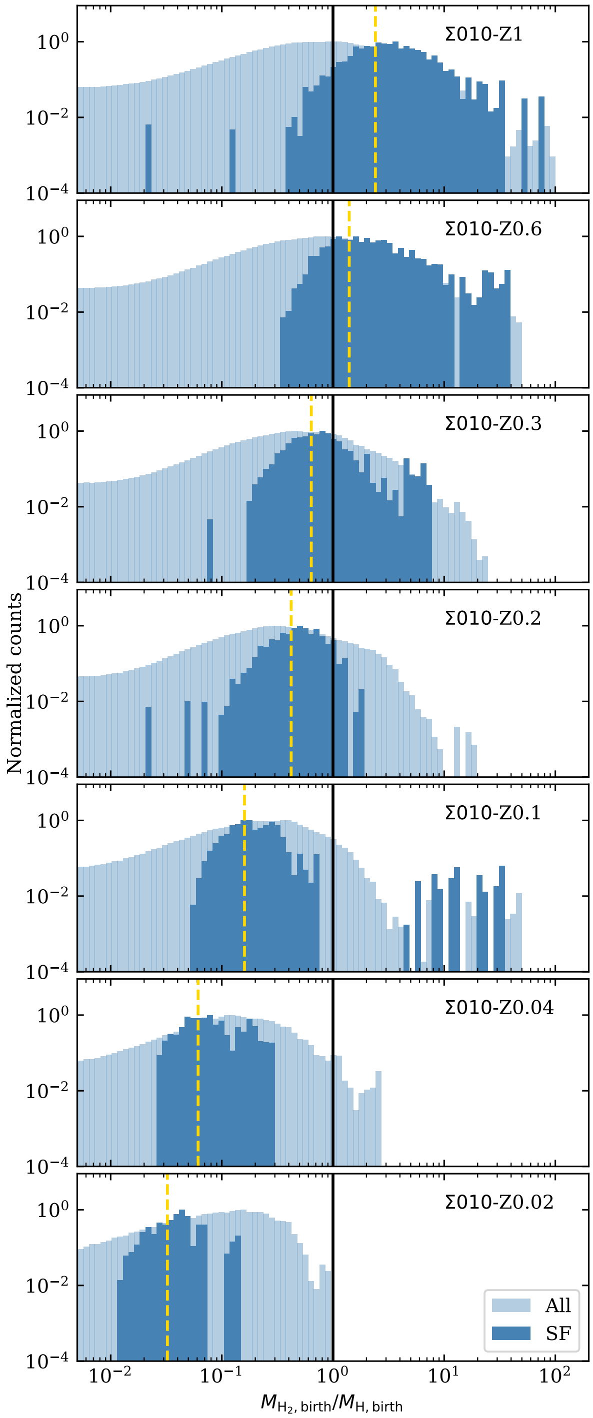

Figure 12. Distribution of the H_2 to HI mass ratio for the total gas (transparent distribution), and the star-forming gas (opaque). The dashed yellow line is the median of the distribution for the star-forming gas, whereas the black line indicates $M_{\mathrm{H_2}}/M_{\mathrm{HI}} = 1$.

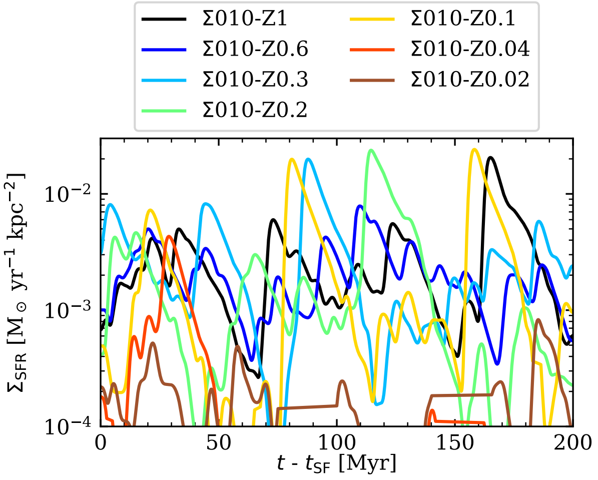

Figure 13. Observable star formation rate surface density Σ_{SFR} as a function of time. Σ_{SFR} oscillates in time, therefore a star-forming phase is followed by a more quiescent phase during which star formation diminishes or halts completely. The Σ_{SFR} for the Σ010-Z0.1 and Σ010-Z0.04 are significantly lower than those of the more metal-rich runs.

Table 5. A few key quantities regarding star formation and feedback in every simulation. t_{SF} is the time at which the first star cluster forms, N_{stars} is the number of massive stars formed in the time interval [t_{SF}, t_{SF} + 200 Myr]. We add the median of Σ_{SFR} computed in the same interval. The value of 0 for the Σ010-Z0.04 is justified since for the majority of its evolution, the Σ_{SFR} is zero, and in the median calculation repetitions are counted. The mean final CR ionisation rate $\overline{\zeta}_{\mathrm{fin}}$ is computed at t_{SF}+ 200 Myr for every run (see Sec. 3.7.2).

Simulation	t_{SF} [Myr]	N_{stars}	Σ_{SFR} [10^{-3} M$_\odot$ yr^{-1} kpc^{-2}]	$\overline{\zeta}_{\mathrm{fin}}$ [10^{-17} s^{-1}]
Σ010-Z1	23.6	1231	$1.8\,^{3.5}_{1.1}$	5.7
Σ010-Z0.6	23.9	1013	$1.9\,^{2.7}_{1.0}$	7.3
Σ010-Z0.3	26.1	1118	$1.8\,^{3.3}_{0.8}$	4.9
Σ010-Z0.2	21.1	975	$0.9\,^{2.0}_{0.3}$	9.9
Σ010-Z0.1	28.7	1121	$0.7\,^{2.5}_{0.2}$	2.6
Σ010-Z0.04	33.3	307	$0\,^{0.07}_{0}$	1.8
Σ010-Z0.02	44.2	54	$0.07\,^{0.2}_{0}$	0.6

function of metallicity, as expected from the bottom panel of Fig. A2, and because low-metallicity runs form fewer stars. For the most metal-rich runs, the energy injected by winds is higher than the energy injected by SNe in the same runs. Moreover, we do not see a clear trend of the cumulative amount of emitted radiation with metallicity for $Z > 0.1$ Z$_\odot$. We also note that the energy input from the emitted radiation is three orders of magnitude higher than that due to winds and SNe. However, e.g. Walch et al. (2012); Haid et al. (2018) report that less than 0.1 per cent of the ionising radiation emitted by a star couples with the surrounding gas as the conversion of radiative energy to thermal and kinetic energy is very inefficient (Peters et al. 2017). This implies that all feedback channels are of comparable importance in shaping ISM dynamics.

3.7.2 *Cosmic rays*

In this section, we analyse the temporal and spatial variability of ζ. We compute ζ for every cell in a region $|z| < 250$ pc. We then bin the values of ζ in 100 logarithmically spaced bins and compute the relative frequency of each bin. We do this for every snapshot in all our runs, obtaining the time evolution shown in Fig. 15.

We note that at fixed time, ζ varies by several orders of magnitude, ranging from around 10^{-19} to 10^{-14} s^{-1}. The highest spikes (10^{-15}

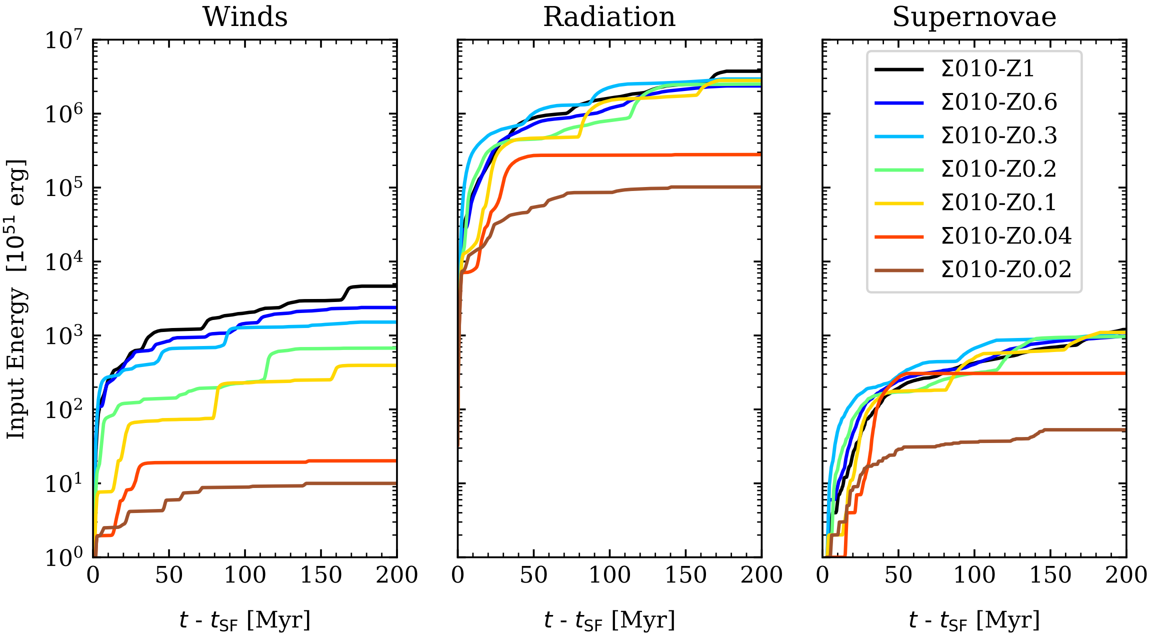

Figure 14. Cumulative energy input per feedback channel as a function of time. From left to right we show stellar winds, radiation, and supernovae. The contribution of stellar winds scales with metallicity, and overall it is comparable to the contribution by supernovae. The contribution of the emitted radiation is around four orders of magnitude higher than winds and supernovae, and, as for supernovae, it mostly depends on the number of formed stars, rather than metallicity. Note however, that not all of the emitted radiative energy is converted to thermal or kinetic energy of the gas.

– 10^{-14} s^{-1}) correspond to regions in the vicinity of SNe, where the injection of CR energy takes place. The lower values (10^{-18} – 10^{-17} s^{-1}) correspond, as already seen in Fig. 11, to the star-forming gas. We do not observe dramatic changes in the values of ζ for different metallicities, and only for the two lowest-metallicity runs ζ is overall smaller. This is due to the number of SNe exploding in our simulations, dependent on the SFR (see Sec. 3.6.2), which determines the amount of CR energy injection. We report in Table 5 the average value of ζ at t_{SF} + 200 Myr, $\overline{\zeta}_{\mathrm{fin}}$, when the ISM is the most evolved in our runs. However, we do not see a clear correlation with metallicity, except for the two most metal-poor runs.

3.8 Outflows

3.8.1 Mass outflows

As mentioned above, stellar feedback leads to the outflow of gas from the midplane. We compute the amount of mass instantaneously traversing the surface $|z|$ = 1 kpc, meaning the mass outflow rate $\dot{M}_{\mathrm{out}}$, and we show its distribution as a function of metallicity in the top panel of Fig. 16. We also show the distribution of the mass loading $\eta = \dot{M}_{\mathrm{out}}/\langle \mathrm{SFR} \rangle$ in the bottom panel. Red lines indicate the mean for every run, and orange lines the median. The boxes extend from the 75th percentile down to the 25th percentile. The plus markers represent the maximum of each distribution.

We do not see major differences in the mean $\dot{M}_{\mathrm{out}}$ and η values for all runs, except for the most metal-poor one, which has a much lower outflow rate and mass loading, as expected from the fact that it does not form many stars. This behaviour suggests that, if the star formation rate is high enough, the outflows do not seem to strongly depend on metallicity if the medium has the same surface density. Since outflows are mainly driven by supernova feedback, this result can also be observed in the values of the VFF of the hot gas in Fig. 3, which do not change substantially down to a metallicity of 0.1 $\mathrm{Z}_{\odot}$.

3.8.2 Vertical acceleration profiles

We analyse the outflows taking place in our runs by calculating vertical acceleration profiles, as shown in Fig. 17. For this calculation, we consider the entire box and average the profiles in the interval [t_{SF} + 100 Myr, t_{SF} + 150 Myr] to avoid the influence of the initial conditions. We decide to average the profiles in a time interval of 50 Myr to eliminate fluctuations occurring on very short timescales, without, at the same time, losing the contributions of the outflow/inflow motions, which would average out to some degree when considering the entire time span of the simulations. Positive accelerations are oriented in the direction of positive z-coordinates. We define the accelerations in the vertical direction due to pressure forces, as

$$a_i = -\frac{1}{\rho}\frac{dP_i}{dz}, \tag{18}$$

where the subscript i denotes the different pressure components, meaning due to the thermal, magnetic and CR pressure gradients. The total pressure is defined as

$$P_{\mathrm{tot}} = P_{\mathrm{th}} + P_{\mathrm{mag}} + P_{\mathrm{CR}} \tag{19}$$

$$= (\gamma - 1)e_{\mathrm{th}} + \frac{B^2}{8\pi} + (\gamma_{\mathrm{CR}} - 1)e_{\mathrm{CR}}, \tag{20}$$

where $\gamma = 5/3$ and $\gamma_{\mathrm{CR}} = 4/3$. In the calculation of P_{mag} we do not account for the magnetic tension, which is likely negligible since we are dominated by small-scale fields. The relative importance of the magnetic tension with respect to the magnetic pressure in SILCC has

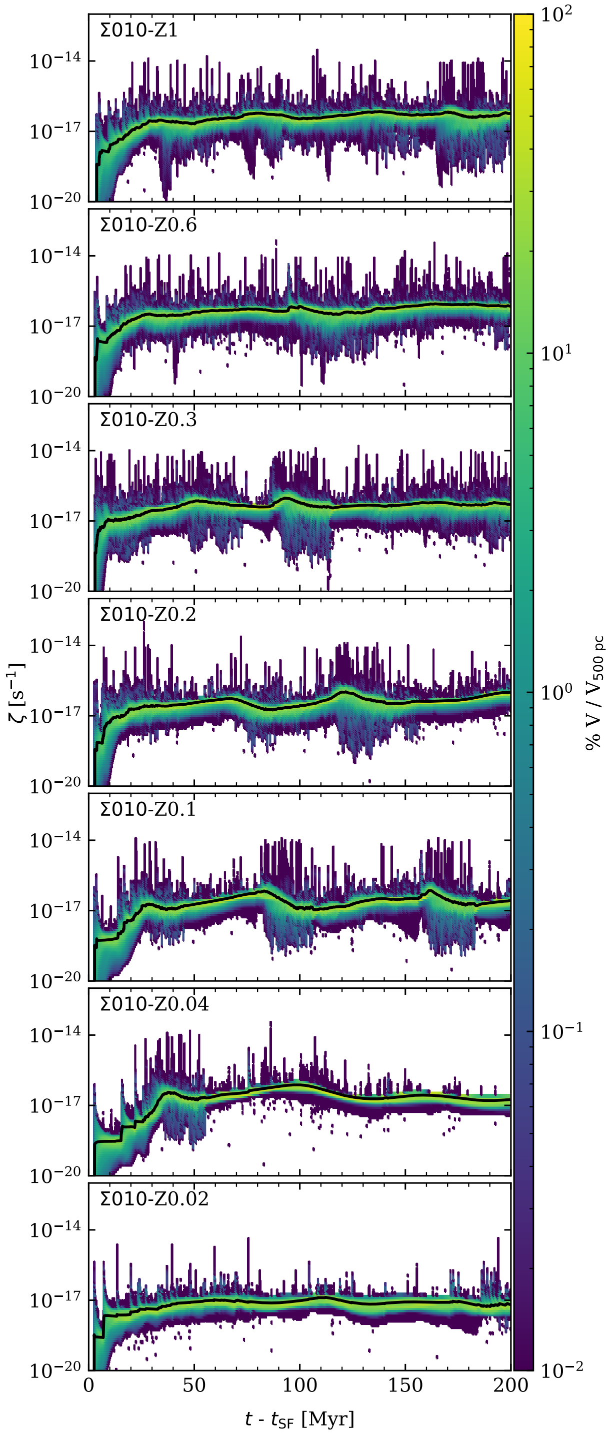

Figure 15. Variations of the CR ionisation rate in space and time in all our runs, computed within $|z| < 250$ pc around the midplane. The black line is the average of ζ computed in the same region.

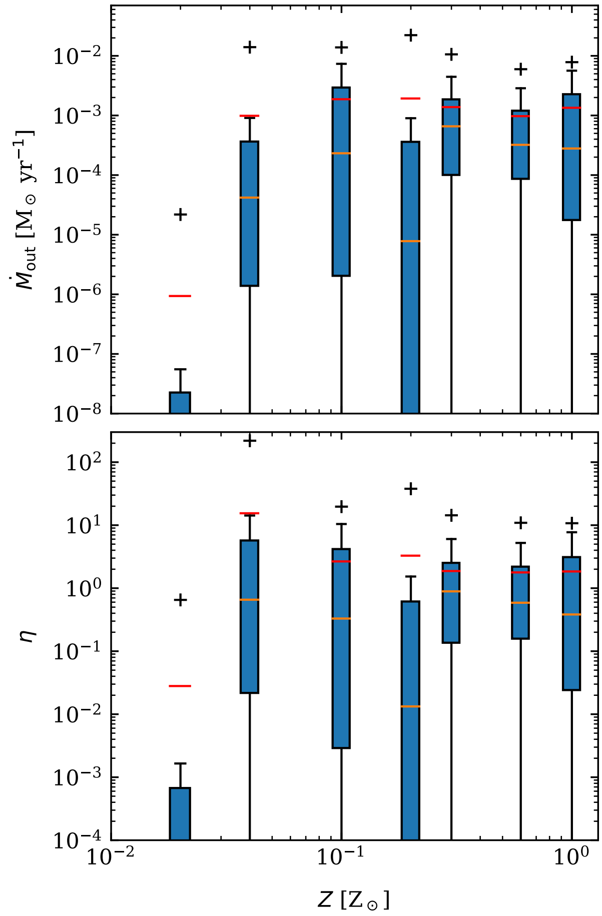

Figure 16. Box plot of the distributions of $\dot{M}_{\rm out}$ (top panel), and of the mass loading η (bottom panel), as a function of metallicity. The orange lines are the median of each distribution, the red lines the mean. The boxes extend from the 75th percentile down to the 25th percentile. The plus markers represent the maximum of each distribution. We observe no strong correlation of the $\dot{M}_{\rm out}$ with Z for $Z > 0.1\ Z_\odot$. The most metal-poor run does not have enough SNe to experience a strong outflow. A similar behaviour is observed for η.

been shown in Fig. C1 of Girichidis (2021). The acceleration due to gravity is defined as

$$a_{\rm grav} = -\frac{d\Phi_{\rm tot}}{dz}, \tag{21}$$

where $\Phi_{\rm tot}$ is the total gravitational potential, which takes into account the contributions of gas, sink particles, the external potential due to the presence of an old stellar population, and dark matter. We calculate all the accelerations in our 3D box, and then we compute the vertical acceleration profiles taking into account all the cells j present in a slice k, with the thickness of one cell, and averaging in mass as

$$a_k = \frac{\sum_j m_{j,\,k} a_{j,\,k}}{\sum_j m_{j,\,k}} \tag{22}$$

where $m_{j,\,k}$ is the mass of the $j^{\rm th}$ cell in the $k^{\rm th}$ slice.

The vertical profiles of the total acceleration, computed as $a_i + a_{\rm grav}$, are shown as black lines in Fig. 17. For better comprehension, the red-shaded regions in Fig. 17 indicate accelerations that push the gas out of the midplane in the outward direction - both for positive and negative z - and the turquoise-shaded regions indicate accelerations that push the gas back to the midplane.

We notice that in all runs $a_{\rm CR}$ is almost zero near the midplane and up to 100 km s^{-1} Myr^{-1} in the outward direction for higher heights, helping to lift the gas off the midplane, which is in agreement with the results from Fig. 8 in Girichidis et al. (2018a). On the other hand, $a_{\rm th}$ is either almost zero or it weakly pushes the gas out of the midplane for the first few hundred parsec, and inward for larger heights. The profiles for $a_{\rm CR}$ and $a_{\rm th}$ are similar in shape but opposite in sign,

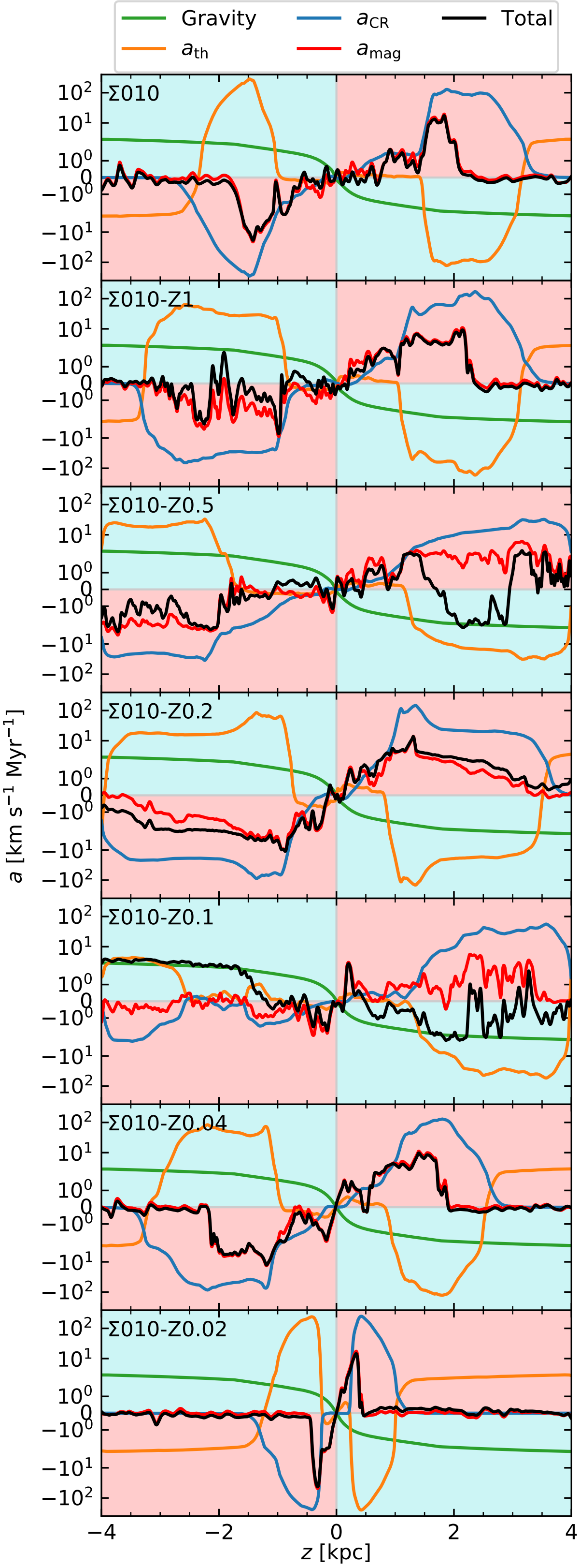

Figure 17. Vertical acceleration profiles for all runs. We consider the acceleration due to CR (blue), thermal (orange), turbulent (purple), magnetic (red) pressure gradients, as well as the acceleration due to total gravity (green). The black line is the sum of these five accelerations. The red-shaded regions indicate the accelerations that push the gas in the outward direction from the midplane, the turquoise-shaded ones those in the inward direction.

for many heights, therefore, they tend to compensate each other. This occurs because thermal pressure dominates in high-temperature regions, where the gas is heated by supernovae, while CR pressure is more significant in colder regions. At the interfaces between these regions, the pressure gradients have opposite signs, resulting in their partial cancellation. If there were regions with both high (or both low) thermal and CR pressure, they would rapidly expand or collapse, causing one form of pressure to quickly dominate over the other. Since $a_{\rm th}$ and $a_{\rm CR}$ tend to compensate each other, the total acceleration is dominated by the acceleration due to the magnetic pressure gradient. However, for the Σ010-Z0.02 run, the total acceleration is significant only within 500 pc from the midplane, whereas the gas at higher heights experiences almost no acceleration. This explains why the values of $\dot{M}_{\rm out}$ measured at 1 kpc shown in Fig. 16 for Σ010-Z0.02 are much lower compared to the other runs. A more detailed analysis of how these different accelerations impact the dynamics of the ISM will be presented in a following paper.

4 DISCUSSION

4.1 Validity of the model

In Table 1 we have compared the metallicity of our runs with that of known real galaxies. In this regard, it is good to remember that such galaxies might have different conditions with respect to those of our runs, e.g. a different gas surface density, strength of the magnetic field, stellar surface density, etc., so a direct comparison is not trivial. In our simulations many parameters can be fine-tuned in order to get more realistic results to be compared to observations; therefore, the parameter space that can be analysed with our simulations is quite large. However, given that our computational resources are limited, we need to restrict ourselves to a set of parameters for which it is also possible to compare with our previous work. Since in this study we are interested in understanding the effects of metallicity on the ISM, we choose the same setup as in Brugaletta et al. 2025, which adds the implementation of a variable CR ionisation rate to the setup used in Rathjen et al. 2025, and we change only the metallicity, the metal abundances and the dust-to-gas ratio, as already described in Sec. 2.8. SILCC setups have been originally implemented to study environments in solar-neighbourhood conditions, therefore the only change in metallicity and dust-to-gas ratio might not be enough to accurately describe the metal-poor ISM. In our treatment of low-metallicity environments we are neglect that nearby dwarf galaxies with these metallicities might have a much higher gas surface density, for which they could cool more efficiently and form more stars. For example, a gas surface density in the range 10 – 60 $\mathrm{M}_\odot\ \mathrm{pc}^{-2}$ has been observed in the LMC (see Fig. 7 in Hughes et al. 2010), 10 – 200 $\mathrm{M}_\odot\ \mathrm{pc}^{-2}$ in the SMC (see e.g. Fig. 3 in Bolatto et al. 2011), and up to 100 $\mathrm{M}_\odot\ \mathrm{pc}^{-2}$ in IZw18 (Lelli et al. 2012). Therefore, if a comparison with a specific galaxy is intended, our parameters would have to be fine-tuned to match those of the target environment.

4.2 Comparison to previous works

Hu et al. (2016, 2017) simulate an isolated dwarf galaxy employing a similar chemical network based on Nelson & Langer (1997); Glover & Mac Low (2007a); Glover & Clark (2012b) to treat non-equilibrium cooling and chemistry. They also model a variable ISFR (in Hu et al. 2017), star formation and stellar feedback. They assume a constant CR ionization rate $\zeta = 10^{-18}\ \mathrm{s}^{-1}$, and a fixed metallicity of 0.1 $\mathrm{Z}_\odot$. The G1D01 run in Hu et al. (2016) is the most similar to our

Σ010-Z0.1 run, however with a fixed $G_0 = 1.7$. The MF of formed cold gas in this run is around 2-3%, an order of magnitude lower than what we find for the Σ010-Z0.1 run (see Table 2). This difference can be traced back to the assumption of fixed G_0 and ζ parameters. The PE-PI-SN run in Hu et al. (2017) is the most similar to our Σ010-Z0.1 run. This run has a $\Sigma_{\rm SFR}$ of around 2×10^{-5} M$_\odot$ yr^{-1} kpc^{-2} at a gas surface density of around 1 M$_\odot$ pc^{-2}, whereas in our Σ010-Z0.1 we have a mean $\Sigma_{\rm SFR} = 7 \times 10^{-4}$ M$_\odot$ yr^{-1} kpc^{-2} at a gas surface density of 10 M$_\odot$ pc^{-2}. Scaling the $\Sigma_{\rm SFR}$ value of the PE-PI-SN run by the gas surface density of Σ010-Z0.1, we obtain a value similar to the $\Sigma_{\rm SFR}$ for the Σ010-Z0.1 run.

Lahén et al. (2020) simulate a gas-rich dwarf galaxy merger, adopting a metallicity of 0.1 Z$_\odot$, and the same chemical network as in Hu et al. (2016). Between 0 and 100 Myr, the $\Sigma_{\rm SFR}$ they find is around 10^{-3} M$_\odot$ yr^{-1} kpc^{-2}, which is in accordance with our mean value for the Σ010-Z0.1 run. With a similar setup, Lahén et al. (2023) simulate a dwarf galaxy with an initial metallicity of around 0.02 Z$_\odot$, including stellar feedback as stellar winds, supernovae and radiation, by means of the BoOST stellar tracks. They find a $\Sigma_{\rm SFR}$ in range 10^{-5}–10^{-3} M$_\odot$ yr^{-1} kpc^{-2}, which is in accordance with the median value reported in Table 5 for the Σ010-Z0.02 run.

Whitworth et al. (2022) simulate an isolated dwarf galaxy with varying metallicity and UV strength, non-equilibrium chemistry, shielding, and supernova feedback. The chosen values of metallicity are 0.1 Z$_\odot$ and 0.01 Z$_\odot$, that can be compared with our Σ010-Z0.1 and Σ010-Z0.02. They assume a fixed value of G_0 in the range 0.017 – 0.17 and a fixed ζ in the range $3 \times 10^{-19} - 3 \times 10^{-18}$ s^{-1}. They find that the MF of H$_2$ is always lower than 1%, it scales with metallicity and decreases for higher values of the G_0 parameter. The MF of cold gas scales with metallicity when G_0 is fixed, and it anticorrelates with G_0 at fixed metallicity. The MF of cold gas they find at 0.1 Z$_\odot$ and 0.01 Z$_\odot$ is around one to two orders of magnitude lower than the values reported in Table 2 for the Σ010-Z0.1 and Σ010-Z0.02 runs. This difference can be partially explained as we define the cold gas phase for $T < 300$ K, whereas Whitworth et al. (2022) use a temperature threshold of 100 K. Moreover, they did not observe a significant effect on the SFR when reducing both the metallicity and UV field strength by a factor of 10.

Our runs have a similar setup to the TIGRESS-NCR simulations presented in Kim et al. 2024, where the influence of metallicity is investigated with respect to the pressure-regulated feedback-modulated star formation theory. They consider metallicities in a range 0.1 – 3 Z$_\odot$ and gas surface densities in the range 5 – 150 M$_\odot$ pc^{-2}. They scale the dust abundance linearly with metallicity, except for the runs with $Z = 0.1$ Z$_\odot$ where they assume a dust abundance of 0.025. The simulations include supernova feedback, metal cooling, PE heating, heating and cooling processes due to H$_2$ formation and dissociation processes, among others. They also add CR heating assuming that the CR ionisation rate ζ (in our nomenclature) scales as $\zeta \propto \Sigma_{\rm SFR}/\Sigma_{\rm gas}$. Here the $\Sigma_{\rm SFR}$ is computed from the stars formed in the past 40 Myr of evolution. This scaling is such that a value $\zeta_0 = 2 \times 10^{-16}$ s^{-1} is assumed in solar-neighbourhood conditions when $\Sigma_{\rm SFR} = 2.5 \times 10^{-3}$ M$_\odot$ yr^{-1} kpc^{-2} and $\Sigma_{\rm gas} = 10$ M$_\odot$. In addition to this linear scaling, they include an attenuation $\zeta \propto N_{\rm eff}^{-1}$, with $N_{\rm eff} = 1.5 \times 10^{21}$ cm$^{-2}(n_{\rm H}/100$ cm$^{-3})^{0.3}$, when the local column density exceeds $N_0 = 9.35 \times 10^{20}$ cm^{-2} (Neufeld & Wolfire 2017). Given our gas surface density of 10 M$_\odot$ pc^{-2}, we can only compare our runs with their R8-Z simulations, which adopt an initial gas surface density of 12 M$_\odot$ pc^{-2}. In the case of solar metallicity and 0.1 Z$_\odot$, they find $\Sigma_{\rm SFR}$ to be about a factor of two higher. However, they also observe that the $\Sigma_{\rm SFR}$ anticorrelates with metallicity.

4.3 Caveats

In our simulations, we assume for simplicity that the dust-to-gas ratio always scales linearly with respect to metallicity. However, some studies have pointed out that this assumption might not hold in very metal-poor environments. Rémy-Ruyer et al. (2014) analyse the variation of the dust-to-gas ratio with metallicity for a set of 126 galaxies, and find that the observed dust-to-gas ratio vs metallicity relation cannot be described with a power law with a single exponent of -1, as for metallicities below that of the SMC this relation becomes steeper. This break in the power law could affect several of our low-metallicity runs. Feldmann (2015) identifies a critical value of the metallicity for which the linear dependence breaks down, which depends on the competition of dust growth in the ISM and the dilution of the gas by infall of dust-poor gas onto the galactic plane. Bialy & Sternberg (2019) study the thermal properties and the multiphase behaviour of the gas for varying metallicity, down to very metal-poor conditions. For the scaling of the dust-to-gas ratio they assume a linear dependence for $Z \geq 0.2$ Z$_\odot$, and for lower values a broken power law of the kind $0.2 \times (Z/0.2\ {\rm Z}_\odot)^3$. Kim et al. (2023) compare a linear scaling of the dust-to-gas ratio as a function of metallicity with the prescription of Bialy & Sternberg (2019). They note that a superlinear dependence of the dust abundance with respect to the gas metallicity decreases the strength of the PE heating and recombination cooling with respect to the CR heating, which becomes dominant in metal-poor environments. As the CR heating does not depend on the metallicity, this means that a lower overall heating rate is present, and the gas can cool down more efficiently. In a previous related work (Brugaletta et al. 2025), we have investigated how a variable CR ionisation rate affects the cooling of the gas at very low metallicity ($Z = 0.02$ Z$_\odot$), as well as the impact of a different scaling (linear, or power law) of the dust-to-gas ratio with metallicity at 0.02 Z$_\odot$. We have observed that using the scaling proposed by Bialy & Sternberg (2019) instead of a linear relation results in a slightly enhanced average star formation rate at $Z = 0.02$ Z$_\odot$, since the photoelectric heating is lower because of the reduced dust-to-gas ratio. However, at higher metallicities up to 0.1 Z$_\odot$ this difference might become more and more important, since photoelectric heating is more efficient at higher metallicity.

Moreover, for simplicity, we have assumed that the abundances of C, O, and Si scale linearly with the metallicity. However, these elements, especially carbon and oxygen, are enriched differently due to stellar nucleosynthesis. Furthermore, since at low metallicity a smaller fraction of metals is locked up in dust grains, this changes the relative abundances of C, O and Si. Bisbas et al. (2024) study the impact of the α-enhanced gas on the abundances of C, C$^+$ and CO, concluding that the relative carbon-to-oxygen abundance is of high importance at low metallicity. In this regard, we do not model chemical enrichment from stellar evolution, which would change our local abundances of metals, mainly affecting our metal-line cooling rates.

Finally, we assume that all the massive stars formed in our simulations will end their life as supernovae. However, at sub-solar metallicities this assumption might not be correct, as pointed out by Heger et al. (2003). In fact, metal-poor single massive stars above 40 M$_\odot$ are predicted to collapse directly into a black hole, whereas those in range $25 < M < 40$ M$_\odot$ produce a black hole by fallback, without exploding as supernovae. Therefore, in our prescription, we tend to overestimate of around 25% the impact of supernova feedback in low-metallicity environments.

5 SUMMARY AND CONCLUSIONS

In this work, we analyse the structure and evolution of the ISM at low metallicity, by means of a set of SILCC simulations. We include stellar feedback in the form of radiation, stellar winds, cosmic rays, and supernovae. Considering a gas surface density of 10 $M_\odot$ pc^{-2}, a variable strength of the interstellar radiation field in Habing units G_0, and a variable CR ionisation rate ζ. We vary the initial metallicity of the gas as well as the metallicity of the stellar evolutionary tracks (BoOST) from a solar value down to 0.02 $Z_\odot$. We employ a non-equilibrium chemical network to follow the time evolution of the hydrogen and carbon abundances, which is particularly important to understand the heating and cooling rates for metal-poor environments. We add an additional simulation at solar metallicity using the Geneva stellar models, employed in previous SILCC works. We highlight our most important results in the following.

Metal-poor environments tend to be warmer than media at solar metallicity. This is due to the fact that metals are the main coolants for the atomic gas up to a few 10^6 K, therefore a lack in metals means a higher temperature of the medium on average. We find that the mass fraction of cold gas decreases from 61% at solar metallicity to 2.3% at 0.02 $Z_\odot$. Moreover, we find that the warm medium (both neutral and ionized) is the dominant phase in mass and volume filling fractions at low metallicity. The amount of hot gas is dependent on the number of supernovae, and this decreases for lower metallicity.

We find that the molecular hydrogen mass fraction scales linearly with metallicity, with a slope of 0.13 ± 0.01 when considering the total H_2, and a slope of 0.42 ± 0.04 if we take into account only the dense gas with $\rho > 10^{-22}$ g cm^{-3}. We also find that the mass of H_2 found in the diffuse phase ($\rho < 10^{-22}$ g cm^{-3}) is around 50% for the most metal-rich runs and it drops to around 30% for the most metal-poor run. Moreover, we find that the density of H_2 spans a wide range, from 10^{-26} to slightly above 10^{-20} g cm^{-3} for all runs. We measure H_2 temperatures up to 600 K for the most metal-rich runs, and the maximum of the temperature anticorrelates with metallicity.

Using a dendrogram analysis, we find that metallicity is not the main physical parameter affecting the fragmentation of the gas in the range 0.1–1 $Z_\odot$. However, at lower metallicity, the gas forms a smaller number of fragments. We see that low-metallicity fragments are more diffuse and bigger than at solar metallicity, however with comparable masses. The mass fraction of H_2 present in the fragments also decreases with metallicity. The degree of fragmentation of the gas directly affects the star formation rate.

We observe that stars in low-metallicity runs form in a medium that experiences lower PE and CR heating rates, compared to the solar-neighbourhood values. This is due to two effects, namely the smaller number of formed stars, that decrease both the PE and CR heating rates; and less efficient cooling of the gas implies that lower PE and CR heating rates are needed to allow the gas to collapse and form stars. We also see that in low-metallicity runs, stars are formed in atomic gas, in contrast to solar-metallicity environments where star formation occurs in molecular gas.

Regarding stellar feedback, we note that the contribution of winds increases for higher metallicity, and is higher than the contribution from supernovae in the same runs, if the metallicity is higher than 0.1 $Z_\odot$. The distribution of ζ varies between 10^{-18} and 10^{-14} s^{-1} irrespective of the metallicity, except for the two most metal-poor runs, which have less supernovae.

The distribution of mass outflow rates does not show dramatic changes with metallicity, except for the run with 0.02 $Z_\odot$ metallicity. This implies that, if the star formation rate is high enough, the mass outflow rate does not strongly depend on the metallicity at fixed gas surface density.

We investigate the role of the thermal, magnetic and CR pressures in determining the acceleration of the gas in the vertical direction. Accelerations due to thermal and CR pressures tend to balance each other, therefore the total acceleration is dominated by the magnetic pressure gradient, and it is directed in the outward direction in most cases.

ACKNOWLEDGEMENTS

VB thanks Masato Kobayashi for the fruitful discussions regarding gas fragmentation at low metallicity. VB, SW, TER, DS, and PCN thank the Deutsche Forschungsgemeinschaft (DFG) for funding through the SFB 1601 “Habitats of massive stars across cosmic time” (sub- projects B1, B4 and B6). SW, TER, and DS further acknowledge support by the project ”NRW-Cluster for data-intensive radio astronomy: Big Bang to Big Data (B3D)” funded through the programme ”Profilbildung 2020”, an initiative of the Ministry of Culture and Science of the State of North Rhine-Westphalia. VB and SW thank the Bonn-Cologne Graduate School. TN acknowledges support from the DFG under Germany’s Excellence Strategy - EXC-2094 - 390783311 from the DFG Cluster of Excellence "ORIGINS". PG and SCOG acknowledge funding by the European Research Council via the ERC Synergy Grant “ECOGAL” (project ID 855130). RW acknowledges support by the institutional project RVO:67985815 and by the INTER-COST LUC24023 project of the Czech Ministry of Education, Youth and Sports. SCOG also acknowledges support from the Heidelberg Cluster of Excellence EXC 2181 (Project-ID 390900948) ‘STRUCTURES: A unifying approach to emergent phenomena in the physical world, mathematics, and complex data’ supported by the German Excellence Strategy. The software used in this work was in part developed by the DOE NNSA-ASC OASCR Flash Centre at the University of Rochester (Fryxell et al. 2000; Dubey et al. 2009). Part of the data visualisation has been done with the Python package YT (Turk et al. 2011) and the FLASH_AMR_TOOLS Python package[2] developed by PCN. The data analysis has been performed using the following Python packages: NUMPY (van der Walt et al. 2011), MATPLOTLIB (Hunter 2007), H5PY (Collette et al. 2020), IPYTHON (Perez & Granger 2007), SCIPY (Virtanen et al. 2020), ASTRODENDRO[3].

DATA AVAILABILITY

The derived data underlying this article will be shared on reasonable request to the corresponding author. The simulation data will be made available on the SILCC data web page: `http://silcc.mpa-garching.mpg.de`.

REFERENCES

Ackermann M., Ajello M., Allafort A., et al., 2013, Science, 339, 807
Aller L. H., 1942, ApJ, 95, 52
Aloisi A., Tosi M., Greggio L., 1999, AJ, 118, 302
Aloisi A., Clementini G., Tosi M., et al., 2007, ApJ, 667, L151
Asplund M., Grevesse N., Sauval A. J., Scott P., 2009, ARA&A, 47, 481
Bakes E. L. O., Tielens A. G. G. M., 1994, ApJ, 427, 822

---

[2] `https://pypi.org/project/flash-amr-tools/`
[3] `http://www.dendrograms.org/`

Balser D. S., Rood R. T., Bania T. M., et al., 2011, ApJ, 738, 27
Bate M. R., 2019, MNRAS, 484, 2341
Bate M. R., 2025, MNRAS, 537, 752
Bate M. R., Bonnell I. A., Price N. M., 1995, MNRAS, 277, 362
Baumgardt H., Parmentier G., et al., 2013, MNRAS, 430, 676
Bekki K., Beasley M. A., Forbes D. A., Couch W. J., 2004, ApJ, 602, 730
Belfiore F., et al., 2017, MNRAS, 469, 151
Bergin E. A., Hartmann L. W., et al., 2004, ApJ, 612, 921
Bialy S., Sternberg A., 2019, ApJ, 881, 160
Bigiel F., Leroy A., Walter F., et al., 2008, AJ, 136, 2846
Bisbas T. G., Zhang Z.-Y., Gjergo E., et al., 2024, MNRAS, 527, 8886
Bohlin R. C., Savage B. D., Drake J. F., 1978, ApJ, 224, 132
Bolatto A. D., Leroy A. K., Rosolowsky E., et al., 2008, ApJ, 686, 948
Bolatto A. D., Leroy A. K., Jameson K., et al., 2011, ApJ, 741, 12
Bortolini G., Östlin G., Habel N., et al., 2024, A&A, 689, A146
Brott I., de Mink S. E., Cantiello M., et al., 2011, A&A, 530, A115
Brugaletta V., Walch S., Naab T., et al., 2025, MNRAS, 537, 482
Cameron A. J., Saxena A., Bunker A. J., et al., 2023, A&A, 677, A115
Chevance M., Madden S. C., Lebouteiller V., et al., 2016, A&A, 590, A36
Clark P. C., Glover S. C. O., Klessen R. S., 2012, MNRAS, 420, 745
Collette A., Kluyver T., Caswell T. A., et al., 2020, h5py/h5py: 3.1.0, doi:10.5281/zenodo.4250762
Contreras Ramos R., Annibali F., Fiorentino G., et al., 2011, ApJ, 739, 74
Corbett Moran C., Grudić M. Y., Hopkins P. F., 2018, arXiv e-prints, p. arXiv:1803.06430
Curti M., D'Eugenio F., Carniani S., et al., 2023, MNRAS, 518, 425
Dalgarno A., McCray R. A., 1972, ARA&A, 10, 375
Dinnbier F., Walch S., 2020, MNRAS, 499, 748
Doan S., et al., 2024, arXiv e-prints, p. arXiv:2408.04774
Draine B. T., 2011, Physics of the Interstellar and Intergalactic Medium
Draine B. T., Dale D. A., Bendo G., et al., 2007, ApJ, 663, 866
Dubey A., Reid L. B., Fisher R., 2008, Physica Scripta, T132, 014046
Dubey A., Reid L. B., et al., 2009, arXiv e-prints, p. arXiv:0903.4875
Dufour R. J., Esteban C., Castaneda H. O., 1996, ApJ, 471, L87
Ekström S., et al., 2011, in Neiner C., Wade G., Meynet G., Peters G., eds, IAU Symposium Vol. 272, Active OB Stars: Structure, Evolution, Mass Loss, and Critical Limits. pp 62–72 (`arXiv:1010.3838`), doi:10.1017/S1743921311009987
Ekström S., Georgy C., et al., 2012, A&A, 537, A146
Elmegreen B. G., 1989, ApJ, 338, 178
Federrath C., Banerjee R., Clark P. C., et al., 2010, ApJ, 713, 269
Feldmann R., 2015, MNRAS, 449, 3274
Field G. B., Goldsmith D. W., Habing H. J., 1969, ApJ, 155, L149
Fryxell B., Olson K., Ricker P., et al., 2000, ApJS, 131, 273
Fujii K., Minamidani T., Mizuno N., et al., 2014, ApJ, 796, 123
Fukushima H., Yajima H., Sugimura K., et al., 2020, MNRAS, 497, 3830
Garnett D. R., Skillman E. D., Dufour R. J., et al., 1997, ApJ, 481, 174
Gatto A., Walch S., et al., 2015, MNRAS, 449, 1057
Gatto A., Walch S., Naab T., et al., 2017, MNRAS, 466, 1903
Girichidis P., 2021, MNRAS, 507, 5641
Girichidis P., Walch S., et al., 2016a, MNRAS, 456, 3432
Girichidis P., Naab T., Walch S., et al., 2016b, ApJ, 816, L19
Girichidis P., Naab T., Hanasz M., et al., 2018a, MNRAS, 479, 3042
Girichidis P., Seifried D., et al., 2018b, MNRAS, 480, 3511
Girichidis P., Pfrommer C., Hanasz M., et al., 2020, MNRAS, 491, 993
Glassgold A. E., Langer W. D., 1974, ApJ, 193, 73
Glover S. C. O., 2003, ApJ, 584, 331
Glover S. C. O., Clark P. C., 2012a, MNRAS, 421, 9
Glover S. C. O., Clark P. C., 2012b, MNRAS, 421, 116
Glover S. C. O., Clark P. C., 2012c, MNRAS, 426, 377
Glover S. C. O., Clark P. C., 2014, MNRAS, 437, 9
Glover S. C. O., Mac Low M.-M., 2007a, ApJS, 169, 239
Glover S. C. O., Mac Low M.-M., 2007b, ApJ, 659, 1317
Gnat O., Ferland G. J., 2012, ApJS, 199, 20
Goldman I., 2007, arXiv e-prints, pp astro–ph/0703793
Goldsmith P. F., Langer W. D., 1978, ApJ, 222, 881
Górski K. M., Hivon E., et al., 2005, ApJ, 622, 759
Grishunin K., Weiss A., Colombo D., et al., 2024, A&A, 682, A137
Guadarrama R., Vorobyov E. I., Rab C., et al., 2022, A&A, 667, A28
Habing H. J., 1968, Bull. Astron. Inst. Netherlands, 19, 421
Haid S., Walch S., Seifried D., et al., 2018, MNRAS, 478, 4799
Heger A., Fryer C. L., et al., 2003, ApJ, 591, 288
Heintz K. E., Giménez-Arteaga C., Fujimoto S., et al., 2023, ApJ, 944, L30
Hollenbach D., McKee C. F., 1989, ApJ, 342, 306
Hu C.-Y., Naab T., Walch S., et al., 2016, MNRAS, 458, 3528
Hu C.-Y., Naab T., Glover S. C. O., et al., 2017, MNRAS, 471, 2151
Hughes A., Wong T., Ott J., et al., 2010, MNRAS, 406, 2065
Hunter J. D., 2007, Computing in Science & Engineering, 9, 90
Issa M. R., MacLaren I., Wolfendale A. W., 1990, A&A, 236, 237
Jameson K. E., et al., 2016, ApJ, 825, 12
Jameson K. E., Bolatto A. D., Wolfire M., et al., 2018, ApJ, 853, 111
Jeřábková T., Hasani Zonoozi A., et al., 2018, A&A, 620, A39
Joshi P. R., Walch S., Seifried D., et al., 2019, MNRAS, 484, 1735
Ju M., Wang X., Jones T., et al., 2025, ApJ, 978, L39
Kennicutt Jr. R. C., Calzetti D., Walter F., et al., 2007, ApJ, 671, 333
Kim C.-G., Ostriker E. C., 2015, ApJ, 802, 99
Kim J.-G., Gong M., Kim C.-G., et al., 2023, ApJS, 264, 10
Kim C.-G., et al., 2024, ApJ, 972, 67
Kippenhahn R., Weigert A., Weiss A., 2012, Stellar Structure and Evolution, doi:10.1007/978-3-642-30304-3.
Krumholz M. R., 2012, ApJ, 759, 9
Krumholz M. R., McKee C. F., Tumlinson J., 2009, ApJ, 693, 216
Krumholz M. R., Leroy A. K., McKee C. F., 2011, ApJ, 731, 25
Lahén N., Naab T., Johansson P. H., et al., 2020, ApJ, 891, 2
Lahén N., Naab T., Kauffmann G., et al., 2023, MNRAS, 522, 3092
Langer N., Maeder A., 1995, A&A, 295, 685
Legrand F., 2000, A&A, 354, 504
Legrand F., Tenorio-Tagle G., Silich S., et al., 2001, ApJ, 560, 630
Leitherer C., Robert C., Drissen L., 1992, ApJ, 401, 596
Lelli F., Verheijen M., Fraternali F., et al., 2012, A&A, 537, A72
Leroy A. K., Walter F., Brinks E., et al., 2008, AJ, 136, 2782
Leroy A. K., Bolatto A., Bot C., et al., 2009, ApJ, 702, 352
Lian J., Bergemann M., Pillepich A., et al., 2023, Nature Astronomy, 7, 951
Maeder A., Meynet G., 2000, ARA&A, 38, 143
Maloney P., Black J. H., 1988, ApJ, 325, 389
McKee C. F., 1989, ApJ, 345, 782
Méndez-Delgado J. E., Amayo A., et al., 2022, MNRAS, 510, 4436
Meschin I., Gallart C., et al., 2013, MNRAS, 438, 1067
Mingozzi M., Belfiore F., Cresci G., et al., 2020, A&A, 636, A42
Murray C. E., Peek J. E. G., Di Teodoro E. M., et al., 2019, ApJ, 887, 267
Musella I., Marconi M., Fiorentino G., et al., 2012, Memorie della Societa Astronomica Italiana Supplementi, 19, 146
Naab T., Ostriker J. P., 2017, ARA&A, 55, 59
Nava L., Gabici S., 2013, MNRAS, 429, 1643
Navarro J. F., Frenk C. S., White S. D. M., 1996, ApJ, 462, 563
Nelson R. P., Langer W. D., 1997, ApJ, 482, 796
Neufeld D. A., Wolfire M. G., 2017, ApJ, 845, 163
Omukai K., Tsuribe T., Schneider R., et al., 2005, ApJ, 626, 627
Omukai K., Hosokawa T., Yoshida N., 2010, ApJ, 722, 1793
Osterbrock D. E., 1988, Publications of the Astronomical Society of the Pacific, 100, 412
Padovani M., Galli D., Glassgold A. E., 2009, A&A, 501, 619
Padovani M., Bialy S., Galli D., et al., 2022, A&A, 658, A189
Palla F., Salpeter E. E., Stahler S. W., 1983, ApJ, 271, 632
Papadopoulos P. P., Thi W. F., Viti S., 2002, ApJ, 579, 270
Pelupessy F. I., Papadopoulos P. P., van der Werf P., 2006, ApJ, 645, 1024
Perez F., Granger B. E., 2007, Computing in Science & Engineering, 9, 21
Peters T., Naab T., Walch S., et al., 2017, MNRAS, 466, 3293
Pfrommer C., Pakmor R., et al., 2017, MNRAS, 465, 4500
Piatti A. E., 2023, MNRAS, 526, 391
Polzin A., Kravtsov A. V., Semenov V. A., et al., 2024, ApJ, 966, 172
Ramachandran V., Hamann W. R., et al., 2019, A&A, 625, A104
Rathjen T.-E., Naab T., et al., 2021, MNRAS, 504, 1039
Rathjen T.-E., Naab T., et al., 2023, MNRAS, 522, 1843
Rathjen T.-E., Walch S., Naab T., et al., 2025, MNRAS, 540, 1462
Rémy-Ruyer A., Madden, S. C. Galliano, F. et al., 2014, A&A, 563, A31

Rubele S., Kerber L., Girardi L., 2009, MNRAS, 403, 1156
Rubio M., Lequeux J., Boulanger F., 1993, A&A, 271, 9
Sabbi E., et al., 2009, arXiv e-prints, p. arXiv:0908.3500
Salpeter E. E., 1955, ApJ, 121, 161
Sandstrom K. M., Bolatto A. D., Bot C., et al., 2012, ApJ, 744, 20
Savaglio S., Glazebrook K., Le Borgne D., et al., 2005, ApJ, 635, 260
Schruba A., Leroy A. K., Walter F., et al., 2011, AJ, 142, 37
Searle L., 1971, ApJ, 168, 327
Seifried D., Walch S., Girichidis P., et al., 2017, MNRAS, 472, 4797
Sembach K. R., Howk J. C., Ryans R. S. I., et al., 2000, ApJ, 528, 310
Sextl E., Kudritzki R.-P., Burkert A., et al., 2024, ApJ, 960, 83
Sharda P., Amarsi A. M., et al., 2023, MNRAS, 518, 3985
Shaver P. A., McGee R. X., Newton L. M., et al., 1983, MNRAS, 204, 53
Smart B. M., Haffner L. M., Barger K. A., et al., 2019, ApJ, 887, 16
Strong A. W., Moskalenko I. V., et al., 2007, Annual Review of Nuclear and Particle Science, 57, 285
Szécsi D., Agrawal P., Wünsch R., et al., 2022, A&A, 658, A125
Tacchella S., Johnson B. D., et al., 2023, MNRAS, 522, 6236
Tanaka K. E. I., Tan J. C., Zhang Y., et al., 2018, ApJ, 861, 68
Tielens A. G. G. M., 2005, The Physics and Chemistry of the Interstellar Medium
Togi A., Smith J. D. T., 2016, ApJ, 830, 18
Tremonti C. A., Heckman T. M., Kauffmann G., et al., 2004, ApJ, 613, 898
Turk M. J., Smith B. D., et al., 2011, ApJS, 192, 9
Virtanen P., et al., 2020, Nature Methods, 17, 261
Walch S., Wünsch R., et al., 2011, ApJ, 733, 47
Walch S. K., Whitworth A. P., et al., 2012, MNRAS, 427, 625
Walch S., Girichidis P., et al., 2015, MNRAS, 454, 238
Walter F., Cannon J. M., Roussel H., et al., 2007, ApJ, 661, 102
Weiß A., Grishunin K., Czubkowski N., et al., 2023, in Ossenkopf-Okada V., Schaaf R., Breloy I., Stutzki J., eds, Physics and Chemistry of Star Formation: The Dynamical ISM Across Time and Spatial Scales. p. 72
Welty D. E., Xue R., Wong T., 2012, ApJ, 745, 173
Whitcomb C. M., Smith J. D. T., Sandstrom K., et al., 2024, ApJ, 974, 20
Whitworth D. J., Smith R. J., et al., 2022, MNRAS, 510, 4146
Wolfire M. G., Hollenbach D., et al., 1995, ApJ, 443, 152
Wong T., Blitz L., 2002, ApJ, 569, 157
Wünsch R., Walch S., Dinnbier F., et al., 2018, MNRAS, 475, 3393
Wünsch R., Walch S., et al., 2021, MNRAS, 505, 3730
Wyse R. F. G., Silk J., 1989, ApJ, 339, 700
Yoon S. C., Langer N., Norman C., 2006, A&A, 460, 199
Zaritsky D., 1992, ApJ, 390, L73
Zwicky F., 1966, ApJ, 143, 192
van der Marel R. P., 2006, in Livio M., Brown T. M., eds, Vol. 17, The Local Group as an Astrophysical Laboratory. pp 47–71 (`arXiv:astro-ph/0404192`), doi:10.48550/arXiv.astro-ph/0404192
van der Walt S., Colbert S. C., Varoquaux G., 2011, Computing in Science & Engineering, 13, 22

APPENDIX A: STELLAR FEEDBACK AT DIFFERENT METALLICITIES

In the following paragraphs, we will express the metallicity of the stellar models in units of solar metallicity, assuming 1 $Z_\odot = 0.014$. Regarding the BoOST models, we compute their metallicity in solar units taking the value of Z reported in Table 1 from Szécsi et al. 2022 and dividing by 0.014.

A1 Massive star lifetime

In Fig. A1, we show how the lifetime of the stellar models depends on their initial (Zero Age Main Sequence, ZAMS) mass and metallicity. More massive stars have a briefer main sequence (Kippenhahn et al. 2012). A similar behaviour is observed for low–metallicity models, which are short-lived compared to metal-rich ones. Since metal-poor stars are more compact (Yoon et al. 2006, Ekström et al. 2011), and their convective core is larger and hotter, the region where nuclear burning is taking place is more expanded. Therefore, comparing two models with the same initial mass but different metallicity, the most metal–poor model will burn the same amount of fuel faster. However, the discrepancy seen between the Geneva and BoOST models is not only due to the different metallicities. In fact, BoOST models predict a larger convective core - due to a higher overshoot parameter - that brings more hydrogen from the outer layers into the burning regions. Hence, stars in the BoOST models exhaust their fuel sooner.

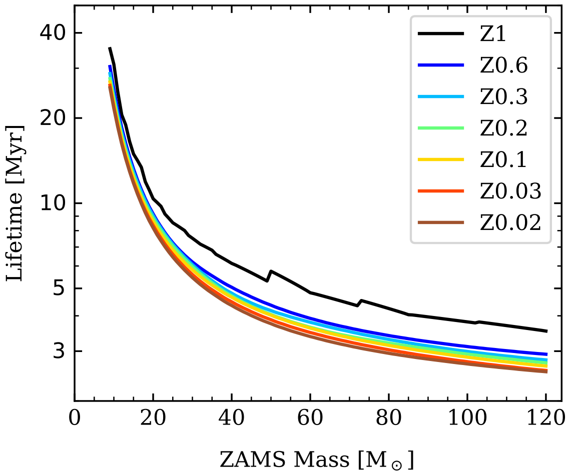

Figure A1. Lifetime of massive stars (in Myr) as a function of their initial mass (in M$_\odot$) for every considered stellar grid. The Z1 line refers to the models at solar metallicity from Ekström et al. 2012, whereas the others refer to the stellar models from Brott et al. 2011, Szécsi et al. 2022 with respectively $Z = 0.64\ Z_\odot$ (Z0.6), 0.34 $Z_\odot$ (Z0.3), 0.15 $Z_\odot$ (Z0.2), 0.075 $Z_\odot$ (Z0.1), 0.03 $Z_\odot$ (Z0.03), 0.015 $Z_\odot$ (Z0.02). Here we note two facts: the lifetime of a star decreases as a function of its initial mass, a well–known result from the theory of stellar evolution (see e.g. Kippenhahn et al. 2012). The second is that models with a lower metallicity live for a shorter time.

A2 Bolometric and wind luminosity

In the top panel of Fig. A2 the time evolution of the bolometric luminosity is shown for some representative models at the metallicities considered. The luminosity has a positive correlation with the initial mass of the stars, as dictated by the mass-luminosity relation (Kippenhahn et al. 2012) for which $L_{\rm bol} \sim M^{3.37}$. We also note that the bolometric luminosity increases with decreasing metallicity. As mentioned above, in metal–poor stars, nuclear burning takes place in a more extended region. The direct consequence is that the luminosity due to nuclear burning is higher, as well as the total luminosity radiated by the surface.

In the bottom panel of Fig. A2, the ratio $L_{\rm wind}/L_{\rm bol}$ of the wind luminosity to the bolometric luminosity is represented. The wind luminosity is the energy lost per unit time because of stellar winds, and is defined as

$$L_{\rm wind} = \frac{1}{2}\dot{M}_{\rm wind} \times v_{\rm wind}^2 \qquad \text{(A1)}$$

where $\dot{M}_{\rm wind}$ is the mass loss rate due to the wind and $v_{\rm wind}$ is the terminal velocity of the wind. As seen above, the bolometric luminosity increases with decreasing metallicity, and also the strength of winds is lower for metal-poor stars (Leitherer et al. 1992). From this follows

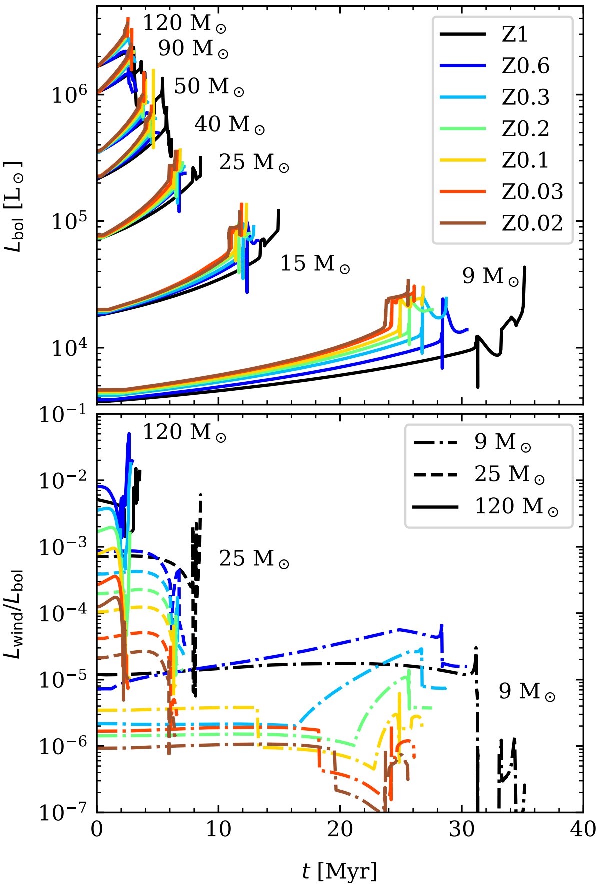

Figure A2. Evolution of the bolometric luminosity $L_{\rm bol}$ in time (upper panel) and ratio of the wind luminosity $L_{\rm wind}$ over $L_{\rm bol}$ in time (bottom panel) for some representative models at all considered metallicities. In the bottom panel we use solid lines for models with an initial mass of 120 M$_\odot$, dashed lines for 25 M$_\odot$ and dash-dotted lines for 9 M$_\odot$. In the top panel we note that $L_{\rm bol}$ depends both on the initial mass – the larger, the brighter – as well as on the metallicity, for which we have more luminous stars in low–metallicity conditions. In the bottom panel we observe that the ratio $L_{\rm wind}/L_{\rm bol}$ scales with the metallicity, as metal-poor stars have weaker winds and higher bolometric luminosities. Regarding the dependence $L_{\rm wind}/L_{\rm bol}$ with initial mass, this is dominated by the wind luminosity.

that the ratio $L_{\rm wind}/L_{\rm bol}$ scales with metallicity at fixed initial mass of the models. Moreover, this ratio has a positive correlation with initial mass, meaning that the wind luminosity dependence on the initial mass is stronger than the mass-luminosity relation.

A3 Ionizing radiation

Another quantity that is of interest when studying the effects of stellar feedback is the amount of radiation emitted by stars that is able to ionise the hydrogen atoms of the surrounding ISM. We assume the stars to be black bodies, such that their spectrum can be described using Planck's law. We can rewrite the latter as a function of $E = h\nu$, where h is the Planck constant and ν is the frequency of the emitted photons:

$$B_E = \frac{2E^3}{c^2h^2}\frac{1}{\exp\frac{E}{k_{\rm B}T} - 1} \tag{A2}$$

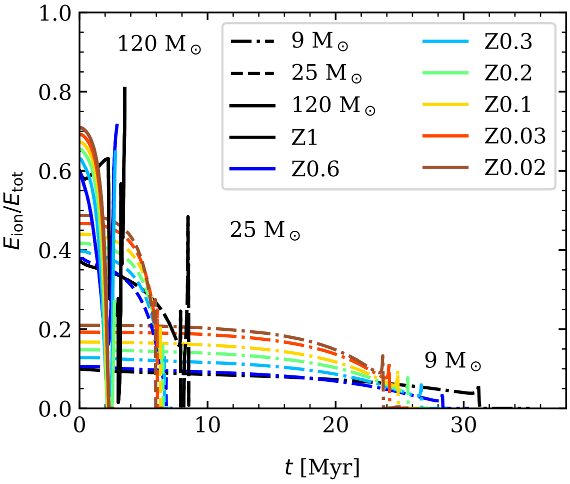

Figure A3. Ratio of the ionising radiation energy $E_{\rm ion}$ over the total radiation energy $E_{\rm tot}$ emitted by stars as a function of time. We use solid lines for the stellar models with initial mass of 120 M$_\odot$, dashed lines for 25 M$_\odot$ and dash-dotted lines for 9 M$_\odot$ models. We note that the fraction of ionising radiation increases with initial mass at the same metallicity, and scales with decreasing metallicity for fixed initial mass.

where c is the speed of light, k_B the Boltzmann constant and T the effective temperature of the star at a given time. Given that the ionisation energy for hydrogen is 13.6 eV, we can compute the fraction of ionising radiation as

$$\frac{E_{\rm ion}}{E_{\rm tot}} = \frac{\int_{13.6}^{\infty} B_E dE}{\int_0^{\infty} B_E dE} \tag{A3}$$

To be noted in this calculation is that the only parameter that actually depends on a given stellar model is the effective temperature at the surface of the star. Calculating the ratio from Eq. A3 for every timestep, we obtain its time evolution as shown in Fig. A3. We notice that low-metallicity models have a higher ionisation energy fraction compared to metal-rich models at the same initial mass and that the ionisation energy fraction scales with initial mass when fixing the metallicity. Both behaviours are a consequence of how the effective temperature of a star varies with metallicity and initial mass. In the first case, the higher effective temperature is due to lower opacities in metal-poor conditions (Kippenhahn et al. 2012). In the second case, the effective temperature of a star during the main sequence correlates with its mass (again, see Kippenhahn et al. 2012).

APPENDIX B: GAS FRAGMENTATION AS FUNCTION OF METALLICITY

We show in Fig. B1 the distributions for all runs that have already been discussed in Sec. 3.5. We note that the shown distributions behave similarly for metallicities larger than 0.1 Z$_\odot$, whereas they show a different behaviour for lower metallicities.

APPENDIX C: GAS SCALE HEIGHT

In Fig. C1 we show the evolution in time of the scale height of the disc, defined as the height $\pm z$, below and above the midplane, which contains 68% of the total mass of the gas present in the box. We note

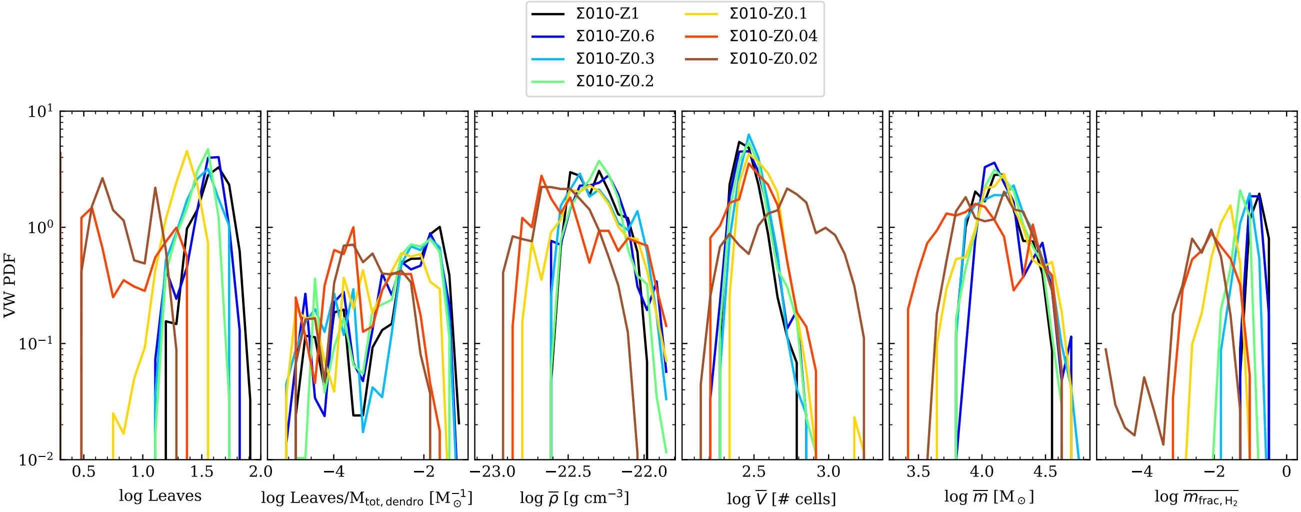

Figure B1. Same plot as Fig. 10, but showing the distributions computed for all runs.

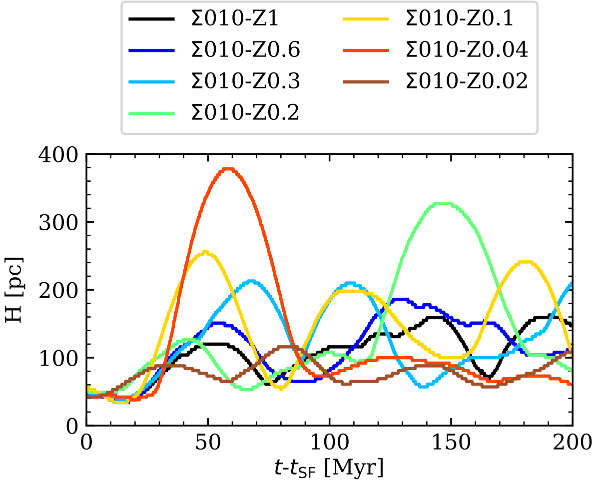

Figure C1. Scale height H of the disc as a function of time, for every run. H is defined as the height $\pm z$ around the midplane that encompasses 68% of the total mass in the box.

that the peaks in the scale height of the disc correspond to the peaks in the star formation rate surface density (see Fig. 13) for each run, but delayed by a few tens of Myr. This delay is due to the fact that the first SNe explode in a cold and dense environment; therefore, they have a lower efficiency. As more SNe go off, the gas near the midplane becomes warmer and stellar feedback is more effective in lifting the gas, therefore increasing the scale height of the disc. We notice that at low metallicity the disc becomes thicker because of the fact that a higher amount of warm gas is present (see Fig. 3). The exception is the Σ010-Z0.02 run, where the scale height remains around 90 – 100 pc due to the lack of a sufficient number of SNe.

CHAPTER 6

PAPER III

In this chapter, we present a novel study of the possibility of equilibrium conditions in SILCC simulations, and of the self-regulation of the interstellar medium. We employ the new method to calculate the cosmic rays ionization rate already presented in Chapter 4 (Paper I), and we apply our knowledge of low-metallicity environments, explored in Chapter 5 (Paper II).

6.1 Publication

This is an unpublished manuscript. The simulations, data analysis and the writing have been performed by Vittoria Brugaletta. The coauthors S. Walch, T. Naab, P. Girichidis and T.-E. Rathjen have engaged in meaningful discussions that have been determinant for the success of this work.

MNRAS **000**, 1–22 (2025) Preprint 1 July 2025 Compiled using MNRAS LaTeX style file v3.3

Investigating the importance of variability in the interstellar medium using SILCC simulations

Vittoria Brugaletta[1,2★], Stefanie Walch[1], Thorsten Naab[2], Tim-Eric Rathjen[1], Philipp Girichidis[3], Daniel Seifried[1], Pierre Colin Nürnberger[1], Richard Wünsch[4] and Simon C. O. Glover[3]
[1] *I. Physikalisches Institut, Universität zu Köln, Zülpicher Str. 77, 50937 Köln, Germany*
[2] *Max Planck Institute for Astrophysics, Karl-Schwarzschild-Str. 1, 85748 Garching, Germany*
[3] *Universität Heidelberg, Zentrum für Astronomie, Institut für Theoretische Astrophysik, Albert-Ueberle-Str. 2, D-69120 Heidelberg, Germany*
[4] *Astronomical Institute of the Czech Academy of Sciences, Boční II 1401, 141 00 Prague, Czech Republic*

Accepted XXX. Received YYY; in original form ZZZ

ABSTRACT

We investigate whether the interstellar medium (ISM) can attain a steady state, and how time variability in its governing processes influences its evolution. Using magnetohydrodynamic simulations within the SILCC framework, we incorporate non-equilibrium chemistry, detailed heating and cooling processes, anisotropic cosmic ray transport, and spatially and temporally varying far-UV backgrounds and cosmic ray ionisation rates. Feedback from massive stars is included via stellar winds, radiation (far-UV and ionising), supernovae, and cosmic rays. Our simulations span gas surface densities of 10–300 $\mathrm{M_{\odot}\,pc^{-2}}$ and metallicities of 0.02, 0.1, and 1 $\mathrm{Z_{\odot}}$. We test the applicability of the pressure-regulated, feedback-modulated (PRFM) star formation theory and recover its numerical predictions for the total gas content. However, we challenge the assumption of steady state: over 300 Myr, the gas experiences sustained outward accelerations of 1–10 $\mathrm{km\,s^{-1}\,Myr^{-1}}$. In the absence of a steady state, we examine the role of star formation rate (SFR) variability, finding that over 50% of stars form during starburst episodes. Strong outflows, primarily driven by the warm gas phase, reduce the initial gas mass by up to 70%, with 80% of the outflowing material occurring during periods of above-average mass outflow rate ($\dot{M}_{\mathrm{out}}$). Outflows are delayed by 10-20 Myr relative to peaks in the SFR and are dominated by warm gas, followed by hot and cold components. Our results highlight the dynamical nature of the ISM and underscore the crucial role of time-variable feedback in regulating its evolution.

Key words: methods:numerical – ISM: structure – ISM: jets and outflows – ISM: kinematics and dynamics – ISM: abundances – galaxies: ISM

1 INTRODUCTION

Star formation takes place in the cold and dense interstellar medium (ISM). Therefore, the amount of stars that are able to form depends on the availability of gas. Early studies connected the gas surface density with the star formation rate (SFR) surface density, the so-called Kennicutt-Schmidt (KS) relation (Schmidt 1959; Kennicutt 1989, 1998). More recent studies have also found a molecular version of the KS law, connecting the star formation rate and the amount of available molecular hydrogen (Wong & Blitz 2002; Bigiel et al. 2008; Schruba et al. 2011). Both the KS relation and its molecular version are applicable on galactic scales, but they break down at around 500 pc or lower (Schruba et al. 2010; Liu et al. 2011; Feldmann et al. 2011; Kruijssen & Longmore 2014), due to the dependency of molecular cloud evolution on the specific conditions of the environment. Moreover, the slope of these relations depend on the gas surface density, the redshift and the presence of starbursts (Bigiel et al. 2008; Daddi et al. 2010). Therefore, understanding the interplay between gas availability and consequent star formation is a non-trivial problem.

In fact, the properties of the local ISM, where star formation takes place, are influenced, among others, by the stellar feedback from massive stars in the form of supernovae (SNe, Mac Low & McCray 1988; Mac Low et al. 1989; Gatto et al. 2015; Kim & Ostriker 2015; Walch et al. 2015; Haid et al. 2016; Lucas et al. 2020), far-ultraviolet (FUV, Li et al. 2018; Ali & Harries 2019; Bisbas et al. 2021; Rathjen et al. 2024) and ionising (EUV, see e.g. Spitzer 1978; Whitworth 1979; Dale et al. 2005; Walch et al. 2012; Figueira et al. 2017; Haid et al. 2018, 2019; Santoro et al. 2022) radiation, the presence of cosmic rays (CRs, Dorfi & Breitschwerdt 2012; Girichidis et al. 2016b, 2018a; Dashyan & Dubois 2020; Brugaletta et al. 2025) and stellar winds (Castor et al. 1975; Weaver et al. 1977; Wünsch et al. 2011; Dale et al. 2014; Mackey et al. 2015). This self-regulation mechanism plays a fundamental role in establishing the star formation rates that we observe in galaxies. The presence of magnetic fields can also impact star formation (Price & Bate 2007, 2008; Federrath 2015), as well as large-scale turbulence (see e.g. a review by Mac Low & Klessen 2004), and gas metallicity (Dib et al. 2011; Jeřábková

★ E-mail: brugaletta@ph1.uni-koeln.de

et al. 2018; Tanaka et al. 2018; Brugaletta et al. 2025, Brugaletta et al. in prep.).

On the other hand, the gas availability depends on cosmological-scale dynamics of galaxies, such as mergers and collisions (Springel 2000; Barnes 2002; Teyssier et al. 2010; Moster et al. 2012; Blumenthal & Barnes 2018; Moreno et al. 2019), and the presence of a hot circumgalactic medium (Carr et al. 2023). Moreover, many galaxies are subjected to galactic outflows (Veilleux et al. 2005; Girichidis et al. 2016a; Hayward & Hopkins 2017; Heckman & Thompson 2017; Fielding et al. 2018; Hu 2019), which decrease the amount of gas available for star formation.

Therefore, the process of star formation is dependent both on the large-scale dynamics and evolution of the gas, and on the small-scale local conditions of the ISM. The best approach to understand the interplay between the two, by testing several kinds of environments, can be achieved by means of simulations. However, given that the spatial scales of interest for this problem span several orders of magnitude, there are no simulation setups able to simulate all spatial scales at high resolution.

To tackle this problem several approaches have been experimented in previous works, focusing on specific spatial scales. For example, cosmological zoom-ins extend this analysis to cosmological scales, being able to describe the dynamics of the gas in discs while taking into account the effects due to the galactic environment, at the cost of the resolution necessary to properly resolve the ISM (Agertz et al. 2013; Hopkins et al. 2014, 2018, 2023; Schaye et al. 2015; Agertz & Kravtsov 2015; Davé et al. 2016, 2019; Buck et al. 2020; Gurvich et al. 2020; Hassan et al. 2024). These setups employ sub-grid models to describe star formation and feedback (see e.g. Springel & Hernquist 2003). Another approach is examined in isolated galaxy simulations, where the cosmological dynamics of the gas is neglected, but a higher resolution is allowed to model the ISM dynamics (Hopkins et al. 2011, 2012; Benincasa et al. 2016, 2020). However, simulations at galaxy scale are not able to resolve directly the self-regulation process, therefore the employment of sub-grid models is necessary to describe the ISM physics. A higher resolution is achieved in dwarf galaxy simulations, which employ more explicit ISM physics and are able to resolve SN feedback (Hu et al. 2016; Steinwandel et al. 2023b,a). Additionally, the physics of the ISM has been investigated in detail using stratified box simulations (Walch et al. 2015; Rathjen et al. 2021, 2023, 2024; Kim et al. 2023, 2024; Brugaletta et al. 2025, Brugaletta et al. in prep.). These setups neglect cosmological and galactical dynamics of the gas, however, they can describe the ISM physics in a detailed manner.

In particular, using this setup, the relation between star formation and the balance between mid-plane pressure and gravity of the gas has been tested in TIGRESS(-NCR) simulations (see e.g. Kim et al. 2023, 2024). They develop the so-called "Pressure-regulated, feedback-modulated" (PRFM) star formation theory, based on the analytical studies by Ostriker et al. (2010); Ostriker & Shetty (2011). In this theory, they assume that the ISM is in a quasi-steady state on long time scales, which leads to the balance between the mid-plane pressure, due to the stellar feedback, and the gravity of the ISM. In their simulations (see e.g. Ostriker & Kim 2022), this quasi-steady state is achieved within a few tenths of galactic orbital time. In more recent studies (Kim et al. 2024) they extend this analysis also to the low-metallicity ISM, finding that their hypothesis of vertical dynamical equilibrium is always satisfied, and that the total mid-plane pressure is metallicity-invariant. Some observations at galactic scales have reported an accordance with the principles of the PRFM theory (Herrera-Camus et al. 2017; Fisher et al. 2019; Barrera-Ballesteros et al. 2021; Sun et al. 2020; Kado-Fong et al. 2022; Sun et al. 2023).

However, while a theory of dynamical equilibrium, such as the PRFM, is appealing for its simplicity and easiness to compare simulations with observations, it is not certain that real galaxies can achieve a steady state and a vertical dynamical equilibrium. Moreover, the previous TIGRESS-NCR simulations do not employ CR transport, which has been proven playing an important role in lifting the gas from the mid-plane (Girichidis et al. 2016b). In this study, we will make use of our elongated box simulations from the SILCC framework (Walch et al. 2015; Girichidis et al. 2016a; Gatto et al. 2017; Peters et al. 2017; Girichidis et al. 2018b; Rathjen et al. 2021, 2023, 2024, Brugaletta et al. in prep.) to challenge the validity of the PRFM theory at sub-galactic scales. In the following, we are in particular interested in testing the following assumptions: (*i*) the presence of a vertical dynamical equilibrium in the disc and of a quasi-steady state; (*ii*) the dependence of the total yield, which is the ratio of the total pressure with the star formation rate, on the total pressure. Moreover, we aim to use our setup to understand how the variability of the processes that occur in the ISM, such as star formation and outflows, can shape the evolution of the ISM.

This work is organized as follows. In Sec. 2 we describe the numerical methods and the setup of our simulations. In Sec. 3 we define the most important quantities that are relevant for this study. We briefly explain the key concepts of the PRFM theory in Sec. 4. We present our results in Sec. 5, and the discussion in Sec. 6. Finally, we summarize our findings and expose our conclusions in Sec. 7.

2 NUMERICAL METHODS AND SIMULATION SETUP

This work employs SILCC simulations (Walch et al. 2015; Girichidis et al. 2016a; Gatto et al. 2017; Peters et al. 2017; Girichidis et al. 2018b; Rathjen et al. 2021, 2023, 2024, Brugaletta et al. in prep.), and it is based on the setup developed in Brugaletta et al. (2025) and further explored in Brugaletta et al. in prep. in a low-metallicity regime. In the following we present the most important physics relevant for this study, and we refer to Brugaletta et al. (2025) and previous SILCC papers for a more detailed description of the physics involved.

We employ the adaptive mesh refinement code Flash (Fryxell et al. 2000; Dubey et al. 2008; Dubey et al. 2009), version 4.6, to model the evolution of the gas in stratified galactic patches using a modified version of the ideal magnetohydrodynamic (MHD) equations, which take into account CR transport. CRs are coupled to the MHD equations in our code as a separate relativistic fluid adopting an advection-diffusion approximation. The modified MHD equations read:

$$\frac{\partial \rho}{\partial t} + \nabla \cdot (\rho \boldsymbol{v}) = 0, \tag{1}$$

$$\frac{\partial \rho \boldsymbol{v}}{\partial t} + \nabla \cdot \left(\rho \boldsymbol{v} \boldsymbol{v}^T - \frac{\boldsymbol{B}\boldsymbol{B}^T}{4\pi} \right) + \nabla P_{\mathrm{tot}} = \rho \boldsymbol{g} + \dot{\boldsymbol{q}}_{\mathrm{sn}}, \tag{2}$$

$$\begin{aligned} \frac{\partial e}{\partial t} + \nabla \cdot \left[(e + P_{\mathrm{tot}}) \boldsymbol{v} - \frac{\boldsymbol{B}(\boldsymbol{B} \cdot \boldsymbol{v})}{4\pi} \right] \\ = \rho \boldsymbol{v} \cdot \boldsymbol{g} + \nabla \cdot (\mathbf{K} \nabla e_{\mathrm{cr}}) + \dot{u}_{\mathrm{chem}} + \dot{u}_{\mathrm{sn}} + Q_{\mathrm{cr}}, \end{aligned} \tag{3}$$

$$\frac{\partial \boldsymbol{B}}{\partial t} - \nabla \times (\boldsymbol{v} \times \boldsymbol{B}) = 0, \tag{4}$$

$$\frac{\partial e_{\mathrm{cr}}}{\partial t} + \nabla \times (e_{\mathrm{cr}} \boldsymbol{v}) = -P_{\mathrm{cr}} \nabla \cdot \boldsymbol{v} + \nabla \cdot (\mathbf{K} \nabla e_{\mathrm{cr}}) + Q_{\mathrm{cr}}. \tag{5}$$

Table 1. List of simulations with initial parameters: the gas surface density Σ, the metallicity Z, the modulus of the magnetic field $|\boldsymbol{B}|$, the thickness of the initial Gaussian gas density profile, the root mean squared velocity of the initial turbulence driving $v_{\rm rms}$, the employed stellar models.

Run	Σ [$\mathrm{M_\odot\ pc^{-2}}$]	Z [$\mathrm{Z_\odot}$]	$\lvert\boldsymbol{B}\rvert$ [μG]	$\sigma_{\rm gas}$ [pc]	$v_{\rm rms}$ [$\mathrm{km\ s^{-1}}$]	Stellar models
Σ010	10	1	6	30	10	Geneva
Σ050	50	1	13	45	20	Geneva
Σ050-Z0.1	50	0.1	13	45	20	BoOST
Σ050-Z0.02	50	0.02	13	45	20	BoOST
Σ100	100	1	19	60	30	Geneva
Σ100-Z0.1	100	0.1	19	60	30	BoOST
Σ100-Z0.02	100	0.02	19	60	30	BoOST
Σ300-Z0.02	300	0.02	32.7	127	74	BoOST

Here ρ is the density, t the time, $\boldsymbol{v}$ is the velocity of the gas, $\boldsymbol{B}$ the magnetic field, $P_{\rm tot} = P_{\rm thermal} + P_{\rm magnetic} + P_{\rm cr}$ the total pressure, $\boldsymbol{g}$ the total gravitational acceleration, $\dot{\boldsymbol{q}}_{\rm sn}$ the momentum injected due to unresolved supernovae. The total energy density e is defined as $e = \frac{\rho v^2}{2} + e_{\rm thermal} + e_{\rm cr} + \frac{B^2}{8\pi}$. For the cosmic ray diffusion tensor $\boldsymbol{K}$ we adopt a constant diffusion coefficient $K_\parallel = 10^{28}\ \mathrm{cm^2\ s^{-1}}$ parallel to the magnetic field lines, and a $K_\perp = 10^{26}\ \mathrm{cm^2\ s^{-1}}$ perpendicular to them (Strong et al. 2007; Nava & Gabici 2013). $\dot{u}_{\rm chem}$ is the change in thermal energy due to heating and cooling processes, $\dot{u}_{\rm sn}$ is the thermal energy injection due to resolved supernovae, $Q_{\rm cr} = Q_{\rm cr,injection} + \Lambda_{\rm hadronic}$ takes into account the injection of 10^{50} erg per supernova event, as well as the hadronic and adiabatic losses.

The computational domain is an elongated box oriented perpendicularly with respect to the galactic disc, with size 500 × 500 pc × 8 kpc. Near the midplane we adopt a resolution $\Delta x = 3.9$ pc, whereas for $|z| > 1$ kpc the resolution can reach up to 7.8 pc. We assume periodic boundary conditions in x- and y-direction, and outflow conditions in the z-direction. From this choice follows that the gas crossing the surfaces at ± 4 kpc at the top and bottom of the box is not allowed to fall back in. We do not include shear, therefore we do not take into account the effects of galactic differential rotation.

We model gravity using an Octtree-based method from Wünsch et al. (2018), which takes into account four different terms: the self-gravity of the gas; the contribution of sink particles (see below); a constant dark matter potential, and a constant external potential due to the presence of an old stellar disc with stellar surface density $\Sigma_* = 30\ \mathrm{M_\odot\ pc^{-2}}$ and scaleheight $H_* = 300$ pc. We include magnetic fields, which are initialized to be directed in the x-direction, which vary in the z-direction as

$$B_x(z) = B_{x,0}\sqrt{\rho(z)/\rho(z=0)} \tag{6}$$

with $\rho(z)$ the density at height z from the midplane, and $B_{x,0}$ chosen differently for each simulation, see Table 1.

To model star formation, we employ star-cluster sink particles (Bate et al. 1995; Federrath et al. 2010; Gatto et al. 2017; Dinnbier & Walch 2020), which are collisionless and able to accrete gas. For each 120 $\mathrm{M_\odot}$ of gas accreted onto a sink particle, we form one massive star whose mass is sampled from a Salpeter-like IMF (Salpeter 1955) in the mass range 9–120 $\mathrm{M_\odot}$. The rest of the mass is assumed to form low-mass stars inside the star cluster, which contribute to the dynamics of the gas only because of their gravitational field, and the emission of far-UV (FUV) radiation. The stellar feedback from massive stars, on the other hand, includes stellar winds, FUV and ionizing (EUV) radiation, supernovae and cosmic rays. To model stellar winds, radiation, and the lifetime of massive stars, we employ the Geneva non-rotating stellar models from Ekström et al. (2012) in our solar metallicity simulations, and BoOST stellar tracks (Brott et al. 2011; Szécsi et al. 2022) in our sub-solar metallicity runs. The propagation of the FUV radiation is treated employing the novel AdaptiveG0 module presented in Rathjen et al. (2024). We employ the TreeRay/OnTheSpot module (Wünsch et al. 2018, 2021), a backward propagating radiation transport scheme, to treat the propagation of EUV radiation in the On-The-Spot approximation (Osterbrock 1988).

We assume all massive stars to explode as SNe Type II at the end of their life, and we inject either an energy of 0.9×10^{51} erg if the Sedov-Taylor phase is resolved with at least three cells (Gatto et al. 2015), corresponding to ∼ 11.7 pc, otherwise the corresponding momentum is injected. At the same time we inject an energy of 10^{50} erg (10% of the total injection, Ackermann et al. 2013) in form of cosmic rays.

We model heating and cooling processes, as well as molecules formation, on-the-fly by using a chemical network based on Nelson & Langer (1997); Glover & Mac Low (2007); Glover & Low (2007), which calculates the non-equilibrium abundances of H, $\mathrm{H^+}$, $\mathrm{H_2}$, CO, $\mathrm{C^+}$, O, and free electrons (see Walch et al. (2015) for details). At solar metallicity, we assume the following abundances, taken from Sembach et al. (2000): $x_{\rm C} = 1.4 \times 10^{-4}, x_{\rm O} = 3.2 \times 10^{-4}, x_{\rm Si} = 1.5 \times 10^{-5}$. We also assume a dust-to-gas mass ratio of 1%. In the low-metallicity regime, we scale these abundances and the dust-to-gas ratio linearly with metallicity. Concerning cooling processes, if the temperature of the gas is higher than 10^4 K we assume collisional ionization equilibrium for helium and metals, and we employ the tabulated cooling rates from Gnat & Ferland (2012). Regarding heating processes, we model, among others, the photoelectric heating (PE) of dust grains and the heating due to low-energy CRs. For the former we adopted the novel AdaptiveG0 module presented in Rathjen et al. (2024), for the latter the new method presented in Brugaletta et al. (2025).

2.1 Simulation parameters

For this work we use the Σ010-Z1 simulation from Brugaletta et al. in prep. (here called Σ010 for convenience) and run seven new simulations, whose initial parameters are listed in Table 1. In the new simulations, we set a gas surface density Σ in the range 50 – 300 $\mathrm{M_\odot\ pc^{-2}}$, and metallicity values of 1, 0.1 and 0.02 $\mathrm{Z_\odot}$. In this way, we make sure that our calculations do not refer only to solar-neighbourhood conditions, but can also describe environments found elsewhere, for example dwarf galaxies like the Magellanic Clouds or I Zwicky 18. Since the gas surface density chosen for these simulations is higher than the stellar surface density $\Sigma_* = 30\ \mathrm{M_\odot\ pc^{-2}}$, chosen for the old stellar disc, these simulations have a gravitational potential that is dominated by the self-gravity of the gas, or, in other words, that is gas-dominated. In the following, the names of the runs indicate both the gas surface density and the metallicity, for example the Σ100-Z0.02 run has a gas surface density of 100 $\rm M_\odot\ pc^{-2}$ and a metallicity of 0.02. All simulations have been run for 300 Myr after the onset of star formation, to avoid the influence of initial conditions on our results.

3 KEY QUANTITIES

In this work we will make use of some key physical quantities, which we describe here.

3.1 Star Formation Rate

The first important quantity is the star formation rate surface density $\Sigma_{\rm SFR}$, defined as (Gatto et al. 2017)

$$\Sigma_{\rm SFR}(t) = \frac{\rm SFR}{A} = \frac{1}{A}\sum_{i=1}^{N_*(t)} \frac{120\ {\rm M}_\odot}{t_{{\rm OB},i}}, \tag{7}$$

where $A = (500\ {\rm pc})^2$ is the area of our computational domain, $N_*(t)$ is the number of active massive stars at a time t, and $t_{{\rm OB},i}$ is the duration of the lifetime of the $\rm i^{th}$ formed massive star. This formula takes into account that for 120 $\rm M_\odot$ of gas mass accreted on to a cluster, one massive star is formed.

3.2 Gas phases

We also divide the gas in our simulations in different phases as in previous works (Walch et al. 2015; Gatto et al. 2017; Rathjen et al. 2021, 2023, 2024; Brugaletta et al. 2025, Brugaletta et al. in prep.),

- Cold Neutral Medium (CNM): $T < 300$ K;
- Warm Neutral Medium (WNM): 300 K $< T <$ 3× 10^5 K, and an H mass fraction > 50%;
- Warm Ionized Medium (WIM): 300 K $< T <$ 3× 10^5 K, and an $\rm H^+$ mass fraction > 50%;
- Hot Ionized Medium (HIM): $T >$ 3× 10^5 K.

Additionally, we include in this work a fifth phase from Kim et al. 2024, meaning the warm-cold two-phase gas (2p), to better compare with their results. This phase it defined as the gas with $T < 3.5\times10^4$ K and an H mass fraction > 50%. Since this definition overlaps in part with our definitions of the CNM and WNM, we will show this phase only for comparison reasons.

3.3 Mass outflow rate and mass loading

To describe the outflows in our simulations, we employ the instantaneous mass outflow rate $\dot M_{\rm out}$, described as the amount of mass traversing a surface at a height z. Here this height is assumed to be z = 1 kpc or z = 2 kpc. Additionally, we define the mass loading factor η as

$$\eta = \frac{\dot M_{\rm out}}{\overline{\overline{\rm SFR}}}. \tag{8}$$

4 THE PRFM THEORY

The PRFM theory has been first theoretically formulated in Ostriker et al. (2010); Ostriker & Shetty (2011), and then tested in Kim et al. (2011, 2013); Shetty & Ostriker (2012); Kim & Ostriker (2015, 2018); Ostriker & Kim (2022); Kim et al. (2023, 2024); Armillotta et al. (2024). This theory assumes that the ISM is on average in a steady state, either on long time scales or large spatial scales. This vision is not in disagreement with the possibility of having galactic fountains for the gas, and/or galactic winds for the hot phase, the latter having a mass loading of around 0.1 (see Kim & Ostriker 2018). In this theory, assuming a steady state leads to a condition of vertical dynamical equilibrium. In fact, following Armillotta et al. (2024), we can compute the horizontal and temporal averages of the momentum equation (Eq. 2) in the vertical direction,

$$\left\langle \frac{\partial}{\partial t}(\rho v_z)\right\rangle(z)+\frac{d}{dz}\langle P_{\rm tot,PRFM}\rangle(z) = -\left\langle \rho\frac{\partial}{\partial z}\Phi_{\rm tot}\right\rangle(z)+\langle \dot q_{\rm sn}\rangle(z). \tag{9}$$

Here, the brackets notation indicates horizontal and temporal averages. We define

$$P_{\rm tot,PRFM} = P_{\rm thermal} + P_{\rm turb} + \Pi_{\rm mag} + P_{\rm cr}, \tag{10}$$

where $P_{\rm turb} = \rho v_z^2$, and

$$\Pi_{\rm mag} = \frac{B^2}{8\pi} - \frac{B_z^2}{4\pi}. \tag{11}$$

In Eq. 9 we have used

$$g_z(z) = -\frac{\partial}{\partial z}\Phi_{\rm tot}(z), \tag{12}$$

with $\Phi_{\rm tot}$ total gravitational potential, comprising the contributions of the self-gravity of the gas, the gravity due to the sink particles, the dark matter potential and the old stellar disc potential. Moreover, the last term of Eq. 9, $\langle \dot q_{\rm sn}\rangle$, is negligible compared to the other terms, therefore we will omit it in the following. We can express the time- and space-averaged momentum equation as momentum flux differences in the vertical direction, simply integrating Eq. 9 from an initial height z_i to an arbitrary z:

$$\int_{z_i}^{z}\left\langle \frac{\partial}{\partial t}(\rho v_z)\right\rangle(z')dz' + \int_{z_i}^{z}\frac{d}{dz'}\langle P_{\rm tot,PRFM}\rangle(z')dz' = -\int_{z_i}^{z}\left\langle \rho\frac{\partial}{\partial z'}\Phi_{\rm tot}\right\rangle(z')dz'. \tag{13}$$

In a steady state, the first term of Eq. 13 becomes negligible. Setting z_i = 4 kpc, meaning the boundary of the box, Eq. 13 reduces to

$$P_{\rm tot,PRFM}(z) - P_{\rm tot,PRFM}(4\ {\rm kpc}) = W(z), \tag{14}$$

where we have used

$$W(z) = \int_{z}^{4\ {\rm kpc}}\left\langle \rho\frac{\partial}{\partial z'}\Phi_{\rm tot}\right\rangle(z')dz'. \tag{15}$$

The quantity W is the weight of the ISM. We therefore see that the assumption of steady state leads to a condition of vertical equilibrium (Eq. 14), where the pressure difference between a height z and the boundary of the box equals the weight of the ISM computed in the same vertical distance.

Moreover, in the PRFM theory, the $P_{\rm tot,PRFM}$ is determined by the star formation feedback, which adjusts to maintain the correct pressure to balance the ISM weight. The connection between the $P_{\rm tot,PRFM}$ and $\Sigma_{\rm SFR}$ is given by the total yield $\Upsilon_{\rm tot}$,

$$\Upsilon_{\rm tot} = \frac{P_{\rm tot,PRFM}}{\Sigma_{\rm SFR}}, \tag{16}$$

which has units of velocity.

In Sec. 5.2, we will test the PRFM theory in our SILCC setup, and compare the results with Ostriker & Kim (2022) and Kim et al. (2024).

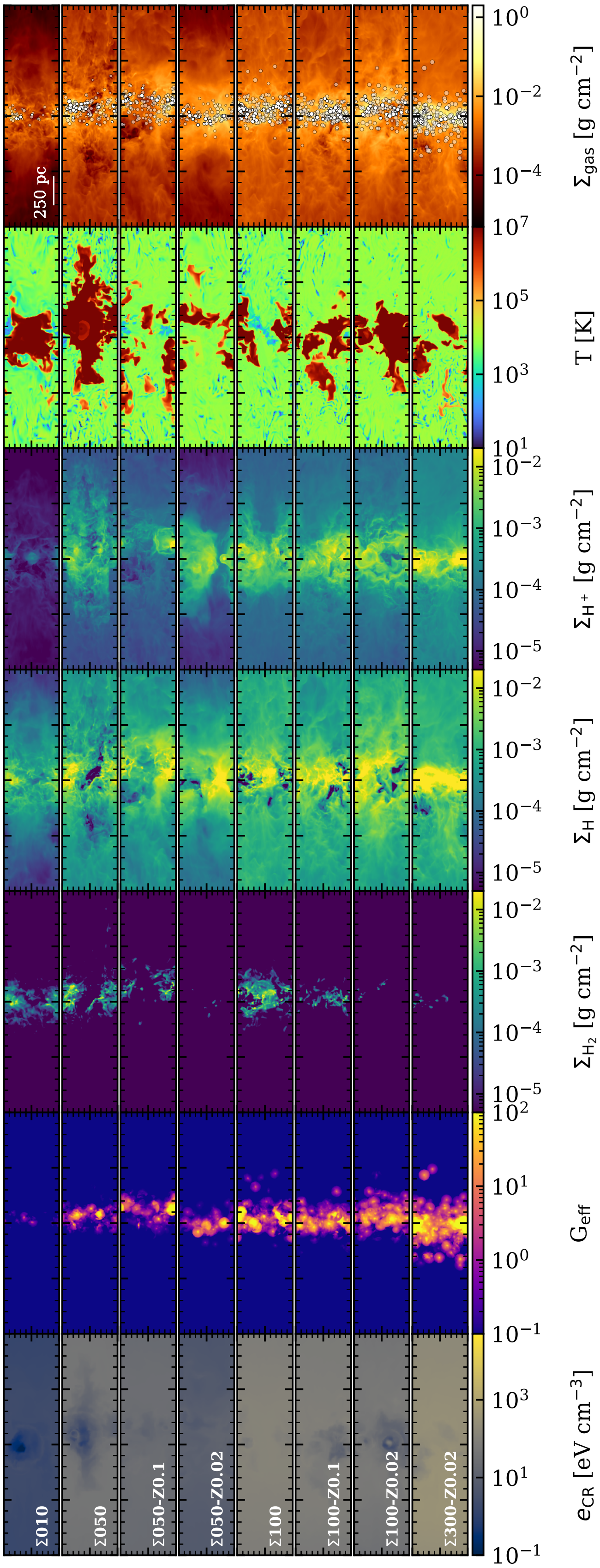

Figure 1. Overview of our runs at t-$t_{\rm SF}$ = 150 Myr. We show the ± 1 kpc edge-on view of the following quantities, from top to bottom: the projection of the gas density, a slice of the temperature, the projection of the $\rm H^{+}$, H, $\rm H_2$, the density-weighted projection of $\rm G_{eff}$, a slice of the $e_{\rm cr}$. The white circles in the first row indicate the active (opaque) and inactive (transparent) star clusters.

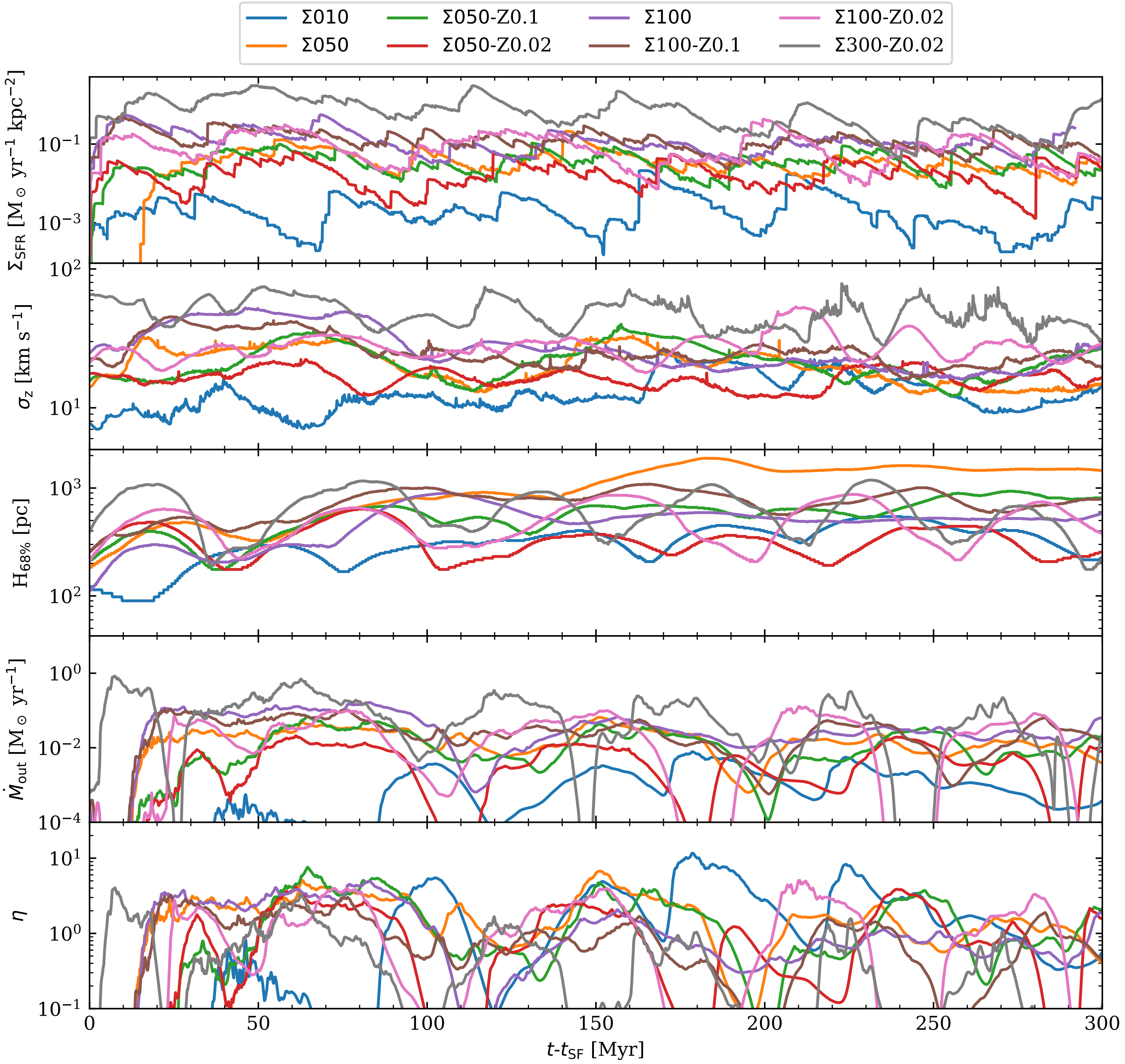

Figure 2. Time evolution of the relevant quantities for all runs. From top to bottom, we show the star formation rate surface density $\Sigma_{\rm SFR}$, the velocity dispersion of the gas in the z-direction σ_z, the scaleheight of the gas $H_{68\%}$, the mass outflow rate $\dot{M}_{\rm out}$, the mass loading η.

5 RESULTS

5.1 Overview

In this section, we provide an overview of our simulations, before discussing the implications for the PRFM theory and the self-regulation of star formation. In Fig. 1 we present the edge-on view of all our runs, focusing on the region within ± 1 kpc around the midplane, 150 Myr after the onset of star formation. Table 2 reports the time $t_{\rm SF}$ at which the first episode of star formation occurs in each run, and throughout this work, we express the time evolution of the simulations as t-$t_{\rm SF}$, where t is the simulation time. From top to bottom, Fig. 1 shows the projected density, a temperature slice, the projected densities of H$^+$, H, and H$_2$, the density-weighted projected $G_{\rm eff}$, and a slice of the CR energy density. The value of $G_{\rm eff}$ is the interstellar radiation field (ISRF) strength expressed in Habing units, and accounts for dust attenuation. The white circles in the top row of panels indicate the presence of star clusters, containing active (opaque) and inactive (transparent) massive stars. Qualitatively, we observe a higher number of formed stars in the runs with higher gas surface density, as expected. The temperature slices reveal the presence of cold gas in the outflow, particularly in runs with solar metallicity. Regarding the projected H$^+$ and H densities, we observe no significant variation with metallicity, as they mainly depend on the density distribution. Moreover, we see a larger amount of H$_2$ at solar metallicity, whereas there is very little H$_2$ in the runs with a metallicity of 0.02 Z$_\odot$. Regarding the $G_{\rm eff}$ panels, we see that the FUV emission

Table 2. Time of the onset of star formation $t_{\rm SF}$, time-averaged star formation rate surface density $\Sigma_{\rm SFR}$, $\dot{M}_{\rm out}$, η for all runs.

Run	$t_{\rm SF}$ [Myr]	$\Sigma_{\rm SFR}$ [10^{-1} M$_\odot$ yr^{-1} kpc^{-2}]	$\dot{M}_{\rm out}$ [10^{-2} M$_\odot$ yr^{-1}]	η
Σ010	23.6	0.03 ± 0.04	0.14 ± 0.17	2.0 ± 2.5
Σ050	9.3	0.4 ± 0.3	1.8 ± 1.2	1.8 ± 1.3
Σ050-Z0.1	10.6	0.4 ± 0.2	1.4 ± 1.3	1.5 ± 1.4
Σ050-Z0.02	13.1	0.2 ± 0.1	0.5 ± 0.5	1.1 ± 1.0
Σ100	8.8	1.3 ± 1.0	4.2 ± 3.7	1.3 ± 1.1
Σ100-Z0.1	7.8	1.4 ± 0.8	3.1 ± 2.4	0.9 ± 0.7
Σ100-Z0.02	6.0	1.0 ± 0.8	3.0 ± 3.1	1.2 ± 1.3
Σ300-Z0.02	4.1	8.3 ± 6.8	11.2 ± 13.8	0.5 ± 0.7

distribution corresponds closely to the positions of the star clusters seen in the density panels, as expected. Finally, we see that the CR energy density shows a noticeable gradient near the midplane, where the majority of supernovae go off, whereas it appears almost uniform at heights above 500 pc.

In Fig. 2 we show the time evolution of the star formation rate surface density $\Sigma_{\rm SFR}$, the vertical velocity dispersion of the gas σ_z, the scaleheight of the disc $H_{68\%}$, the mass outflow rate $\dot{M}_{\rm out}$ measured at 1 kpc, and of the mass loading η. The $\Sigma_{\rm SFR}$ exhibits temporal fluctuations, with periods of heightened star formation activity succeeded by periods of diminished star formation intensity. Over all its evolution, the $\Sigma_{\rm SFR}$ maintains an oscillatory nature, without reaching a quasi-steady state. We note that the $\Sigma_{\rm SFR}$ increases as a function of the gas surface density. The velocity dispersion of the gas in the vertical direction has a similar behaviour, although it presents smoother oscillations, whose peaks roughly correspond to those of the $\Sigma_{\rm SFR}$. A similar behaviour is observed in the evolution of the scaleheight of the disc, defined as the height z such that the region $\pm z$ contains 68% of the total mass. The scaleheight oscillates in time, however, its peaks are delayed of a few Myr compared to the peaks of the $\Sigma_{\rm SFR}$. This is due to the fact that the turbulence due to stellar feedback needs some time to propagate through the gas. A similar delay is visible in the evolution of the mass outflow rate, although its evolution is smoother (see Sec. 5.4.2). We notice a positive correlation of the $\dot{M}_{\rm out}$ with the gas surface density, where for the Σ300-Z0.02 the $\dot{M}_{\rm out}$ reaches almost 1 M$_\odot$ yr^{-1}. The mass loading η is comprised between 1 and 10 almost at every time, and for all runs. This indicates that our simulations experience strong outflows over time, which explains why the $H_{68\%}$ can reach values of up to 2 kpc. We discuss the mass and volume filling fractions of the different gas phases in our runs in Appendix A.

5.2 The PRFM theory in SILCC

In this section, we test the validity of the PRFM theory explained in Sec. 4. Even though Ostriker & Kim (2022); Kim et al. (2024) test this theory for the `2p` phase, and not for the total gas, we also include the latter in our analysis, since the momentum equation is valid for all the gas present in our box, and not only for a specific phase. To compute the $P_{\rm tot,PRFM,2p}$ pressure due to the `2p` phase, we identify the cells in our computational domain where the definition of the `2p` phase is fulfilled, and compute the $P_{\rm tot,PRFM,2p}$ from Eq. 10. We do not divide this value by the area filling factor as done in Eq. 5 in Kim et al. (2024), as this would artificially increase the value of this pressure in our setup.

We show in Fig. 3 the time-averaged $P_{\rm tot,PRFM,gas}$ for the total gas (left panel) and the time-averaged $P_{\rm tot,PRFM,2p}$ for the `2p` phase (right panel), as a function of the time-averaged weight. For the computation (see Eq. 14), we use as starting height the midplane (z = 0), and for the value of the total pressure at the boundaries we compute the average between the $P_{\rm tot,PRFM}$ at the bottom (z = -4 kpc) and the top (z = 4 kpc) boundary. In the case of $P_{\rm tot,PRFM,gas}$, we note that the points computed for our runs are well in agreement with the one-to-one line, meaning that we recover the numerical results of the PRFM theory for the total gas. However, in the case of the $P_{\rm tot,PRFM,2p}$, our points are mainly below the one-to-one line, therefore there is no equality with the weight. This is due to the fact that, restricting ourselves to the `2p` phase only, we omit the pressure contribution of the hot and partly of the warm gas, which is not negligible (see Sec. 5.3). In Appendix B we analyse $P_{\rm tot,PRFM,gas}$ and its pressure components in more detail, showing the pressure components-density phase diagrams for all our runs.

In Fig. 4 we compute the total yield $\Upsilon_{\rm tot}$, as defined in Eq. 16, for the total gas, as a function of $P_{\rm tot,PRFM,gas}$. We do not include the yield for the `2p` phase, because, as seen in Fig. 3, this phase does not fulfil the vertical equilibrium condition. Therefore, the regulation of the $P_{\rm tot,PRFM,2p}$ pressure from the stellar feedback does not adjust in a way that leads to vertical equilibrium. For the total gas, we find that the total yield scales with the $P_{\rm tot,PRFM,gas}$, as

$$\log\Upsilon_{\rm tot} = (-0.217 \pm 0.426)\log(P_{\rm tot,PRFM,gas}) + (4.04 \pm 2.29), \quad (17)$$

which is in very good agreement with the slope of -0.212 found by Ostriker & Kim (2022) (Eq. 25c) for their `2p` phase. For this comparison, we have assumed that $P_{\rm tot,PRFM,gas}$ is equal to the weight estimator $P_{\rm DE}$ defined in Ostriker & Kim (2022). This assumption is motivated by the fact that $P_{\rm tot,PRFM,gas}$ is equal to the weight W (Fig. 3), and that $W \sim P_{\rm DE}$ (Eq. 7 in Ostriker & Kim 2022). The similarity between the slope from Eq. 17 and that found by Ostriker & Kim (2022) is remarkable, and indicates that the equations described in Sec. 4 do not depend on the details of the model we employ to describe stellar feedback, and on the pressures we obtain from that. For example, as seen above, we include in our setup CR pressure, which is not included in the setup of Ostriker & Kim (2022). This means that with these calculations we simply recover the momentum equation, which is given as input to our code (see Sec. 2).

From the dependence of the total yield $\Upsilon_{\rm tot}$ on the total pressure $P_{\rm tot,PRFM,gas}$, we can predict a star formation relation from the PRFM theory applied to our runs. A similar approach has been employed in Burger et al. (2025), where they calculate the star formation relation predicted by the PRFM theory for TIGRESS simulations, obtaining a relation $\Sigma_{\rm SFR} = \Sigma_{\rm gas}^{2.40}$. We can estimate the PRFM-predicted star formation relation substituting Eq. 16 in Eq. 17, and solving for $\Sigma_{\rm SFR}$. This leads to a relation of the form

$$\Sigma_{\rm SFR} \propto P_{\rm tot,PRFM,gas}^{1.217}. \quad (18)$$

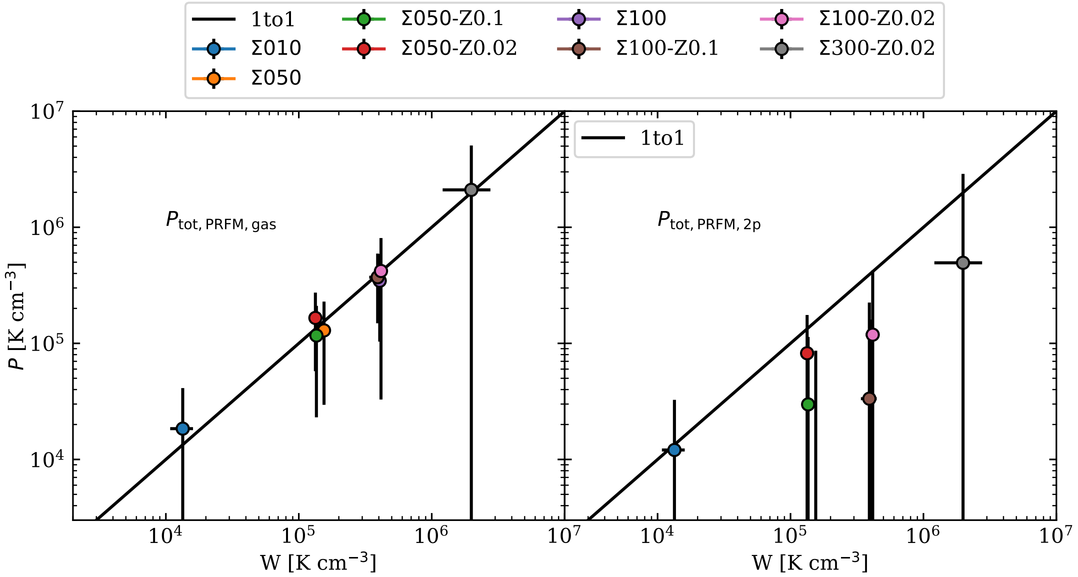

Figure 3. Time-averaged $P_{\rm tot,PRFM}$ as a function of W, for all our runs. We recover in our simulations the numerical results predicted by the PRFM theory for the pressure of the total gas (left panel). The total pressure of the 2p phase (right panel), does not equal the weight in the majority of our simulations, therefore we do not verify the equilibrium for this phase. The black line indicates the one-to-one relation.

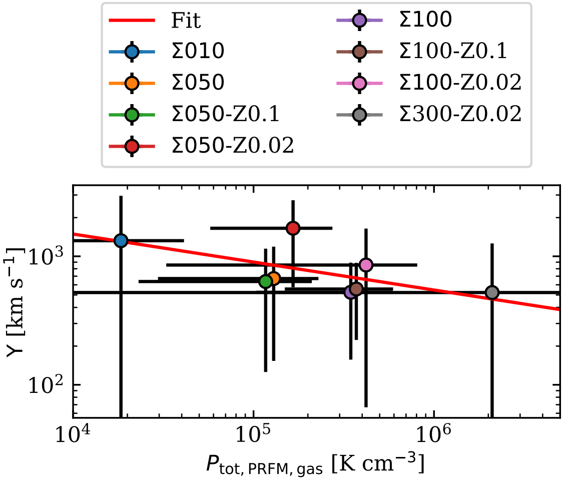

Figure 4. Time-averaged total yield as a function of the time-averaged $P_{\rm tot,PRFM,gas}$, for all runs. We add the best-fit line in red. We note that total yield and $P_{\rm tot,PRFM,gas}$ anticorrelate.

We can then substitute $P_{\rm tot,PRFM,gas} \propto \Sigma^2$ (Ostriker & Kim 2022), assuming a gas-dominated gravity, as it is the case for all our runs with $\Sigma > 10\ {\rm M}_\odot\ {\rm pc}^{-2}$, and obtain a relation

$$\Sigma_{\rm SFR,PRFM} \propto \Sigma^{2.43}. \tag{19}$$

The slope we obtain in Eq. 19 is remarkably similar to the value of 2.40 predicted by Burger et al. (2025) for TIGRESS simulations, given also the similarity of the slope obtained from the yield calculation. However, the slope predicted by the PRFM theory is much steeper than the slope found by Kennicutt (1998), overestimating the $\Sigma_{\rm SFR}$ at high gas surface densities. Therefore, in the left panel of Fig. 5, we show the time-averaged $\Sigma_{\rm SFR}$ as a function of the $\Sigma_{\rm gas} = \Sigma_{\rm HI} + \Sigma_{\rm H_2}$, to understand whether our runs follow the PRFM-predicted star formation relation. We overplot as black solid line the Kennicutt-Schmidt (KS) relation, and we note that our runs are in accordance with KS within one sigma. We also add the observational data from Leroy et al. (2008) (grey points), and Belfiore et al. (2022) (red points, PHANGS). Moreover, we fit the relation between $\Sigma_{\rm SFR}$ and $\Sigma_{\rm gas}$ for all our runs, and we obtain a $\Sigma_{\rm SFR} \propto \Sigma_{\rm gas}^{2.26\pm0.51}$. However, if we consider the gas-dominated runs only ($\Sigma > 10\ {\rm M}_\odot\ {\rm pc}^{-2}$), we obtain $\Sigma_{\rm SFR} \propto \Sigma_{\rm gas}^{2.67\pm0.72}$. The reason for our estimates of the star formation relation being steeper than KS, could be connected to the fact that the majority of our runs are gas-dominated (see Sec. 2.1), for which a slope of 2 is predicted (see e.g. Elmegreen 2018). In conclusion, our prediction of a star formation relation is not conclusive: our runs are in agreement with KS within their uncertainty, but their best-fit is much steeper than KS. This discrepancy can be attributed to the large uncertainties and lack of statistics. To improve in this regard, many more runs would be needed, covering the interval in $\Sigma_{\rm gas}$ uniformly, and testing several stellar disc-dominated and gas-dominated setups.

Moreover, we show the $\Sigma_{\rm SFR}$ as a function of the H$_2$ surface density for all our runs, in the right panel of Fig. 5. In addition to the observational data already shown in the left panel, we add the data points from Lenkić et al. (2024) in blue (DYNAMO). We also add as red solid line the relation from Bigiel et al. (2008). We note that, for our lowest-metallicity runs, the corresponding points lay above the Bigiel et al. (2008) relation, implying that star formation might also occur in the atomic gas, given the lack of available molecular gas, as already seen in the simulations from Brugaletta et al. (2025). Furthermore, we fit a power law to our points, dividing the runs according to their metallicity. In particular, we obtain the following relations: $\Sigma_{\rm SFR} \propto \Sigma_{\rm H_2}^{2.8\pm1.1}$ ($Z = 1\ {\rm Z}_\odot$), $\Sigma_{\rm SFR} \propto \Sigma_{\rm H_2}^{3.7\pm2.5}$ ($Z = 0.1\ {\rm Z}_\odot$), $\Sigma_{\rm SFR} \propto \Sigma_{\rm H_2}^{3.5\pm1.0}$ ($Z = 0.02\ {\rm Z}_\odot$). These relations are steeper than the Bigiel et al. (2008) relation, however, this difference can be attributed to star formation (partly) happening in the atomic gas, at the two lowest metallicities, and to the small size of our sample.

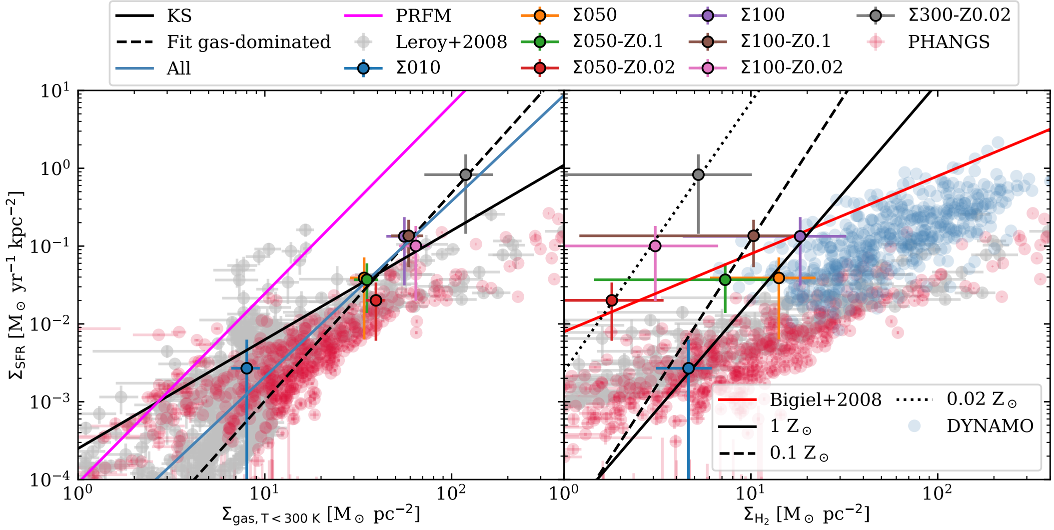

Figure 5. Star formation rate surface density as function of the gas surface density of cold gas (left panel), and of the H_2 surface density. We add the following observational data points: grey from Leroy et al. (2008), red from Belfiore et al. (2022), blue from Lenkić et al. (2024). In the left panel, the black solid line is the Kennicutt-Schmidt (KS) relation from Kennicutt (1998), and the magenta line the prediction from the PRFM theory. In the right panel, the red solid line is the relation from Bigiel et al. (2008).

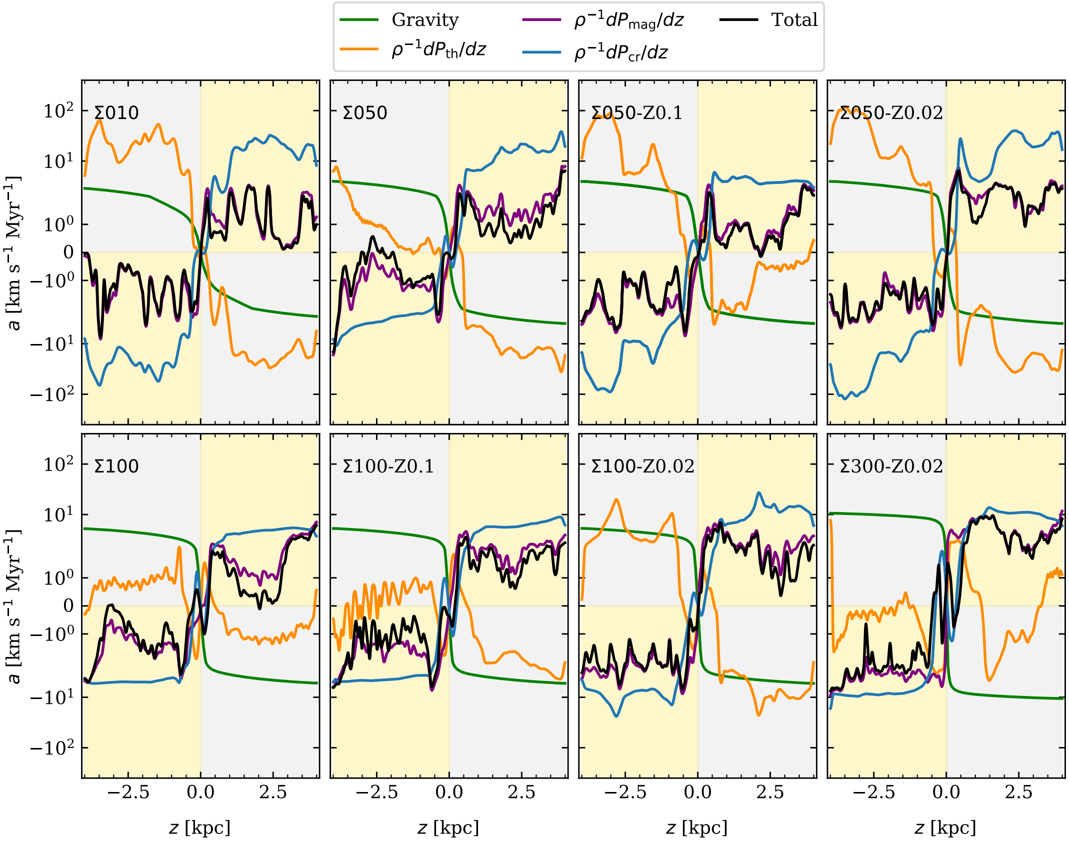

Figure 6. Mass-weighted acceleration profiles as a function of the vertical coordinate. The profiles are averaged in a 300 Myr period after the onset of star formation. For clarity reasons, the yellow regions indicate the values of the accelerations that push the gas away from the disc, and the grey regions indicate that the accelerations are pushing the gas towards the disc. We notice that the total acceleration is not zero, therefore the system is on average not in a steady state.

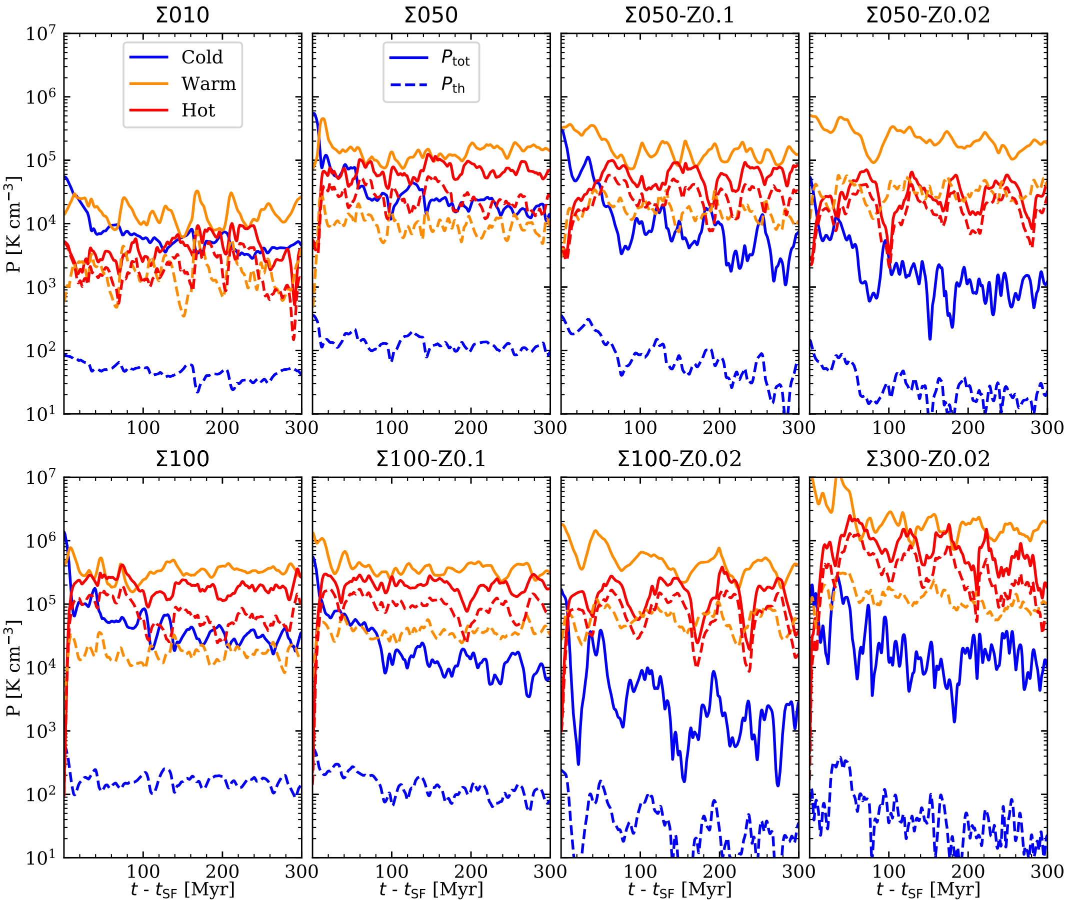

Figure 7. Total (solid lines) and thermal (dashed) pressures of the cold (blue), warm (orange), hot (red) gas phases as a function of time, for all runs. The pressures are volume-weighted means computed in a region $|z| < 100$ pc. We note the absence of a pressure equilibrium, with differences in pressures that increase for low-metallicity runs.

5.3 An out-of-equilibrium ISM

In the previous section, we have seen how we can recover the numerical results of the PRFM theory. However, this theory is based on the assumption of the ISM being in a (quasi) steady state, which might not be compatible with the mass loading values described in Sec. 5.1. In fact, to get the vertical equilibrium condition shown in Fig. 3, we have imposed a "steady state" condition simply by setting $\langle \partial(\rho v_z)/\partial t \rangle = 0$. This condition means, that on average the momentum per unit volume of each fluid parcel remains constant in time, therefore the resultant of all forces is zero. However, since the product $\rho \boldsymbol{v}$, and not ρ and $\boldsymbol{v}$ alone, is conserved, this momentum conservation condition does not necessarily mean that the energy of the system cannot change. In fact, the ISM is characterized by several processes, e.g. heating/cooling, energy injections, shocks, compressions, expansions, etc., that can change the energy of the system. These effects can impact the pressure gradients in our box, and accelerate the gas as a consequence. In this regard, the condition $\langle \partial(\rho v_z)/\partial t \rangle = 0$ would be too weak to guarantee the ISM to be in a real steady state, where outflows would move at a constant speed.

To understand whether the ISM is in a steady state, we compute the mean acceleration profiles from the pressure gradients. In an analogous way as done in Brugaletta et al. in prep., we define the accelerations due to pressure gradients as

$$a_i = -\frac{1}{\rho}\frac{dP_i}{dz}, \qquad (20)$$

with i denoting the different pressure components P_i, meaning the thermal, magnetic, and CR pressures. For the magnetic pressure, we do not take here into account the magnetic tension. The acceleration due to gravity is defined as

$$a_{\rm grav} = -\frac{d\Phi_{\rm tot}}{dz}. \qquad (21)$$

The accelerations are computed in our 3D box, and then we compute vertical acceleration profiles considering all cells j present in a one-cell-thick slice k, and averaging in mass as

$$a_k = \frac{\Sigma_j m_{j,k} a_{j,k}}{\Sigma_j m_{j,k}} \qquad (22)$$

with $m_{j,k}$ is the mass of the $j^{\rm th}$ cell in the $k^{\rm th}$ slice. We represent the time-averaged acceleration profiles as a function of the z-coordinate in Fig. 6. The total acceleration is computed as $a_{\rm tot} = a_{\rm thermal} + a_{\rm magnetic} + a_{\rm cr}$. The positive sign of the accelerations is directed as the z-axis. For clarity reasons, we highlight in yellow the acceleration intervals where the accelerations push the gas away from the disc, and in grey those for which the accelerations push the gas towards the disc. As already seen in Brugaletta et al. in prep., the acceleration due to CRs becomes important at a few hundred pc, and lifts the gas away from the disc. The thermal pressure pushes the gas away from the disc in the vicinity of the midplane, but can change behaviour at higher $|z|$. The total acceleration is mostly dominated by the magnetic pressure, which pushes the gas outwards at almost every height. From these profiles we can see that the modulus of the time-averaged total acceleration is around $1-10\ \mathrm{km\ s^{-1}\ Myr^{-1}}$ in all runs, which is not negligible. From this result we see that non-zero forces are applied to the gas, therefore the ISM is not in a steady state.

Another way of investigating the possibility of having a steady state is by calculating the total pressure of the cold, warm, and hot phases. In fact, if the ISM is in a steady state, there should be (at least approximately) pressure balance among the different phases (McKee & Ostriker 1977), otherwise some phases would expand and others contract, which would not compatible with a steady state.

In Fig. 7 we show the total pressure $P_{\rm tot}$, as defined in Sec. 2 ($P_{\rm tot} = P_{\rm thermal} + P_{\rm magnetic} + P_{\rm cr}$), and the thermal pressure for the cold, warm, and hot gas phases, for all our runs. The pressures are volume-weighted and computed in a region of ± 100 pc around the midplane. We see that for all runs, both for the total and thermal pressure, there is no pressure balance among the three gas phases. In the total pressure, the warm component dominates, followed by the total pressure of the hot gas. The total pressure of the cold gas, instead, correlates with the gas surface density and anticorrelates with the metallicity of the runs. This is due to the fact that at higher surface density the cooling of the gas is more efficient, and that the amount of cold gas is lower in metal-poor runs, as can be seen in Fig. A1. Moreover, we note here that the total pressure of the hot gas is not negligible compared to the other phases. This explains why in the right panel of Fig. 3, the $P_{\rm tot,PRFM,2p}$ is much lower than that computed for the total gas (left panel), and therefore it is lower than the weight. Regarding thermal pressures, that of the hot and warm gas is very similar, although that of hot gas tends to dominate. Instead, the thermal pressure due to the cold medium is around two orders of magnitude lower.

5.4 Variability in the ISM

Having ruled out the possibility that the ISM is in a steady state in the previous section, we investigate here its variability, and the consequent outflows.

5.4.1 Burstiness of the ISM

We have already seen in Fig. 2 that the $\Sigma_{\rm SFR}$ oscillates in time for every run, as well as the σ_z, $\dot{M}_{\rm out}$ and η. In particular, we introduce here a new quantity, the burstiness of the ISM, defined as

$$\sigma_{\rm SFR} = \sigma({\rm SFR}), \tag{23}$$

where $\sigma({\rm SFR})$ is the standard deviation of the SFR. This quantity indicates how much the SFR changes in time, meaning its variability, computed in the 300 Myr interval after the onset of star formation. We show $\sigma_{\rm SFR}$ in the central panel of Fig. 8, together with the time-averaged $\Sigma_{\rm SFR}$ (top panel), and the time-averaged $\dot{M}_{\rm out}$ of the warm (WNM + WIM) gas (bottom panel), for all our runs. We measure $\dot{M}_{\rm out}$ both at 1 kpc (round markers) and 2 kpc (triangular markers). The $\dot{M}_{\rm out}$ measured at 2 kpc is smaller than that measured at 1 kpc, as the amount of gas mass that reaches this height is less. Overall, $\overline{\Sigma_{\rm SFR}}$, $\sigma_{\rm SFR}$ and $\overline{\dot{M}_{\rm out}}$ show a similar trend, as they all increase for higher gas surface density, and weakly anticorrelate with metallicity. The positive correlation of the $\overline{\Sigma_{\rm SFR}}$ with gas surface density is expected from the KS relation, whereas its behaviour with metallicity has been treated in (Kim et al. (2024), Brugaletta et al. in prep.). Regarding the $\overline{\dot{M}_{\rm out}}$, we see a similarity with the trends of the $\overline{\Sigma_{\rm SFR}}$. This is due to the fact that, the higher the SFR, and the stronger the supernova feedback in our runs, which lifts the gas to large heights in the box.

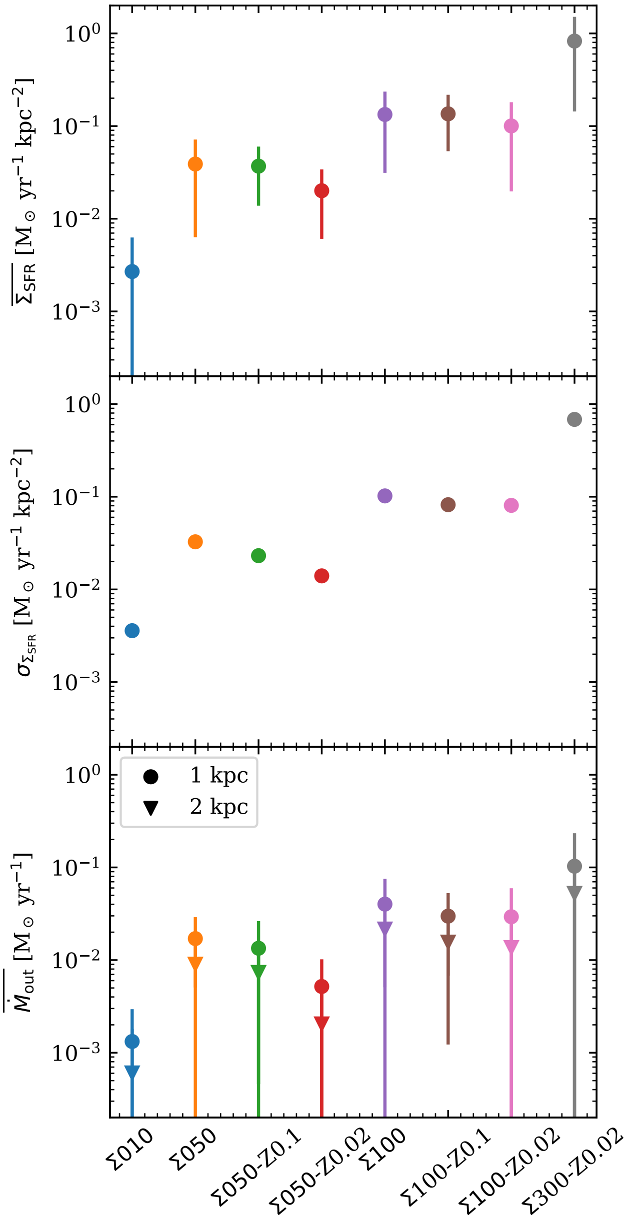

Figure 8. Time-averaged $\Sigma_{\rm SFR}$ (top panel), burstiness (central panel), and time-average $\dot{M}_{\rm out}$ for the warm gas (bottom panel) for every run. The time averages have been computed in 300 Myr after the onset of star formation. The different markers in the bottom panel indicate whether the $\dot{M}_{\rm out}$ has been measured at 1 or 2 kpc. We see that $\overline{\Sigma_{\rm SFR}}$, $\sigma_{\rm SFR}$ and $\overline{\dot{M}_{\rm out}}$ positively correlate with gas surface density, and weakly anticorrelate with metallicity at fixed gas surface density.

Finally, we show in more detail the positive correlation of the $\sigma_{\rm SFR}$ with the $\overline{\Sigma_{\rm SFR}}$ in Fig. 9. There we fit a power law, finding a relation of the kind

$$\log\,(\sigma_{\rm SFR}) = (0.92 \pm 0.05)\,\log\,(\overline{\Sigma_{\rm SFR}}) - (0.20 \pm 0.07), \tag{24}$$

which is a slightly sub-linear relation. Therefore, the higher the mean $\Sigma_{\rm SFR}$, and the higher its variability in time.

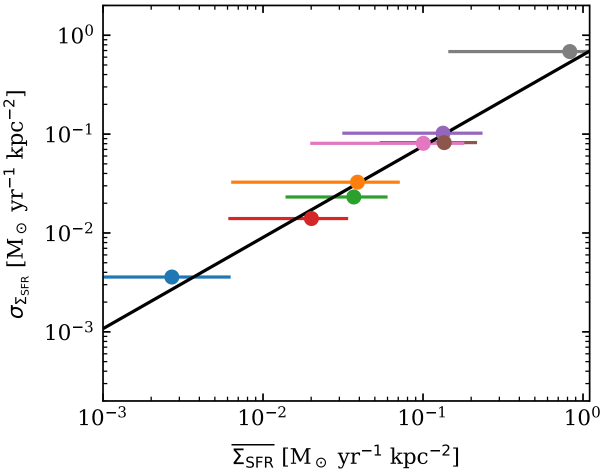

Figure 9. Burstiness of the ISM, $\sigma_{\rm SFR}$, as a function of the average $\Sigma_{\rm SFR}$ in every run. We see a positive correlation. The black line is the best-fit, with a slope of 0.92.

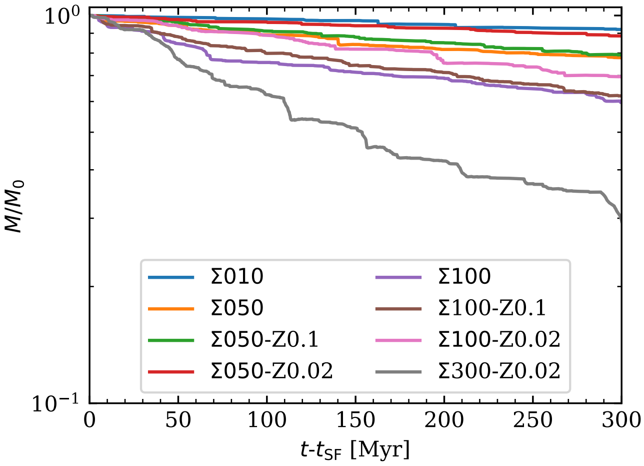

Figure 11. Mass in the entire box divided by the mass of the box at the beginning of the simulations, as function of time. The amount of lost mass is greater for the highest surface densities, where we lose up to 70% of the initial mass in the Σ300-Z0.02 run.

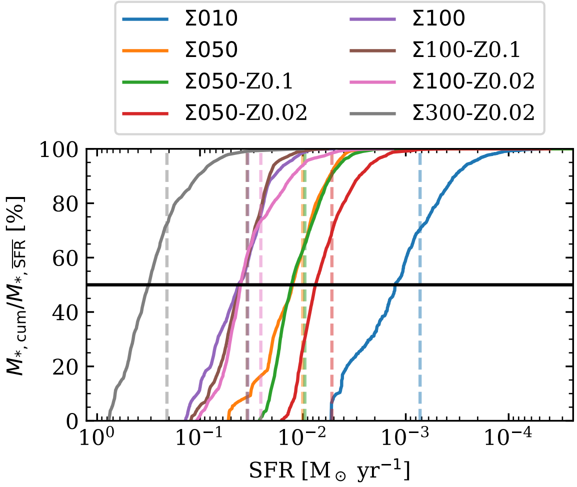

Figure 10. Cumulative stellar mass, normalised by the total mass that would form under a constant SFR equal to its average, plotted as a function of the SFR. The x-axis is inverted, so higher SFR values appear on the left. Vertical lines mark the average SFR for each simulation, with colours matching their corresponding cumulative curves. Notably, around 60–75% of the stars form when the SFR is above its mean value.

We might ask the question whether the variability of the SFR is relevant or not for the star formation process. In Fig. 10, we plot the cumulative distribution of the stellar mass formed in our simulations, normalized by the total mass of stars that we would have if the SFR was constant and equal to its average value, as a function of the SFR. We show an inverted x-axis, meaning that the higher values of the SFR are found on the left. We add an horizontal black line to indicate the 50% mark of formed stars, and dashed vertical lines to indicate the average SFR for each run, with colours matching their corresponding run. We see that the solid coloured lines cross the solid black line at values of the SFR higher than its average. This means that in all our runs, more than 50% of the stars are formed when the SFR is higher than its average value. Therefore, the above-average variability of the SFR is of great importance, as the majority of our stars are formed during starburst periods, and not more steadily over time. This behaviour is seen in all runs, and we observe no dramatic differences in the fraction of stars formed above the average SFR (where the solid coloured lines cross the vertical lines), which is in the range 60–75%. Therefore, the different gas surface density or the metallicity do not play a major role in this regard.

5.4.2 Variability in outflows

In this section, we investigate the variability of the outflows in our runs, and their delay compared to the SFR. In Fig. 11 we quantify the importance of the outflows for the evolution of the ISM. We plot the total mass of the gas in the box in time, normalized by the total gas mass at the beginning of the runs. We note that by the end of each run, at 300 Myr after the onset of star formation, part of the available mass has been lost due to outflows. In particular, the higher the gas surface density, and the lower the final mass in the box, therefore the more the lost mass. Moreover, we observe an additional trend in metallicity. In fact, for the same gas surface density, the amount of lost mass increases for higher metallicities. This is due to the larger amount of stars formed in metal-rich environments, as already seen in Brugaletta et al. in prep., and in Fig. 5. Because of the large amount of lost gas mass during the 300 Myr of evolution, we see here one more time that the ISM in our simulations is still evolving, and not in a steady state.

In Fig. 12 we show the cumulative distribution of the outflowing mass, measured at 1 kpc, normalized by the total mass that has traversed the surface at 1 kpc, as a function of the mass outflow rate computed at 1 kpc. The x-axis is inverted, therefore the larger values of $\dot{M}_{\rm out}$ are found on the left. We add vertical lines to indicate the average $\dot{M}_{\rm out}$ for each run, colour-coded to match the corresponding cumulative curve. We see that around 80% of the mass traversing the surface $|z| = 1$ kpc is associated with periods when the $\dot{M}_{\rm out}$ is above its average value. This percentage does not change depending on the run, therefore the different gas surface density and metallicity do not play a role in setting this percentage.

In Fig. 13 we further investigate the phase composition of the outflows, measured at 1 and 2 kpc, as a function of time. An analogous plot with time-averaged values can be found in Appendix C. We show in Fig. 13 the $\dot{M}_{\rm out}$ for the cold, warm (WNM + WIM) and hot gas.

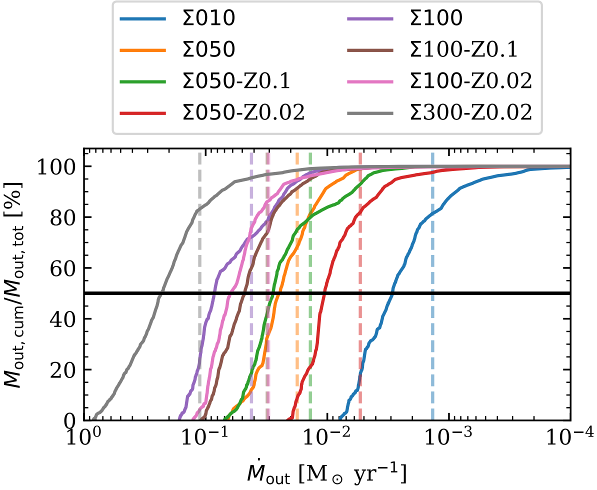

Figure 12. Cumulative outflow mass, measured at 1 kpc, normalised by the total outflow mass, plotted as a function of the mass outflow rate. The x-axis is inverted, so higher $\dot{M}_{\rm out}$ values appear on the left. Vertical lines mark the average $\dot{M}_{\rm out}$ for each simulation, with colours matching their corresponding cumulative curves. Around 80% of the mass is outflowing when the $\dot{M}_{\rm out}$ is above its mean value.

We note that, both at a height of 1 and 2 kpc, the warm gas dominates the outflow at every time, followed by the cold and hot gas, which have similar time-averages, see Appendix C. Therefore, we see that the hot gas is not the main carrier of the outflowing gas, in contrast to what observed in Kim & Ostriker (2018). The reason for this discrepancy is due to CRs, which lift the gas from the midplane. Since the mass fraction of the hot gas is small compared to that of the warm gas (see Appendix A), the hot gas contributes less in mass to the outflow, compared to the warm gas. Moreover, we see for every gas phase and height that the mass outflow rate is not steady, rather it presents a bursty behaviour, where the peaks are delayed by a few Myr compared to the peaks in $\Sigma_{\rm SFR}$ shown in Fig. 2. In addition, the $\dot{M}_{\rm out}$ of the three phases behave synchronously, meaning that they experience the same peaks at the same time (less visible for the hot gas, due to the small amount of carried mass). This means that outflows are a coherent movement of multiphase gas. According to Rathjen et al. (2023), the outflow being multiphase is due to the presence of CRs. In fact, in absence of CRs, only the warm and hot phase would be able to reach a height of 1 or 2 kpc. Moreover, this synchronization of the peaks suggests that the gas does not heat up or cool down much during the outflow, rather it keeps the same phase. For instance, the peaks of cold gas matching in time with those of the warm gas, suggest that the cold gas does not evaporate significantly to become warm.

In Fig. 14 we investigate the delay, d, between the star formation rate and the mass outflow rate, by treating these two quantities as time-dependent signals. The delay between two signals can be estimated by computing their cross correlation function; its peak indicates the time at which the two signals are best aligned, thus providing a measure of their relative delay. The time lag between the SFR and $\dot{M}_{\rm out}$ arises from two main factors. The first is the lifetime of massive stars, which determines when they explode as supernovae, typically a few Myr for the most massive stars within a cluster. After the onset of supernovae, the resulting gas perturbation must travel distances of up to 1 (or 2) kpc, where the $\dot{M}_{\rm out}$ is measured.

We present the measured time delay as a function of the time-averaged $\Sigma_{\rm SFR}$, and we find a weak anticorrelation. Black lines show the best-fitting power-law relations for all runs: we find that $d \propto \overline{\Sigma_{\rm SFR}}^{-0.09}$ for the $\dot{M}_{\rm out}$ measured at 1 kpc, and $d \propto \overline{\Sigma_{\rm SFR}}^{-0.12}$ when measured at 2 kpc. Since the lifetime of massive stars is taken from the stellar models, and does not depend on the ISM dynamics, the reason for a difference in the delay measured for the different runs can be attributed to the propagation of stellar feedback. We have already seen in Fig. 2 that the runs with the highest gas surface densities have a higher SFR. Therefore, they also experience higher supernova rates, which more efficiently evacuate gas from star-forming regions, forming superbubbles that can travel faster to heights of 1 and 2 kpc.

In Fig. 15 we show the maximum velocity of the outflow for the WIM phase, measured at 1 kpc (left panel) and 2 kpc (right panel), as a function of the $\Sigma_{\rm SFR}$. We show the evolution of these quantities averaged in 1 Myr as small round markers for each run, and the mean and median values as big circles and triangles, respectively. We see that the maximum outflow velocity of the WIM is weakly positively correlated with the $\Sigma_{\rm SFR}$. Moreover, we add data from observations, from Reichardt Chu et al. (2025) (light blue), Chisholm et al. (2015) (light green), Xu et al. (2022) (light red), and Heckman et al. (2015) (teal). We note that our points with velocities above 20 km s^{-1} are well in agreement with observations. Moreover, we add a black linear best fit line in both panels, where we fit the 1-Myr averaged points from simulations. We obtain the following relations:

$$\log v_{\rm out,1\,kpc} = (0.15 \pm 0.02) \log \Sigma_{\rm SFR} + (2.25 \pm 0.02), \tag{25}$$

at 1 kpc, and

$$\log v_{\rm out,2\,kpc} = (0.10 \pm 0.03) \log \Sigma_{\rm SFR} + (1.94 \pm 0.04), \tag{26}$$

at 2 kpc. The slopes obtained in both cases are in agreement with those from Reichardt Chu et al. (2025), which are the expected correlation if the main drivers of the outflows are supernovae (Chen et al. 2010).

6 DISCUSSION

6.1 Caveats

In our model we neglect the galactic environment, to focus more on the ISM dynamics happening at smaller scales than a galactic radius. In fact, we adopt a static gravitational potential for both the dark matter and the old stellar disc. In our setup we are therefore missing the radial inflow/outflow motion of the gas, due to the presence of spiral arms in galaxies, which is an additional source of turbulence (see Falceta-Gonçalves et al. 2015; Krumholz et al. 2018, and references therein), affecting star formation rates (Bonnell et al. 2013). However, no evidence is found of a coherent star formation onset mechanism due to the sole presence of spiral arms (Schinnerer et al. 2017). Moreover, we neglect galactic differential rotation and shear, which help reducing the star formation rate (Colling et al. 2018). Furthermore, the interaction of galaxies with their surroundings can trigger gas inflows, which can fuel star formation (Martin et al. 2019; Barbani et al. 2025). Galaxies can also merge, impacting star formation (Carpineti et al. 2012; Luo et al. 2014; Fensch et al. 2017; Silva et al. 2018; Pearson et al. 2019; Ellison et al. 2022).

Not only the lack of galactic environment can affect the self-regulation of star formation, but also the assumptions we have in our setup. For example, assuming outflowing boundary conditions in the z-direction, affects the mass and energy lost during the evolution of each run, lowering the gas reservoir needed for star formation. Moreover, we do not change the stellar density when changing the gas surface density of the runs, therefore we obtain a star-dominated gravity (in run Σ010) and gas-dominated gravity (in all other runs).

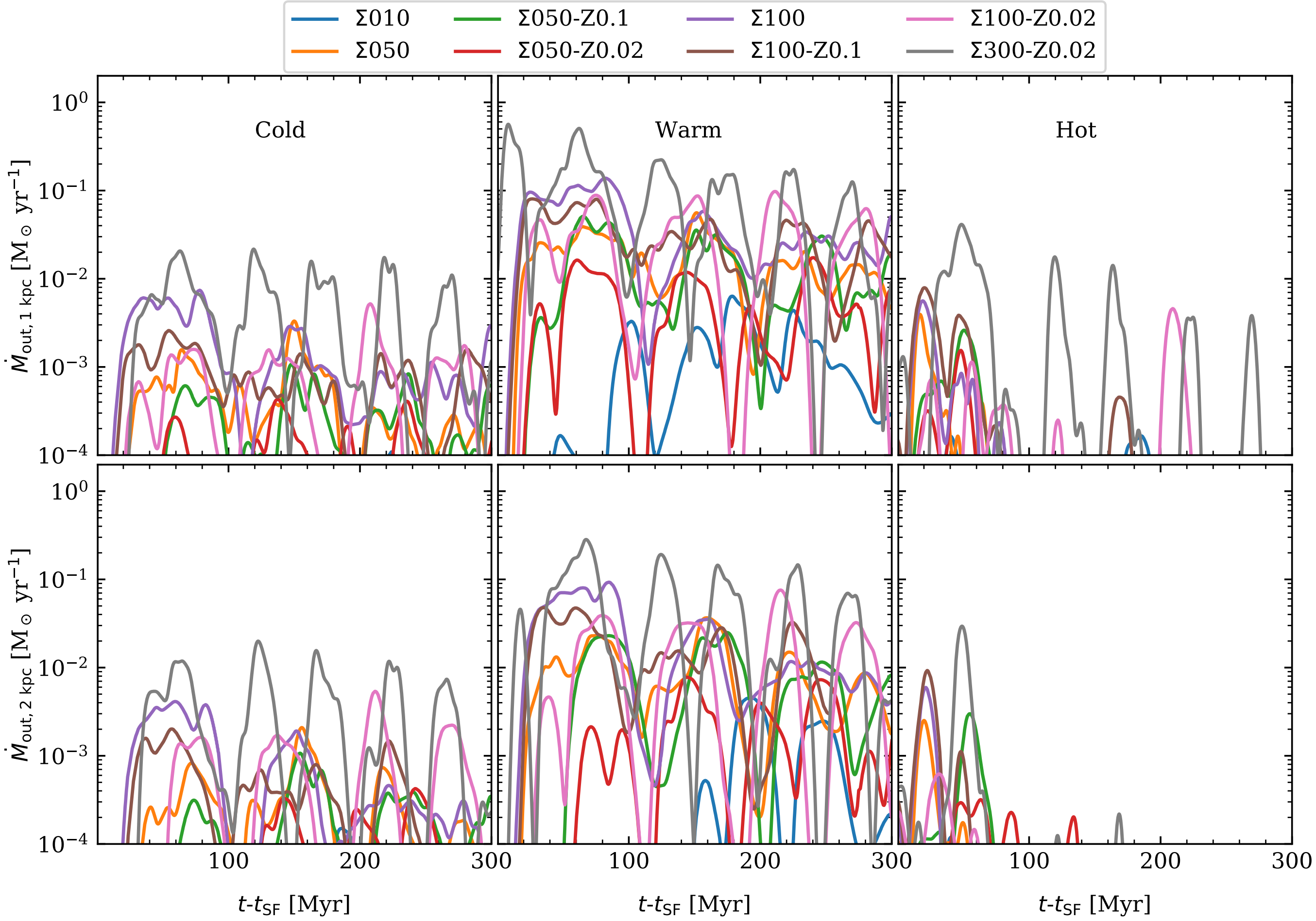

Figure 13. Time evolution of the $\dot{M}_{\rm out}$ measured at 1 kpc (top panels) and 2 kpc (bottom panels), for the cold, warm (WNM + WIM) and hot gas. The warm gas mass dominates, followed by the cold gas mass, and the hot gas mass.

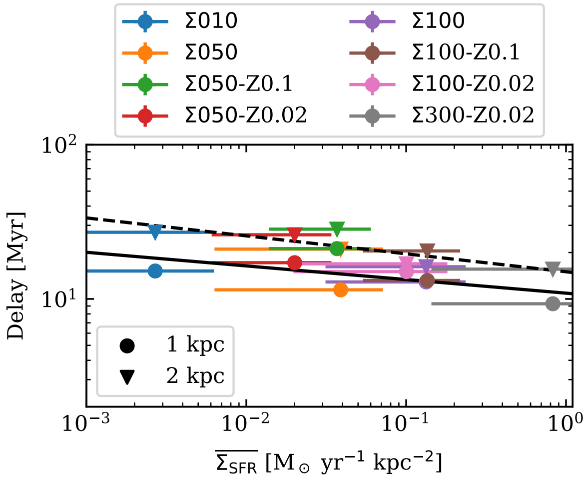

Figure 14. Time delay between the SFR and the $\dot{M}_{\rm out}$ measured at 1 kpc (round markers) and at 2 kpc (triangles), for each run, as a function of the average $\Sigma_{\rm SFR}$. The black lines indicate the best fit for the points measured at 1 kpc (solid line), and at 2 kpc (dashed). We see only a weak anticorrelation of the delay with $\Sigma_{\rm SFR}$.

Finally, we do not include radiation pressure, which is an important feedback mechanism in the regulation of star formation, especially in the dense gas (Andrews & Thompson 2011). In fact, radiation pressure can disrupt luminous giant molecular clouds (Murray 2011), and launch galactic outflows (Murray et al. 2011; Chattopadhyay et al. 2012; Gupta et al. 2016; Menon et al. 2023).

6.2 Comparison to previous works

Elmegreen (2015, 2018) propose a dynamical model for star formation on galactic scales, in which the KS relation can have three distinct powers. They find a power of 1 when considering the molecular gas, at average densities lower than the characteristic density for the observation of the molecule. They find a power of 1.5 for the main discs of galaxies with constant thickness, and a power of 2 for the outer parts of spirals, dwarf irregulars and giant molecular clouds, where the thickness is regulated by self-gravity and the velocity dispersion is constant. The power of 2.26 that we find in Sec. 5.2 is compatible, within the uncertainty, to the power of 2 found in this study.

Hu (2019) simulate an isolated dwarf galaxy at a metallicity of 0.1 $Z_\odot$, including stellar feedback in the form of photoelectric heating, photoionization and supernovae. In their Fig. 3, they show the SFR for their runs, of around 10^{-4}–10^{-3} M$_\odot$ yr^{-1}, which is compatible with the SFR of the runs with gas surface density 10, 50 M$_\odot$ pc^{-2}

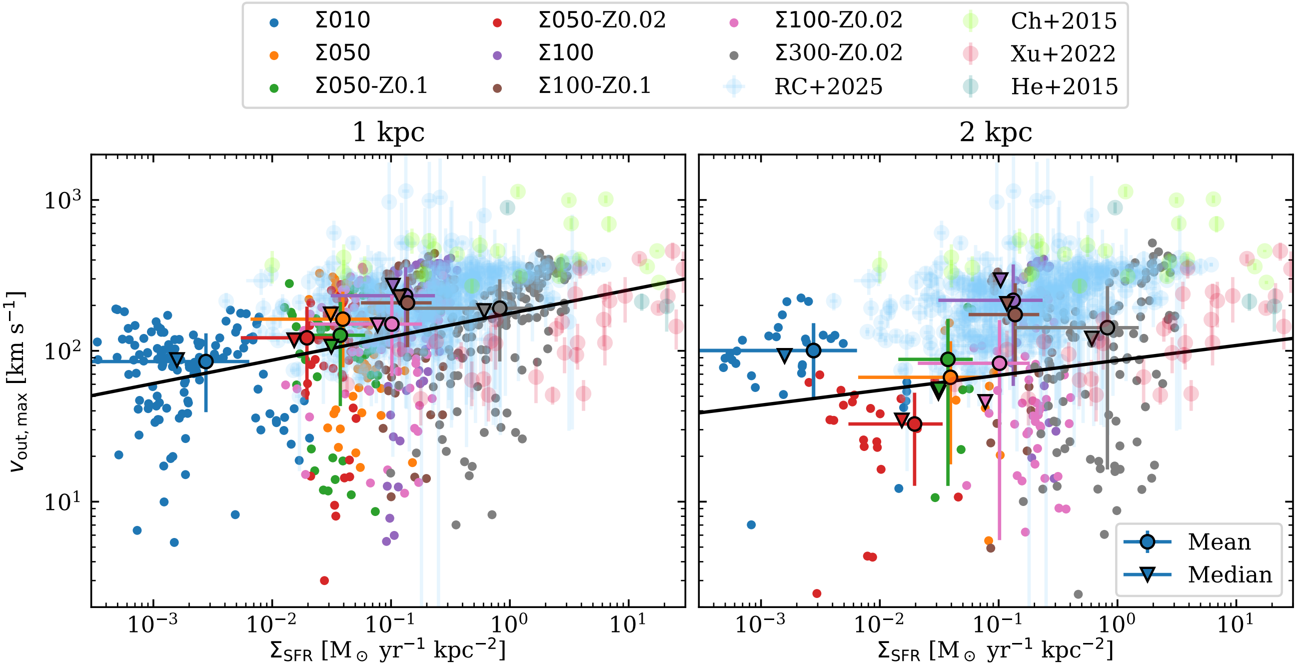

Figure 15. Maximum velocity of the outflow of the WIM measured at 1 kpc (left panel) and 2 kpc (right), for all our runs, as a function of the Σ_{SFR}. We show as small round markers the time evolution of the maximum WIM outflow velocity averaged in 1 Myr, whereas the show its mean and the median as big round markers and triangles, respectively. We add observational data from Reichardt Chu et al. (2025) (light blue), Chisholm et al. (2015) (light green), Heckman et al. (2015) (teal), and Xu et al. (2022) (light red). We note a good agreement between our runs and the observational data. The solid lines are the best fit of the 1-Myr-averaged points from our runs.

shown in Fig. 2 (considering that SFR = $\Sigma_{\mathrm{SFR}}\times$ 0.25 kpc^2). Moreover, they find mass outflow rates of around 10^{-3}-10^{-2} M$_\odot$ yr^{-1}, which is in agreement with the values we find, although our runs can reach up to 1 M$_\odot$ pc^{-2}, for the Σ300-Z0.02.

Orr et al. (2020) simulate Milky Way-mass disc galaxies using the FIRE-2 cosmological simulations. They also define a burstiness parameter of the ISM, defined as $\eta_{\mathrm{burst}} = (\Sigma^{10\mathrm{Myr}}_{\mathrm{SFR}} - \Sigma^{100\mathrm{Myr}}_{\mathrm{SFR}})/(\Sigma^{10\mathrm{Myr}}_{\mathrm{SFR}} + \Sigma^{100\mathrm{Myr}}_{\mathrm{SFR}})$. This definition is slightly different from ours, since it takes into account only two time snapshots. However, they also see in the bottom right panel of their Fig. 4, that, at least for positive values, the burstiness parameter scales with the SFR, similarly to what we have seen in our Fig. 9.

Steinwandel et al. (2024) simulate an isolated galaxy including non-equilibrium cooling and heating, and stellar feedback in the form of photoelectric heating, photoionizing radiation, and supernovae, adopting a metallicity of 0.1 Z$_\odot$. They find a SFR in the range 3×10^{-2}–2×10^{-1} (see their Fig. 4), which is compatible with the Σ_{SFR} runs with gas surface density of 100 M$_\odot$ pc^{-2}. They also find mass outflow rates at a height of 1 kpc of about 10^{-3}–10^{-2} M$_\odot$ yr^{-1}, which are compatible with those found for the Σ010, however they are smaller than those found for the runs with higher surface density.

Kim et al. (2024) simulate tall boxes in the framework of the TIGRESS simulations, including cooling and heating processes, UV radiation transfer, SN feedback, etc. They do not include CR injection and transport, however, they model CR heating by scaling $\zeta_0 = 2\times10^{-16}$ s^{-1} with $\Sigma_{\mathrm{SFR}}/\Sigma$ and applying an attenuation in the dense gas. Some of their runs can be compared to ours, in particular: R8-Z1.0 with Σ010, LGR4-Z1.0 with Σ050, LGR4-Z0.1 with Σ050-Z0.1, S100-Z1.0 with Σ100, and S100-Z0.1 with Σ100-Z0.1. We compare the time-averaged values of Σ_{SFR} reported in Table 2 with those reported in their Table 2, and we find a good agreement within the uncertainty for all runs. Moreover, we compare the values of the $P_{\mathrm{tot,PRFM,gas}}$ and W shown in Fig. 3 with their value of P_{tot} and W reported in their Table 3, and we find also a reasonable agreement. Note that in Kim et al. (2024) the P_{tot} is computed for the `2p` phase only.

Vijayan et al. (2025) perform tall-box 3D hydrodynamic simulations of the ISM in a $1\times1\times8$ kpc^3 domain using the code QUOKKA. They model SN feedback computing the star formation rate from the KS relation, for a given gas surface density, and then estimate a SN surface density from a Chabrier IMF (Chabrier 2001). Among their runs, the most similar to ours are those with gas surface density of 13 or 50 M$_\odot$ pc^{-2}, and with a metallicity of either 1 or 0.2 Z$_\odot$. In their Fig. 4, they show mass outflow rates of around 10^{-2} M$_\odot$ yr^{-1} for the two solar-metallicity runs with Σ = 13, 50 M$_\odot$ pc^{-2}. This value is higher than the average $\dot{M}_{\mathrm{out}}$ at 1 kpc of the Σ010 run, and slightly smaller than that run Σ050. This discrepancy can be attributed to the different modelling of the SN rate, which in their case is decoupled from the gas dynamics. They also find that low-metallicity outflows are on average cooler than those in solar-neighbourhood conditions, because the lack of cooling does not allow the ISM to quickly break up into dense clumps, and this traps the SN-heated gas near the midplane. However, we see in Fig. C1, that the $\dot{M}_{\mathrm{out}}$ measured both at 1 and 2 kpc is higher for solar metallicity. This difference can be attributed to the fact that our massive stars form in the dense gas, and explode there as clustered supernovae, therefore the hot gas is not trapped near the midplane.

6.3 Comparison to observations

6.3.1 Outflows

Bolatto et al. (2013) report observations of NGC 253, a starburst galaxy, and find a molecular mass outflow rate of around 3–9 $\mathrm{M_\odot\ yr^{-1}}$, and a molecular mass loading between 1 and 3. This molecular mass outflow, driven by the starburst, is supposed to suppress star formation. Their value for mass outflow rate is at least a factor of 3 higher than the peaks in $\dot{M}_{\rm out}$ measured at 1 kpc for our Σ300-Z0.02 run. However, their mass loading in compatible with the range we find for our runs (see Fig. 2). Pereira-Santaella et al. (2016) present 60 pc resolution observations with ALMA and HST of the isolated galaxy ESO 320-G030. They find a high-velocity (450 km $\mathrm{s^{-1}}$) molecular outflow with a molecular mass outflow rate of 2–8 $\mathrm{M_\odot\ yr^{-1}}$ and a mass loading factor of 0.1–0.5. Again, these values of the $\dot{M}_{\rm out}$ are higher than what we find, but the mass loading factors are around a factor of 2 or 3 smaller. The outflow is powered by supernovae, but does not contain ionized gas. Moreover, its velocity is lower than the escape velocity, so the gas will likely fall back to the disc and refuel star formation. Xu et al. (2022) analyse the warm ionized galactic outflows in a sample of 45 low-redshift starburst galaxies from the CLASSY survey, and find mass loadings of around 10 for the dwarf galaxies. This is in agreement with the η found for our Σ010 run. Moreover, they find a relation $\dot{M}_{\rm out} \propto \mathrm{SFR}^{0.4}$, and that the outflows carry away 10–100% of the momentum injected by massive stars, and 1%–20% of the kinetic energy.

Roberts-Borsani (2020) study the characteristics of multiphase outflows in normal star-forming galaxies at redshift $z \sim 0$ using large spectroscopic surveys. They find upper limits for the total mass outflow rate, $\dot{M}_{\rm tot} < 27\ \mathrm{M_\odot\ yr^{-1}}$ and for the total mass loading factor $\eta_{\rm tot} < 6.39$. While our runs are in agreement with the upper limit of the mass outflow rate, we find higher values for η. The molecular gas contributes around 72% of the total mass outflow rate, the neutral gas around 28% and the ionized gas less than one per cent. In this regard, we find that the warm gas dominates the outflow mass, followed by the cold gas. Romano et al. (2023) analyse the characteristics of outflows in 29 dwarf galaxies from the Dwarf Galaxy Survey. They estimate atomic mass loading factors of around one. Even though the outflows in these dwarf galaxies have a low efficiency, their are thought to regulate their star formation histories. Chisholm et al. (2015) report on a sample of 48 nearby star-forming galaxies observed with HST. They measure the properties of the warm galactic outflows, finding that the outflow velocities scale as $\mathrm{SFR}^{0.08-0.22}$, and that mergers drive 32% faster outflows than non-merging galaxies.

6.3.2 Star formation

We have seen that, at high surface density, the large $\Sigma_{\rm SFR}$ corresponds is characterized by strong variations. Neumann et al. (2025) present new results of the ALMA ALMOND survey of galaxies in the local Universe, and observe around a factor of 20 in variation of their SFR for high stellar masses (see their Fig. 1), which is similar to the variations we see in our runs.

Moreover, as seen in Fig. 5, if we fit a relation $\Sigma_{\rm SFR} \propto \Sigma_{\rm gas}^{N}$, we obtain a slope that is steeper than KS. Morokuma-Matsui & Muraoka (2017) study the variability of the KS slope depending on the ratio CO(J=3-2)/CO(J=1-0). In their estimates from their Fig. 12-13, they find slopes in range 1.35 - 3.6, which is in agreement with our best-fits for the gas-dominated galaxies as well as when considering all our runs. López-Sánchez et al. (2018) estimate a slope of 2.19 for the KS relation in low surface brightness galaxies. Wilson et al. (2019) analyse ALMA data of luminous or ultraluminous infrared galaxies, finding a slope for the KS relation of 1.74, which is in agreement with the best-fit for all galaxies shown in Fig. 5 within the uncertainty.

6.3.3 PRFM theory

In Sec. 5.2 we have applied the PRFM theory to our data, recovering the numerical results from Ostriker & Kim (2022). Here we compare with similar observational studies. Herrera-Camus et al. (2017) measure thermal pressure from neutral gas in 534 regions in 31 galaxies from the Herschel KINGFISH sample. They find a distribution in thermal pressures in range 10^3–10^5 K $\mathrm{cm^{-3}}$, which is compatible with the range of thermal pressures shown in Fig. B1 and Fig. B2. Sun et al. (2020) measure the turbulent pressure of the ISM using PHANGS-ALMA data, finding that $P_{\rm turb} > 10^3$ K $\mathrm{cm^{-3}}$, compatible with the distributions found for our runs in Fig. B1-B2. Barrera-Ballesteros et al. (2021) study star formation happening in 96 galaxies from the EDGE-CALIFA survey, and compute the pressure yields (see their Fig. 10). They are in accordance with the yields computed for our runs (see Fig. 4). Sun et al. (2023) measure the empirical relationship between the SFR and the $P_{\rm DE}$, which according to Ostriker & Kim (2022) corresponds to the weight $W \sim P_{\rm tot,PRFM,gas}$ (from Fig. 3). Our measured values of Υ (see Fig. 4) are in accordance, within the uncertainty, with their reported pressure yields in the range 0.7–3.4 10^3 km $\mathrm{s^{-1}}$.

7 SUMMARY AND CONCLUSIONS

In this study, we employ SILCC simulations to understand whether the ISM can be in a steady state, and we investigate how the time variability of the processes occurring in the ISM can actually drive its evolution. Our magnetohydrodynamic simulations include non-equilibrium chemistry, heating and cooling mechanisms, cosmic ray transport, stellar feedback due to massive stars, in the form of winds, far-UV and ionizing radiation, supernovae and cosmic rays. We perform a new set of simulations with gas surface densities in range 10–300 $\mathrm{M_\odot\ pc^{-2}}$, and three metallicity values of 0.02, 0.1 and 1 $\mathrm{Z_\odot}$. With this new set, we can describe the evolution of the ISM in a variety of different environments. Our main results are the following.

We first investigate the validity of the pressure-regulated, feedback-modulated (PRFM) theory (see e.g. Ostriker et al. 2010; Ostriker & Kim 2022; Kim et al. 2024) in our simulations. As seen in Fig. 3, the values of the $P_{\rm tot,PRFM,gas}$ for the total gas are in agreement with the weight, whereas those of the $P_{\rm tot,PRFM,2p}$ for the `2p` phase are lower than the weight. This means that, to recover the numerical results of the PRFM theory, the pressure due to the WIM and hot gas cannot be neglected. Moreover, we find that the total yield $\Upsilon_{\rm tot}$, computed for the $P_{\rm tot,PRFM,gas}$, scales as $\Upsilon_{\rm tot} \propto P_{\rm tot,PRFM,gas}^{-0.217}$, which is in very good agreement with the slope of -0.212 found by Ostriker & Kim (2022) for their `2p` phase. This remarkable similarity indicates that the way we implement the stellar feedback, which in our case includes also cosmic rays, is not important to recover their results. Therefore, with these calculations we simply recover the momentum equation, which is given as input in our code (see Sec. 2). Using the definition of $\Upsilon_{\rm tot}$ and its dependence on $P_{\rm tot,PRFM,gas}$, we compute a star formation relation of the kind $\Sigma_{\rm SFR} \propto \Sigma_{\rm gas}^{2.43}$, in accordance with the slope of 2.40 found by Burger et al. (2025) for TIGRESS simulations. In Fig. 5 we see that our simulations are in agreement with the KS slope within the uncertainty, however, the best fit that we obtain for all our runs has a slope of 2.26 ± 0.51, which is steeper than KS. We attribute this discrepancy to large uncertainties and lack of statistics, therefore our prediction of the slope of the star formation relation is not conclusive.

Even though we are able to recover the numerical results from Ostriker & Kim (2022), we challenge here the assumption of steady state, checking whether our simulations experience net forces, and therefore accelerations, when averaging on long time scales. We see from Fig. 6 that on average the total acceleration is directed such that it pushes the gas outwards, with a modulus of 1–10 km s^{-1} Myr^{-1} in all runs, which is not negligible. We also find no pressure balance among the cold, warm, and hot gas phases, which is not compatible with the condition of steady state.

Since the gas in our simulations is not in a steady state, we analyse how the variability of the processes occurring in the ISM can drive its evolution. In particular, we introduce a new quantity, the burstiness of the ISM, defined as the standard deviation of the SFR. We note from Fig. 9 that the burstiness increases for higher SFR. Moreover, we see in Fig. 10 that more than 50% of our massive stars are formed when the SFR is higher than its average value, meaning in starburst periods.

Moreover, we investigate the importance of outflows and their variability. In Fig. 11, we have seen that part of the initial mass in the box is lost due to outflows, and that this lost mass increases with higher gas surface density and metallicity. In the case of our Σ300-Z0.02 run, up to 70% of the original mass is lost. In Fig. 12 we show that around 80% of the mass traversing the surface $|z| = 1$ kpc is associated with periods when the mass outflow rate is above its average value, irrespective of the run. Moreover, we see from Fig. 13 that the outflows are dominated by the warm gas, with the secondary contributions of hot and cold gas mass. Therefore, the hot gas is not the main carrier of the outflows. Furthermore, we observe a synchronized behaviour in time of the $\dot{M}_{\rm out}$ of the different gas phases, and this suggests that the gas does not heavily cool down or heat up during the outflow, but it tends to maintain its original phase.

We also compute the time delay between the SFR and $\dot{M}_{\rm out}$, in the range 10–20 Myr depending on the run and height from the disc, and finding a weak anticorrelation with average $\Sigma_{\rm SFR}$. Finally, we plot the maximum velocity of the outflow in the WIM phase as a function of the $\Sigma_{\rm SFR}$. We find a good agreement with observations, and find a best-fit slope of around 0.1, which indicates that the outflow is driven by supernova feedback.

ACKNOWLEDGEMENTS

VB, SW, TER, DS, and PCN thank the Deutsche Forschungsgemeinschaft (DFG) for funding through the SFB 1601 “Habitats of massive stars across cosmic time” (sub- projects B1, B4 and B6). SW, TER, and DS further acknowledge support by the project ”NRW-Cluster for data-intensive radio astronomy: Big Bang to Big Data (B3D)” funded through the programme ”Profilbildung 2020”, an initiative of the Ministry of Culture and Science of the State of North Rhine-Westphalia. VB and SW thank the Bonn-Cologne Graduate School. TN acknowledges support from the DFG under Germany’s Excellence Strategy - EXC-2094 - 390783311 from the DFG Cluster of Excellence "ORIGINS". PG and SCOG acknowledge funding by the European Research Council via the ERC Synergy Grant “ECOGAL” (project ID 855130). RW acknowledges support by the institutional project RVO:67985815. SCOG also acknowledges support from the Heidelberg Cluster of Excellence EXC 2181 (Project-ID 390900948) ‘STRUCTURES: A unifying approach to emergent phenomena in the physical world, mathematics, and complex data’ supported by the German Excellence Strategy. The software used in this work was in part developed by the DOE NNSA-ASC OASCR Flash Centre at the University of Rochester (Fryxell et al. 2000; Dubey et al. 2009). Part of the data visualisation has been done with the Python package YT (Turk et al. 2011) and the FLASH_AMR_TOOLS Python package (`https://pypi.org/project/flash-amr-tools/`) developed by PCN. The data analysis has been performed using the following Python packages: NUMPY (van der Walt et al. 2011), MATPLOTLIB (Hunter 2007), H5PY (Collette et al. 2020), IPYTHON (Perez & Granger 2007), SCIPY (Virtanen et al. 2020).

DATA AVAILABILITY

The derived data underlying this article will be shared on reasonable request to the corresponding author. The simulation data will be made available on the SILCC data web page: `http://silcc.mpa-garching.mpg.de`.

REFERENCES

Ackermann M., Ajello M., Allafort A., et al., 2013, Science, 339, 807
Agertz O., Kravtsov A. V., 2015, ApJ, 804, 18
Agertz O., Kravtsov A. V., Leitner S. N., et al., 2013, ApJ, 770, 25
Ali A. A., Harries T. J., 2019, MNRAS, 487, 4890
Andrews B. H., Thompson T. A., 2011, ApJ, 727, 97
Armillotta L., Ostriker E. C., Kim C.-G., et al., 2024, ApJ, 964, 99
Barbani F., Pascale R., Marinacci F., et al., 2025, A&A, 697, A121
Barnes J. E., 2002, MNRAS, 333, 481
Barrera-Ballesteros J. K., et al., 2021, MNRAS, 503, 3643
Bate M. R., Bonnell I. A., Price N. M., 1995, MNRAS, 277, 362
Belfiore F., Santoro F., Groves B., et al., 2022, A&A, 659, A26
Benincasa S. M., Wadsley J., et al., 2016, MNRAS, 462, 3053
Benincasa S. M., Wadsley J. W., et al., 2020, MNRAS, 499, 2028
Bigiel F., Leroy A., Walter F., et al., 2008, AJ, 136, 2846
Bisbas T. G., Tan J. C., Tanaka K. E. I., 2021, MNRAS, 502, 2701
Blumenthal K. A., Barnes J. E., 2018, MNRAS, 479, 3952
Bolatto A. D., Warren S. R., Leroy A. K., et al., 2013, Nature, 499, 450
Bonnell I. A., Dobbs C. L., Smith R. J., 2013, MNRAS, 430, 1790
Brott I., de Mink S. E., Cantiello M., et al., 2011, A&A, 530, A115
Brugaletta V., Walch S., Naab T., et al., 2025, MNRAS, 537, 482
Buck T., Obreja A., Macciò A. V., et al., 2020, MNRAS, 491, 3461
Burger J. D., et al., 2025, arXiv e-prints, p. arXiv:2502.13244
Carpineti A., Kaviraj S., Darg D., et al., 2012, MNRAS, 420, 2139
Carr C., Bryan G. L., Fielding D. B., et al., 2023, ApJ, 949, 21
Castor J., McCray R., Weaver R., 1975, ApJ, 200, L107
Chabrier G., 2001, ApJ, 554, 1274
Chattopadhyay I., Sharma M., Nath B. B., et al., 2012, MNRAS, 423, 2153
Chen Y.-M., Tremonti C. A., Heckman T. M., Kauffmann G., Weiner B. J., Brinchmann J., Wang J., 2010, AJ, 140, 445
Chisholm J., Tremonti C. A., Leitherer C., et al., 2015, ApJ, 811, 149
Collette A., Kluyver T., Caswell T. A., et al., 2020, h5py/h5py: 3.1.0, doi:10.5281/zenodo.4250762
Colling C., Hennebelle P., Geen S., et al., 2018, A&A, 620, A21
Daddi E., Elbaz D., Walter F., et al., 2010, ApJ, 714, L118
Dale J. E., Bonnell I. A., Clarke C. J., et al., 2005, MNRAS, 358, 291
Dale J. E., Ngoumou J., et al., 2014, MNRAS, 442, 694
Dashyan G., Dubois Y., 2020, A&A, 638, A123
Davé R., Thompson R., Hopkins P. F., 2016, MNRAS, 462, 3265
Davé R., Anglés-Alcázar D., Narayanan D., et al., 2019, MNRAS, 486, 2827
Dib S., Piau L., Mohanty S., et al., 2011, MNRAS, 415, 3439
Dinnbier F., Walch S., 2020, MNRAS, 499, 748
Dorfi E. A., Breitschwerdt D., 2012, A&A, 540, A77
Dubey A., Reid L. B., Fisher R., 2008, Physica Scripta, T132, 014046
Dubey A., Reid L. B., et al., 2009, arXiv e-prints, p. arXiv:0903.4875
Ekström S., Georgy C., et al., 2012, A&A, 537, A146
Ellison S. L., Wilkinson S., Woo J., et al., 2022, MNRAS, 517, L92
Elmegreen B. G., 2015, ApJ, 814, L30
Elmegreen B. G., 2018, ApJ, 854, 16
Falceta-Gonçalves D., Bonnell I., Kowal G., et al., 2015, MNRAS, 446, 973
Federrath C., 2015, MNRAS, 450, 4035

Federrath C., Banerjee R., Clark P. C., et al., 2010, ApJ, 713, 269
Feldmann R., Gnedin N. Y., Kravtsov A. V., 2011, ApJ, 732, 115
Fensch J., Renaud F., Bournaud F., et al., 2017, MNRAS, 465, 1934
Fielding D., Quataert E., Martizzi D., 2018, MNRAS, 481, 3325
Figueira M., Zavagno A., Deharveng L., et al., 2017, A&A, 600, A93
Fisher D. B., Bolatto A. D., White H., et al., 2019, ApJ, 870, 46
Fryxell B., Olson K., Ricker P., et al., 2000, ApJS, 131, 273
Gatto A., Walch S., Low M. M. M., et al., 2015, MNRAS, 449, 1057
Gatto A., Walch S., Naab T., et al., 2017, MNRAS, 466, 1903
Girichidis P., Walch S., Naab T., et al., 2016a, MNRAS, 456, 3432
Girichidis P., Naab T., Walch S., et al., 2016b, ApJ, 816, L19
Girichidis P., Naab T., Hanasz M., et al., 2018a, MNRAS, 479, 3042
Girichidis P., Seifried D., Naab T., et al., 2018b, MNRAS, 480, 3511
Glover S. C. O., Low M.-M. M., 2007, ApJ, 659, 1317
Glover S. C. O., Mac Low M.-M., 2007, ApJS, 169, 239
Gnat O., Ferland G. J., 2012, ApJS, 199, 20
Gupta S., Nath B. B., Sharma P., et al., 2016, MNRAS, 462, 4532
Gurvich A. B., Faucher-Giguère C.-A., et al., 2020, MNRAS, 498, 3664
Haid S., Walch S., Naab T., et al., 2016, MNRAS, 460, 2962
Haid S., Walch S., Seifried D., et al., 2018, MNRAS, 478, 4799
Haid S., Walch S., Seifried D., et al., 2019, MNRAS, 482, 4062
Hassan S., Ostriker E. C., Kim C.-G., et al., 2024, ApJ, 975, 151
Hayward C. C., Hopkins P. F., 2017, MNRAS, 465, 1682
Heckman T. M., Thompson T. A., 2017, arXiv e-prints, p. arXiv:1701.09062
Heckman T. M., Alexandroff R. M., Borthakur S., et al., 2015, ApJ, 809, 147
Herrera-Camus R., Bolatto A., Wolfire M., et al., 2017, ApJ, 835, 201
Hopkins P. F., Quataert E., Murray N., 2011, MNRAS, 417, 950
Hopkins P. F., Quataert E., Murray N., 2012, MNRAS, 421, 3488
Hopkins P. F., Kereš D., Oñorbe J., et al., 2014, MNRAS, 445, 581
Hopkins P. F., Wetzel A., Kereš D., et al., 2018, MNRAS, 480, 800
Hopkins P. F., Wetzel A., Wheeler C., et al., 2023, MNRAS, 519, 3154
Hu C.-Y., 2019, MNRAS, 483, 3363
Hu C.-Y., Naab T., Walch S., et al., 2016, MNRAS, 458, 3528
Hunter J. D., 2007, Computing in Science & Engineering, 9, 90
Jeřábková T., Zonoozi A. H., Kroupa P., et al., 2018, A&A, 620, A39
Kado-Fong E., Kim C.-G., Greene J. E., et al., 2022, ApJ, 939, 101
Kennicutt Jr. R. C., 1989, ApJ, 344, 685
Kennicutt Jr. R. C., 1998, ApJ, 498, 541
Kim C.-G., Ostriker E. C., 2015, ApJ, 802, 99
Kim C.-G., Ostriker E. C., 2018, ApJ, 853, 173
Kim C.-G., Kim W.-T., Ostriker E. C., 2011, ApJ, 743, 25
Kim C.-G., Ostriker E. C., Kim W.-T., 2013, ApJ, 776, 1
Kim C.-G., Kim J.-G., Gong M., et al., 2023, ApJ, 946, 3
Kim C.-G., Ostriker E. C., Kim J.-G., et al., 2024, ApJ, 972, 67
Kruijssen J. M. D., Longmore S. N., 2014, MNRAS, 439, 3239
Krumholz M. R., Burkhart B., Forbes J. C., et al., 2018, MNRAS, 477, 2716
Lenkić L., Fisher D. B., Bolatto A. D., et al., 2024, ApJ, 976, 88
Leroy A. K., Walter F., Brinks E., et al., 2008, AJ, 136, 2782
Li Q., Tan J. C., Christie D., et al., 2018, PASJ, 70, S56
Liu G., Koda J., Calzetti D., et al., 2011, ApJ, 735, 63
López-Sánchez Á. R., et al., 2018, MNRAS, 480, 210
Lucas W. E., Bonnell I. A., Dale J. E., 2020, MNRAS, 493, 4700
Luo W., Yang X., Zhang Y., 2014, ApJ, 789, L16
Mac Low M.-M., Klessen R. S., 2004, Reviews of Modern Physics, 76, 125
Mac Low M.-M., McCray R., 1988, ApJ, 324, 776
Mac Low M.-M., McCray R., Norman M. L., 1989, ApJ, 337, 141
Mackey J., Gvaramadze V. V., Mohamed S., et al., 2015, A&A, 573, A10
Martin D. C., et al., 2019, Nature Astronomy, 3, 822
McKee C. F., Ostriker J. P., 1977, ApJ, 218, 148
Menon S. H., Federrath C., Krumholz M. R., 2023, MNRAS, 521, 5160
Moreno J., Torrey P., Ellison S. L., et al., 2019, MNRAS, 485, 1320
Morokuma-Matsui K., Muraoka K., 2017, ApJ, 837, 137
Moster B. P., et al., 2012, MNRAS, 423, 2045
Murray N., 2011, ApJ, 729, 133
Murray N., Ménard B., Thompson T. A., 2011, ApJ, 735, 66
Nava L., Gabici S., 2013, MNRAS, 429, 1643
Nelson R. P., Langer W. D., 1997, ApJ, 482, 796
Neumann L., Jiménez-Donaire M. J., et al., 2025, A&A, 693, L13
Orr M. E., Hayward C. C., Medling A. M., et al., 2020, MNRAS, 496, 1620
Osterbrock D. E., 1988, Publications of the Astronomical Society of the Pacific, 100, 412
Ostriker E. C., Kim C.-G., 2022, ApJ, 936, 137
Ostriker E. C., Shetty R., 2011, ApJ, 731, 41
Ostriker E. C., McKee C. F., Leroy A. K., 2010, ApJ, 721, 975
Pearson W. J., Wang L., Alpaslan M., et al., 2019, A&A, 631, A51
Pereira-Santaella M., Colina L., et al., 2016, A&A, 594, A81
Perez F., Granger B. E., 2007, Computing in Science & Engineering, 9, 21
Peters T., Naab T., Walch S., et al., 2017, MNRAS, 466, 3293
Price D. J., Bate M. R., 2007, MNRAS, 377, 77
Price D. J., Bate M. R., 2008, MNRAS, 385, 1820
Rathjen T.-E., Naab T., et al., 2021, MNRAS, 504, 1039
Rathjen T.-E., Naab T., et al., 2023, MNRAS, 522, 1843
Rathjen T.-E., Walch S., et al., 2024, arXiv e-prints, p. arXiv:2410.00124
Reichardt Chu B., Fisher D. B., Chisholm J., et al., 2025, MNRAS, 536, 1799
Roberts-Borsani G. W., 2020, MNRAS, 494, 4266
Romano M., Nanni A., Donevski D., et al., 2023, A&A, 677, A44
Salpeter E. E., 1955, ApJ, 121, 161
Santoro F., Kreckel K., Belfiore F., et al., 2022, A&A, 658, A188
Schaye J., Crain R. A., Bower R. G., et al., 2015, MNRAS, 446, 521
Schinnerer E., Meidt S. E., Colombo D., et al., 2017, ApJ, 836, 62
Schmidt M., 1959, ApJ, 129, 243
Schruba A., Leroy A. K., Walter F., et al., 2010, ApJ, 722, 1699
Schruba A., Leroy A. K., Walter F., et al., 2011, AJ, 142, 37
Sembach K. R., Howk J. C., Ryans R. S. I., et al., 2000, ApJ, 528, 310
Shetty R., Ostriker E. C., 2012, ApJ, 754, 2
Silva A., Marchesini D., Silverman J. D., et al., 2018, ApJ, 868, 46
Spitzer L., 1978, Physical processes in the interstellar medium, doi:10.1002/9783527617722.
Springel V., 2000, MNRAS, 312, 859
Springel V., Hernquist L., 2003, MNRAS, 339, 289
Steinwandel U. P., et al., 2023a, arXiv e-prints, p. arXiv:2310.11495
Steinwandel U. P., et al., 2023b, MNRAS, 526, 1408
Steinwandel U. P., Kim C.-G., Bryan G. L., et al., 2024, ApJ, 960, 100
Strong A. W., Moskalenko I. V., et al., 2007, Annual Review of Nuclear and Particle Science, 57, 285
Sun J., Leroy A. K., Ostriker E. C., et al., 2020, ApJ, 892, 148
Sun J., Leroy A. K., Ostriker E. C., et al., 2023, ApJ, 945, L19
Szécsi D., Agrawal P., Wünsch R., et al., 2022, A&A, 658, A125
Tanaka K. E. I., Tan J. C., Zhang Y., et al., 2018, ApJ, 861, 68
Teyssier R., Chapon D., Bournaud F., 2010, ApJ, 720, L149
Turk M. J., Smith B. D., et al., 2011, ApJS, 192, 9
Veilleux S., Cecil G., Bland-Hawthorn J., 2005, ARA&A, 43, 769
Vijayan A., Krumholz M. R., Wibking B. D., 2025, MNRAS, 539, 1706
Virtanen P., Gommers R., Oliphant T. E., Haberland M., et al., 2020, Nature Methods, 17, 261
Walch S. K., Whitworth A. P., Bisbas T., et al., 2012, MNRAS, 427, 625
Walch S., Girichidis P., et al., 2015, MNRAS, 454, 238
Weaver R., McCray R., Castor J., et al., 1977, ApJ, 218, 377
Whitworth A., 1979, MNRAS, 186, 59
Wilson C. D., Elmegreen B. G., Bemis A., et al., 2019, ApJ, 882, 5
Wong T., Blitz L., 2002, ApJ, 569, 157
Wünsch R., Silich S., Palouš J., et al., 2011, ApJ, 740, 75
Wünsch R., Walch S., Dinnbier F., et al., 2018, MNRAS, 475, 3393
Wünsch R., Walch S., et al., 2021, MNRAS, 505, 3730
Xu X., Heckman T., Henry A., et al., 2022, ApJ, 933, 222
van der Walt S., Colbert S. C., Varoquaux G., 2011, Computing in Science & Engineering, 13, 22

APPENDIX A: MASS AND VOLUME FILLING FRACTIONS

In Fig. A1 we show the time evolution of the mass fractions (MF, solid lines) and the volume filling fractions (VFF, dashed lines) of the CNM (blue), WNM (orange), WIM (brown), hot gas (red) and

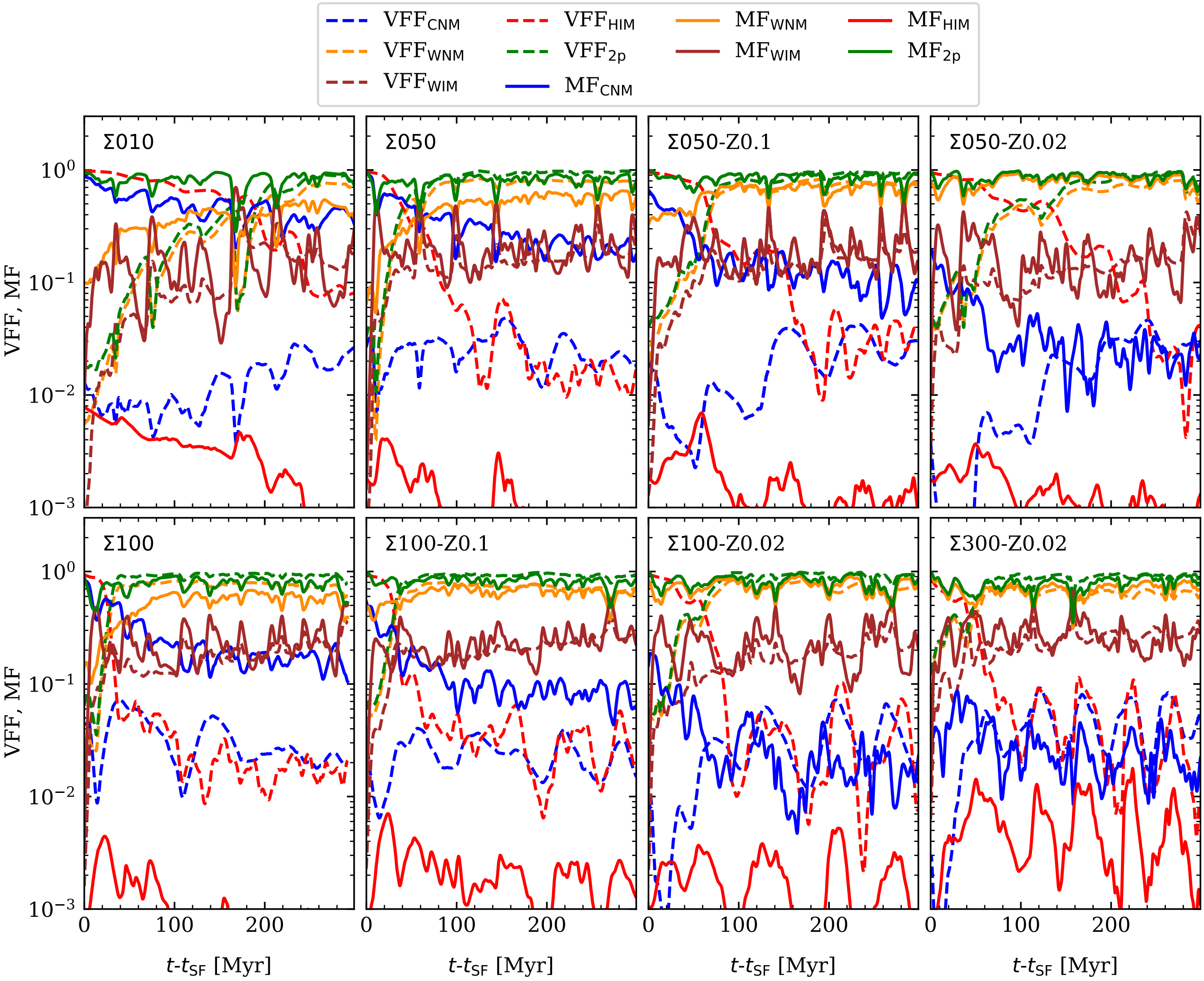

Figure A1. Mass (solid lines) and volume filling fractions (dashed lines) of the CNM (blue), WNM (orange), WIM (brown), hot (red) and `2p` (green) gas phases.

for the `2p` phase. Since the `2p` phase comprises both the cold gas and part of the WNM, its MF and VFF are dominant compared to the rest of the phases, as already seen in Kim et al. (2024). Regarding the CNM, we note that its MF is a function of the metallicity of the gas, as already seen in Brugaletta et al. in prep., and that its VFF is around one to two orders of magnitude lower. Without considering the `2p` phase, the MF and VFF of the WNM are dominant, being above 50% in all runs. Moreover, the time evolution of both the MF and VFF of the WNM is observed to be smooth, in contrast to the more oscillating behaviour of the MF and VFF of the WIM. In fact, the presence of the WIM is related to the presence of stars, which ionize the medium, and we observe its MF to be anti-correlated with that of the CNM. Both the MF and VFF of the WIM are around 10% – 20% for all runs. Regarding the hot gas, its MF is below 1% in all runs, independently on metallicity, as already seen in Brugaletta et al. in prep. However, its VFF is around a few per cents, and up to 10%, depending on the run.

APPENDIX B: PRESSURES IN THE PRFM THEORY

In this section we describe more in detail the pressure component which, summed up, determine the $P_{\rm tot,PRFM,gas}$.

In Fig. B1 and B2 we show the temperature-density and pressure-density phase diagrams for all our runs. For the pressures, we show the different components defined in Sec. 4, as well as the $P_{\rm tot,PRFM,gas}$. The phase diagrams have been computed considering the entire computational domain, at a time t-$t_{\rm SF}$ = 150 Myr. In the temperature and thermal pressure panels we add as a red dashed line the equilibrium curves, computed running our chemistry module in standalone mode for 1 Gyr, after which the gas has reached thermal and chemical equilibrium. These curves have been computed assuming $A_{\rm V,3D} = 0$, $G_0 = 1.7$ and $\zeta = 3 \times 10^{-17}$ s^{-1}. Moreover, we represent here the modulus of the $\Pi_{\rm mag}$, as this quantity can reach negative values when the magnetic tensor is larger than the magnetic pressure. We also add a pink dashed line in all pressure panels, that indicates the median value of the weight in the midplane ($z = 0$), computed considering the entire evolution of the runs after the onset of star formation. Regarding the temperature-density phase diagrams, we

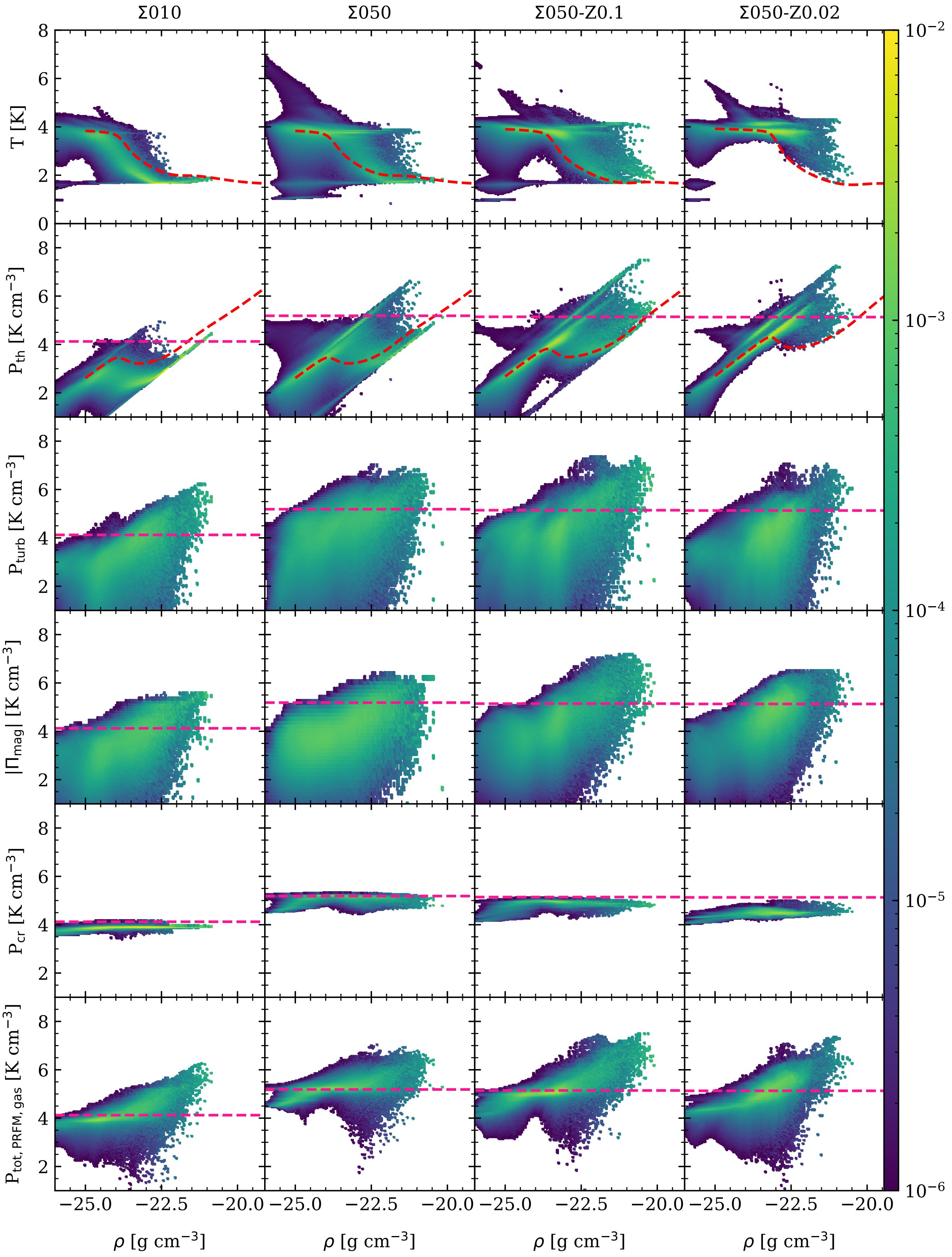

Figure B1. Temperature-density and pressure components-density phase diagrams, computed considering the entire box, at t - $t_{\rm SF}$ = 150 Myr. The red dashed line in the temperature and thermal pressure panels is the equilibrium curve. The pink dashed line is the median, computed in 300 Myr, of the weight in z = 0. The runs represented here are Σ010, Σ050, Σ050-Z.1, Σ050-Z0.02. We note that at low density, the pressure is dominated by $P_{\rm cr}$, whereas at high density $P_{\rm th}$ and $P_{\rm turb}$ dominate.

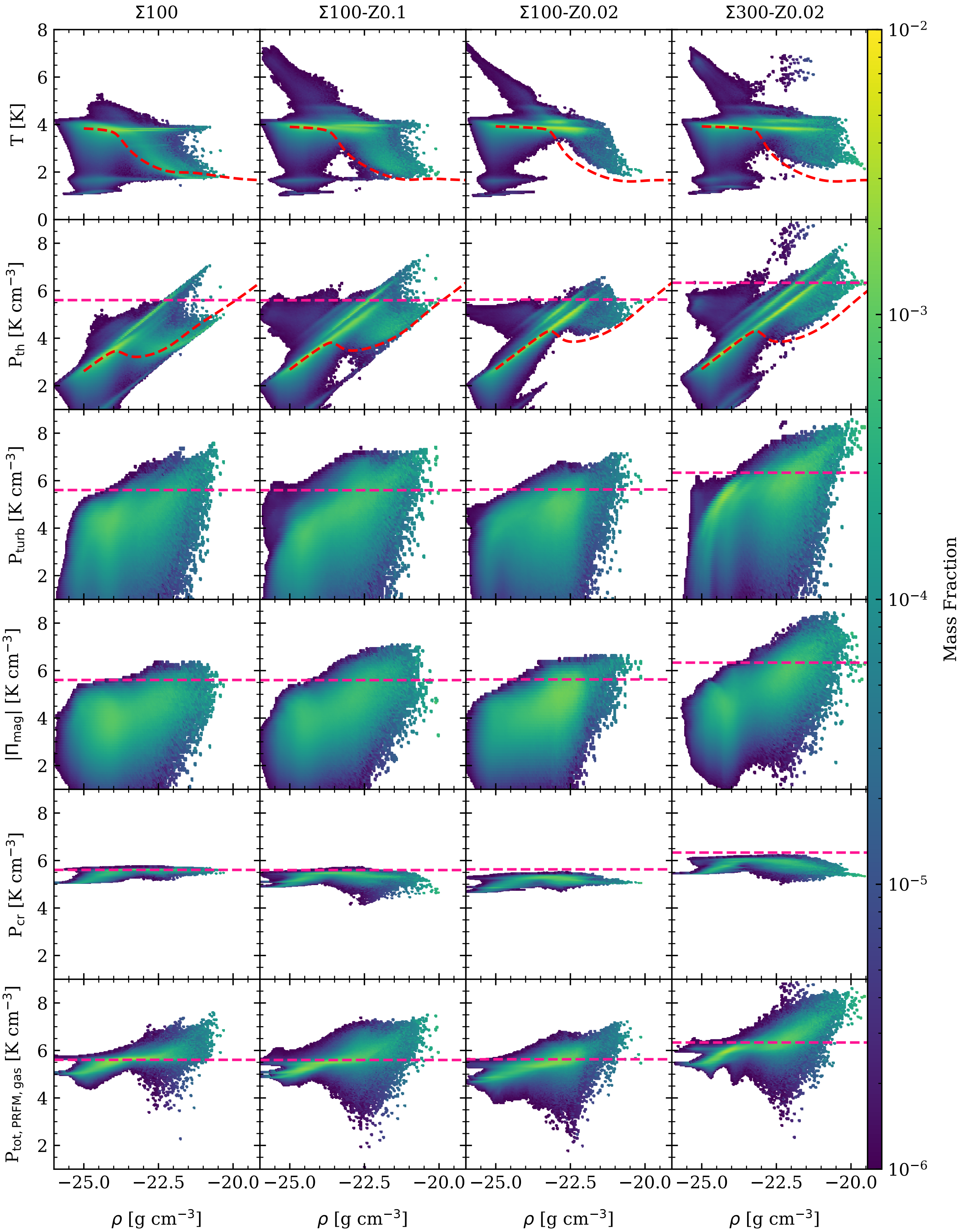

Figure B2. Same as Fig. B2, but representing the runs Σ100, Σ100-Z0.1, Σ100-Z0.02, Σ300-Z0.02.

note that the minimum temperature of the cold gas increases for the runs at low-metallicity, compared to those in solar-neighbourhood conditions at the same gas surface density. Moreover, the gas at temperatures higher than 10^6 K and at low density corresponds to the shock-heated gas from supernovae. Concerning the pressure components, we see that at low density, the $P_{\rm tot,PRFM,gas}$ is dominated by the CR pressure. We also notice that $P_{\rm cr}$ is almost constant in density for all runs, in accordance with the fact that CRs travel fast in our computational domain, providing an almost uniform $P_{\rm cr}$. On the other hand, at the high-density end the $P_{\rm tot,PRFM,gas}$ is dominated by the contribution of the $P_{\rm turb}$ and $\Pi_{\rm mag}$. In the case of $P_{\rm turb}$, the contribution to the velocity v_z due to the propagation of shocks, and gravitational collapse in the high density gas, determine an increase in $P_{\rm turb}$. In the case of $\Pi_{\rm mag}$, the magnetic pressure increases at high density.

APPENDIX C: GAS PHASES IN THE OUTFLOW

In Fig. C1 we show the time-averaged version of Fig. 13. In this representation, it is clearer to see that the warm gas dominates in mass the outflow in each run, followed by the cold and hot phase.

This paper has been typeset from a TEX/LATEX file prepared by the author.

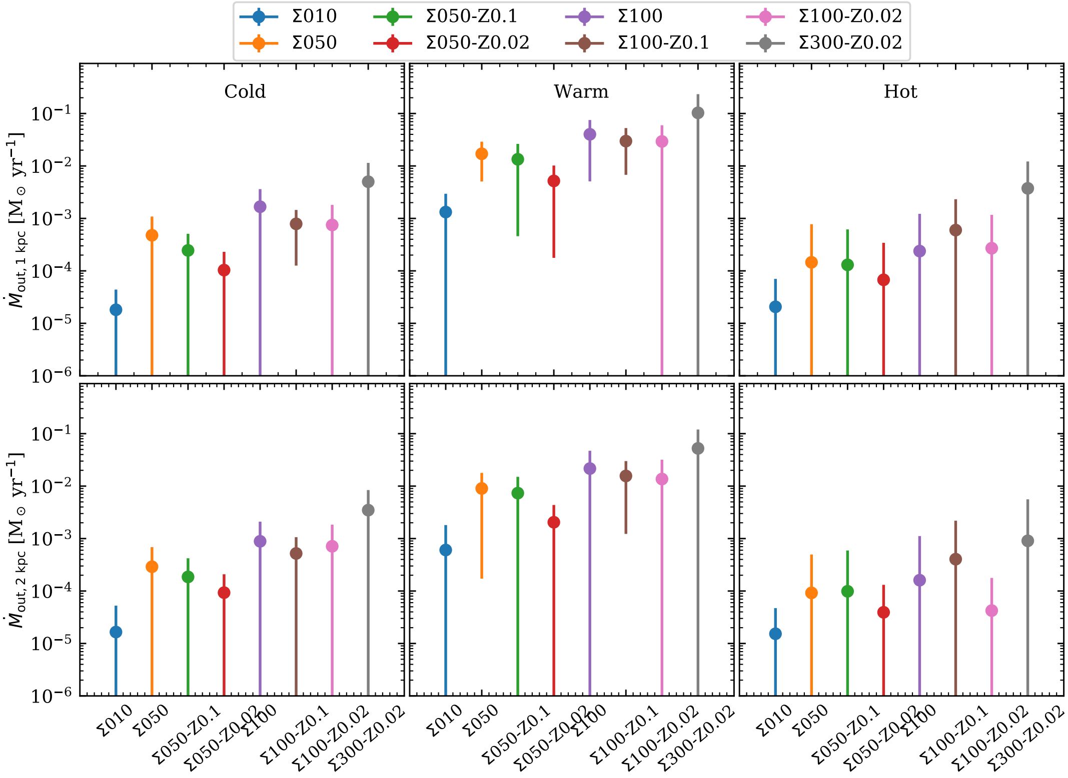

Figure C1. Same as Fig. 13, but with time-averaged mass outflow rates.

Chapter 7

Summary and conclusions

7.1 Summary

This work investigates the evolution of the interstellar medium, the self-regulation of star formation and galactic outflows in low-metallicity environments. Our aim is to understand how photoelectric and cosmic ray heating rates vary in the metal-poor gas, how the cooling inefficiency affects the subsequent star formation, stellar feedback and outflows, and how the variability of the star formation and outflow rates shape the structure of the interstellar medium.

We employ numerical simulations within the SILCC framework, modelling the evolution of the interstellar medium in a stratified disc, with a maximum resolution of 4 pc, by solving the magnetohydrodynamical equations. The simulations include non-equilibrium chemistry, detailed heating and cooling processes, and anisotropic cosmic ray (CR) transport in the advection-diffusion approximation. We employ stellar tracks for massive stars, including stellar feedback in the form of far-UV and EUV radiation, stellar winds, supernovae and CR injection.

This thesis is organized as follows.

In **Paper I**, we develop a new method to compute the CR ionization rate self-consistently. In this method, we compute the CR ionization rate by linearly scaling the CR energy density, already computed in our code, in the diffuse gas, and applying an attenuation factor to this scaling in the dense gas. A CR ionisation rate that varies in space and time is valuable in itself, as it allows for more accurate modelling of CR heating across a wide range of environments. However, we show that this temporal and spatial variability is essential for correctly describing CR heating in low-metallicity environments, where inefficient cooling plays a major role. Previous SILCC studies (see e.g. Rathjen et al., 2021, 2023, 2024) typically assumed a constant CR ionisation rate of $3 \times 10^{-17}\mathrm{s}^{-1}$, a standard value for the solar neighbourhood. In this work, we adopt a metallicity of 0.02 $\mathrm{Z}_{\odot}$ and we test this new method. We see that employing the constant "standard" CR ionization rate of 3×10^{-17} s^{-1} hinders the ability of the gas to cool down properly, leading to no or few and delayed star formation, depending on the model we use for photoelectric heating. In contrast, allowing the CR ionisation rate to vary enables substantial star formation even at such low metallicity.

In **Paper II**, we apply the method developed in Paper I to a new set of simulations with different metallicities (Z), in the range 0.02 $Z_\odot$–1 $Z_\odot$. Our goal is to determine how metallicity influences the structure and evolution of the interstellar medium, including its effects on star formation and outflows. We see that low metallicity environments are warmer than those in solar-neighbourhood conditions, with lower mass fractions of cold gas and molecular hydrogen. This is due to the lack of metals, which are the primary coolants of the gas colder than a few 10^6 K. However, for $Z > 0.1$ $Z_\odot$, we observe no dramatic differences in gas fragmentation, star formation, or mass outflow rates, suggesting that metallicity is not the dominant factor, above this threshold. Significant changes only occur at lower metallicities.

In **Paper III** we build on the CR heating model from Paper I, and the insights gained in Paper II, to assess whether the interstellar medium reaches a steady state. We recover the numerical results from the pressure-regulated, feedback-modulated star formation theory (see e.g. Ostriker & Kim, 2022) for the total gas, which is based on the assumption of steady state. However, these results primarily reflect the momentum equation we input in our code. To evaluate the validity of the steady state assumption, we compute accelerations due to pressure gradients and find that the interstellar medium is subjected on average to a total outward acceleration in the range of 1–10 km s^{-1} Myr^{-1}, indicating it is not in a steady state. Furthermore, we find no pressure equilibrium between the cold, warm, and hot gas phases, which is likewise inconsistent with a steady state. We therefore investigate the variability of star formation and outflows to assess their role in shaping interstellar medium evolution. We find that over half of the stars in our simulations form during starbursts, and that the majority of mass reaching 1 kpc above and below the midplane is associated with mass outflow rates exceeding their time-averaged values. Additionally, we measure a delay of approximately 10–20Myr between the star formation rate and the corresponding mass outflow rate at 1 kpc.

7.2 Conclusions

Low-metallicity environments are widespread throughout the Universe. Understanding how heating and cooling processes affect the formation of cold gas in such conditions, and consequently regulate star formation, is essential for interpreting the evolution of both nearby dwarf galaxies and galaxies at high redshift. This thesis advances previous SILCC studies by systematically extending the metallicity range probed by two orders of magnitude, providing new insights into the physics of metal-poor interstellar media.

A major contribution of this work is the development of a novel, self-consistent method for computing the CR ionisation rate, presented in Paper I. Unlike previous simulations that assumed a fixed value, this approach yields a spatially and temporally variable CR ionisation rate derived from the evolving CR energy density and local gas conditions. This refinement allows for a more realistic characterisation of CR heating across a wide range of environments, and directly challenges the prevailing assumption that fixed ionisation rates suffice for modelling star formation in galaxy-scale or cosmological simulations. Using this enhanced framework, we show in Paper I that CR heating becomes dominant with respect to photoelectric heating at extremely low metallicity ($Z = 0.02\ Z_{\odot}$), consistent with earlier expectations (e.g. Bialy & Sternberg 2019). We further find that the local variability in the CR ionisation rate is crucial: star formation preferentially occurs where the CR ionization rate is moderate, indicating that CRs act as a regulator of star formation in metal-poor environments. At fixed, solar-neighbourhood ionisation rates, star formation is significantly suppressed; with variable rates, it proceeds even in highly metal-poor gas.

In Paper II, we extend this analysis to a SILCC suite with varying metallicity (0.02–1 $Z_{\odot}$). We find that while the ISM at moderate metallicity ($Z > 0.1\ Z_{\odot}$) does not changes dramatically compared to solar-neighbourhood conditions in structure, star formation, and outflow behaviour, a qualitative shift occurs below this threshold. At very low metallicity, the gas is warmer, cold and molecular phases are diminished, and the ISM fails to fragment efficiently. As a result, both star formation and mass outflow rates are significantly reduced. This threshold behaviour suggests that metallicity not only influences ISM thermodynamics but defines distinct regimes of star formation and feedback.

In Paper III, we adopt the same metallicity range as in Paper II, but extend the range of gas surface densities, spanning from 10 to 300 $M_{\odot}\ \mathrm{pc}^{-2}$, in order to capture a broader variety of galactic environments. We find that the interstellar medium is not in a steady state, but rather a system in continuous evolution. This is in contrast with previous works (see e.g. McKee & Ostriker, 1977; Ostriker et al., 2010). In this work, we find that the variability of the star formation and mass outflow rate are fundamental for the evolution of the interstellar medium, as stars are mostly formed in starbursts and the majority of the outflowing mass is carried in periods of intense mass outflow rates.

7.3 Outlook

The work presented in this thesis can be improved in several ways, for example by including additional physical processes that have not been accounted for. One important extension would be to treat metallicity as a variable quantity that evolves in space and time, thereby allowing for a more realistic representation of chemical enrichment from stellar winds and supernovae. Such enrichment alters the local metallicity and enhances gas cooling (Shen et al., 2010), while also influencing the efficiency of supernova feedback (Karpov et al., 2020). Although the metal mixing timescale from a single enrichment event ranges from 100 Myr to 1 Gyr (Emerick et al., 2020b), a sufficiently high frequency of such events could reduce this timescale, making their impact noticeable even within the timescales explored in our simulations. Observational evidence also supports the need for variable metallicity modelling. For instance, Lebouteiller et al. (2013) observe that in the I Zwicky 18 dwarf galaxy (metallicity of around 0.02 $Z_\odot$), the atomic gas regions have a metallicity which is a factor of two lower than the metallicity measured for H II regions in the same galaxy. If we could reproduce this environment in our simulations, we would probably see some regions with enhanced star formation rates, and more metal-poor neutral atomic gas that is more susceptible to stellar feedback, launching outflows. Moreover, using appropriate stellar models for the winds and nucleosynthesis models for the enrichment due to supernovae, would ensure a more accurate treatment of chemical enrichment, recognising that massive stars contribute differently to the enrichment of the interstellar medium, depending on their mass (see e.g. Goswami et al., 2021; Wu et al., 2021). In this context, adopting realistic initial abundances for elements such as carbon, oxygen, and silicon, rather than scaling all species linearly with total metallicity, would provide a more physically accurate representation of chemical evolution. This is particularly relevant because total metallicity alone does not convey the relative abundances of individual species, each of which contributes differently to chemical reactions and cooling rates. Furthermore, our current assumption of a constant dust-to-gas ratio could be replaced with a variable ratio that evolves with metallicity and enrichment. This would allow us to model the depletion of metals onto dust grains more accurately. Including a treatment of polycyclic aromatic hydrocarbons (PAHs), which play a critical role in photoelectric heating (Okada et al., 2013; Berné et al., 2022), would also represent an important improvement in the physical realism of our simulations.

Another important extension would be to include binary massive stars, which are observed to be more prevalent in low-metallicity environments (see e.g. Villaseñor et al., 2025). The feedback from such systems is modified by their mutual interactions, significantly affecting the surrounding interstellar medium (Götberg et al., 2020; Lau et al., 2023; Matsuoka & Sawada, 2024). Additionally, not all massive stars end their lives as core-collapse supernovae; some may undergo direct collapse into black holes without a significant explosion (Heger et al., 2003). In the current implementation, all massive stars are assumed to explode as Type II supernovae, likely leading to an overestimation of supernova feedback. A more realistic treatment would involve accounting for the fraction of massive stars that do not explode, thereby refining our modelling of stellar feedback. Furthermore, radiation pressure constitutes another key physical process that could be incorporated. It is expected to be particularly relevant in high-density regions, where it can influence star formation and potentially contribute to driving galactic outflows (Andrews & Thompson, 2011; Murray et al., 2011; Chattopadhyay et al., 2012; Gupta et al., 2016; Menon et al., 2023). Finally, conducting high-resolution zoom-in simulations at low metallicity would provide valuable insight into the formation of cold and molecular gas. Such simulations would allow for a more accurate treatment of gas fragmentation in metal-poor conditions, offering a better understanding of massive star formation in these environments.

CHAPTER 8

OTHER PUBLICATIONS

The following work has been published during the PhD project, as a coauthor contribution: Geen, S. et al., 2023, Publications of the Astronomical Society of the Pacific, Volume 135, Issue 1044. The writing of Sec. 2.4 has been in part performed by Vittoria Brugaletta.

Chapter 9

The carbon footprint of this thesis

The simulations carried out for this thesis fall under the category of High Performance Computing (HPC), as they were executed across multiple computing clusters and supercomputers located in different data centres. The electrical efficiency of computing, defined as the number of computations performed per kilowatt-hour (kWh) of electricity, doubled approximately every 1.5 years between 1945 and 2010 (Koomey et al., 2011). While this is a remarkable trend, the overall power consumption of HPC systems continues to rise over time.

According to Gupta et al. (2020), the information and communication technology (ICT) sector is projected to account for 20% of global electricity demand by 2030, with data centres responsible for nearly half of this consumption. The environmental impact of HPC in astronomy has been specifically examined by Portegies Zwart (2020), who find that GPU-based simulations tend to have a smaller carbon footprint than their CPU-based counterparts. Furthermore, they highlight that programming languages such as CUDA, FORTRAN, and C++ are significantly more energy-efficient than high-level languages like Python.

Despite this, awareness of the environmental costs associated with simulations remains limited, even among researchers. In this chapter, we aim to provide a rough estimate of the carbon dioxide (CO_2) emissions associated with the simulations conducted for this project. Our assessment focuses exclusively on the computational aspects of the simulations, excluding the emissions related to routine data analysis, commuting, and conference travel.

9.1 The emitted CO_2 calculation

Calculating the emitted carbon dioxide (eCO_2) resulting from the simulations is not straightforward and relies on several assumptions. The main challenges include the lack of detailed usage statistics and the absence of a conversion factor from CPU hours (CPUh) to eCO_2 mass for some machines. This conversion depends not only on the specific hardware and its utilisation, but also on the energy mix of the data centre's electricity supplier. Energy may be sourced in varying proportions from nuclear, renewable, or fossil fuel-based generation, which significantly affects the associated emissions. Given these uncertainties, we adopt conservative assumptions likely to underestimate the true emissions, in order to avoid overstatement. A summary of the machines used, their total CPUh consumption, and the corresponding eCO_2 emissions is presented in Table 9.1. These estimates are based on the reference values published by the Max Planck Computing and Data Facility (MPCDF)[1], where part of the simulations were carried out.

Table 9.1

List of machines, of the total usage in CPUh, and the total eCO_2. The † symbol indicates that the total CPUh have been estimated from the output of the simulations.

Machine	Total CPUh $[10^6$ CPUh$]$	Total eCO2 [t]
MPCDF machines	7.97	21.2
RAMSES	$8.84^\dagger$	18.8
ODIN	$7^\dagger$	28.3
FREYA	?	?

MPCDF machines

A portion of the simulations was carried out on three supercomputers hosted at MPCDF in Garching: COBRA, RAVEN, and VIPER-cpu. For these systems, we have accurate records of CPU usage in core-hours, as this information is provided directly to users by MPCDF. To calculate the corresponding eCO_2 emissions, we first determined the total CPU usage per year of the three machines. This value was then divided by the reported HPC efficiency (in core-hours/kWh), and the result was multiplied by the CO_2 conversion factor (in g/kWh) specific to each year, as published on the MPCDF website.

RAMSES

RAMSES is a computing cluster hosted by the Regional Computing Centre (RRZK) at the University of Cologne. Unfortunately, no official usage data, HPC efficiency figures, or eCO_2 conversion factors are currently provided by RRZK. As a result, the total CPUh have been estimated from the output logs of the simulations.

To convert this estimate into eCO_2, we adopted the HPC efficiency and CO_2 conversion factor for the year 2024 as published on the MPCDF website. This choice is motivated by the fact that RAMSES is a recently installed machine (at the time of writing), and we therefore adopt the highest HPC efficiency available from MPCDF data as a conservative estimate. Conversely, assuming the same CO_2 conversion factor

---

[1] https://www.mpcdf.mpg.de/about/co2-footprint

implies that we neglect any differences in the electricity supply mix between Bavaria (where MPCDF is located) and North Rhine-Westphalia, where RRZK is based.

ODIN

ODIN is another cluster hosted by RRZK at the University of Cologne. As with RAMSES, no official data regarding CPU usage, HPC efficiency, or eCO_2 conversion factors is publicly available. Consequently, the total CPUh has been estimated based on the simulation outputs. Given that ODIN is an older machine, we adopt the HPC efficiency reported by MPCDF for the year 2015, which reflects the expected performance of legacy systems. For the CO_2 conversion factor, we use the average value across the period 2015–2024, in order to account for changes in the energy mix over the lifetime of the machine.

FREYA

The FREYA cluster is hosted at the Max Planck Institute for Astrophysics (MPA) in Garching. Unfortunately, no usage data have been provided for this machine, and it is not possible to reliably reconstruct usage estimates from the simulation outputs. As a result, FREYA is excluded from the formal CO_2 emission calculations presented here. Nevertheless, a substantial portion of the work in this thesis was carried out using this cluster. Based on typical run times and simulation complexity, the total usage may reasonably lie in the range of 10–20 million core-hours (MCPUh).

Total eCO_2

The total estimated eCO_2, excluding the substantial contribution from the FREYA cluster, amounts to approximately 68.3 tonnes of eCO_2. This figure is comparable to around 40.4 one-way flights between Frankfurt and Beijing, based on estimates from the Atmosfair emissions calculator[2].

To offset this quantity of eCO_2, direct air carbon capture technologies can achieve efficiencies of approximately 85–93% (Deutz & Bardow, 2021). However, the cost of such services is currently around €0.96 per kilogram of CO_2 captured[3]. Offsetting 68.3 tonnes would therefore amount to an expense of roughly €65,570. It is important to note that the author is not affiliated with Atmosfair or any carbon capture company; the figures presented here are for illustrative purposes only, to provide a tangible sense of the environmental footprint associated with the computational work behind this thesis.

Looking ahead, advances in hardware and software are expected to improve the

---

[2] `https://www.atmosfair.de/de/kompensieren/`

[3] `https://climeworks.com/`

energy efficiency of high-performance computing, potentially reducing the environmental cost of simulations. Nevertheless, it remains essential to advocate for:

- improved reporting and accessibility of core usage statistics from data centres, and
- the procurement of electricity from low-carbon or renewable sources for supercomputing facilities.

CHAPTER 10

ACKNOWLEDGEMENTS

During my PhD, I received support from many people, whom I would like to thank here. First and foremost, I am deeply grateful to my supervisors, Prof. Dr. Stefanie Walch-Gassner and Dr. Thorsten Naab, for their guidance, encouragement, and timely feedback throughout the course of this work. I would also like to thank Prof. Dr. Dominik Riechers for his insightful input as a TAC member, Prof. Dr. Peter Schilke for kindly agreeing to act as the second reviewer for this thesis, and Prof. Dr. Dennis Mücher for chairing the examination committee.

A heartfelt thank you goes to my co-authors, Dr. Philipp Girichidis, Dr. Tim-Eric Rathjen, Dr. Daniel Seifried, Pierre Nürnberger, Dr. Richard Wünsch, and Prof. Dr. Simon Glover, for sharing their expertise, supporting me along the way, and engaging in many valuable discussions that made the realisation of my papers possible. I am especially grateful to Dr. Masato Kobayashi, Dr. Daniel Seifried, Dr. Tim-Eric Rathjen, and Pierre Nürnberger for proofreading this thesis. I would also like to thank my research group for their support, especially during challenging times.

I gratefully acknowledge the SFB956, the Max Planck Institute for Astrophysics, and the SFB1601 for their financial support of this project. I also thank the Max Planck Computing and Data Facility for their assistance in estimating the carbon footprint of my simulations.

My PhD journey took me between Cologne and Munich, a transition that brought its own logistical and emotional challenges, including moving twice within twelve months over a distance of 600 km. I would not have made it without the help of incredible people. I am deeply thankful to Tim-Eric and Constantina for helping me find accommodation in Munich, and to Sabine for her help in finding accommodation back home in Bonn. I also thank my parents for their unwavering emotional support during the PhD and for their help, both practical and financial, during the moves.

Finally, my deepest thanks go to Philipp, who never stopped reminding me of how beautiful life is, even when I forgot to look outside the window.

Chapter 11

CURRICULUM VITAE

Personal information

Name: Vittoria Brugaletta
Nationality: Italian
Email: brugaletta@ph1.uni-koeln.de

Skills and expertise

- **General**: Time and project management, scientific writing, problem solving, continuous learning, analytical skills, independent work.
- **Technical skills**:Experience with high-performance computing clusters and supercomputers, good command of Unix, Linux, MacOS, Windows, Git, LaTeX.
- **Programming languages**: 7 years of experience in Python, with good command of the libraries numpy, scipy, matplotlib, pandas. Basic knowledge of Fortran.
- **Data analysis**: Proficient in analyzing large astrophysical datasets (> 100 TB) using Python, statistical methods, data visualization.
- **Interpersonal**: Strong communication and public speaking skills, including presentation experience at international conferences. Experience mentoring students and organizing scientific events.
- **Languages**: Italian (mother tongue), English (C1/C2), German (C1)

Education

- **PhD in Theoretical Astrophysics**, *University of Cologne and Max Planck Institute for Astrophysics*, February 2022 - Present. PhD supervisors: Prof. Dr. Stefanie Walch-Gassner (UoC) and Thorsten Naab (MPA)
- **M.Sc. in Astrophysics**, *University of Bonn*, Sept. 2019 - Dec 2021. Supervisor: Prof. Dr. Stefanie Walch-Gassner.
- **B.Sc. in Physics**, *University of Pisa, Italy*, Sept. 2015 - Sept. 2019

Honors and awards

- **Tonielli Award**, *University of Cologne*, faculty prize for PhD thesis.
- **Honors certificate**, *University of Bonn*, for outstanding grades during the Master.
- **Deutschlandstipendium 2020/2021**, *University of Bonn*.

Publications

- Brugaletta V., et al., 2025, Monthly Notices of the Royal Astronomical Society, 537, 482
- Geen S., et al., 2023, Publications of the Astronomical Society of the Pacific, Volume 135, Issue 1044 (as coauthor)

Contributed talks and posters in conferences

- Star Formation in Different Environments, Quy Nhon, Vietnam, August 2025 (Talk)
- Puzzles of Star Formation II, Ringberg Castle, May 2025 (Talk)
- AG Meeting, Cologne, September 2024 (Talk)
- International HPC Summer School, Kobe, Japan, July 2024 (Poster)
- Alpbach workshop, Alpbach, Austria, June 2024 (Talk)
- Star@Lyon, Lyon, France, June 2023 (Poster)

Bibliography

Ackermann M., et al., 2012, ApJ, 750, 3

Ackermann M., et al., 2013, Science, 339, 807

Afflerbach A., Churchwell E., Werner M. W., 1997, ApJ, 478, 190

André P., et al., 2010, A&A, 518, L102

Andrews B. H., Thompson T. A., 2011, ApJ, 727, 97

Asplund M., Grevesse N., Sauval A. J., Scott P., 2009, ARA&A, 47, 481

Baade W., Zwicky F., 1934, Physical Review, 46, 76

Bacalla X. L., et al., 2019, A&A, 622, A31

Bakes E. L. O., Tielens A. G. G. M., 1994, ApJ, 427, 822

Ballesteros-Paredes J., et al., 2024, MNRAS, 534, 1043

Barnes J., Hut P., 1986, Nature, 324, 446

Barnes A. T., Longmore S. N., Dale J. E., Krumholz M. R., Kruijssen J. M. D., Bigiel F., 2020, MNRAS, 498, 4906

Barnes A. T., et al., 2021, MNRAS, 508, 5362

Bate M. R., 2014, MNRAS, 442, 285

Bate M. R., 2019, MNRAS, 484, 2341

Bate M. R., Bonnell I. A., Price N. M., 1995, MNRAS, 277, 362

Beltrán M. T., Cesaroni R., Moscadelli L., Sánchez-Monge Á., Hirota T., Kumar M. S. N., 2016, A&A, 593, A49

Berné O., Foschino S., Jalabert F., Joblin C., 2022, A&A, 667, A159

Bialy S., Sternberg A., 2019, ApJ, 881, 160

Bieri R., Naab T., Geen S., Coles J. P., Pakmor R., Walch S., 2023, MNRAS, 523, 6336

Black J. H., Dalgarno A., 1977, ApJS, 34, 405

Blitz L., Rosolowsky E., 2004, ApJ, 612, L29

Blitz L., Rosolowsky E., 2006, ApJ, 650, 933

Blondin J. M., Wright E. B., Borkowski K. J., Reynolds S. P., 1998, ApJ, 500, 342

Bohlin R. C., Savage B. D., Drake J. F., 1978, ApJ, 224, 132

Bouchut F., Klingenberg C., Waagan K., 2007, Numerische Mathematik, 108, 7

Bouchut F., Klingenberg C., Waagan K., 2010, Numerische Mathematik, 115, 647

Boulares A., Cox D. P., 1990, ApJ, 365, 544

Bromm V., Ferrara A., Coppi P. S., Larson R. B., 2001, MNRAS, 328, 969

Brott I., et al., 2011, A&A, 530, A115

Brunetti G., Jones T. W., 2014, International Journal of Modern Physics D, 23, 1430007

Cabedo V., Maury A., Girart J. M., Padovani M., Hennebelle P., Houde M., Zhang Q., 2023, A&A, 669, A90

Castor J., McCray R., Weaver R., 1975, ApJ, 200, L107

Ceccarelli C., Dominik C., López-Sepulcre A., Kama M., Padovani M., Caux E., Caselli P., 2014, ApJ, 790, L1

Chastenet J., et al., 2021, ApJ, 912, 103

Chattopadhyay I., Sharma M., Nath B. B., Ryu D., 2012, MNRAS, 423, 2153

Chevance M., et al., 2016, A&A, 590, A36

Chevance M., et al., 2020, Space Sci. Rev., 216, 50

Chevance M., Krumholz M. R., McLeod A. F., Ostriker E. C., Rosolowsky E. W., Sternberg A., 2023, in Inutsuka S., Aikawa Y., Muto T., Tomida K., Tamura M., eds, Astronomical Society of the Pacific Conference Series Vol. 534, Protostars and Planets VII. p. 1 (`arXiv:2203.09570`), doi:10.48550/arXiv.2203.09570

Chon S., Omukai K., 2024, arXiv e-prints, p. arXiv:2412.14900

Chon S., Omukai K., Schneider R., 2021, MNRAS, 508, 4175

Chruślińska M., Jeřábková T., Nelemans G., Yan Z., 2020, A&A, 636, A10

Clark P. C., Glover S. C. O., Klessen R. S., 2008, ApJ, 672, 757

Clark P. C., Glover S. C. O., Klessen R. S., 2012, MNRAS, 420, 745

Congiu E., Matar E., Kristensen L. E., Dulieu F., Lemaire J. L., 2009, MNRAS, 397, L96

Cormier D., et al., 2014, A&A, 564, A121

Cormier D., et al., 2015, A&A, 578, A53

Cormier D., et al., 2019, A&A, 626, A23

Creasey P., Theuns T., Bower R. G., 2013, MNRAS, 429, 1922

Crocker R. M., Krumholz M. R., Thompson T. A., 2021, MNRAS, 503, 2651

Cummings A. C., et al., 2016, ApJ, 831, 18

Dale J., Ngoumou J., Ercolano B., Bonnell I., 2014, Monthly Notices of the Royal Astronomical Society, 442, 694

Dalgarno A., Yan M., Liu W., 1999, ApJS, 125, 237

Dempsey J., et al., 2022, Publ. Astron. Soc. Australia, 39, e034

Deutz S., Bardow A., 2021, Nature Energy, 6, 203

Dickey J. M., Mebold U., Stanimirovic S., Staveley-Smith L., 2000, ApJ, 536, 756

Dinnbier F., Walch S., 2020, MNRAS, 499, 748

Dopcke G., Glover S. C. O., Clark P. C., Klessen R. S., 2011, ApJ, 729, L3

Dorfi E. A., Breitschwerdt D., 2012, A&A, 540, A77

Draine B. T., 2011, Physics of the Interstellar and Intergalactic Medium

Draine B. T., et al., 2007, ApJ, 663, 866

Dubey A., Reid L. B., Fisher R., 2008, Physica Scripta Volume T, 132, 014046

Dubey A., Reid L. B., Weide K., Antypas K., Ganapathy M. K., Riley K., Sheeler D., Siegal A., 2009, arXiv e-prints, p. arXiv:0903.4875

Ekström S., et al., 2012, A&A, 537, A146

Elmegreen B. G., 1989, ApJ, 338, 178

Emerick A., Bryan G. L., Mac Low M.-M., 2018, ApJ, 865, L22

Emerick A., Bryan G. L., Mac Low M.-M., 2020a, arXiv e-prints, p. arXiv:2007.03702

Emerick A., Bryan G. L., Mac Low M.-M., 2020b, ApJ, 890, 155

Falgarone E., Pineau des Forets G., Roueff E., 1995, A&A, 300, 870

Farmer R., Laplace E., Ma J.-z., de Mink S. E., Justham S., 2023, ApJ, 948, 111

Favre C., et al., 2018, ApJ, 859, 136

Federrath C., Banerjee R., Clark P. C., Klessen R. S., 2010, ApJ, 713, 269

Ferrière K. M., 2001, Reviews of Modern Physics, 73, 1031

Field G. B., Goldsmith D. W., Habing H. J., 1969, ApJ, 155, L149

Fielding D., Quataert E., Martizzi D., Faucher-Giguère C.-A., 2017, MNRAS, 470, L39

Fixsen D. J., 2009, ApJ, 707, 916

Fontani F., et al., 2017, A&A, 605, A57

Fryxell B., et al., 2000, ApJS, 131, 273

Fullerton A. W., Gies D. R., Bolton C. T., 1992, ApJ, 390, 650

Gabici S., 2022, A&ARv, 30, 4

Galliano F., et al., 2021, A&A, 649, A18

Ganguly S., Walch S., Seifried D., Clarke S. D., 2023, in Ossenkopf-Okada V., Schaaf R., Breloy I., Stutzki J., eds, Physics and Chemistry of Star Formation: The Dynamical ISM Across Time and Spatial Scales. p. 142

Gatto A., et al., 2015, MNRAS, 449, 1057

Gatto A., et al., 2017, MNRAS, 466, 1903

Geen S., Rosdahl J., Blaizot J., Devriendt J., Slyz A., 2015, MNRAS, 448, 3248

Geen S., Pellegrini E., Bieri R., Klessen R., 2020, MNRAS, 492, 915

Genzel R., et al., 2010, MNRAS, 407, 2091

Ginzburg V. L., Syrovatskii S. I., 1964, The Origin of Cosmic Rays

Girart J. M., Beltrán M. T., Zhang Q., Rao R., Estalella R., 2009, Science, 324, 1408

Girichidis P., Naab T., Walch S., Hanasz M., 2014, arXiv e-prints, p. arXiv:1406.4861

Girichidis P., Walch S., et al., 2016a, MNRAS, 456, 3432

Girichidis P., et al., 2016b, ApJ, 816, L19

Girichidis P., Naab T., Hanasz M., Walch S., 2018a, MNRAS, 479, 3042

Girichidis P., Seifried D., et al., 2018b, MNRAS, 480, 3511

Glassgold A. E., Langer W. D., 1973, ApJ, 186, 859

Glassgold A. E., Langer W. D., 1974, ApJ, 193, 73

Glassgold A. E., Galli D., Padovani M., 2012, ApJ, 756, 157

Glover S. C. O., Clark P. C., 2012a, MNRAS, 421, 9

Glover S. C. O., Clark P. C., 2012b, MNRAS, 421, 116

Glover S. C. O., Clark P. C., 2012c, MNRAS, 426, 377

Glover S. C. O., Mac Low M.-M., 2007a, ApJS, 169, 239

Glover S. C. O., Mac Low M.-M., 2007b, ApJ, 659, 1317

Glover S. C. O., Mac Low M. M., 2011, MNRAS, 412, 337

Glover S. C. O., Federrath C., Mac Low M. M., Klessen R. S., 2010, MNRAS, 404, 2

Gnat O., Ferland G. J., 2012a, ApJS, 199, 20

Gnat O., Ferland G. J., 2012b, ApJS, 199, 20

Godard B., Falgarone E., Pineau Des Forêts G., 2009, A&A, 495, 847

Goldsmith P. F., Langer W. D., 1978, ApJ, 222, 881

Gordon K. D., Clayton G. C., Misselt K. A., Landolt A. U., Wolff M. J., 2003, ApJ, 594, 279

Górski K. M., Hivon E., Banday A. J., Wandelt B. D., Hansen F. K., Reinecke M., Bartelmann M., 2005, ApJ, 622, 759

Goswami S., et al., 2021, A&A, 650, A203

Götberg Y., de Mink S. E., McQuinn M., Zapartas E., Groh J. H., Norman C., 2020, A&A, 634, A134

Greenberg J. M., Chlewicki G., 1983, ApJ, 272, 563

Grenier I. A., Black J. H., Strong A. W., 2015, ARA&A, 53, 199

Gupta S., Nath B. B., Sharma P., Shchekinov Y., 2016, MNRAS, 462, 4532

Gupta U., Kim Y. G., Lee S., Tse J., Lee H.-H. S., Wei G.-Y., Brooks D., Wu C.-J., 2020, arXiv e-prints, p. arXiv:2011.02839

Guszejnov D., Grudić M. Y., Offner S. S. R., Faucher-Giguère C.-A., Hopkins P. F., Rosen A. L., 2022, Monthly Notices of the Royal Astronomical Society, 515, 4929

Haardt F., Madau P., 2012, ApJ, 746, 125

Habegger R., Zweibel E. G., 2024, arXiv e-prints, p. arXiv:2412.12249

Habing H. J., 1968, Bull. Astron. Inst. Netherlands, 19, 421

Hacar A., Clark S. E., Heitsch F., Kainulainen J., Panopoulou G. V., Seifried D., Smith R., 2023, in Inutsuka S., Aikawa Y., Muto T., Tomida K., Tamura M., eds, Astronomical Society of the Pacific Conference Series Vol. 534, Protostars and Planets VII. p. 153 (`arXiv:2203.09562`), doi:10.48550/arXiv.2203.09562

Haid S., Walch S., Naab T., Seifried D., Mackey J., Gatto A., 2016, MNRAS, 460, 2962

Haid S., Walch S., Seifried D., Wünsch R., Dinnbier F., Naab T., 2018, MNRAS, 478, 4799

Hainich R., Pasemann D., Todt H., Shenar T., Sander A., Hamann W. R., 2015, A&A, 581, A21

Hanasz M., Lesch H., Naab T., Gawryszczak A., Kowalik K., Wóltański D., 2013, ApJ, 777, L38

Heger A., Fryer C. L., Woosley S. E., Langer N., Hartmann D. H., 2003, ApJ, 591, 288

Hennebelle P., 2013, A&A, 556, A153

Hennebelle P., Inutsuka S.-i., 2019, Frontiers in Astronomy and Space Sciences, 6, 5

Hocuk S., Spaans M., 2010, A&A, 522, A24

Hollenbach D., McKee C. F., 1979, ApJS, 41, 555

Hollenbach D., McKee C. F., 1989, ApJ, 342, 306

Hu C.-Y., Schruba A., Sternberg A., van Dishoeck E. F., 2022, ApJ, 931, 28

Hull C. L. H., Zhang Q., 2019, Frontiers in Astronomy and Space Sciences, 6, 3

Hunt L. K., Thuan T. X., Izotov Y. I., Sauvage M., 2010, ApJ, 712, 164

Hunt L. K., et al., 2015, A&A, 583, A114

Hunt L. K., et al., 2023, A&A, 675, A64

Iffrig O., Hennebelle P., 2015, A&A, 576, A95

Iffrig O., Hennebelle P., 2017, A&A, 604, A70

Indriolo N., Geballe T. R., Oka T., McCall B. J., 2007, ApJ, 671, 1736

Indriolo N., et al., 2015, ApJ, 800, 40

Jameson K. E., et al., 2018, ApJ, 853, 111

Jameson K. E., et al., 2019, ApJS, 244, 7

Jecmen M. C., Oey M. S., 2023, ApJ, 958, 149

Jenkins E. B., 2009, ApJ, 700, 1299

Joung M. K. R., Mac Low M.-M., 2006, ApJ, 653, 1266

Joung M. R., Mac Low M.-M., Bryan G. L., 2009, ApJ, 704, 137

Kálosi Á., et al., 2023, ApJ, 955, L26

Kannan R., Marinacci F., Simpson C. M., Glover S. C. O., Hernquist L., 2020, MNRAS, 491, 2088

Kaper L., Henrichs H. F., Nichols J. S., Telting J. H., 1998, Long- and short-term variability in O-star winds II. Quantitative analysis of DAC behaviour (`arXiv:astro-ph/9812427`), `https://arxiv.org/abs/astro-ph/9812427`

Karpov P. I., Martizzi D., Macias P., Ramirez-Ruiz E., Kolborg A. N., Naiman J. P., 2020, ApJ, 896, 66

Kawada M., et al., 2011, PASJ, 63, 903

Kennicutt Jr. R. C., 1998, ApJ, 498, 541

Kennicutt R. C., Evans N. J., 2012, ARA&A, 50, 531

Kim C.-G., Ostriker E. C., 2015, ApJ, 802, 99

Kim J.-G., Kim W.-T., Ostriker E. C., 2018, ApJ, 859, 68

Kim C.-G., et al., 2024, ApJ, 972, 67

Klessen R. S., Glover S. C. O., 2016, Saas-Fee Advanced Course, 43, 85

Kobayashi C., Karakas A. I., Lugaro M., 2020, ApJ, 900, 179

Koomey J., Berard S., Sanchez M., Wong H., 2011, IEEE Annals of the History of Computing, 33, 46

Korpi M. J., Brandenburg A., Shukurov A., Tuominen I., Nordlund Å., 1999, ApJ, 514, L99

Koutsoumpou E., Fernández-Ontiveros J. A., Dasyra K. M., Spinoglio L., 2025, A&A, 693, A215

Koyama H., Ostriker E. C., 2009, ApJ, 693, 1346

Kroupa P., 2001, MNRAS, 322, 231

Krumholz M. R., 2011, ApJ, 743, 110

Krumholz M. R., 2014, Phys. Rep., 539, 49

Krumholz M. R., Matzner C. D., 2009, ApJ, 703, 1352

Krumholz M. R., McKee C. F., Klein R. I., 2004, ApJ, 611, 399

Krumholz M. R., McKee C. F., Tumlinson J., 2009, ApJ, 693, 216

Kulsrud R., Pearce W. P., 1969, ApJ, 156, 445

Lau R., Hankins M., WR DustERS Team 2023, in American Astronomical Society Meeting Abstracts. p. 144.04

Le Bourlot J., Le Petit F., Pinto C., Roueff E., Roy F., 2012, A&A, 541, A76

Lebouteiller V., Heap S., Hubeny I., Kunth D., 2013, A&A, 553, A16

Leroy A. K., et al., 2011, ApJ, 737, 12

Li P. S., Myers A., McKee C. F., 2012, ApJ, 760, 33

Li M., Ostriker J. P., Cen R., Bryan G. L., Naab T., 2015, ApJ, 814, 4

Linsky J. L., et al., 2006, ApJ, 647, 1106

Lopez L. A., Krumholz M. R., Bolatto A. D., Prochaska J. X., Ramirez-Ruiz E., 2011, ApJ, 731, 91

Mac Low M.-M., Klessen R. S., 2004, Reviews of modern physics, 76, 125

Mac Low M.-M., McCray R., 1988, ApJ, 324, 776

MacNeice P., Olson K. M., Mobarry C., de Fainchtein R., Packer C., 2000, Computer Physics Communications, 126, 330

Maciel W. J., Quireza C., 1999, A&A, 345, 629

Mackey J., Gvaramadze V. V., Mohamed S., Langer N., 2015, Astronomy & Astrophysics, 573, A10

Madden S. C., 2000, New Astron. Rev., 44, 249

Madden S. C., 2022, in European Physical Journal Web of Conferences. p. 00011, doi:10.1051/epjconf/202226500011

Madden S. C., Poglitsch A., Geis N., Stacey G. J., Townes C. H., 1997, ApJ, 483, 200

Marcolino W. L. F., Bouret J. C., Rocha-Pinto H. J., Bernini-Peron M., Vink J. S., 2022, MNRAS, 511, 5104

Marigo P., 2001, Astronomy and Astrophysics

Markova N., 2002, A&A, 385, 479

Markova N., Puls J., 2008, Astronomy & Astrophysics, 478, 823

Markova N., Puls J., Scuderi S., Markov H., 2005, Astronomy & Astrophysics, 440, 1133

Martín-Navarro I., et al., 2015, ApJ, 806, L31

Martín-Navarro I., et al., 2019, A&A, 626, A124

Martín-Navarro I., et al., 2021, A&A, 654, A59

Martínez-González S., Wünsch R., Tenorio-Tagle G., Silich S., Szécsi D., Palouš J., 2022, ApJ, 934, 51

Martizzi D., Faucher-Giguère C.-A., Quataert E., 2015, MNRAS, 450, 504

Massa D., et al., 1995, The Astrophysical Journal, 452, L53

Matsuoka T., Sawada R., 2024, ApJ, 963, 105

McKee C. F., Ostriker J. P., 1977, ApJ, 218, 148

McKee C. F., Ostriker E. C., 2007, ARA&A, 45, 565

McLeod A. F., Dale J. E., Evans C. J., Ginsburg A., Kruijssen J. M. D., Pellegrini E. W., Ramsay S. K., Testi L., 2019, MNRAS, 486, 5263

Menon S. H., Federrath C., Krumholz M. R., 2023, MNRAS, 521, 5160

Milgrom M., Panagia N., Salpeter E. E., 1973, Astrophys. Lett., 14, 73

Mizuno A., Onishi T., Yonekura Y., Nagahama T., Ogawa H., Fukui Y., 1995, ApJ, 445, L161

Muller S., et al., 2016, A&A, 595, A128

Murray N., Ménard B., Thompson T. A., 2011, ApJ, 735, 66

Myers A. T., Krumholz M. R., Klein R. I., McKee C. F., 2011, ApJ, 735, 49

Nagahama T., Mizuno A., Ogawa H., Fukui Y., 1998, AJ, 116, 336

Nanni A., Burgarella D., Theulé P., Côté B., Hirashita H., 2020, A&A, 641, A168

Nava L., Gabici S., 2013, MNRAS, 429, 1643

Navarro J. F., Frenk C. S., White S. D. M., 1996, ApJ, 462, 563

Nelson R. P., Langer W. D., 1997, ApJ, 482, 796

Neronov A., Malyshev D., Semikoz D. V., 2017, A&A, 606, A22

Okada Y., et al., 2013, A&A, 553, A2

Oku Y., Tomida K., Nagamine K., Shimizu I., Cen R., 2022, ApJS, 262, 9

Olivier G. M., Lopez L. A., Rosen A. L., Nayak O., Reiter M., Krumholz M. R., Bolatto A. D., 2021, ApJ, 908, 68

Onishi T., et al., 1999, PASJ, 51, 871

OpenAI 2023, ChatGPT (GPT-4), `https://www.openai.com/chatgpt`

Orr M. E., Fielding D. B., Hayward C. C., Burkhart B., 2022, ApJ, 932, 88

Osorio M., et al., 2017, ApJ, 840, 36

Osterbrock D. E., 1988, PASP, 100, 412

Ostriker E. C., Kim C.-G., 2022, ApJ, 936, 137

Ostriker E. C., McKee C. F., Leroy A. K., 2010, ApJ, 721, 975

Ou P.-S., Chen K.-J., Chu Y.-H., Tsai S.-H., 2023, ApJ, 944, 34

Padoan P., Zweibel E., Nordlund Å., 2000, ApJ, 540, 332

Padovani M., Galli D., Glassgold A. E., 2009, A&A, 501, 619

Padovani M., et al., 2020, Space Sci. Rev., 216, 29

Padovani M., et al., 2022, A&A, 658, A189

Parikh T., et al., 2018, MNRAS, 477, 3954

Pattle K., Fissel L., Tahani M., Liu T., Ntormousi E., 2023, in Inutsuka S., Aikawa Y., Muto T., Tomida K., Tamura M., eds, Astronomical Society of the Pacific Conference Series Vol. 534, Protostars and Planets VII. p. 193 (`arXiv:2203.11179`), doi:10.48550/arXiv.2203.11179

Peters T., Schleicher D. R. G., Smith R. J., Schmidt W., Klessen R. S., 2014, MNRAS, 442, 3112

Peters T., et al., 2017, MNRAS, 466, 3293

Pfrommer C., Pakmor R., Schaal K., Simpson C. M., Springel V., 2017, MNRAS, 465, 4500

Piontek R. A., Ostriker E. C., 2005, ApJ, 629, 849

Piontek R. A., Ostriker E. C., 2007, ApJ, 663, 183

Poglitsch A., Krabbe A., Madden S. C., Nikola T., Geis N., Johansson L. E. B., Stacey G. J., Sternberg A., 1995, ApJ, 454, 293

Polles F. L., et al., 2019, A&A, 622, A119

Polzin A., Kravtsov A. V., Semenov V. A., Gnedin N. Y., 2024, ApJ, 966, 172

Pon A., Johnstone D., Kaufman M. J., 2012, ApJ, 748, 25

Portegies Zwart S., 2020, Nature Astronomy, 4, 819

Prinja R. K., Fullerton A. W., 1994, ApJ, 426, 345

Prinja R., Smith L., 1992, Astronomy and Astrophysics (ISSN 0004-6361), vol. 266, no. 1, p. 377-384., 266, 377

Prinja R., Fullerton A., Crowther P., 1996, Astronomy and Astrophysics, v. 311, p. 264-272, 311, 264

Prodanović T., Steigman G., Fields B. D., 2010, MNRAS, 406, 1108

Ramambason L., et al., 2022, A&A, 667, A35

Rathjen T.-E., Naab T., et al., 2021, MNRAS, 504, 1039

Rathjen T.-E., Naab T., et al., 2023, MNRAS, 522, 1843

Rathjen T.-E., Walch S., et al., 2024, arXiv e-prints, p. arXiv:2410.00124

Rauw G., Morrison N. D., Vreux J. M., Gosset E., Mulliss C. L., 2001, A&A, 366, 585

Reichardt Chu B., et al., 2022, MNRAS, 511, 5782

Rémy-Ruyer A., et al., 2014, A&A, 563, A31

Rix H.-W., et al., 2022, ApJ, 941, 45

Rodríguez-Kamenetzky A., et al., 2017, ApJ, 851, 16

Rolleston W. R. J., Smartt S. J., Dufton P. L., Ryans R. S. I., 2000, A&A, 363, 537

Röllig M., Ossenkopf V., Jeyakumar S., Stutzki J., Sternberg A., 2006, A&A, 451, 917

Rosen A. L., 2022, ApJ, 941, 202

Roser J. E., Swords S., Vidali G., Manicò G., Pirronello V., 2003, ApJ, 596, L55

Ruszkowski M., Pfrommer C., 2023, A&ARv, 31, 4

Ryu D., Kim J., Hong S. S., Jones T. W., 2003, ApJ, 589, 338

Sales L. V., Marinacci F., Springel V., Petkova M., 2014, MNRAS, 439, 2990

Salpeter E. E., 1955, ApJ, 121, 161

Sanders R. L., et al., 2023, ApJ, 942, 24

Sanna A., et al., 2019, A&A, 623, L3

Schlickeiser R., Lerche I., 1985, A&A, 151, 151

Schneider P., 2015, Extragalactic Astronomy and Cosmology: An Introduction, doi:10.1007/978-3-642-54083-7.

Schneider R., Omukai K., Inoue A. K., Ferrara A., 2006, MNRAS, 369, 1437

Schneider R., Omukai K., Bianchi S., Valiante R., 2012, MNRAS, 419, 1566

Schruba A., et al., 2012, AJ, 143, 138

Schruba A., Bialy S., Sternberg A., 2018, ApJ, 862, 110

Seifried D., Haid S., Walch S., Borchert E. M. A., Bisbas T. G., 2020, MNRAS, 492, 1465

Sembach K. R., Howk J. C., Ryans R. S. I., Keenan F. P., 2000, ApJ, 528, 310

Seo J., Kang H., Ryu D., 2018, Journal of Korean Astronomical Society, 51, 37

Sharda P., Krumholz M. R., 2022, MNRAS, 509, 1959

Sharda P., Amarsi A. M., Grasha K., Krumholz M. R., Yong D., Chiaki G., Roy A., Nordlander T., 2023, MNRAS, 518, 3985

Shaver P. A., McGee R. X., Newton L. M., Danks A. C., Pottasch S. R., 1983, MNRAS, 204, 53

Shen S., Wadsley J., Stinson G., 2010, MNRAS, 407, 1581

Simpson C. M., Pakmor R., Marinacci F., Pfrommer C., Springel V., Glover S. C. O., Clark P. C., Smith R. J., 2016, ApJ, 827, L29

Smith R. J., Glover S. C. O., Klessen R. S., Fuller G. A., 2016, MNRAS, 455, 3640

Spitzer Jr. L., 1942, ApJ, 95, 329

Stanway E. R., Eldridge J. J., Becker G. D., 2016, MNRAS, 456, 485

Stephens T. L., Dalgarno A., 1973, ApJ, 186, 165

Stone E. C., Cummings A. C., Heikkila B. C., Lal N., 2019, Nature Astronomy, 3, 1013

Strong A. W., Moskalenko I. V., Ptuskin V. S., 2007, Annual Review of Nuclear and Particle Science, 57, 285

Su K.-Y., et al., 2018, MNRAS, 480, 1666

Szécsi D., Agrawal P., Wünsch R., Langer N., 2022, A&A, 658, A125

Tanvir T. S., Krumholz M. R., 2024, MNRAS, 527, 7306

Telford O. G., Chisholm J., Sander A. A. C., Ramachandran V., McQuinn K. B. W., Berg D. A., 2024, ApJ, 974, 85

Thompson T. A., Heckman T. M., 2024, ARA&A, 62, 529

Tielens A. G. G. M., 2005, The Physics and Chemistry of the Interstellar Medium

Tokuda K., et al., 2021, ApJ, 922, 171

Tokuda K., et al., 2025, arXiv e-prints, p. arXiv:2501.02190

Veilleux S., Maiolino R., Bolatto A. D., Aalto S., 2020, A&ARv, 28, 2

Villaseñor J. I., et al., 2025, A&A, 698, A41

Waagan K., 2009, Journal of Computational Physics, 228, 8609

Waagan K., Federrath C., Klingenberg C., 2011, Journal of Computational Physics, 230, 3331

Walch S., Wünsch R., Burkert A., Glover S., Whitworth A., 2011, ApJ, 733, 47

Walch S., Girichidis P., et al., 2015, MNRAS, 454, 238

Watkins E. J., et al., 2023, ApJ, 944, L24

Weaver R., McCray R., Castor J., Shapiro P., Moore R., 1977, ApJ, 218, 377

Welty D. E., Lauroesch J. T., Wong T., York D. G., 2016, ApJ, 821, 118

Wise J. H., Abel T., Turk M. J., Norman M. L., Smith B. D., 2012, MNRAS, 427, 311

Wolfire M. G., Hollenbach D., McKee C. F., Tielens A. G. G. M., Bakes E. L. O., 1995, ApJ, 443, 152

Wolfire M. G., McKee C. F., Hollenbach D., Tielens A. G. G. M., 2003, ApJ, 587, 278

Wolfire M. G., Hollenbach D., McKee C. F., 2010, ApJ, 716, 1191

Wu R.-Q., Zhu C.-H., Lü G.-L., Wang Z.-J., Liu H.-L., 2021, Research in Astronomy and Astrophysics, 21, 129

Wünsch R., Walch S., Dinnbier F., Whitworth A., 2018, MNRAS, 475, 3393

Wünsch R., Walch S., Dinnbier F., Seifried D., Haid S., Klepitko A., Whitworth A. P., Palouš J., 2021, MNRAS, 505, 3730

Xu Y., et al., 2024, AJ, 167, 285

Yang R.-z., de Oña Wilhelmi E., Aharonian F., 2014, A&A, 566, A142

Yasui C., Izumi N., Saito M., Lau R. M., Kobayashi N., Ressler M. E., 2024, ApJ, 975, 152

Zamora-Avilés M., et al., 2019, MNRAS, 487, 2200

Zijlstra A. A., et al., 2006, MNRAS, 370, 1961

Zweibel E. G., 2017, Physics of Plasmas, 24, 055402

van Dishoeck E. F., Black J. H., 1988, ApJ, 334, 771